DTIC FILE COPY

①

SECURITY CLASSIFICATION OF THIS PAGE

REPORT DOCUMENTATION PAGE

Form Approved
OMB No. 0704-0188

1a. REPORT SECURITY CLASSIFICATION
UNCLASSIFIED

1b. RESTRICTIVE MARKINGS
NONE

AD-A217 396

3. DISTRIBUTION/AVAILABILITY OF REPORT
APPROVED FOR PUBLIC RELEASE;
DISTRIBUTION UNLIMITED.

5. MONITORING ORGANIZATION REPORT NUMBER(S)
AFIT/CI/CIA- 89-107

6a. NAME OF PERFORMING ORGANIZATION
AFIT STUDENT AT
MERTON COLLEGE OXFORD

6b. OFFICE SYMBOL (If applicable)

7a. NAME OF MONITORING ORGANIZATION
AFIT/CIA

6c. ADDRESS (City, State, and ZIP Code)

7b. ADDRESS (City, State, and ZIP Code)
Wright-Patterson AFB OH 45433-6583

8a. NAME OF FUNDING/SPONSORING ORGANIZATION

8b. OFFICE SYMBOL (If applicable)

9. PROCUREMENT INSTRUMENT IDENTIFICATION NUMBER

8c. ADDRESS (City, State, and ZIP Code)

10. SOURCE OF FUNDING NUMBERS

PROGRAM ELEMENT NO.	PROJECT NO.	TASK NO	WORK UNIT ACCESSION NO.

11. TITLE (Include Security Classification) (UNCLASSIFIED)
HEAT TRANSFER NEAR THE ENTRANCE TOA A FILM COOLING HOLE IN A GAS TURBINE BLADE

12. PERSONAL AUTHOR(S)
Aaron R. Byerley

13a. TYPE OF REPORT
THESIS/~~DISSERTATION~~

13b. TIME COVERED
FROM ________ TO ________

14. DATE OF REPORT (Year, Month, Day)
1989

15. PAGE COUNT
229

16. SUPPLEMENTARY NOTATION
APPROVED FOR PUBLIC RELEASE IAW AFR 190-1
ERNEST A. HAYGOOD, 1st Lt, USAF
Executive Officer, Civilian Institution Programs

17. COSATI CODES

FIELD	GROUP	SUB-GROUP

18. SUBJECT TERMS (Continue on reverse if necessary and identify by block number)

19. ABSTRACT (Continue on reverse if necessary and identify by block number)

DTIC
S ELECTE D
FEB 01 1990
D Cb

Original contains color plates: All DTIC reproductions will be in black and white

90 02 01 038

20. DISTRIBUTION/AVAILABILITY OF ABSTRACT
☒ UNCLASSIFIED/UNLIMITED ☐ SAME AS RPT. ☐ DTIC USERS

21. ABSTRACT SECURITY CLASSIFICATION
UNCLASSIFIED

22a. NAME OF RESPONSIBLE INDIVIDUAL
ERNEST A. HAYGOOD, 1st Lt, USAF

22b. TELEPHONE (Include Area Code)
(513) 255-2259

22c. OFFICE SYMBOL
AFIT/CI

DD Form 1473, JUN 86

Previous editions are obsolete.

SECURITY CLASSIFICATION OF THIS PAGE

AFIT/CI "OVERPRINT"

HEAT TRANSFER
NEAR THE ENTRANCE TO A FILM COOLING HOLE
IN A GAS TURBINE BLADE

Accesion For
NTIS CRA&I ☑
DTIC TAB ☐
Unannounced ☐
Justification
By
Distribution /
Availability Codes
Dist | Avail and/or Special
A-1

Aaron R. Byerley

Merton College
Oxford

A thesis submitted in partial fulfilment of the requirements of the degree of Doctor of Philosophy at the University of Oxford, Trinity Term 1989.

Department of Engineering Science
Parks Road, Oxford

To Sue, Ashley, and Jonathan

ABSTRACT

A thesis submitted in partial fulfilment of the requirements of the degree of
Doctor of Philosophy at the University of Oxford, Trinity Term 1989.

Aaron R. Byerley
Merton College

Heat Transfer Near the Entrance to a Film Cooling Hole In a Gas Turbine Blade

Film cooling is a method used to prevent jet engine turbine blade failure due to overheating. It consists of bleeding relatively cool air from the engine's compressor stage and discharging it through small holes in the turbine blade surface. This air provides a protective, insulating film which keeps the blade surface temperature well below the destructively high temperature levels of the combustor gases. This thesis presents for the first time, detailed pictures of the convective heat transfer distribution on the wall of an internal turbine blade passage near the entrance to a film cooling hole. The physical situation was modelled at 100X geometric scale as flow extraction into a single circular hole from a two-dimensional, fully developed, turbulent channel flow. High resolution heat transfer measurements were made using a transient technique with liquid crystals as surface temperature indicators. During the experiments, the two-dimensional channel Reynolds number was held constant while the flow extraction rate was varied for each of four hole inclination angles (90°, 150°, 30°, and 30° *sideways* relative to the approach flow direction). The main region of heat transfer enhancement was found to be downstream of the hole with local heat transfer levels up to 6.5 times the levels associated with turbulent channel flow. Additional experimental, analytical, and computational flow field studies showed that the enhancement was caused mainly by the removal of the upstream boundary layer and the formation of a new laminar boundary layer at the downstream hole edge. This new boundary layer was also influenced by downwash from a vortex pair. The detailed heat transfer data and the descriptions of the enhancement mechanisms presented in this thesis will be important to jet engine designers in their attempts to improve turbine blade cooling.

ACKNOWLEDGEMENTS

I am deeply indebted to Professor Terry Jones for his energetic, enthusiastic, and inspirational support and supervision over the past three years. I am also very grateful to Dr. Peter Ireland for introducing me to the transient method and the tunnel operation. I was fortunate to be able to meet frequently with both Peter and Terry for progress reviews and technical discussions. Much credit must also be given to Pat Timms for his expert technical assistance and professional craftsmanship. Pat's creativity and problem solving abilities were a source of constant amazement. I would also like to express my appreciation to my fellow research student, Zuolan Wang, for providing assistance during the experiments.

Almost everyone at the Osney Lab contributed in some way to this research effort, although regrettably I will only be able to mention a few. I would like to thank Paul Bonnet for assistance with the shear-sensitive liquid crystals; Lawrence Morland for providing the two-dimensional analytical flow field predictions; Ian Pitcher for the design and construction of several electronic devices used during the experiments; Dr's Roger Ainsworth and Martin Oldfield for their helpful comments and suggestions made during periodic Lab presentations; John Allen for providing help and advice on photographic techniques and equipment; Dr. Bernard Bewley for introducing me to **Fluent**; Dr. Simon Hogg for describing the internal workings of CFD codes; Ken Dunford for solving various computer problems; Esther Rose for tracking down obscure technical papers; Judith Takacs for the experimental apparatus drawings; Jon Mooney and Janet Hovard for the experimental apparatus photographs; and Jo Hoare and Sarah Harrison for performing the never ending task of ordering supplies.

My liaison with *Rolls-Royce* engineers was also invaluable. I benefitted greatly from technical discussions with Rob Davenport, Chris Graham, Bill Pierce, Dave Bryant, Sarah Ashton, Dave Hicklin, and Jenny Bonsell. *Rolls-Royce plc* also provided funding for the research program.

I would like to express my deep appreciation to my wife and children for their cheerful encouragement, warm support, and understanding over the duration. I am also grateful to my parents, grandparents, brothers, and sisters and to my close friend John Gills.

Finally, I am extremely grateful to Col Michael L. Smith, the US Air Force Academy, and the US Air Force Institute of Technology for the opportunity to study at Oxford.

TABLE OF CONTENTS

Chapter 1 INTRODUCTION 1

1.1 Historical Background of Blade Cooling 1
1.2 Survey of Cooling Methods 2
1.3 The Need for Detailed Heat Transfer Information 5
1.4 The Present Work 7
1.4.1 Similarity considerations 7
1.4.2 Simplifications and approximations 8
1.5 Contents of Thesis 10
1.5.1 Thesis overview 10
1.5.2 Principal accomplishments 12

Chapter 2 THERMODYNAMIC MODELLING OF FILM COOLING 12

2.1 Ideal Cycle 14
2.2 Non-Ideal Cycles with Film Cooling 15

Chapter 3 EXPERIMENTAL METHOD 24

3.1 Summary of the Method 24
3.2 Thermochromic Properties of Cholesteric Liquid Crystals 28
3.3 Previous Heat Transfer Work with Liquid Crystals 33
3.3.1 Thermal-flow visualization 34
3.3.2 Steady-state method 34
3.3.3 Transient method 35
3.4 Issues Related to Data Reduction 37
3.4.1 Characteristic length 37
3.4.2 Reference velocity and temperature 38
3.4.3 Material properties 41
3.4.4 Radiation effects 42
3.4.5 Translating from Nu_L and Re_L to Nusselt and Reynolds numbers based on bulk properties 43

Chapter 4 APPARATUS, INSTRUMENTATION, AND PROCEDURE 44

4.1 Experimental Apparatus 44
4.1.1 The Tunnel 44
4.1.2 The Test Section 48

4.2 Experimental Instrumentation 49
  4.2.1 Temperature measurements 51
    4.2.1.1 Liquid crystals 51
    4.2.1.2 Thermocouples 52
      4.2.1.2.1 A Check for Stem Conduction Losses 52
      4.2.1.2.2 A Check for Radiation Tip Losses 53
      4.2.1.2.3 Thermocouple Reference Junctions 54
  4.2.2 Flow Parameter Measurements 54
  4.2.3 Data Acquisition 55
4.3 Experimental Procedure 58

Chapter 5 EXPERIMENTAL HEAT TRANSFER RESULTS 61

5.1 Previous Work 61
5.2 Base-Level Heat Transfer Results 64
5.3 Enhancement Factor Contours 67
5.4 Effects of Varying Experimental Parameters 86
  5.4.1 Effect of varying the hole inclination angle 86
  5.4.2 Effect of varying Re_L 91
  5.4.3 Effect of varying the upstream velocity and temperature profiles 92
5.5 Uncertainty Analysis Issues 95
  5.5.1 Estimate of the uncertainty in h 95
  5.5.2 Using uncertainty analysis to choose T_{gas} and $T_{crystal}$ 96

Chapter 6 EXPERIMENTAL FLOW FIELD STUDIES 100

6.1 Smoke Visualization 100
6.2 Surface Flow Visualization 104
  6.2.1 Water injection 104
  6.2.2 Oil-of-wintergreen method 106
  6.2.3 Shear-stress sensitive liquid crystals 109
6.3 Wall Static Pressure Measurements 112
  6.3.1 Pressure measurement procedure 112
  6.3.2 Wall static pressure results 114
6.4 Velocity Profile Measurements 118
6.5 Temperature Profile Measurements 122
6.6 Boundary Layer Tripping Study 124

Chapter 7 ANALYTICAL HEAT TRANSFER PREDICTIONS 129

7.1 Predicted Results for the Two-Dimensional (Slot) Case and Comparisons with Experimental Results 129
7.2 Predicted Results for the Three-Dimensional Case and Comparisons with Experimental Results 142

Chapter 8 THREE-DIMENSIONAL COMPUTATIONAL STUDIES 146

8.1 Computational Details 146
8.2 Numerical Heat Transfer Predictions 152
8.3 Numerical Flow Field Predictions 157
8.4 Additional Insight Provided by the Computational Results 170
8.4.1 Possible reason for the underprediction of h 170
8.4.2 "Vortex line" model 171
8.4.3 Location of peak value of h 171

Chapter 9 BLADE METAL TEMPERATURE PREDICTIONS 176

9.1 Previous Work 176
9.2 Computational Details 179
9.3 Computational Results 183

Chapter 10 EXPERIMENTAL Cd MEASUREMENTS 190

10.1 Previous Work 191
10.2 Experimental Results 192

Chapter 11 CONCLUSIONS 197

11.1 The Salient Results 197
11.2 The Mechanisms Responsible for Enhancement 198
11.3 Extensions of the Present Work 201

APPENDIX

A. Details of the Thermodynamic Models of Film Cooling 204
B. Details of the Uncertainty Analysis 213
  B.1 Moffat-Kline method 213
  B.2 Saabas-Arora-Abdel Messeh method 215
  B.3 An independent check provided by a second liquid crystal coating 219
  B.4 Uncertainty analysis summary 223

REFERENCES 224

NOMENCLATURE

A	area, m^2
A_c	cross-sectional area, m^2
a	speed of sound, m/s
C_d	hole discharge coefficient
C_p	coefficient of pressure
D	hole diameter, m
D_h	hydraulic diameter, m
EF	local heat transfer enhancement factor
$\overline{EF}$	area-averaged heat transfer enhancement factor
F	jet engine thrust, N
f	fuel-to-air ratio
h	convective heat transfer coefficient, $W/m^2\ K$
h_f	heating value of fuel, J/kg
h_o	base-level heat transfer coefficient, $W/m^2\ K$
k	thermal conductivity, $W/m\ K$
L	characteristic length of duct, m
L_{hole}	length of film cooling hole, m
M_o	Mach number at engine inlet
$\dot{m}_{coolant}$	coolant mass flow rate, kg/sec
$\dot{m}_f$	fuel mass flow rate, kg/sec
$\dot{m}_o$	total mass flow of air through engine, kg/sec
Nu	Nusselt number
Nu_L	Nusselt number based on L
n_x, n_y	liquid crystal refractive indices
$\dot{\mathcal{P}}_{ke}$	increase in engine air's kinetic energy, J/s
P	liquid crystal molecular pitch; thermocouple stem perimeter, m
Pr	Prandtl number
P_{t1}	total pressure at upstream reference location, N/m^2
P_1	static pressure at upstream reference location, N/m^2
P_2	static pressure at film cooling hole exit, N/m^2
q''_o	heat flux at the wall, W/m^2
R	final experimental result
Re_L	Reynolds number based on L
s	entropy, $J/kg\ K$
St	Stanton number
SR	suction ratio (average hole velocity/u_{cl})
ST	specific thrust, $N\ s/kg$
T	temperature, K

$T_{crystal}$	liquid crystal colour play temperature, K
T_{gas}	gas temperature, K
$T_{initial}$	initial temperature, K
$T_{centreline}$	centreline gas temperature, K
T_{bulk}	bulk temperature, K
$T.E.T$	turbine entry temperature, K
t	time, s
$TSFC$	thrust specific fuel consumption, $(\dot{m}_f\ /F,\ \frac{U_o}{h_f \eta_{pr} \eta_{th}})$
U_o	engine inlet velocity, m/s
u, v, w	components of velocity, m/s
u_{bulk}	bulk velocity, m/s
u_{cl}	centreline velocity, m/s
u_{∞}	freestream velocity, m/s
x, y, z	rectangular coordinates, m
$x_1, x_2, \ldots, x_N$	measured quantities
W	slot width, m
$\dot{W}$	rate at which work is performed, J/s

Greek Letters

α	thermal diffusivity, m^2/s
β	non-dimensional heat transfer coefficient
δ	hydrodynamic boundary layer thickness, m
ϵ	$\dot{m}_{coolant}\ /\ \dot{m}_o$; emissivity
γ	gas property, $\frac{C_p}{C_v}$
η_o	overall efficiency $(\frac{FU_o}{\dot{m}_f h_f},\ \eta_{th}\eta_{pr})$
η_{th}	thermodynamic efficiency, $(\frac{\dot{P}_{ke}}{\dot{m}_f h_f})$
η_{pr}	propulsive efficiency, $(\frac{FU_o}{\dot{P}_{ke}})$
θ	non-dimensional temperature
λ	wavelength, μm
μ	viscosity of air, $kg/s\ m$
ν	kinematic viscosity of air, m^2/s
π_c	compressor pressure ratio
ρ	mass density, kg/m^3
$\sqrt{\rho c k}$	thermal product of perspex, $\frac{W}{m^2 K} sec^{1/2}$
σ	Stefan-Boltzmann constant
τ	shear stress, N/m^2; total temperature ratio

1 INTRODUCTION

This thesis describes an experimental and theoretical study of the heat transfer and flow field near the entrance to a gas turbine blade film cooling hole. Such film cooling holes are used extensively in modern jet engines and yet the important detail around the entrance has not been examined before. The work described here provides an understanding of the relevant phenomena which, in addition to being a contribution to basic fluid mechanics, hopes to provide a basis for more exact turbine blade thermal design.

1.1 Historical Background of Blade Cooling

Since the early 1940's, aircraft jet engine designers have sought to increase the turbine entry temperature (*T.E.T.*) in order to increase thrust and to reduce fuel consumption. The increase in *T.E.T.* over time has meant that the 1000 K *T.E.T.'s* of both Sir Frank Whittle's *W1* engine and Dr. Hans von Ohain's *Junkers Jumo 004B* engine, were less than the coolant temperatures used today in many gas turbine engines whose *T.E.T.'s* approach 1800 K. This huge increase in operating temperature has been the major factor in the dramatic improvement in engine performance since those early days of gas turbine engine development. Although the *Jumo 004B* powered the twin-engined *Messerschmitt Me262* aircraft to speeds of 540 miles/hour in level-flight, the engine's thrust-to-weight ratio was only about 1.25 **(Petty and Henderson, 1986)**. Today, the *Pratt and Whitney F100* engine which powers the *General Dynamics F-16*, has a thrust-to-weight ratio of 7.4, almost 6 times that of the *Jumo* engine. Progress has also been remarkable in terms of maximum thrust; Whittle's *W1* produced about 1000 lb of thrust while today's most powerful *Rolls-Royce* engine, the *RB211-524*, delivers 60,600 lb. Despite this tremendous increase in thrust, the thrust-specific- fuel consumption (*TSFC*) of the *RB211-524* is only 1/4 that of the *W1* **(Frisch, 1988)**.

Clearly the motivation for increasing the *T.E.T.* is strong. However there has always been a practical limit on *T.E.T.* due to turbine blade life considerations as the turbine operates in an extremely hostile environment, not only hostile in terms of temperature, but also in terms of pressure and centrifugal loading. Furthermore, today's *T.E.T.'s* are actually 150 K above the blade material's melting point as indicated in Figure 1.1. While significant progress has been made in developing new blade materials which can better withstand the harsh environment, most of the progress in recent years has come through better blade cooling technology. A brief survey of cooling techniques is presented next.

1.2 Survey of Cooling Techniques

The simplest and oldest form of blade cooling is internal convective cooling in which compressor bleed air is brought in at the blade root and sent through internal passages until it is discharged at the opposite end or at the trailing edge. Improvements in convective cooling efficiency come from increased internal cooling passage Stanton number and increased passage length-to-diameter ratio **(Holland and Thake, 1980)**. Research into ways of increasing the passage Stanton number has included

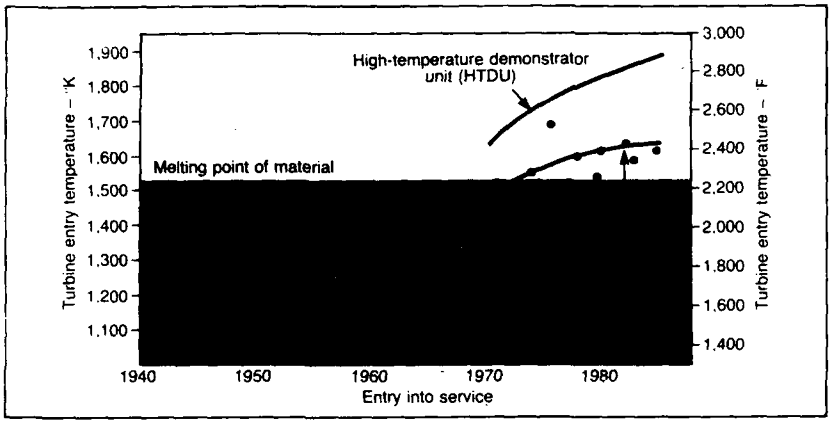

Figure 1.1: **Increase in operating temperatures of Rolls-Royce turbines, showing the benefits of blade cooling from BYWORTH (1986)**

investigations of pedestal and pin fin arrays, and turbulators such as repeated ribs **(Yeh and Stepka, 1984)**. The presence of these devices enhances the heat transfer to levels considerably above the levels associated with the plain passage wall. The main goal, of course, is to increase the heat transfer enhancement without increasing the pressure drop of the flow through the passage.

Another cooling method used frequently in regions of high heat load, such as the leading edge of the blade, is jet impingement. In this method, cooling air from the forward flow channel is directed through an array of small holes to impinge against the inside surface of the blade wall. Very high levels of heat transfer accompany the resultant array of stagnation points. After impingement, the cooling air is often routed back through the internal channel or ejected through holes to be used in film cooling, the next method to be discussed.

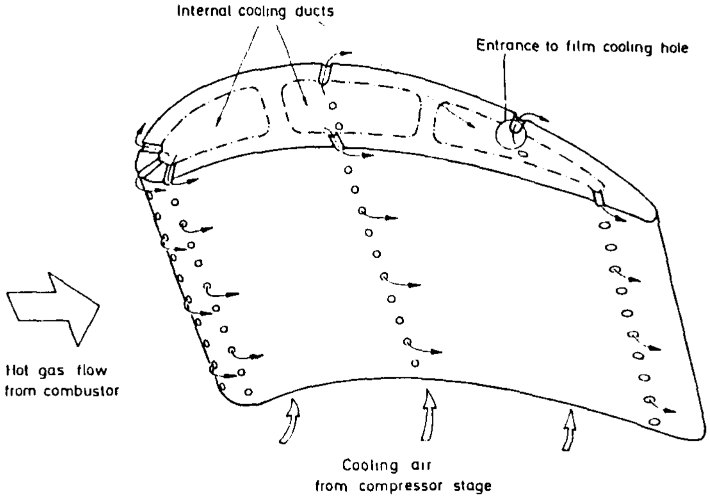
Internal cooling ducts
Entrance to film cooling hole
Hot gas flow
from combustor
Cooling air
from compressor stage

Figure 1.2: **Film cooling**

In film cooling, as illustrated in Figure 1.2, the air is released from the internal blade channel through tiny holes and made to flow along the outside surface of the blade, thus providing an insulating blanket of cooler air between the blade surface and the high temperature gas flow. This reduces the heat flux into the blade and helps to keep the blade metal temperature at an acceptable level. While past research into film cooling has focused almost totally on the insulating effect on the exterior blade surface, the present work shows that significant cooling occurs near the entrance to the film cooling hole on the wall of the internal channel. Since this has never been studied before in great detail, the resultant cooling contribution is probably not being taken fully into account by designers of blade passages.

Unfortunately, all of these methods depend on bleeding a percentage of the engine core air from the compressor stage. This imposes certain aero-thermodynamic penalties which are discussed in greater detail in Chapter 2. Judging from the literature, the ultimate goal is to develop some sort of advanced material such as a fibre-reinforced ceramic which can withstand the operating conditions without the need for cooling air **(Jeal, 1988)**. Until that time however, there is still much potential for improvement in blade cooling technology. The objective is to increase the internal cooling effectiveness so that either the *T.E.T.'s* can be increased for a given coolant flow, or the coolant flow can be decreased for a given *T.E.T.*

1.3 The Need for Detailed Heat Transfer Information

Most of the existing heat transfer information that forms the basis of blade cooling design has come from steady-state experiments which are capable of providing only local area- averaged data. The transient experimental method used in the present work, however, provides very detailed maps of heat transfer distribution. This data can be used to provide more precise convective boundary conditions for numerical solutions to the conduction equation thus yielding more accurate blade metal temperature predictions. This will enable proposed cooling designs to be evaluated more thoroughly during the earlier stages of design, rather than later when the design is in hardware form undergoing testing in a demonstrator unit.

Detailed and accurate blade metal temperature predictions are important mainly because turbine blade failure is a local phenomena. One such failure mode that arises in steady state engine operation is creep, a severe deformation caused by prolonged exposure of the blade to high stresses at high temperatures. High temperature *oxidation is also* a *problem* especially with the stronger superalloys. Finally, thermal fatigue occurs as the result of repeated cycling through the high thermal stresses associated with the temperature transients that are present during engine start-up and later when the engine is throttled from one *T.E.T.* setting to another **(Oates,1978)**. Therefore, a good cooling design must not only keep the maximum blade metal temperature within acceptable levels, but must also reduce the local temperature gradients.

Designers also need to have detailed blade metal temperature predictions to allow for the normal deformation of the blade geometry to prevent mechanical interference caused by differential thermal expansion. Obviously, a mistake in this area can lead to catastrophic failure because of the many precisely dimensioned parts operating at close clearances in a hostile environment; clearances of 50 microns are sometimes required between stationary and rotating parts operating at 9000 rpm in the presence of flows leaving the combustor at 1800 K and 30 atmospheres **(Metzger and Mahle, 1983)**.

Detailed heat transfer data can also be used indirectly to improve blade cooling designs by providing a basis of comparison for computational results. In the present work, numerically predicted patterns of heat transfer enhancement are shown which closely match the patterns observed experimentally. In this way, computational results can be validated which may one day lead to the development of reliable CFD prediction techniques for use in blade cooling design.

Finally, detailed results are flexible in that they can always be averaged over area at some later time. This was done in the present study to better evaluate the overall effect of varying important geometrical and flow parameters.

1.4 The Present Work

This thesis describes a detailed experimental, analytical, and computational investigation of the heat transfer near the entrance to a film cooling hole, a region shown in Figure 1.2. The objective was not only to add to the collection of convective boundary conditions that exist between the internal blade surface and the coolant but also to obtain a solid understanding of the physical reasons behind the observed heat transfer phenomena. This physical understanding will increase the confidence level with which the heat transfer data may be applied in actual cooling passage design.

1.4.1 Similarity Considerations

The important hole/duct geometry and flow conditions were modelled in a large scale (100X), two-dimensional blade cooling passage to allow for detailed observation. The duct-to-hole hydraulic diameter ratio was 5.45 thus falling within the range of ratio's in actual blades of 5 to 15. The hole length-to- diameter ratio (L_{hole}/D) was 10 which is one end of the range in actual blades of 5 to 10. Both ends of the hole were made sharp-edged which is consistent with the results of typical blade production techniques. The hole inclination angle was also varied, as shown in Figure 1.3, to represent the possible orientations of the cooling hole to the duct. Although the

150° *hole* is not common in actual blades, it does represent an extreme case which yields valuable insight into the overall effect of hole inclination angle.

The important flow similarity parameters, namely the duct Reynolds number and the hole velocity (or suction) ratio, were typical of those in present engines. The Reynolds number based on duct height and centreline velocity (Re_L) was held constant at a nominal value of $2.5(10^4)$. The ratio of the average hole velocity to the duct centreline velocity, which from this point on is called the *suction ratio* (SR), was varied from 0 to 8. Air at approximately $100^\circ C$ was used as the test gas, so the Prandtl number was matched exactly (since the Prandtl number for air at both $100^\circ C$ and $1100^\circ C$ is 0.705).

1.4.2 Simplifications and Approximations

While a number of geometric and flow parameters were reproduced in the experimental situation, certain simplifications and approximations were necessary. The simplifications were made to provide a model of the general case so that the most important heat transfer and flow features common to a wide range of film cooling problems could be studied and identified. The resulting heat transfer data could then be applied to specific cases, as appropriate, based on an understanding of the mechanisms involved. The simplifications included: modelling the internal blade passage as a two-dimensional duct; providing a well defined inlet condition (fully developed, turbulent flow); examining a single hole, thereby neglecting multiple hole interaction; and finally using a smooth wall surface (since the actual roughness found in a blade was not scaled up 100X along with the other geometrical features).

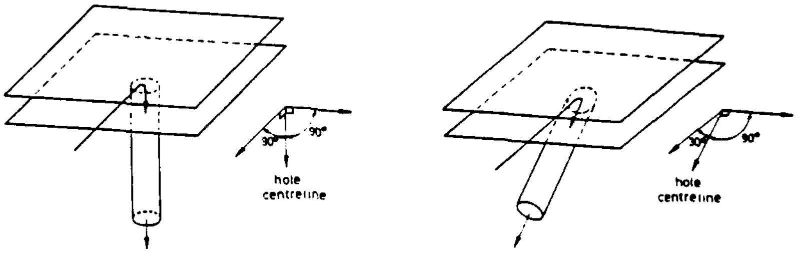
30°
90°
hole
centreline
30°
90°
hole
centreline

90 DEGREE HOLE

150 DEGREE HOLE

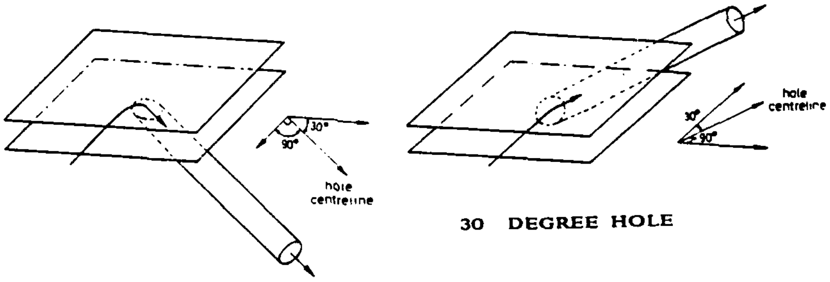
30°
90°
hole
centreline
30°
90°
hole
centreline

30 DEGREE HOLE

SIDEWAYS HOLE
(90 DEGREE HOLE ANGLED SIDEWAYS
AT 30 DEGREES FROM HORIZONTAL)

Figure 1.3: **Hole inclination angles.**

Also several approximations were made to reduce the experimental situation to a tractable level. First of all, Mach number effects were not investigated. This is fairly simple to justify since the flow in multipass channels is normally kept at low speed for pressure drop considerations. Furthermore, **Dunne (1982)** showed in his study of trailing edge passages that the heat transfer was only a weak function of Mach number. Also, the effect of rotation was not possible to examine within the present experimental apparatus. Although research performed elsewhere has shown that rotation does influence heat transfer within rotor blade cooling passages, the results presented in this thesis should still provide useful, first-order guidance. Furthermore, the results are fully applicable to nozzle guide vanes which remain stationary relative to the engine casing.

1.5 Contents of the Thesis

1.5.1 Thesis overview

The following is a brief overview of the remaining chapters.

- Chapter 2 discusses the thermodynamic modelling of film cooling and shows that the use of film cooling yields increases in both engine specific thrust and thermodynamic efficiency.
- Chapter 3 reviews the theory and application of the transient technique using liquid crystals as surface temperature indicators.
- Chapter 4 describes the experimental apparatus, instrumentation, and procedure.

- Chapter 5 presents and discusses the experimental heat transfer results. Detailed maps of the heat transfer distribution are presented for four hole inclination angles at a number of suction ratios. The effects of changing Re_L and the upstream temperature and velocity profiles are also presented.

- Chapter 6 presents the results of experimental flow field studies which gives insight into the physical reasons behind the observed heat transfer results. These results were obtained from smoke visualization, surface flow visualization, and wall static pressure measurements.

- Chapter 7 consists of two-dimensional analytical predictions of heat transfer downstream of a slot, using a theoretical velocity distribution, and also downstream of a hole, using velocities deduced from measured wall static pressures.

- Chapter 8 describes the three-dimensional computational investigation into the present study. The pattern of heat transfer enhancement was successfully reproduced. Also, the suspected presence of a vortex pair downstream of the hole was confirmed.

- Chapter 9 presents the results of three-dimensional blade metal temperature predictions which show the effect of accounting for the measured cooling contribution near the entrance to a single film cooling hole.

- Chapter 10 presents the experimental results for the hole discharge coefficients showing the important influence of the hole inclination angle.

- Chapter 11 presents the final conclusions regarding the nature of the heat transfer enhancement drawn from the experimental, analytical, and computational results. Possible extensions of the present work are also discussed.

1.5.2 Principal accomplishments

The principal accomplishments of the present work include: the design, construction, and commissioning of a test section which successfully modelled the important flow and geometric parameters near the entrance to a film cooling hole; the discovery and detailed measurement of a well defined region of enhanced heat transfer downstream of the film cooling hole; the comprehensive investigation of the three-dimensional flow field which revealed that the enhancement was due primarily to the removal of the upstream velocity and thermal boundary layers and the effects of "downwash" from a vortex pair; the discovery that the boundary layer downstream of the hole was laminar in nature; and finally, the presentation of the heat transfer data in area-averaged form which can be of immediate use to blade passage designers.

As a result of the present work, the following two papers have been published to date: **Byerley, Ireland, Jones, and Ashton (1988)** and **Byerley, Ireland, Jones, and Graham (1988)**.

2 THERMODYNAMIC MODELLING OF FILM COOLING

To obtain insight into the fundamental reasons for increasing the turbine entry temperature in gas turbine engines, the thermodynamics of the ideal Brayton (or Joule) cycle are reviewed. This is followed by an analysis of two, more realistic, non-ideal thermodynamic models of the film cooling process within a turbojet cycle. Thus an understanding of how film cooling helps to boost two important engine performance parameters, namely specific thrust and thermodynamic efficiency, may be obtained. Specific thrust is

$$ST = \frac{F}{\dot{m}_o}$$

where F is engine thrust and $\dot{m}_o$ is the total mass flow rate of air through the engine. Therefore, for a given thrust rating, increasing the ST allows the designer to reduce the size of the engine inlet thereby reducing engine weight and nacelle drag. This effectively results in an increase in the engine's thrust- to-weight ratio. The second engine performance parameter which increases with $T.E.T.$ is thermodynamic efficiency (η_{th}) where

$$\eta_{th} \equiv \frac{increase\ in\ the\ engine\ flow's\ kinetic\ energy}{energy\ input\ into\ the\ burner}$$

This is important since an increase in thermodynamic efficiency, for a given propulsive efficiency, results in a reduction of the engine's thrust specific fuel consumption ($TSFC$). Even a fractional improvement in $TSFC$ yields significant fuel savings over the lifetime of an engine.

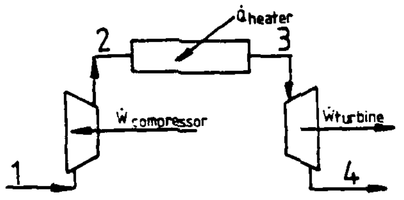

Figure 2.1: **The ideal Brayton (or Joule) cycle.**

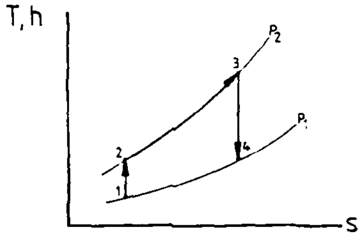

Figure 2.2: **The process representation for the ideal Brayton cycle.**

2.1 Ideal Cycle

The Brayton (or Joule) cycle forms the core of all gas turbine engine propulsion systems. As shown in Figure 2.1, it consists of a compressor, heater, and turbine. The physical basis that allows the Brayton cycle to operate is that lines of constant pressure diverge as temperature increases, as illustrated in Figure 2.2, the temperature-entropy process representation for the ideal case. This figure shows that the higher the temperature leaving the heater and entering the turbine, the larger the enthalpy drop. This drop is proportional to the net power out of the turbine. In the case of a propulsion system, this is equivalent to an increase in ST.

While the ideal Brayton cycle gives us a clear idea of why the specific thrust increases with $T.E.T.$, the reason for an increase in thermodynamic efficiency is

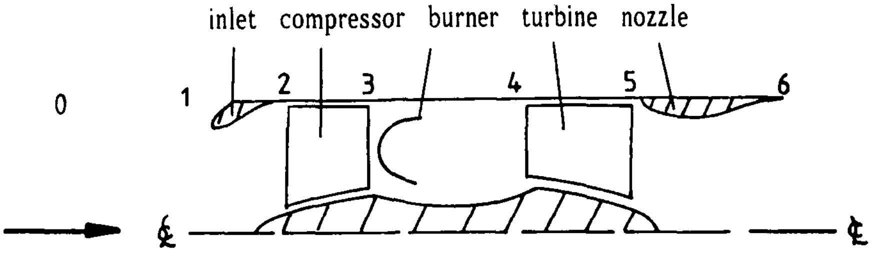

Figure 2.3: **The standard turbojet engine cycle**

more complex. The thermodynamic efficiency for the ideal Brayton cycle is given by

$$\eta_{th} = 1 - \frac{1}{\pi_c^{(\frac{\gamma-1}{\gamma})}}$$

where π_c is the compressor pressure ratio. This expression indicates that thermodynamic efficiency is not a function of $T.E.T.$ at all. When the irreversibilities associated with realistic components are considered, however, η_{th} does indeed increase with $T.E.T.$ as shown in the following section.

2.2 Non-Ideal Turbojet Cycles with Film Cooling

Two thermodynamic models were developed which represent two possible ways of considering the film cooling process operating within a turbojet cycle. Figure 2.3 shows the standard components of a turbojet engine cycle. The thermodynamic analysis of this simple cycle, one without film cooling, is given in many text books. The goal was to modify this cycle to include a realistic and accurate treatment of the thermodynamic effect of film cooling. The two models presented next are similar in that the coolant flow is bled from the compressor outlet. Both models also use a

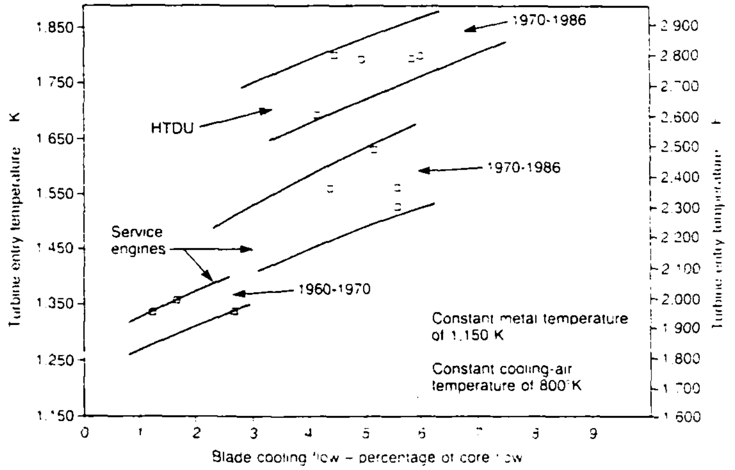

Figure 2.4: **Relationship between *T.E.T.* and percentage coolant flow for Rolls-Royce service engines and the High-Temperature Demonstrator Unit (HTDU) from BYWORTH (1986).**

"real world" relationship between the *T.E.T.* and the fraction of engine mass flow used as coolant (ϵ) defined as

$$\epsilon = \frac{\dot{m}_{coolant}}{\dot{m}_o}$$

According to Figure 2.4, the equation

$$T.E.T. = 5000\epsilon + 1372K$$

represents the best relationship available in actual *Rolls- Royce* service engines of today. Figure 2.4 assumes a constant coolant temperature so the results of this analysis are valid for the case of a fixed engine operating point (flight condition and compressor pressure ratio). The two models differ, however, in the location where the coolant flow is added back to the core flow.

The first model, shown in Figure 2.5 and 2.6 is probably optimistic since all of the coolant flow is added back to the core flow before it passes over the rotor and is therefore capable of doing work. This model assumes that the coolant flow is separated from the core flow at the exit of the compressor and sent through a valve before it is added back to the core flow at the first row of nozzle guide vanes ($NGV's$). The two streams then reach thermal equilibrium in an imaginary, constant pressure, adiabatic mixer before entering an imaginary valve where a pressure drop penalty is imposed. This penalty is a means of accounting for the approximate aerodynamic losses associated with the introduction of film cooling flow into the turbine cascade. Aerodynamic losses occur when the emission of film cooling flow from the blade surface causes slight changes in the effective blade profile and then mixes with the main cascade flow in a turbulent, non-isentropic fashion.

The second model is a more pessimistic treatment since it assumes the coolant flow is not added back to the core flow until after the rotor stage as shown in Figure 2.7 and Figure 2.8. This means that energy as work is not extracted from the coolant flow in the rotor stage. The other features of this model are similar in detail to the first model.

To evaluate these models quantitatively, a detailed component- by-component analysis was performed using the cycle analysis methodology set forth in **Oates (1984)** and is given in Appendix A. Briefly, the analysis made use of energy balances on each component, and a power balance between the compressor and turbine. The analysis began with the calculation of the recovery properties and then pro-

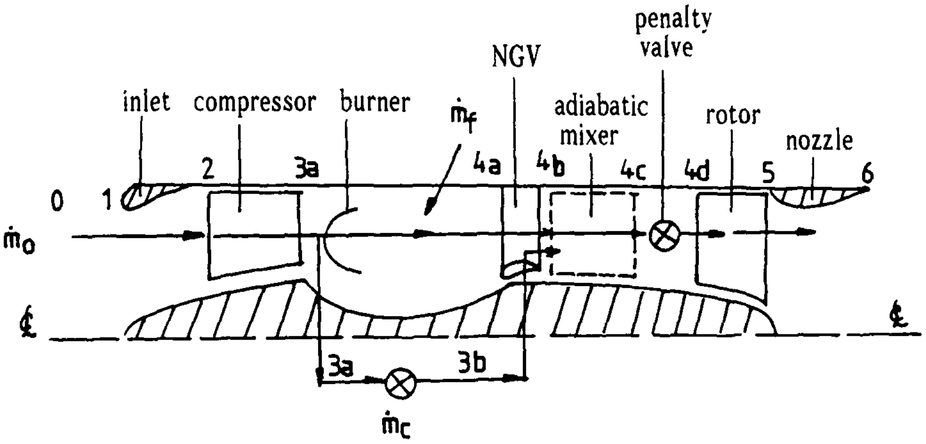
penalty valve
NGV
inlet
compressor
burner
$\dot{m}_f$
adiabatic mixer
rotor
nozzle
0
1
2
3a
4a
4b
4c
4d
5
6
$\dot{m}_0$
℄
℄
3a
3b
$\dot{m}_c$

Figure 2.5: **Model 1- coolant flow is added back to the core flow upstream of the rotor.**

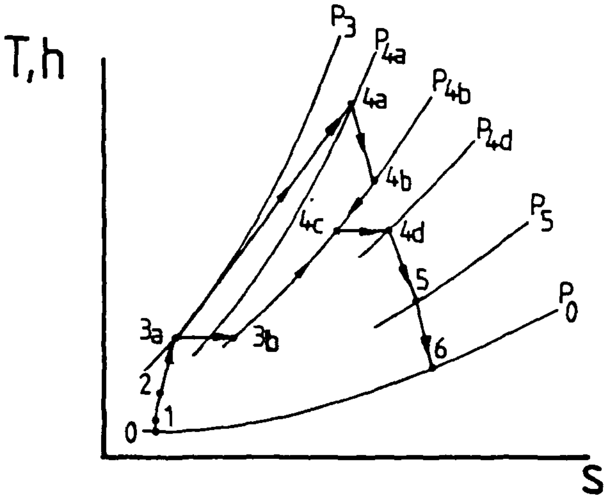
T,h
P_3
P_{4a}
P_{4b}
P_{4d}
P_5
P_0
4a
4b
4c
4d
5
6
3a
3b
2
1
0
S

Figure 2.6: **Process representation for model 1. (Pressure line divergence is exaggerated for clarity.)**

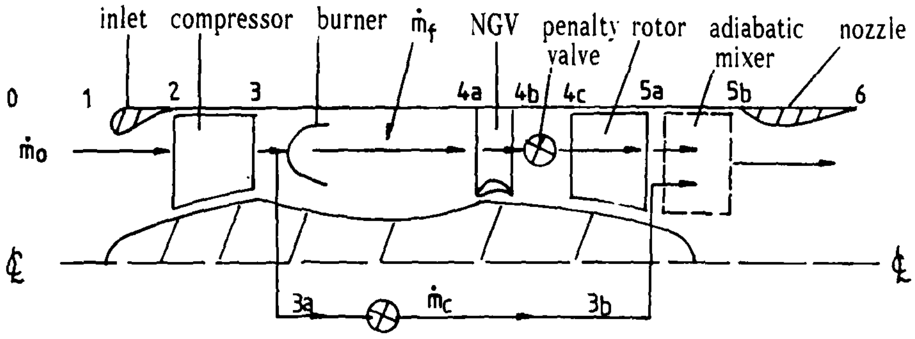
inlet
compressor
burner
ṁf
NGV
penalty valve
rotor
adiabatic mixer
nozzle
0
1
2
3
4a
4b
4c
5a
5b
6
ṁo
℄
℄
3a
ṁc
3b

Figure 2.7: **Model 2- coolant flow is added back to the core flow downstream of the rotor.**

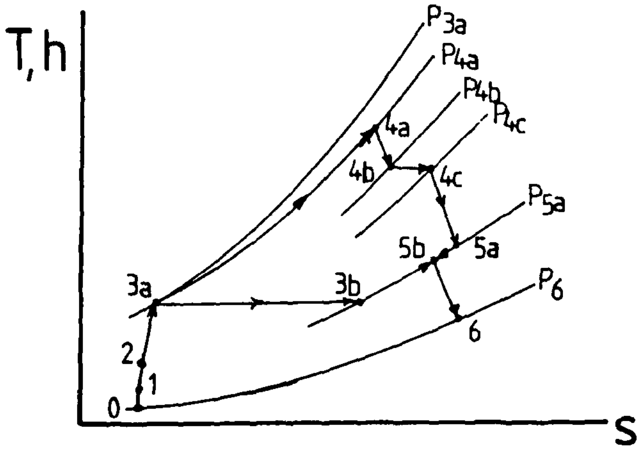
T,h
P3a
P4a
P4b
P4c
4a
4b
4c
P5a
5b
5a
3a
3b
P6
6
2
1
0
S

Figure 2.8: **Process representation for model 2. (Pressure line divergence is exaggerated for clarity.)**

ceeded through each of the cycle's components, starting with the inlet and ending with the nozzle. The total temperature and pressure at the outlet of each component were calculated, thereby fixing the flow's thermodynamic state at that point. Eventually, the velocity at the exit of the nozzle was found. The analysis assumed one- dimensional flow throughout the cycle. However, non-ideal performance was considered through the use of realistic component performance parameters. These performance parameters accounted for the total pressure losses across the diffuser (inlet), burner, NGV, and nozzle; the polytropic efficiencies of the compressor and turbine; and the mechanical efficiency for the power balance between the turbine and compressor. Realistic gas properties were also used; three different pairs of C_p and γ accounted for the effects of fuel addition to the air and the subsequent mixing of the core and the coolant flows. The analysis was performed for a flight condition of Mach 0.7 at a temperature corresponding to the standard altitude at 29,000 feet.

The salient results of this analysis are shown in Figures 2.9 and 2.10 where the incentives for using film cooling to boost $T.E.T.$'s can be seen. Both models show a significant increase in specific thrust and thermodynamic efficiency at all compressor pressure ratios. As expected, the results indicate that the second model, which assumed the coolant was added back to the core flow after the rotor, rather than before, gave a slightly lower level of performance than the first model. Yet the increases in ST and η_{th} are still apparent despite this somewhat pessimistic treatment.

It is interesting to note that Figures 2.9 and 2.10 also illustrate a feature found in actual gas turbine engine designs; engines optimized for maximum η_{th} need a much larger compressor pressure ratio than engines optimized for maximum specific thrust. The results show that for this particular flight condition of Mach 0.7 at 29,000 feet, the optimum π_c for maximum η_{th} is over 30 while the optimum π_c for maximum ST ranges between 12 and 25. This same trend is apparent when comparing the actual $\pi_c's$ of engines designed for transport aircraft with engines designed for combat aircraft. At the maximum engine *rpm* rating, the π_c of the *General Electric CF6-50*, which powers the *Boeing 747*, is 30.4 while the π_c of the *General Electric J79-15*, which powers the *McDonnell Douglas F-4 Phantom*, is 12.9. With respect to blade cooling though, the higher compressor pressure ratio means that the coolant flow is hotter which in turn requires the coolant flow rate be increased in order to reach the same $T.E.T.$ This effect was not modelled in the present analysis since the $T.E.T.$-*coolant flow rate* relationship was based on a constant coolant temperature.

The important conclusion to be drawn from the thermodynamic modelling of film cooling is that increasing the $T.E.T.$, even at the expense of incurring the aerodynamic and thermodynamic penalties inherent in the film cooling process, yields significant improvements in gas turbine engine performance. Of course, the heat transfer data presented in this thesis can be used to improve the internal cooling effectiveness and therefore help to reduce those penalties by decreasing the amount of coolant required to achieve a given $T.E.T.$

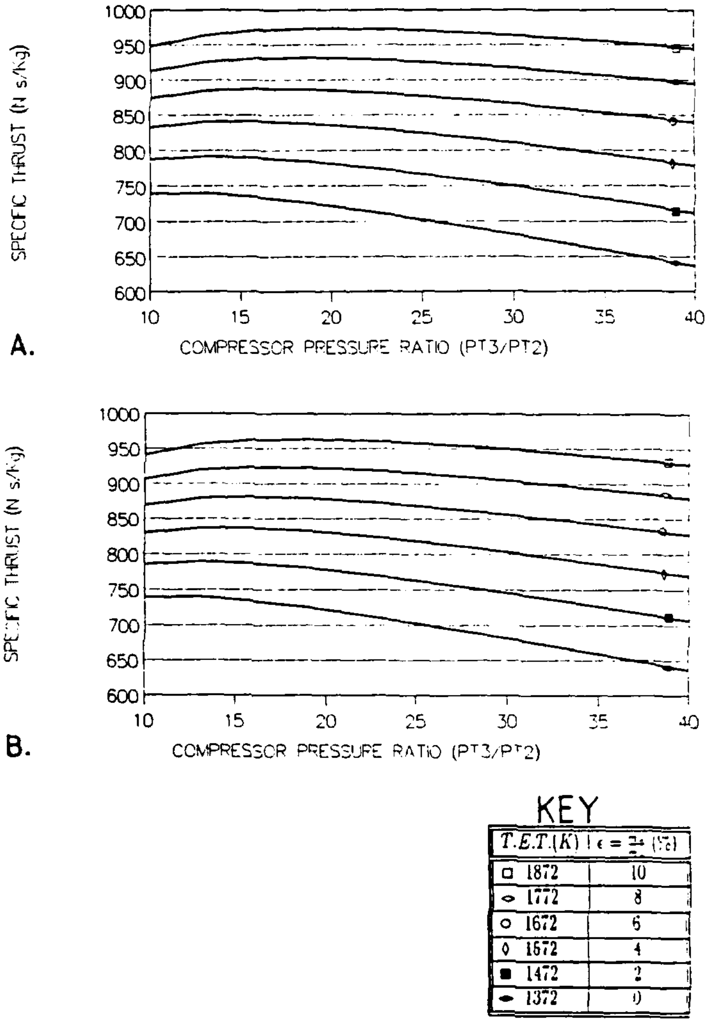

KEY

T.E.T.(*K*)	$\epsilon =$ [illegible] (%)
□ 1872	10
◇ 1772	8
○ 1672	6
◊ 1572	4
■ 1472	2
● 1372	0

Figure 2.9: Effect of *T.E.T.*, % coolant, and compressor pressure ratio on specific thrust. A.) model 1- assuming the coolant flow re-enters the core flow upstream of the rotor. B.) model 2- assuming the coolant flow re-enters the core flow downstream of the rotor.

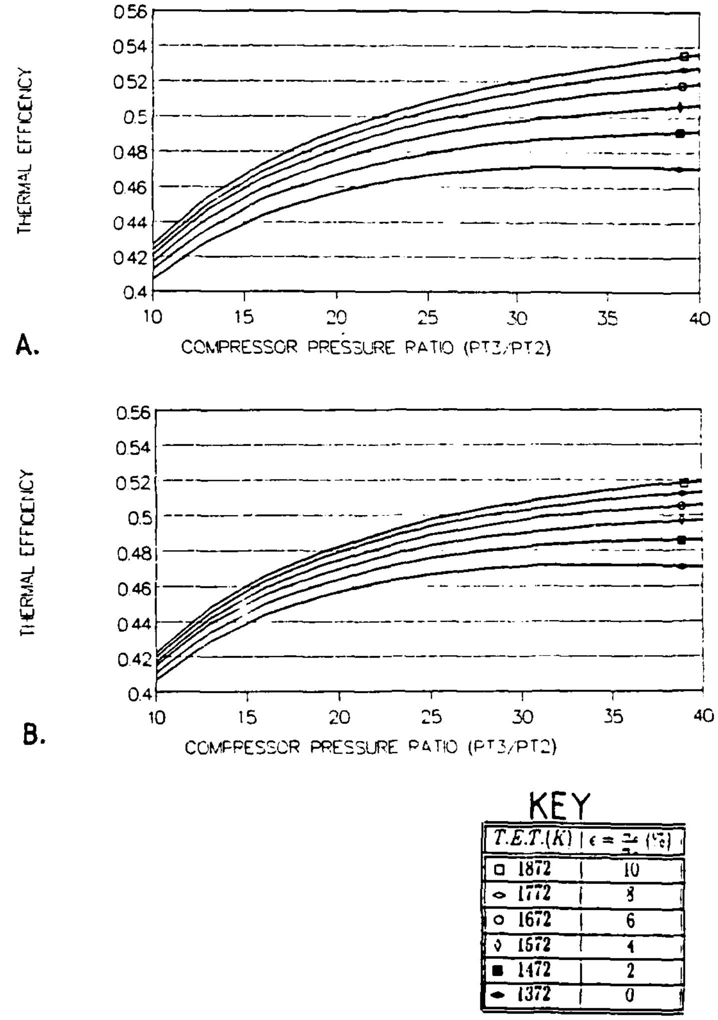

Figure 2.10: **Effect of *T.E.T.*, % coolant, and compressor pressure ratio on thermodynamic efficiency. A.) model 1- assuming the coolant flow re-enters the core flow upstream of the rotor. B.) model 2- assuming the coolant flow re-enters the core flow downstream of the rotor.**

3 EXPERIMENTAL METHOD

The major subject of this thesis is the measurement of the convective heat transfer coefficients within a blade cooling passage. This chapter summarizes the method used in determining the desired values of h. The thermochromic properties of the liquid crystals employed in this method are also explained. This is followed by a review of the previous work involving liquid crystal usage in heat transfer research. Finally, details necessary for data reduction and the subsequent interpretation of results are presented.

3.1 Summary of the Method

The heat transfer measurements were made using a transient test technique employing thermochromic cholesteric liquid crystals as high resolution wall surface temperature indicators. Thermochromic liquid crystals change colour over a known, reproducible range of temperature and can therefore provide highly detailed and accurate pictures of surface temperature distribution. A thin, continuous film of these liquid crystals was applied to the area of interest on one wall of a large (100X) scale, two-dimensional, perspex duct which served as an idealized model of an internal blade cooling passage. A schematic diagram of this duct along with the rest of the tunnel apparatus is given in Figure 3.1. A detail of the test section including the idealized film cooling hole is given in Figure 3.2. Before each experiment began, the tunnel was allowed to reach an isothermal condition at room temperature. Heated air was first directed through a well insulated, upstream plenum chamber, as illus-

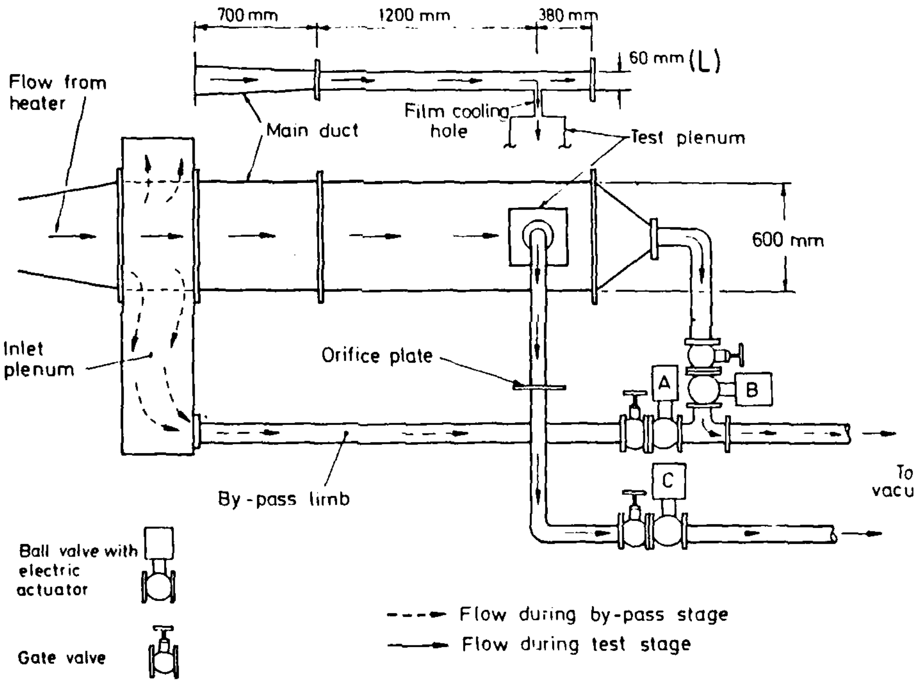
700 mm
1200 mm
380 mm
60 mm (L)
Flow from heater
Main duct
Film cooling hole
Test plenum
600 mm
Inlet plenum
Orifice plate
A
B
C
By-pass limb
To vacu
Ball valve with electric actuator
Gate valve
Flow during by-pass stage
Flow during test stage

Figure 3.1: Schematic diagram of the tunnel apparatus including the idealized internal blade cooling passage (the main duct).

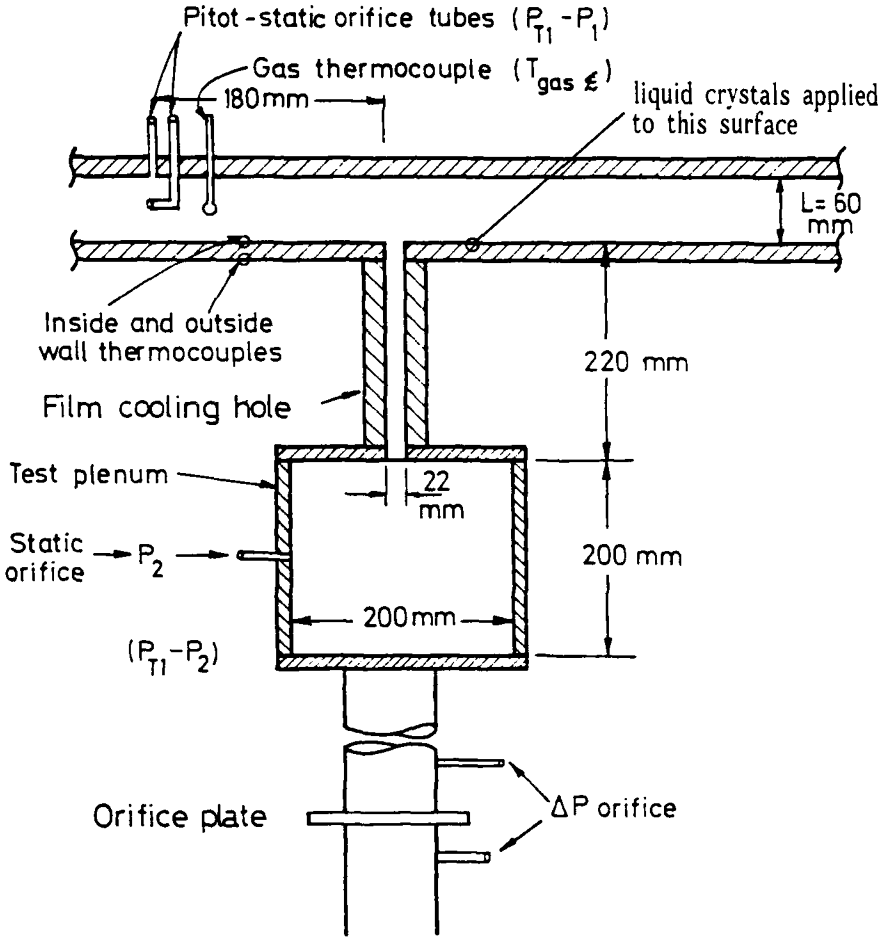
Pitot-static orifice tubes (P_{T1} - P_1)
Gas thermocouple ($T_{gas\,\pounds}$)
180mm
liquid crystals applied to this surface
L= 60 mm
Inside and outside wall thermocouples
220 mm
Film cooling hole
Test plenum
22 mm
Static orifice
P_2
200 mm
200mm
(P_{T1}-P_2)
Orifice plate
ΔP orifice

Figure 3.2: Detail of the test section including the idealized film cooling hole.

trated in Figure 3.1, and then through a similarly insulated bypass limb so eventually the flow could be switched (almost instantaneously) into the test section, thereby approximating a pure step-change in convective heating. As the temperature of the liquid crystals applied to the test wall surface increased, the crystals underwent "colour play" across a narrow, pre-determined band of temperature ($\approx 1°C$). Of course a qualitative understanding of the heat transfer situation could be obtained immediately as the regions on the test surface that changed colour first corresponded to the regions of highest heat transfer. Fortunately, however, quantitative values of h could also be readily obtained from a videotape of the colour play response and a suitable analysis of the unsteady heat conduction into the model. The heat diffusion into the low-conductivity perspex walls of the test surface could be considered one-dimensional, since lateral conduction had a negligible influence on the local surface temperature within the times considered. Furthermore, since the test times were relatively short (on the order of 90 seconds), the thermal pulse did not penetrate through the 12mm thickness of the wall. Therefore the conduction process could also be considered semi-infinite. The governing heat diffusion equation is therefore

$$\frac{\partial^2 T}{\partial x^2} = \frac{1}{\alpha}\frac{dT}{dt} \tag{3.1}$$

and the initial and boundary conditions are

$$T = T_{initial} \ at \ t = 0 \ for \ all \ x \tag{3.2}$$

$$T = T_{initial} \ at \ x = \infty \ for \ all \ t \tag{3.3}$$

$$h(T_{gas} - T_{wall}) = -k\frac{dT}{dx}|_{x=0} \ for \ t > 0 \tag{3.4}$$

Assuming that T_{gas} and h are constant with time, and the thermal properties of the wall are constant with temperature, the exact, analytical solution for these equations is given by

$$\theta = 1 - exp\left(\beta^2\right)(1 - erf(\beta)) = 1 - exp(\beta^2)erfc(\beta) \tag{3.5}$$

where

$$\theta = \frac{(T_{wall} - T_{initial})}{(T_{gas} - T_{initial})} \tag{3.6}$$

and

$$\beta = \frac{h\sqrt{t}}{\sqrt{\rho c k}} \tag{3.7}$$

Since the thermal product of perspex ($\sqrt{\rho c k}$)is known, the time (t) that it takes for the temperature at any point on the test surface wall (T_{wall}) to rise from $T_{initial}$ to $T_{crystal}$ could be used in an iterative solution for h.

3.2 Thermochromic Properties of Cholesteric Liquid Crystals

The characteristic of cholesteric liquid crystals that make them so useful from a heat transfer standpoint is their response to temperature. Cholesteric liquid crystals contain cholesterol and possess the mechanical properties of liquid and the optical properties of solid crystals. When illuminated by white light within a temperature range as narrow as $1°C$, liquid crystals selectively reflect discrete wavelengths of light corresponding to discrete colours in the visible spectrum. At the lower limit of the temperature range, the liquid crystals appear red followed by the rest of the colour spectrum, ending with violet at the upper limit. Above and below the colour play temperature range, the crystals are clear. Since the colour play is reversible, repeatable, and robust, it is quite suitable for experimental measurements. The colour yellow provided a narrow, bright, easy- to-see band so it was chosen to yield the temperature reading and was calibrated to accuracies of $\pm 0.2°C$.

The mechanism responsible for causing the spectrally selective reflections is related to changes in the crystal's molecular structure with temperature. Liquid crystals are arranged in layers which have a helical structure as shown in Figure 3.3. Within each layer, the long axes of the rod-shaped molecules all point in the same direction. The direction of each succeeding layer is offset 10-20 minutes of arc so that the molecules trace out a helical path. The axis of the helix, which is parallel to the *z-axis* in the figure, makes a 90° angle with the supporting substrate (the perspex wall). To quantify the temperature dependent twist of the helix, the pitch length (P) is defined as the longitudinal distance, along the axis of the helix, for the layers to complete one 360° revolution. Therefore, a high level of "twist" corresponds to a small value of pitch. For the liquid crystals used in the present work, the pitch decreased with increasing temperature, eventually corresponding to a length which resulted in the reflection of light within the visible spectrum. This optical phenomenon is now explained.

Consider un-polarized white light that has an angle of incidence aligned with the helical axis of the liquid crystal. This light can be considered the sum of an infinite number of plane- polarized waves, each having a different angle with respect to the direction of the first layer. One of these plane waves makes a zero angle with

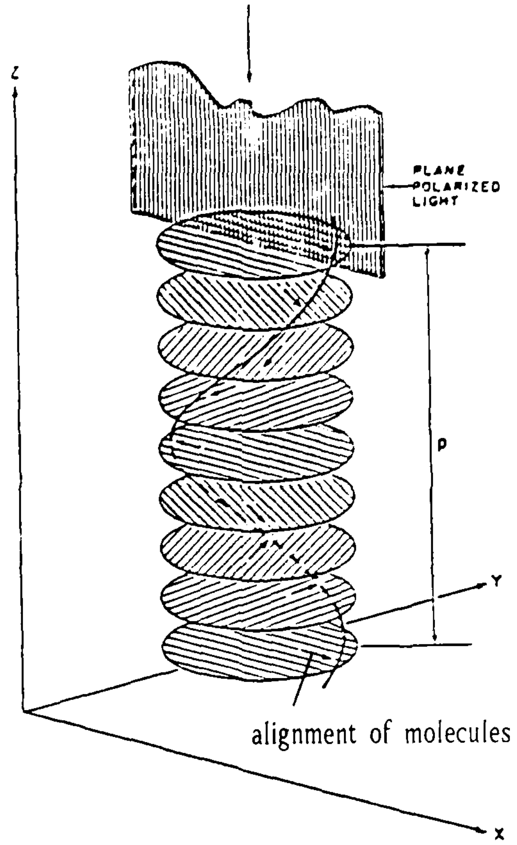
Z
PLANE POLARIZED LIGHT
P
Y
X
alignment of molecules

Figure 3.3: Model of the cholesteric liquid crystal from Makow (1979)

the *x-direction* of the first layer as shown in Figure 3.3. This wave in turn can be considered the sum of left and right-handed circularly polarized waves each containing approximately 50% of the incident energy (the absorptance of liquid crystals is less than 1%). If the crystal substance has a right-handed helical twist then the left-handed circularly polarized wave is at some finite angle to each layer's direction which results in its being transmitted. However, the right- handed circularly polarized wave makes a zero angle with each layer's direction and a small part of the energy is reflected from the interface of the two adjoining molecular layers. The condition for constructive interference of the reflected energy due to the periodicity of the helical molecular structure is satisfied by

$$\lambda_x = n_x P$$

where n_x is the refractive index. Therefore λ_x of the right-handed circularly polarized component of the incident white light is reflected. Also, using the same reasoning, the plane-polarized wave making a 90° angle with the direction of the first layer in the helix reflects light with a wavelength of

$$\lambda_y = n_y P$$

Since the incident white light consists of an infinite number of plane-polarized waves making any angle between 0 and 90° with the direction of the first liquid crystal layer, each wave sees a refractive index between n_x and n_y. The condition for reflection is therefore fulfilled for all wavelengths (λ) in the band between λ_x and λ_y. To eliminate reflections of the transmitted, left-handed circularly polarized components of light from the back surface of the perspex wall, it was painted black ensuring that the transmitted components were absorbed.

It has so far been established that the wavelength of the reflected light (and therefore the colour) for a given crystal substance is dependent upon the helical pitch (P). The pitch dependence on temperature is now explained. The helical pitch is determined by two factors; the twist (or displacement) angle between the layers and the interlayer spacing. When the crystal temperature is increased, its molar volume increases. The dominant effect of this is to increase the displacement angle between adjacent layers of molecules in the helical stack which has a tendency to decrease the pitch (since "twist" increases). Although an increase in molar volume also results in an increase in the intermolecular distance along the helical axis (which tends to increase the pitch), this effect is not as pronounced as the increase in displacement angle. Therefore, the overall effect of increasing the liquid crystal temperature is to decrease the helical pitch.

The following is a brief summary of the thermochromic process that takes place during a heat transfer experiment. Initially, at room temperature the crystals are clear. When the experiment begins the crystals are convectively heated until the helical pitch of their molecular structure decreases to a value which results in a reflection of red light, the longest wavelength within the visible spectrum. As the crystal temperature continues to increase, the pitch continues to decrease causing a reflection of orange, yellow, blue, and then violet light. When the crystal temperature is increased still further, the crystals once again appear clear. Finally, at the end of the experiment the hot gas flow is turned off allowing the crystals to cool and to pass back through the colour spectrum in the reverse order.

Unfortunately, the colour play of liquid crystals in their "raw" form is also sensitive to the effects of normal and shearing forces. To reduce this sensitivity to negligible levels, the liquid crystals are encapsulated with gelatin in a polyvinyl alcohol binder which results in the formation of small spheroids with typical diameters on the order of 5 to 50 microns. In addition to negating the effects of external forces, encapsulation also provides partial protection from the harmful effects of ultraviolet radiation and other environmental contaminants. Furthermore, encapsulation greatly reduces the variation of colour due to the viewing angle. Finally, two or more types of encapsulated liquid crystals, each with a different temperature range, can be mixed together since the colour play of the crystal substances inside the spheroid coatings still occurs independently. A mixture of several liquid crystals results in a matching number of isotherms on the test surface during a heat transfer experiment. Typical results are presented in Chapter 5.

Further details regarding the physics of thermochromic liquid crystals can be found in **Fergason (1964)**, **Makow (1979)**, **McDonnell and Sage (1982)**, **BDH (1986)**, and **Bonnet (1989)**.

3.3 Previous Heat Transfer Work with Liquid Crystals

Liquid crystals have been useful as surface temperature indicators in three main types of heat transfer experimental methods including: qualitative thermal-flow visualization, steady-state, and transient methods. Some examples of prior work are discussed next, focusing particularly on those that have contributed to the method used in the present work. Also, a brief review of new work involving the cold gas transient method is presented.

3.3.1 Thermal-flow visualization

The simplest way to make use of the temperature indicating properties of liquid crystal is to use them for thermal-flow visualization. It is often the case that the standard, steady- state, point-temperature heat transfer methods, which yield only area-averaged results, are unable to reveal the detail which is necessary to understand the physics behind the operative convective heat transfer mechanisms. Liquid crystals have been used to complement these methods simply by revealing detailed pictures of "hot" and "cold" regions without regard to precise temperature levels. Examples where liquid crystals were used to gain a qualitative understanding of the film cooling process can be found in **Brown and Saluja (1978)** and **Linsell (1983)**. **Rhee et al (1984)** used liquid crystals as one means of flow visualization in a study of Taylor-Görtler vortices.

3.3.2 Steady-state method

The most common method for determining h has been to thermally isolate segments of the test surface and to apply a known amount of electrical power to each segment through attached electric resistance heaters. Although the heaters provide a constant heat flux within each segment, the individual power inputs can be controlled so that a series of segments together can produce an approximation to an overall isothermal wall boundary condition. After measuring the power input and the surface temperature for each segment along with the appropriate gas temperature (and after making corrections for conduction and radiation), the value of h can be calculated. The results, however, are regional, area-averaged values of h rather than true, continuous local values. Greater resolution can be obtained, up to a point, by decreasing the segment size and by increasing the number of segments, but this entails great expense.

A variation of this method which yields much better resolution uses a coating of liquid crystals across the top of a single heating element which is designed to reduce lateral conduction to negligible levels while still generating a uniform heat flux boundary condition. The resulting isothermal contours produced by the liquid crystal colour play then correspond to contours of constant heat transfer coefficients. Variations of this method have been proposed by **Cooper, Field and Meyer (1975); Hippensteele, Russell, and Stepka (1981);** and **Simonich and Moffat (1982). Hippensteele, Russell, and Torres (1985)** used the method to determine local values of h along the midchord of a large-scale model of a turbine blade airfoil in a static cascade. **Crane and Sabzvari (1988)** also used a variation of the method to measure h in the presence of laminar Görtler vortices.

3.3.3 Transient method

The current transient method evolved from a transient method which first used phase-change paints and then later liquid crystals to produce isothermal contours.

The method was developed by Jones, and reported in **Clifford, Jones, and Dunne (1983)** and **Dunne (1983)** regarding a study of internal blade trailing-edge cooling passages. Further method development and refinement was reported in **Ireland and Jones (1985), (1986), and (1987a).** Many key concerns regarding the accuracy of this method were addressed and resolved including: the conduction of heat through the perspex wall in a direction parallel to the surface (lateral conduction) was shown to have a negligible effect on the surface temperature rise; the thermal boundary condition produced by the transient method was shown to approximate an isothermal wall boundary condition; the value of h within the test section was experimentally determined to be constant with time, even considering the time variation in the thermal boundary condition within the entrance region of the main duct; the time response of the liquid crystals was found to be on the order of milliseconds which is effectively instantaneous when used in experiments with time scales on the order of 90 seconds; and the thin ($\approx$10 micron) coating of liquid crystals was shown to be "thermally thin" (providing no thermal resistance or capacitance between the flow and the substrate). Other workers have also subsequently used the method and support the above findings including **Metzger and Larson (1986)**; **Saabas, Arora, and Abdel Messeh (1986)**; and **Zharkova, Kiselev, and Khachaturyan (1986)**. Additionally, **Baughn et al (1988)** made a direct comparison between the present transient method and the steady-state, heated-coating method for the measurement of h on a pin fin. The agreement was well within the 7% range of experimental uncertainty.

While the transient method described in this thesis used hot gas passing through a room temperature test section, new experimental work is now taking place using cold gas passing through a pre- heated test section (**Jones and Hippensteele, 1987**) and (**Ireland et al, 1988**). The cold flow transient method is particularly advantageous for high speed flow situations when the energy consumption necessary to heat a large mass flow would be substantial. **Ireland and Jones (1987b)** have also reported on a method using readings from the colour play of two liquid crystals to yield both h and $T_{initial}$, which is useful in cases where the initial temperature in a pre-heated test section cannot be made perfectly uniform. Of course, colour play from multiple crystal coatings can also be used to calculate h and T_{gas} as long as $T_{initial}$ is well defined.

3.4 Issues Related to Data Reduction

This section presents several details regarding the data reduction process which must be specified for a proper understanding of the experimental results. These details include the characteristic length, the reference temperature and velocity, the material properties for air and perspex, and the method for translating from the Nusselt and Reynolds numbers used in the present work to those same parameters based on the hydraulic diameter and bulk properties.

3.4.1 Characteristic length

The length dimension used in the definition of the Reynolds and Nusselt number is L, the distance between the parallel planes forming the top and bottom of the two-dimensional duct as shown in Figure 3.2. The duct can be considered two-dimensional, as far as the test section is concerned, since the duct sides are far enough away that there are no edge effects. The hydraulic diameter of such a duct is $2L$.

3.4.2 Reference velocity and temperature

The reference velocity and temperature are the centreline values measured at the reference location 180mm ($\approx 9D$) upstream of the hole as indicated in Figure 3.2. This location was chosen because it was found to be far enough upstream for the velocity and temperature profiles to be unaffected by changes in the SR. As shown in Figure 3.4, both profiles are in close agreement with the well known *1/7th power law* which is characteristic of fully developed, turbulent channel flow. **Ireland (1987)** also measured the turbulence intensity profile for this same duct and found that it matched the profiles found by other workers. The velocity profile in Figure 3.4 was measured at two Reynolds numbers ($Re_L = 2.0(10^4)$ and $2.5(10^4)$) and for $SR's$ 0 and 8, which represent the two extremes of that flow parameter. Additionally the temperature profile was measured at three different times during the transient test, again for both high and low $SR's$. Therefore, both profiles were effectively constant with respect to the full range of experimental flow parameters, a necessary part of a well specified inlet condition. It is important to point out that the flow upstream of actual film cooling holes does not always correspond to fully developed, turbulent channel flow, but the profiles used in this method provided a well understood starting point so that the effects due exclusively to the flow entering the hole could be studied

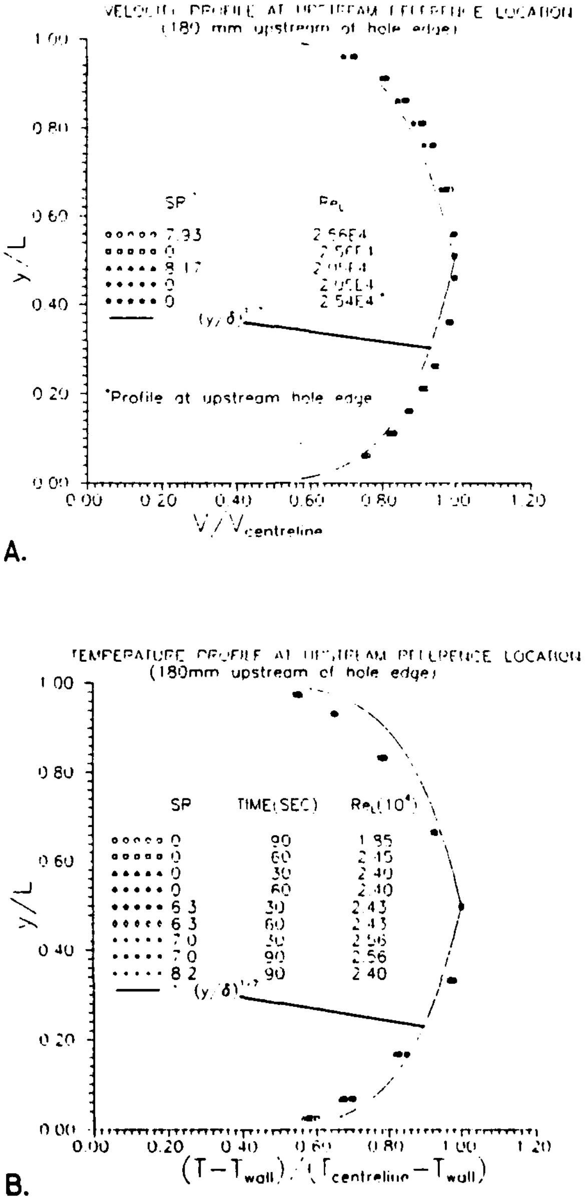

Figure 3.4: Inlet condition at the upstream reference location A.) velocity profile B.) temperature profile.

and understood. Since the profiles were constant, only the centreline values of velocity and temperatures had to be measured during each heat transfer test in order to fully define the energy state at the inlet to the test section. It was also convenient to use these same centreline values as the reference values in the definition of the non-dimensional flow parameters (Re_L and Nu_L). Furthermore, translating these centreline reference values into bulk averaged values is fairly straightforward. Assuming that the 1/7th *power law* adequately describes the velocity and temperature profiles then

$$u = u_{centreline}\left(\frac{y}{\delta}\right)^{1/7}$$

and

$$T = (T_{centreline} - T_{wall})\left(\frac{y}{\delta}\right)^{1/7} + T_{wall}$$

can be substituted into

$$u_{bulk} = \frac{\int_0^\delta u\,dy}{\delta}$$

and

$$T_{bulk} = \frac{\int_0^\delta uT\,dy}{\int_0^\delta u\,dy}$$

to yield

$$u_{bulk} = \frac{7}{8}u_{centreline}$$

and

$$T_{bulk} = \frac{8}{9}(T_{centreline} - T_{wall}) + T_{wall}$$

The upstream centreline temperature was also used as the reference temperature in the definition for h

$$h \equiv \frac{q''_o}{(T_{centreline} - T_{wall})}$$

The above definition for h is different from the definition for h normally used in internal flow which is based on the local bulk temperature, rather than the upstream centreline temperature. The normal definition is desirable when the flow has a preferential direction, since an energy balance can be made in the flow direction, but when the flow has strong three- dimensional features, as in the present work, then the local bulk temperature can no longer be clearly defined. The upstream centreline temperature was therefore a convenient and logical choice for the reference temperature. Furthermore, it is possible to relate the two definitions of h. Since the flow considered in the present work was essentially incompressible ($Mach$ 0.02) with constant properties, the momentum equation can be de-coupled from the governing energy equation. The energy equation is therefore linear in gas temperature. If the thermal boundary condition is an isothermal wall then

$$q''_o = h_{bulk}(T_{bulk} - T_{wall}) = h_{centreline} \ (T_{centreline} - T_{wall})$$

so the two definitions of h can be related according to

$$h_{bulk} = \frac{9}{8} h_{centreline}$$

3.4.3 Material properties (of air and perspex)

The material properties of both air (as the flow) and perspex (as the substrate) must be known to use the present method. In the present work, it is assumed that the properties of air are constant throughout the flow field. Although the transport properties do vary with temperature and thus vary through the boundary layer, the temperature difference is small enough for the property variation to be neglected. The material properties were based on the reference temperature ($T_{centreline}$).

The thermal product of perspex ($\sqrt{\rho ck}$) which is necessary for the solution of h was measured by **Ireland (1987)** and found to be

$$\sqrt{\rho ck} = 569 \pm 29 \frac{W}{m^2 K} sec^{1/2}$$

The implications of this, with respect to experimental uncertainty, are discussed in Chapter 5 and Appendix B.

3.4.4 Radiation effects

Radiation effects were neglected because the maximum temperature differences between important elements were small. The rear surface of the perspex wall remained at room temperature ($T_{initial}$) so there were no radiation losses to the environment. The inside (or test side) surface of the duct wall increased in temperature at close to the same rate (approximating an isothermal wall) so that the temperature differential between various points was small. Therefore convection heat transfer dominated any radiation effects that might have been present. Radiation losses from the gas thermocouple were also small, as shown in Chapter 4.

3.4.5 Translating from Nu_L and Re_L to Nusselt and Reynolds numbers based on bulk properties

Earlier in this chapter, the characteristic length and the reference velocity and temperature values were presented so that taken together the definitions for the non-dimensional parameters are

$$Re_L \equiv \frac{\rho u_{cl} L}{\mu} \qquad and \qquad Nu_L \equiv \frac{h_{cl} L}{k}$$

Therefore, these definitions can be related to definitions based on hydraulic diameter and bulk properties by making the appropriate substitutions as shown below

$$Re = \frac{\rho u_{bulk} D_h}{\mu} = \frac{7}{4} Re_L \qquad and \qquad Nu = \frac{h_{bulk} D_h}{k} = \frac{9}{4} Nu_L$$

These relationships were used to compare the results obtained from the base-level heat transfer experiments (the plain duct heat transfer, without flow extraction effects) with the predictions based on established turbulent channel flow correlations. This comparison is presented in Chapter 5.

4 APPARATUS, INSTRUMENTATION, AND PROCEDURE

This chapter describes the apparatus, instrumentation, and procedure used to obtain the experimental results. Several key features of the apparatus (including the duct piping, electrical resistance flow heaters and heater controls, vacuum pump, inlet plenum, and main duct) were already designed, constructed and commissioned prior to the start of the present work by other members of the Oxford University Internal Cooling Research Group; detailed descriptions of these features are given in **Dunne (1982)** and **Ireland (1987)**. While this chapter describes all aspects of the apparatus, special attention is given to the modifications and additions made to accomplish the present experimental program.

4.1 Experimental Apparatus

The apparatus can actually be thought of as two separate components: the tunnel which for the most part was already in place at the start of the present program, and the test section which was designed and constructed especially for the present work to provide the unique subject of research, namely the entrance to a film cooling hole. Both the tunnel and the test section are described.

4.1.1 The Tunnel

As stated in Chapter 3 (on the Experimental Method), the primary function of the tunnel was to provide a close approximation to a pure step change in convective heating for the test section so that the time for the wall surface temperature to rise from the initial temperature to the colour change temperature could be related to h. This was accomplished by providing an extremely fast flow switching mechanism between two separate flow routes: the bypass limb and the main duct. This enabled the hot flow (and the upstream inlet plenum) to reach thermal equilibrium while the flow was passing through the bypass limb. After the hot flow reached steady state, it was re-directed instantaneously into the main duct and test section. A photograph of the tunnel and the corresponding schematic diagram are given in Figures 4.1 and 3.1. Air was drawn through the heater and into the inlet plenum and then through one of the two flow routes by a high capacity (1000 c.f.m.) vacuum pump. The heater consisted of four banks of 9 kW electrical resistance heater elements, although only two banks were required to achieve the required gas temperature for the present study's flow conditions. The inlet plenum served as a link between the heater and both of the two flow routes; it was insulated with 2" thick slabs of polystyrene to help ensure that the temperature profile of the flow entering the main duct was uniform. As shown in the schematic, there were three gate valves for establishing the correct mass flow conditions; the "B" gate valve for the main duct was used to set the duct Reynolds number (Re_L), the "C" valve for the hole flow was used to set the hole SR, and the "A" valve for the bypass limb was used to obtain a mass flow equal to the sum of the other two flows. Balancing the mass flow between the two routes in this way made certain that the heater did not sense a change in flow rate during the switching process from the bypass limb to the main duct. This enabled the gas temperature to remain constant throughout the 90 second duration of the test. The switching mechanism consisted of three fast acting ball valves which were driven by electrical actuators. Video cameras were used to measure the speed at which the ball valves turned through a 90° arc to open or close. The process took place in less than three videotape frames which corresponds to a time of less than 0.12 seconds. Also incorporated into the present tunnel by earlier workers was a "flow feedback" slide valve, as shown in Figure 4.1, which allowed flow to be drawn backwards from the room into the test section and then into the plenum before leaving through the bypass limb. The slide valve was opened whenever the flow was passing through the bypass limb to keep hot flow from "leaking" into the test section prematurely. The slide was closed immediately prior to switching the flow into the test section.

Also shown in Figure 3.1 are the important dimensions of the main duct. The hole entrance was 1.9 metres downstream of the main duct entrance from the inlet plenum which was long enough to obtain fully developed, turbulent two-dimensional channel flow. Flow in a smooth, straight duct is normally fully developed within approximately 10 hydraulic diameters. The hydraulic diameter of a high aspect ratio, rectangular cross-section duct is $2L$ (120 mm, in this case) so the duct provided a total entrance length of 15.8 hydraulic diameters. As shown in Chapter 3, both temperature and velocity profiles were measured to verify that fully developed flow was indeed obtained. The duct width of 600mm was made relatively large compared to its height of 60mm so that the sidewall effects could be excluded from the area of interest near the hole entrance. The main duct walls were made from commercially

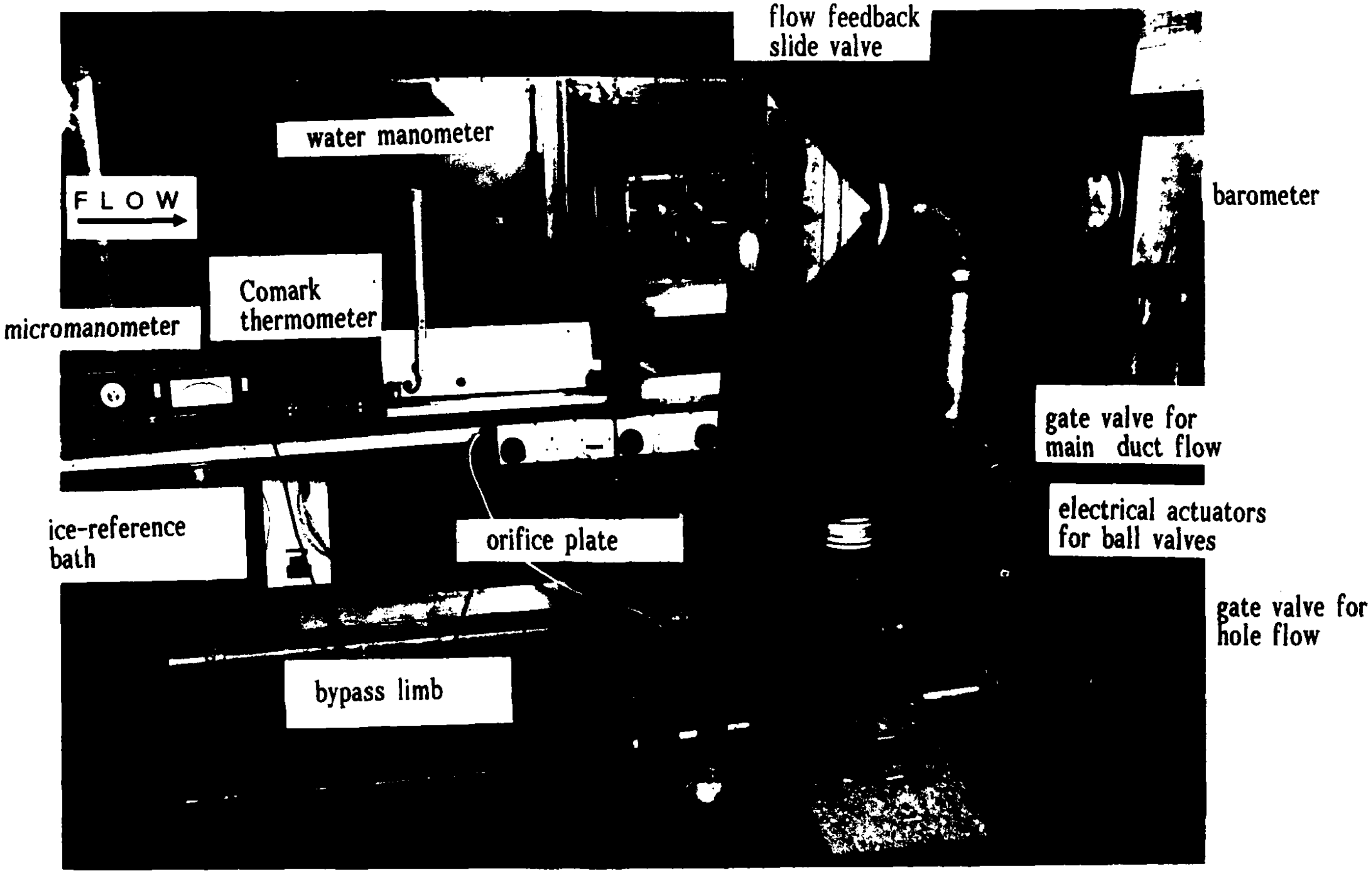
flow feedback slide valve
water manometer
barometer
FLOW
Comark thermometer
micromanometer
gate valve for main duct flow
electrical actuators for ball valves
ice-reference bath
orifice plate
gate valve for hole flow
bypass limb
tunnel trigger

Figure 4.1: **Photograph of the experimental apparatus.**

available perspex sheets, 12 mm in thickness.

4.1.2 The Test Section

The test section is the portion of the main duct which provided the area of interest for the present study. The entrance to the single film cooling hole mounted at four different inclination angles and the associated piping and instrumentation represent the modifications made to the tunnel for the present work.

Figure 4.2 is a photo of the entrance to the 90° *hole* from the perspective of a video camera which was used to record the colour play. The liquid crystals were applied to the surface surrounding the hole both in the upstream and downstream directions (and on either side). In order to accurately map the isothermal contours, grid coordinates were lightly inscribed into the perspex surface around the hole entrance. The depth of the grid lines were made as small as possible so that they would be small relative to the laminar sublayer and therefore be hydrodynamically smooth. The grid lines were also polished to remove any raised edges in the perspex caused by the inscription process. Observations of the liquid crystal colour change during heat transfer runs indicated that the flow was not affected by the grid lines since the colour play contours moved continuously across the surface and not in a stepwise, grid line to grid line fashion.

Figure 4.3 is a photo of the hole itself from behind the outside wall surface while Figure 3.2 is a schematic of the test section showing the important dimensions. The diameter of the film cooling hole was chosen to be 22 mm so that the ratio of hydraulic diameters of the duct to the hole was 5.45, thus falling within the range of ratios in actual blades of 5 to 15. The hole was made large so that the detailed pattern of heat transfer effects inside the hole could be more easily observed. The inside diameter of the hole was machined out of a commercially available cylinder of perspex. The outside diameter of the perspex cylinder was 53mm which provided a wall thickness for the hole of 15.5mm; since heat transfer measurements were made inside the hole as well, the thermal pulse depth was taken into consideration. The length of the hole was chosen to be 220 mm thus providing an L/D for the hole of 10 which fell at one end of the range of 5 to 10 for actual blades. The maximum allowable length of the hole provided enough room for good camera placement so that the colour play within the hole could be viewed. The downstream end of the hole was attached to a cubic plenum with sides 200 mm in length. The size of the plenum was chosen to be large relative to the film cooling hole diameter to prevent interference effects on the exit flow. The edges on both ends of the hole were made sharp to be consistent with the results of typical blade production techniques. All seams were sealed with cellotape and commercial silicone caulking and then carefully leak tested with a soap solution.

4.2 Experimental Instrumentation

This section describes the devices used to measure important experimental parameters such as temperature, pressure, velocity and mass flow. Figure 3.2 reveals the location of the various measurement devices in the test section.

Figure 4.2: **Entrance to the 90°** ***hole.***

Figure 4.3: **Film cooling hole and test plenum.**

4.2.1 Temperature Measurements

There were two types of temperature measurements made in the present work; liquid crystals revealed the surface temperature distribution and thermocouples revealed the gas and initial temperatures. The details of their application and use are now given.

4.2.1.1 Liquid Crystals

The thermochromic properties of liquid crystals were described in Chapter 3 so the discussion in this section is limited to the practical aspects of their use. The type of liquid crystals used in this experimental effort were *microencapsulated chiral nematics* supplied by *BDH Ltd*[1]. The liquid crystals were spray painted on to the areas of interest using an air-brush. Before spraying, however, the liquid crystal mixture from *BDH* was mixed with water and an aqueous binder called *Mowlilith* supplied by *Harlow Chemical Company Ltd*[2]. After coating the test surface with a thin, continuous film, the crystals and the binder were allowed to dry. A black background was painted on the opposite side of the perspex which increased the visual brilliance of the colour play.

The liquid crystals were calibrated at the beginning of the test programme and checked during each run. The calibration procedure involved bringing the perspex wall temperature slowly up to the colour play temperature range given by the manufacturer of 35 to 36°C. When the colour play occurred the flow temperature was held steady so that the colour remained. During a period of about 5 minutes a number of temperature measurements were made using a thin foil, wall thermocouple. The results indicated that the colour play temperature for yellow was $35.6 \pm 0.2°C$. During subsequent heat transfer runs the calibration was checked by observing the temperature measured by the thin foil thermocouple as the yellow isotherm line passed over it. No change in this calibration was ever required as the colour play temperature always remained the same.

---

[1] **BDH Ltd., Poole, Dorset, BH12 4NN**

[2] **Harlow Chemical Company Ltd., Temple Fields, Harlow, Essex CM20 2AH**

4.2.1.2 Thermocouples

All thermocouples used in the present study were copper-constantan (type T). As shown in Figure 3.2, one thermocouple was used to measure the upstream gas centreline temperature and two fast-response, thin foil thermocouples were used to measure the perspex duct wall temperatures: one on the inside of the tunnel and one on the outside. The thermocouples were checked at the boiling point of water at standard pressure. The thermocouple outputs were also in agreement with the outputs from a *Comark Microprocessor Thermometer*, a separate device used to measure the temperature at the heater exit. Even though the thermocouples were checked for accuracy, thermocouples which are used to measure gas temperature should also be checked for installation errors such as stem conduction and tip radiation losses. The first order checks described below reveal that these losses were negligible.

4.2.1.2.1 A Check for Stem Conduction Losses

A first order check was made for stem conduction losses by assuming that the stem which held the gas thermocouple in the centreline of the duct was a fin with a uniform cross-sectional area. If the convective heat gain at the fin tip is assumed to be negligible, then the classical solution for the adiabatic fin tip applies. Therefore the difference between the gas temperature and the thermocouple bead temperature is given by

$$T_{gas} - T_{thermocouple} = \frac{(T_{gas} - T_{wall})}{cosh\left(m\frac{L}{2}\right)}$$

where m is

$$m = \sqrt{\frac{hP}{kA_c}}$$

The h in this expression was evaluated by assuming the thermocouple stem was a cylinder in crossflow. Since the stem was not made of one single material, a one-dimensional approximation of kA_c was used. The thermocouple stem was made from a stainless steel tube (*O.D. 0.05", I.D. 0.04") and contained two teflon* coated 0.003" wires: one copper, the other constantan. The space between the wires and the inside diameter of the stem was filled with superglue. Since the thermal properties and the cross sectional areas of each of these elements were known, an assumption of one-dimensional conduction along the stem was made to obtain an estimated value of kA_c from

$$kA_c = kA_c|_{stainless\ steel} + kA_c|_{teflon} + kA_c|_{copper} + kA_c|_{constantan} + kA_c|_{superglue}$$

The results of this analysis showed that the quantity $(T_{gas} - T_{thermocouple})$ was negligible ($< 0.001°C$).

4.2.1.2.2 A Check for Radiation Tip Losses

A similar first order check was made to see if convection heat transfer did indeed dominate radiation heat transfer as expected. A simple energy balance yielded

$$T_{gas} - T_{thermocouple} = \frac{\epsilon\sigma}{h}\left(T^4_{thermocouple} - T^4_{wall}\right)$$

where ϵ is the emissivity of the thermocouple bead (solder consisting of 60% lead and 40% tin) and σ is the Stefan-Boltzman constant. The h in this expression was evaluated by assuming the thermocouple bead was a short cylinder. A "worst case" situation was examined in which T_{wall} was assumed to be $T_{initial}$; the resultant value of $(T_{gas} - T_{thermocouple})$ was $0.3°C$. The uncertainty analysis presented in Appendix B shows that the error contribution for a gas temperature difference of this level is negligible.

4.2.1.2.3 Thermocouple Reference Junction

The reference junction used with the thermocouples was a *Zeref Thermocouple Ice-Point Reference Unit* manufactured by Isothermal Technology Ltd. As shown in Figure 4.4 the thermocouple-copper leads junctions were maintained at $0°C$ inside the *Zeref* unit which was accurate to within $0.01°C$. The temperature was stabilized within the unit using ice from pure water which was formed inside a copper cylinder fitted with flexible bellows that controlled the on-off action of a heat pump. The junctions were submersed in this ice/water mixture.

4.2.2 Flow Parameter Measurements

The following are details of the velocity, mass flow, and pressure measurements.

The centreline velocity in the main duct was measured with a standard pitot-static orifice arrangement connected to a Furness micromanometer with multiple scales (the least sensitive scale was 0 to 10mm H_2O). The micromanometer was accurate to within $\pm$ 1% of the total scale, and was recently re-calibrated by the manufacturer. The difference between the duct total pressure (P_{t1}) and the hole exit pressure (P_2) was measured with an *Airflow Developments* well-type, 20 inch water manometer. A *Sensym LX1804D2* pressure transducer was used to measure the pressure drop across the British Standard 1042 orifice place which yielded the mass flow rate through the film cooling hole. The average velocity through the hole was then calculated using the continuity equation. The *Sensym* transducer was calibrated against a well-type mercury manometer and was accurate to within 1mm of mercury. Atmospheric pressure was measured with a *Wallace and Tiernan* bourdon gauge barometer accurate to within 1mm of mercury. This barometer's output was frequently compared to the reading from a *Griffin and George* mercury-in-tube barometer and found to be in excellent agreement.

4.2.3 Data Acquisition

Figure 4.4 is a schematic of the data acquisition system. Central to the system was an *IBM PC-AT* microcomputer which was equipped with a 30 megabyte hard disc. The computer was connected to a *CIL DTR 1580* data logger via an *IEEE-488* interface controller card installed in one of the computer's input/output slots. The DTR 1580 has 16 input channels for analogue to digital conversion at a 15 bit resolution with a programmable input range from 1 volt to 10 volts. The conversion time was 20 microseconds per reading for a maximum scanning frequency of 50 kHz. The data logger contained a *Z80* microprocessor which included a program compiler and firmware (software tasks replaced by hardware). The mode of operation was to store the data locally in the data loggers's own 512k of memory at high speed, and then recover the data into the *IBM* during the shut down phase after each experimental run. The data logger collected the data from two amplifiers: one for the thermocouples and one for the pressure transducer. The design and operation of these amplifiers were described in detail in **Dunne (1982)** and **Ireland (1987)**.

In addition to the *IEEE-488* controller card, a *Metrabyte* 24-bit parallel input/output card was installed in another of the *IBM's* I/O slots. This card was used to perform several miscellaneous tasks including: starting the data acquisition program when the tunnel trigger was fired; sending a signal to the thermocouple amplifiers to enable the reading of offset voltages; and controlling the pressure port channel switch box during the static pressure measurement tests described in Chapter 6.

The data acquisition system also included four commercial VHS video systems which were made up of *Panasonic F100* cameras, video tape recorders, and *For-A* video timers. When the tunnel was triggered the video timers were started and the elapsed time superimposed on the signal from the camera. In this way, a particular isotherm could be matched with the time since triggering, so the heat transfer coefficient could then be determined. The timers were checked for accuracy by examining the video one frame at a time and making certain that the difference in time between them was 0.04 seconds, as the camera took 25 frames per second.

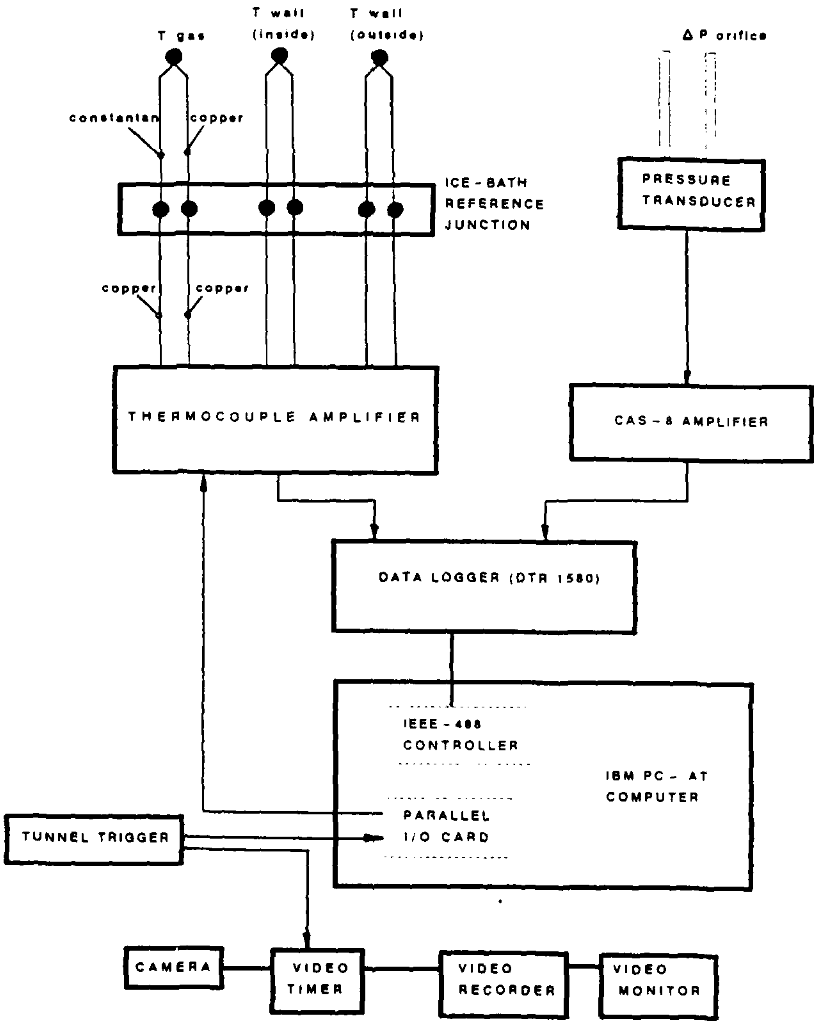
T gas
T wall (inside)
T wall (outside)
Δ P orifice
constantan
copper
ICE - BATH REFERENCE JUNCTION
PRESSURE TRANSDUCER
copper
copper
THERMOCOUPLE AMPLIFIER
CAS - 8 AMPLIFIER
DATA LOGGER (DTR 1580)
IEEE - 488 CONTROLLER
IBM PC - AT COMPUTER
PARALLEL I/O CARD
TUNNEL TRIGGER
CAMERA
VIDEO TIMER
VIDEO RECORDER
VIDEO MONITOR

Figure 4.4: Schematic of the data acquisition system.

4.3 Experimental Procedure

The following is a step-by-step description of the experimental procedure.

1. A thermocouple check was performed each morning before testing began. This was accomplished by taking simultaneous readings of all of the thermocouples to ensure that the measured temperatures were the same (to within $\pm$ 0.1°C).
2. After turning on the vacuum pump to start the flow, the gate valves were adjusted to obtain the desired duct Reynolds number and hole SR.
3. The flow was switched over to the bypass limb and the "flow feedback" slide was opened. The bypass limb gate valve was adjusted so that the mass flow through the heater was the same as before, i.e. when the flow was passing through the main duct and test section at the desired flow parameter settings.
4. The heaters were turned on and the controls set to bring the gas temperature up to the desired level (usually about 90- 100°C).
5. During the 20 to 30 minutes necessary for the flow and the inlet plenum to reach steady-state, the camera position, the test section lighting, and the video tape setting were re-checked. The video timer was also reset to include the day's date and run number on the videotape. Finally, the barometric pressure was read.
6. Immediately before tunnel triggering, all of the thermocouples were read once again to provide the value of $T_{initial}$ used in data reduction. The video tape

recorders were set to the "record" mode. At the last instant before triggering, the "flow feedback" slide was closed.

7. The tunnel was "triggered" which set a number of things in motion including: simultaneously opening the main duct and hole flow ball valves ("B" and "C" in Figure 3.1) and closing the bypass limb ball valve ("A"); starting the "stop watch" feature of the video timer which began superimposing the elapsed time onto the videotape; and starting the data acquisition system which took continuous readings from the gas and surface-mounted thermocouples.

8. During the 90 second test duration, the pressure measurements were obtained from the micromanometer, water manometer, and orifice plate. There was also usually time to watch the liquid crystal colour play.

9. When the test was over, the flow heater was turned off to allow cold air to pass through the test section to bring the tunnel temperature back down to room temperature more quickly. The next test could normally take place within two hours.

10. After the tunnel was turned off, data reduction began by analyzing the results from the data acquisition program. Mass balancing between the two flow routes was checked by examining the time history of the gas thermocouple; proper balancing resulted in a constant gas temperature. Readings from the surface thermocouple mounted on the inside test surface were used to check the calibration of the liquid crystal colour play temperature while readings from

the thermocouple mounted on the opposite surface verified that the thermal pulse from inside the wall had not yet reached the outer surface. The videotape of the colour play was then replayed. The isothermal contours were then traced onto a sheet of acetate which was attached to the monitor screen. The corresponding time since flow initiation was annotated beside each contour. If two liquid crystals had been applied then obviously two times were associated with each contour. The values of h were then calculated according to the method described in Chapter 3.

5 EXPERIMENTAL HEAT TRANSFER RESULTS

This chapter focuses on the central issue of the present work which is the heat transfer enhancement that takes place near the entrance to a film cooling hole on the wall of an internal blade cooling passage. First, a review of the previous work related to this subject is presented, followed by the results for the base-level duct heat transfer (without flow extraction). The heat transfer results are then presented in the form of detailed *enhancement factor contours* where *enhancement factor (EF)* is defined as

$$EF \equiv \frac{h_{local}}{h_{base\ level}}$$

This is followed by area-averaged results which reveal the effects of varying the suction ratio (SR), the hole inclination angle, the duct Reynolds number (Re_L), and the upstream temperature and velocity profiles. Finally, a summary of the uncertainty analysis and its implications in experiment design, is presented. The details and much of the discussion concerning the uncertainty analysis are given in Appendix B.

5.1 Previous Work

The previous work related to the present study is very limited, as far as the author has been able to determine, even after an extensive literature search. Most of the previous work regarding film cooling has focused on exterior blade surface effects rather than the effects on the internal cooling passage wall. Although some area-averaged results for different, but related geometries indicate that heat transfer enhancement does occur, the results are not in sufficient detail to provide insight into the flow field phenomena which could explain the reason for the enhancement.

Evidently, there has been some industrial interest in the problem from both American and British gas turbine engine companies. According to **Mahle (1988)**, *Pratt & Whitney* workers, approximately 10 years ago, used a steady-state method to examine the heat transfer at the entrance to an array of holes with the approach flow parallel to the plane of the hole entrances. Significant enhancement was observed, but the exact results are still restricted. Likewise, *Rolls-Royce*, in a restricted brochure, reported on an aerodynamic and heat transfer investigation into the problem using a 40X scale perspex circular duct model (**Beacock, 1977**). In general terms, the results indicated that heat transfer enhancement occurred downstream of the holes because of a reduction in boundary layer thickness caused by bleeding off the upstream boundary layer. The level of enhancement was also shown to increase with increased bleed rate. Streamline flow visualization was also performed in a water tunnel, which revealed some of the same features that are presented in Chapter 6, namely, a stagnation point downstream of the hole and the presence of a vortex structure.

The work published in the open literature is reviewed next. **Ainsworth and Jones (1979)** used a transient technique based on point measurements from thin film gauges to examine the effect of mass removal through discrete holes from a circular duct with the main flow at Mach 0.6. Enhancement factors on the order of 2 were observed immediately downstream of the hole, the effects being confined to a small portion of the circular periphery. Also, the enhancement increased proportionately with the bleed rate.

Sparrow and Kemink (1979) used a steady-state method to study how fluid withdrawal at a branch point in a tube affected the turbulent heat transfer characteristics of the main line flow downstream of the branch. Although both the main line and the withdrawal tubes had the same diameter (which is a quite different geometry from the one in the present study), the circumferentially averaged results showed that the heat transfer was up to 5 times greater with fluid withdrawal than without. Again, as in **Ainsworth and Jones**, there was a positive correlation between the rate of fluid withdrawal and the enhancement level. **Sparrow and Kemink** also varied the main line Reynolds number and found that it had little effect on the level of enhancement for a given withdrawal ratio; the most important factor in determining the heat transfer enhancement was the withdrawal ratio itself. This finding validates the experimental plan taken in the present work where the main duct Reynolds number (Re_L) was held constant while the SR was varied. It is also important to note that Sparrow's experiment took place in the thermal entrance region of the main line rather than in the fully developed region as in the present study. Therefore Sparrow's enhancement was not caused by bleeding off the upstream thermal boundary layer which was one reason for the enhancement observed in the present study. This implies that the enhancement due to flow removal is rather robust in that it is not completely dependent on special upstream thermal boundary conditions.

Sparrow and Ortiz (1982) used the naphthalene sublimation technique to determine the average heat transfer around an array of tightly spaced holes in a plate positioned normal to the oncoming flow. Significant sublimation, which implies significant heat transfer, was observed near the entrance to these holes. The sublimation was caused by the flow stagnating, then turning and accelerating into the holes. This work might be applicable to internal blade cooling when jet impingement forces the coolant flow straight towards the plane of the hole entrances. Unfortunately, Sparrow's flow arrangement shed little light on the current problem which had the approach flow parallel to the plane of the hole entrance.

While it is obvious from other workers' results that significant enhancement does occur on a duct wall near the flow extraction point and that it increases with bleed rate (or SR), a high- resolution picture of the heat transfer distribution was still needed along with an understanding of the mechanisms involved. This thesis provides both; the heat transfer results are presented next in this chapter and the results from experimental, analytical, and computational flow field studies are presented in Chapters 6,7, and 8, respectively.

5.2 Base-Level Heat Transfer Results

The heat transfer results for the two-dimensional duct in the absence of flow extraction effects are presented in this section. The purpose of measuring the base-level heat transfer was twofold. First of all, a comparison of the results with established correlations served to validate the experimental method and apparatus. Secondly,

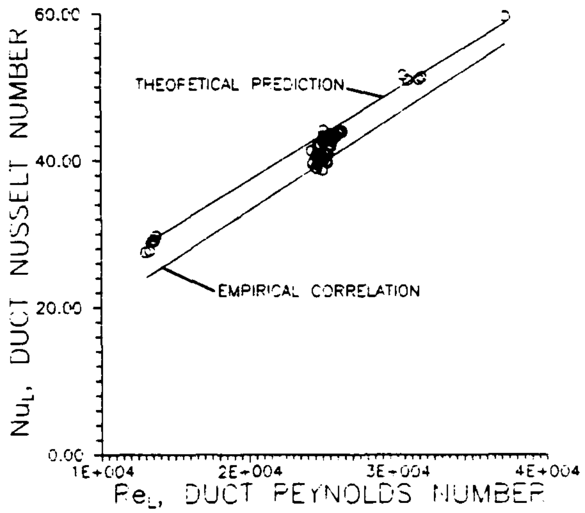

Figure 5.1: **Experimental base-level heat transfer results and predictions from KAYS AND CRAWFORD (1980).**

the results provided a basis with which to compare the level of heat transfer enhancement due to flow extraction into the film cooling hole. The base-level results were obtained from areas within the duct that were outside the influence of the hole which could be easily discerned from the pattern of colour play. Later in the chapter, time- elapsed photographs are presented which show that the colour play due to hole effects occurred first followed by the colour play for the unenhanced (base-level) region. The unenhanced region underwent colour play essentially at the same time which was consistent with a constant value of *h* for fully developed turbulent flow.

Figure 5.1 shows the experimental base-level heat transfer results along with two predictions for fully-developed, turbulent channel flow with an isothermal wall boundary condition. The theoretical prediction is based on values of the Nusselt

number for fully developed, turbulent flow between parallel planes. **Kays and Crawford (1980)** give tabular results for parallel planes with a constant heat flux boundary condition as a function of Reynolds number. These values were converted to values corresponding to the constant surface temperature boundary condition by applying an appropriate factor, also given in **Kays and Crawford** , which resulted in a decrease of the values by a few percent. Also, the theoretical prediction took into account the differing definitions of the Reynolds number and the Nusselt number in accordance with the relationships given earlier in Chapter 3.

The empirical correlation depicted in Figure 5.1 is based on

$$Nu_D = 0.021 Pr^{0.5} Re_D^{0.8}$$

which is valid for fully developed, turbulent flow with a constant surface temperature inside a circular tube. Experimentally it has been found that circular tube correlations are also applicable to non-circular tubes providing the hydraulic diameter is used in place of the circular tube diameter. This is because the greater portion of the heat transfer resistance is in the sublayer region near the wall surface (for Prandtl numbers greater than about 0.5), so the hydraulic diameter becomes the important parameter rather than the particular shape of the channel cross section. This approximation breaks down when the tubes have very sharp corners because of sublayer interaction, but according to **Kays and Crawford**, it is quite good for rectangular cross-sections and therefore presumably for parallel planes as well. When the hydraulic diameter is used in the above equation along with the centreline velocity and temperature, the correlation becomes

$$Nu_L = 0.0146 Pr^{0.5} Re_L^{0.8}$$

which is also plotted in Figure 5.1.

The experimental results are clustered right between these two predictions with the values a little closer to the theoretical prediction for the parallel planes. The agreement is within the estimated uncertainty of 7% which is certainly good enough to consider the experimental method and apparatus to be validated.

5.3 Enhancement Factor Contours

The key experimental results for all four inclination angles are presented in this section. For each inclination angle the following results are given: time-elapsed photographs which show typical colour play for that configuration, EF contours for a range of SR'*s*, and a plot of centreline EF vs x/D showing clearly the effect of SR on enhancement in the axial direction.

Figures 5.2-5.5 are the results for the 90° *hole*. The peak level of enhancement is located at the downstream hole edge with the effects of flow extraction evident up to 6 or 7 hole diameters (D) in the downstream direction. There is also an interesting change in contour shape that occurs between $SR = 1.2$ and 2.5, with a single "lobe" shape being replaced by a double "lobe" shape. Figure 5.5 shows that the centreline EF increases with SR up to $SR = 3.47$, especially near the hole. For SR'*s* greater than 3.47, the centreline EF actually decreases slightly although the extent of the enhanced region continues to increase especially in the lateral direction, as shown in

Figures 5.3 and 5.4.

Figures 5.6-5.9 are the results for the 150° *hole* where two isotherms are shown instead of the single one shown in the 90° *hole* results. For all of the inclination angles, except the 90° angle, a mixture of two liquid crystals were applied to the test surface which produced 2 isotherms approximately 5°C apart. In each test, the colour play from the two types of liquid crystals yielded precisely the same shaped contours while the values of the enhancement factors agreed to within 3% (well within the total experimental uncertainty estimate of 7%). Unlike the 90° *hole*, the location of the peak level of enhancement for $SR's$ less than 4 is located in oval shaped areas on either side of the axial hole centreline and away from the downstream hole edge as indicated in Figure 5.7. At $SR's$ greater than 4, the location of peak enhancement moves to the downstream hole edge which corresponds to the location of peak enhancement for the other three hole inclinations. Another unique feature exhibited by the 150° *hole* is the four-lobe shaped contour at $SR's$ less than four with a double-lobe shaped contour at $SR's$ greater than four. The other three inclination angles produced a single- lobe shaped contour at low $SR's$ and a double-lobe shaped contour at higher $SR's$.

Figures 5.10-5.13 are the results for the *sideways hole* which may be the most common configuration found in actual gas turbine blades. The distinguishing feature about this configuration is the skewing of the area of enhancement in the direction of flow extraction (towards the top of the page in Figures 5.10-5.12). Furthermore, the extent of the enhancement in the lateral direction appears to be greater than in the other configurations. Finally, the peak level of enhancement is always at the downstream hole edge.

Figures 5.14-5.17 are the results for the 30° *hole*. The heat transfer features of this hole configuration are in many ways similar to the 90° configuration with the same shift in the single to double-lobe shape and the location of peak enhancement at the downstream hole edge.

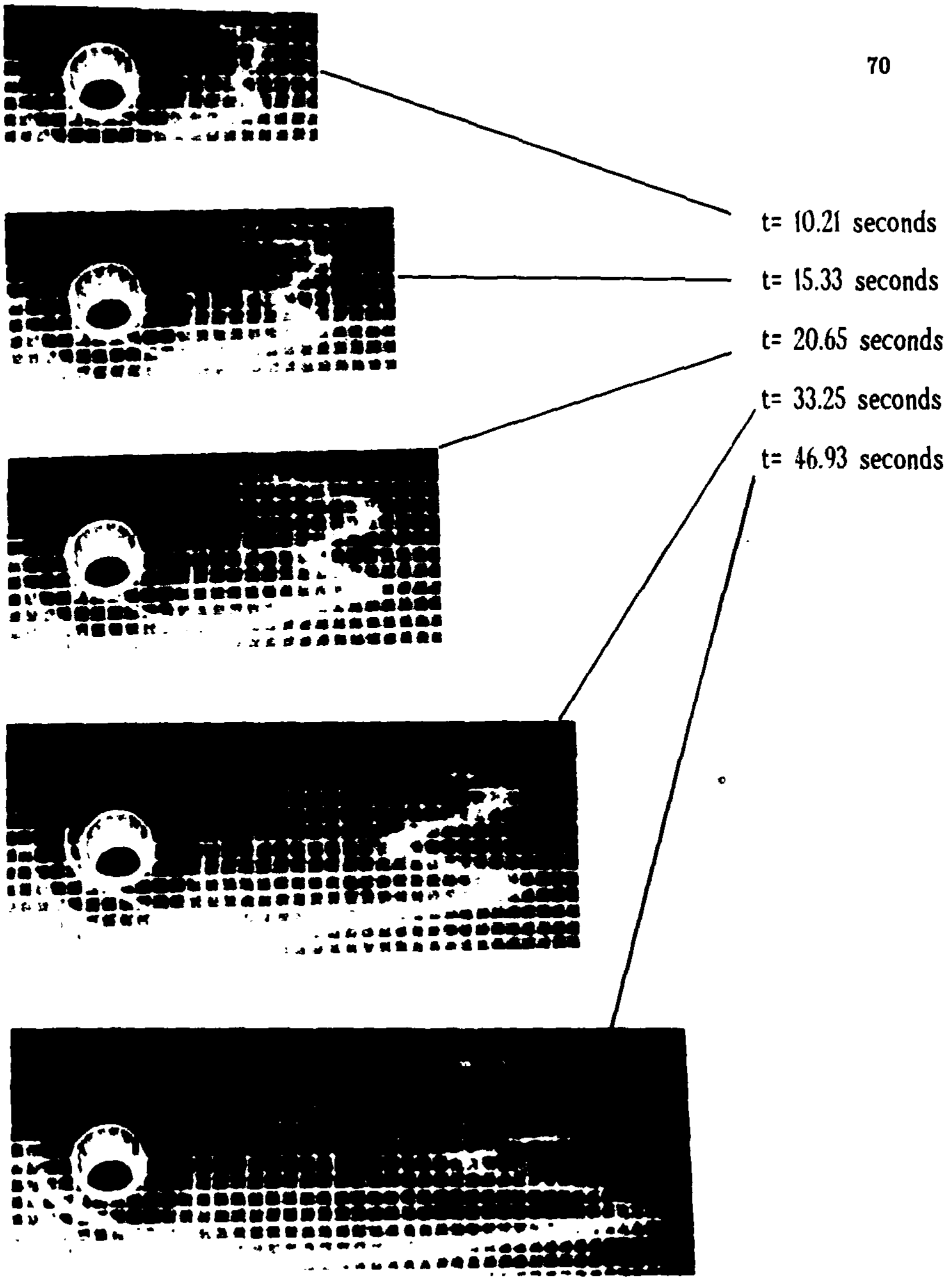
t= 10.21 seconds
t= 15.33 seconds
t= 20.65 seconds
t= 33.25 seconds
t= 46.93 seconds

Figure 5.2: Time-elapsed photographs of colour play for the 90° *hole*

($SR = 7.48$) flow →

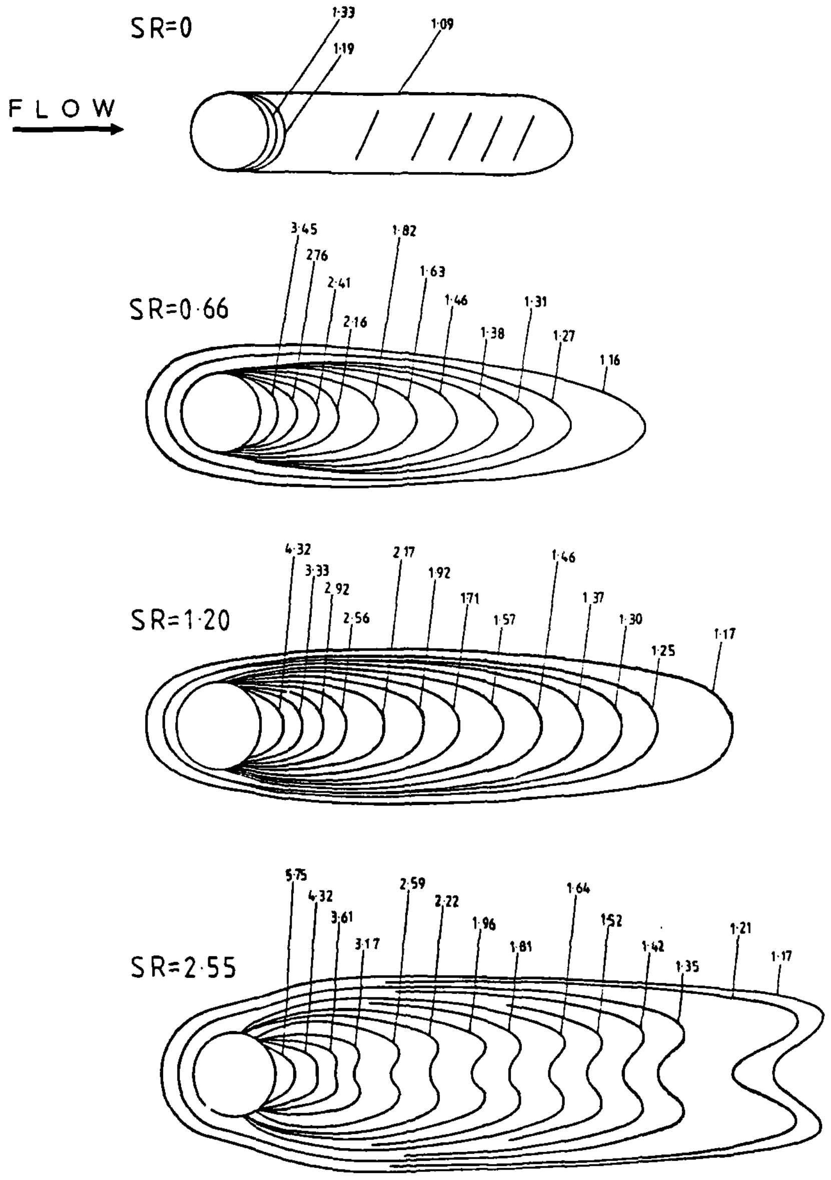

Figure 5.3: Enhancement factor contours for the 90° *hole*

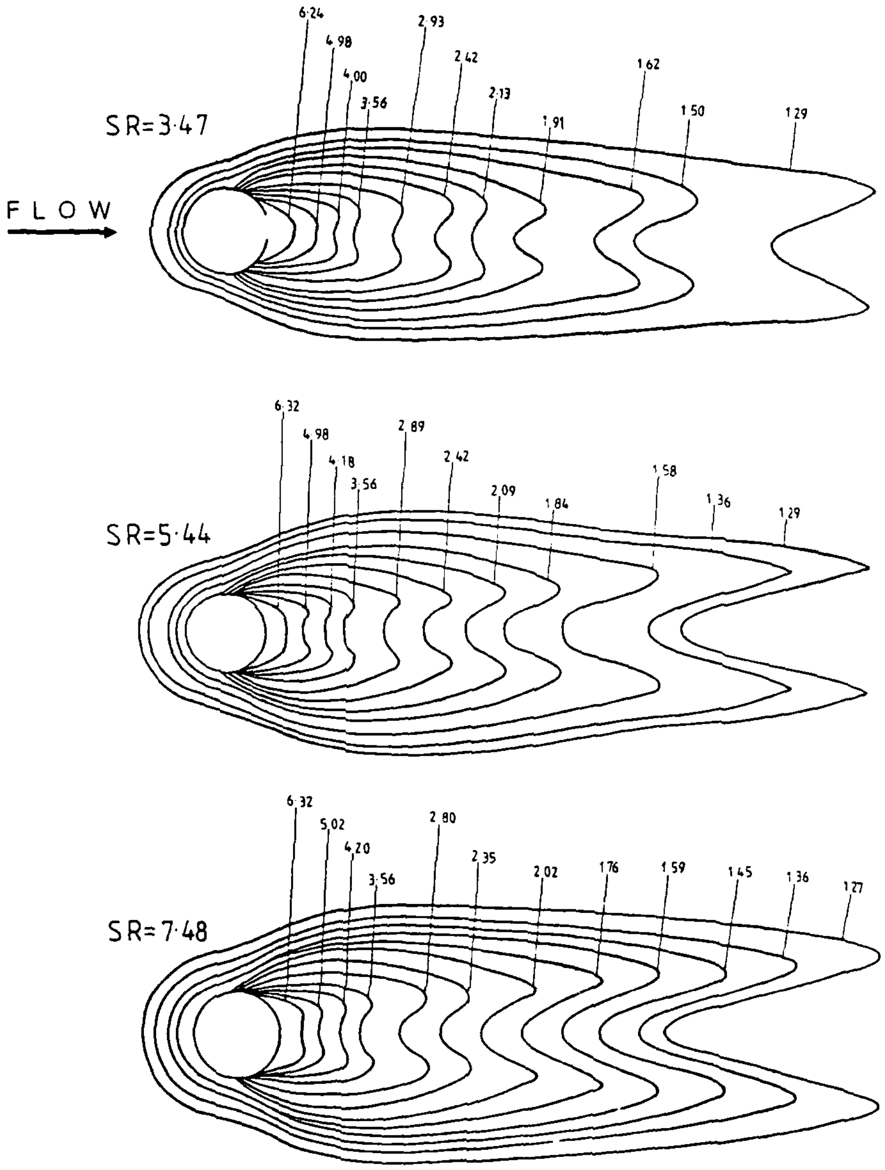

Figure 5.4: **Enhancement factor contours for the** 90° *hole*

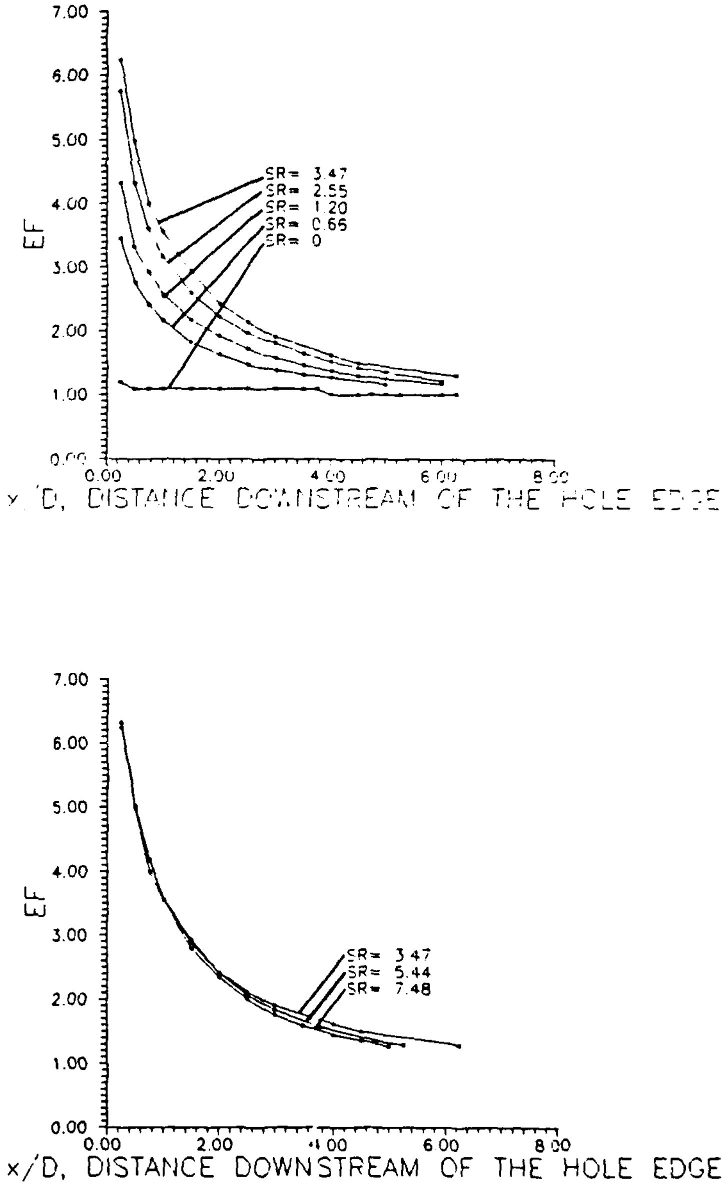

Figure 5.5: Centreline enhancement factor versus x/D for the 90° *hole*

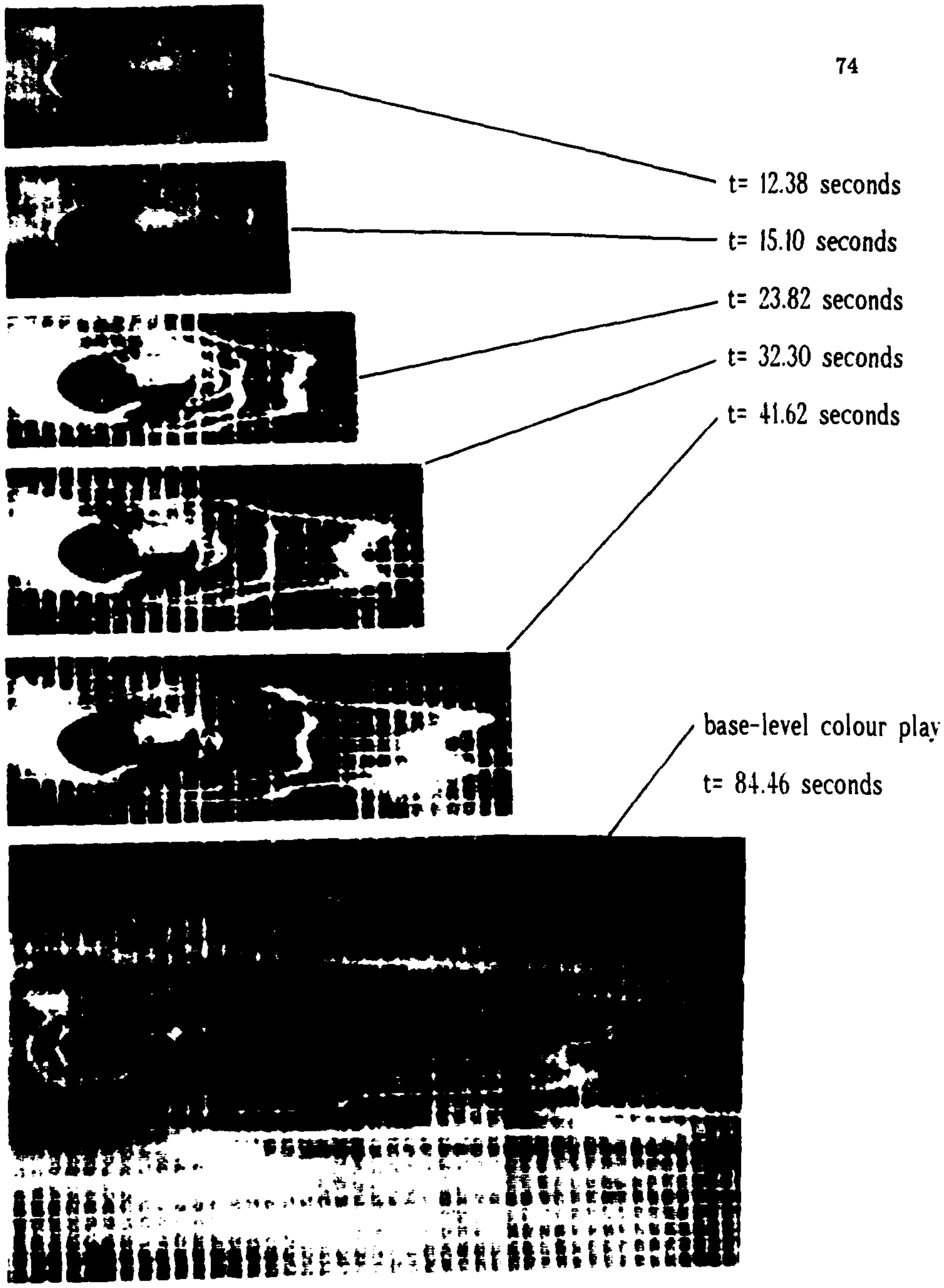
t= 12.38 seconds
t= 15.10 seconds
t= 23.82 seconds
t= 32.30 seconds
t= 41.62 seconds
base-level colour play
t= 84.46 seconds

Figure 5.6: Time-elapsed photographs of colour play for the 150° *hole* ($SR = 1.20$) FLOW →

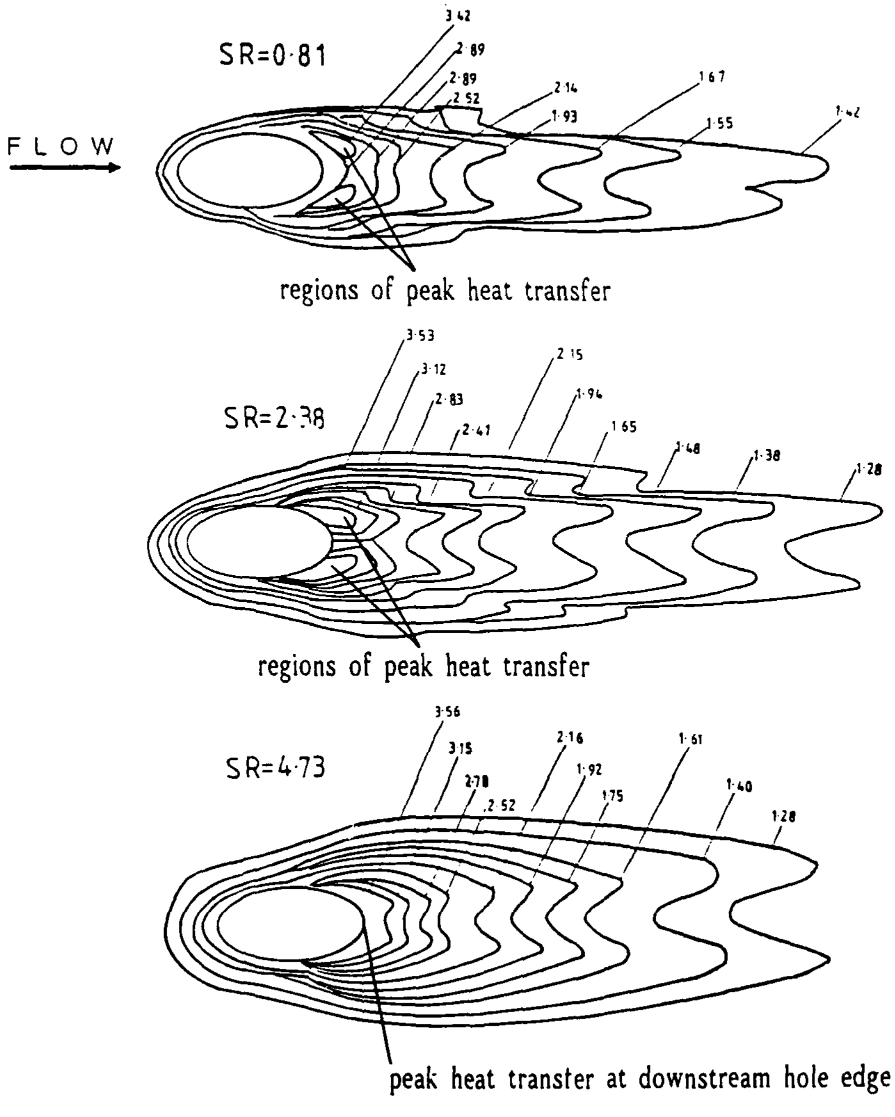

Figure 5.7: **Enhancement factor contours for the 150° *hole***

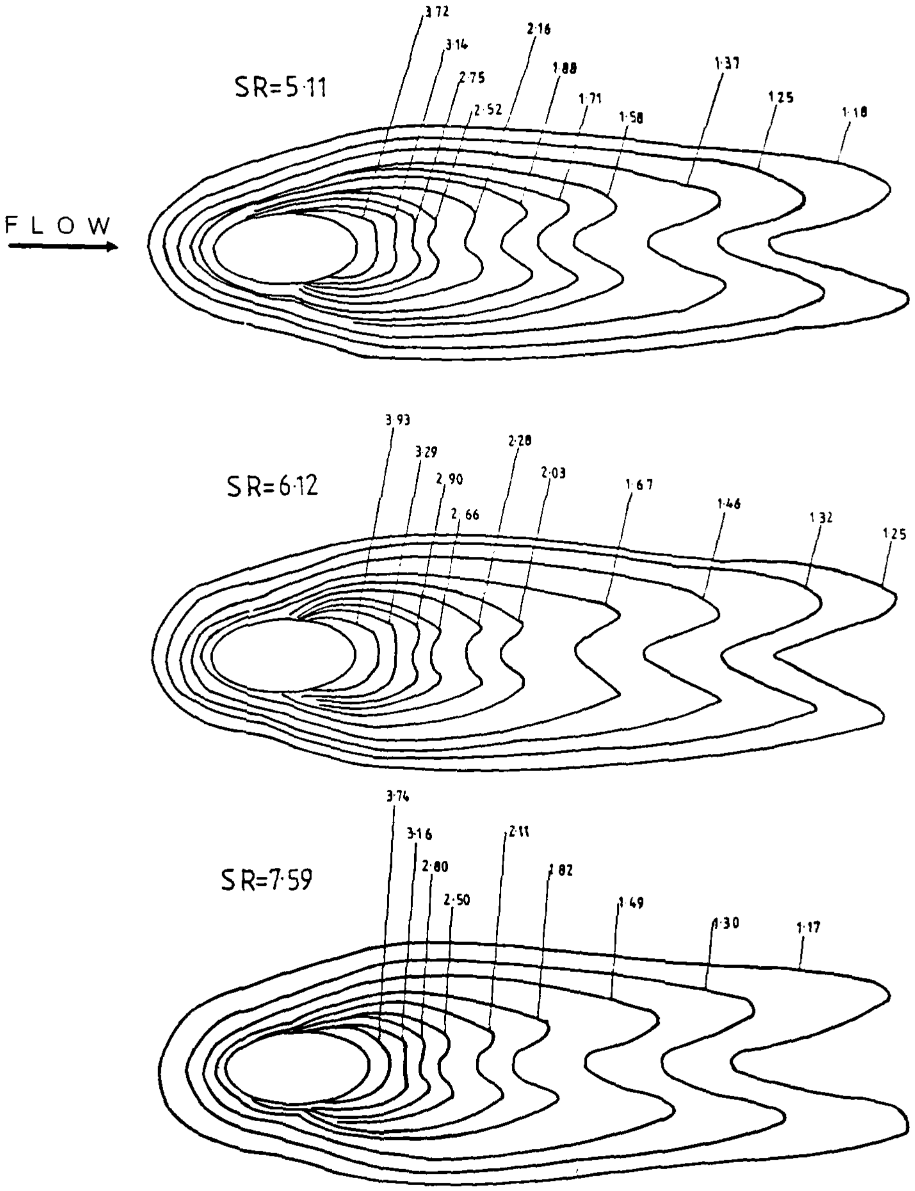

Figure 5.8: **Enhancement factor contours for the** 150° *hole*

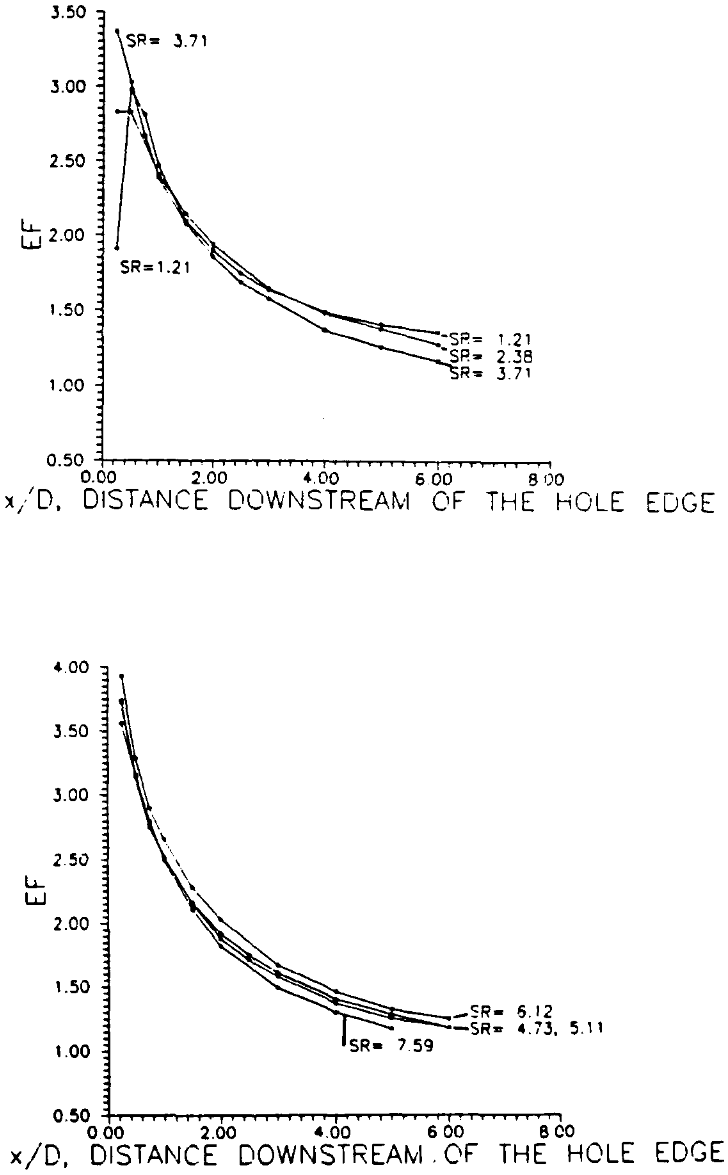

Figure 5.9: Centreline enhancement factor versus x/D for the 150° *hole*

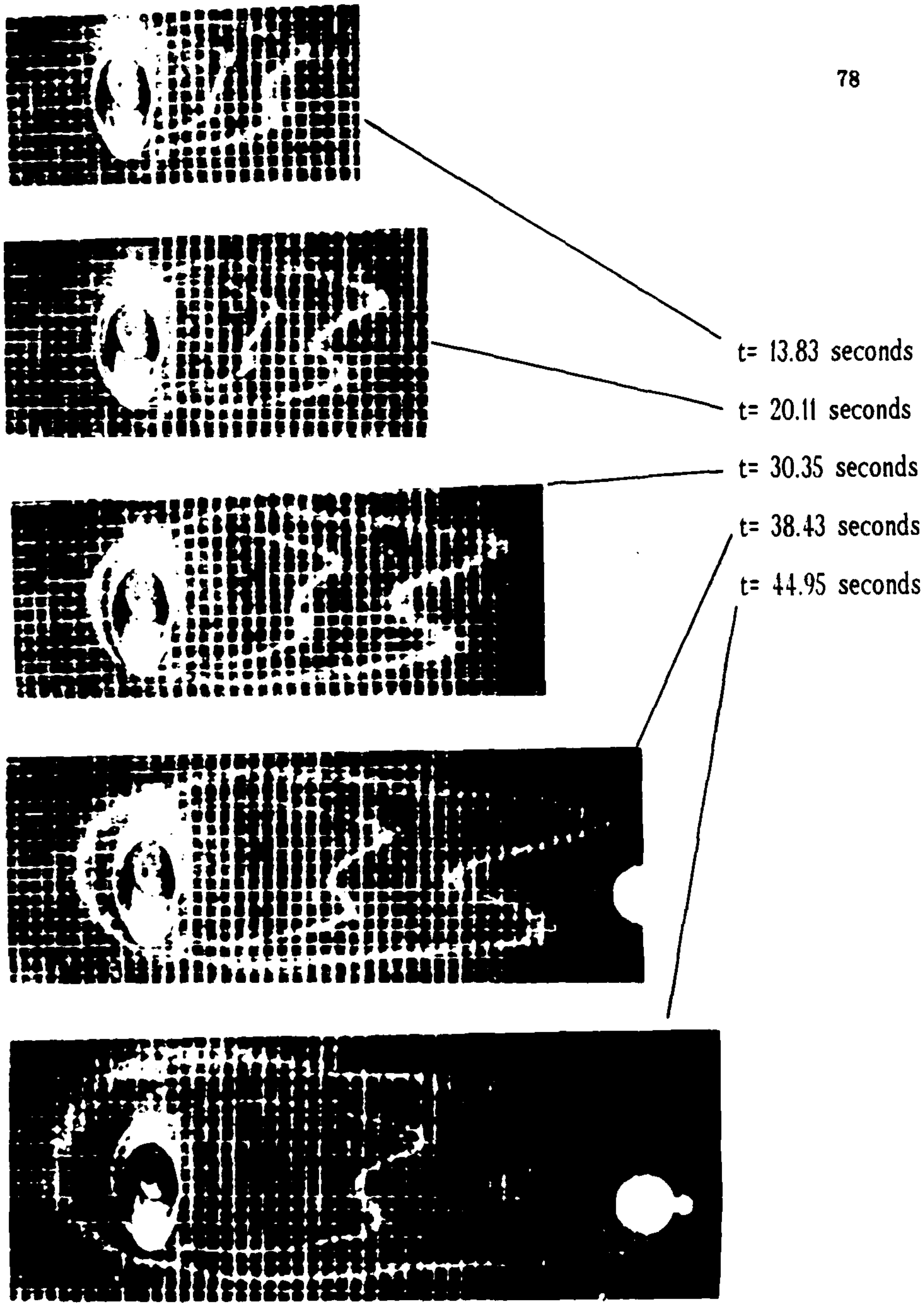
t= 13.83 seconds
t= 20.11 seconds
t= 30.35 seconds
t= 38.43 seconds
t= 44.95 seconds

Figure 5.10: Time-elapsed photographs of colour play for the *sideways hole* ($SR = 7.73$). The hole is angled upwards. FLOW →

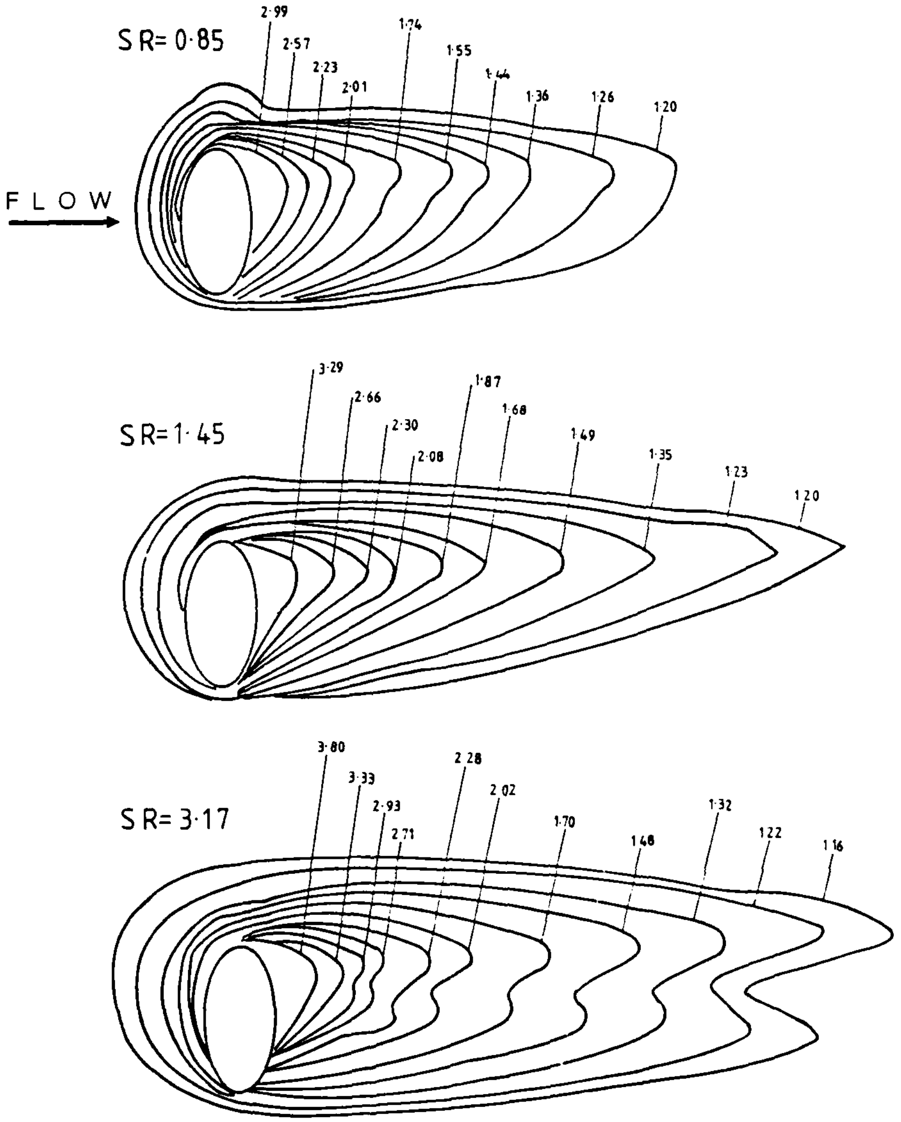

Figure 5.11: Enhancement factor contours for the *sideways hole* The nole is angled upwards.

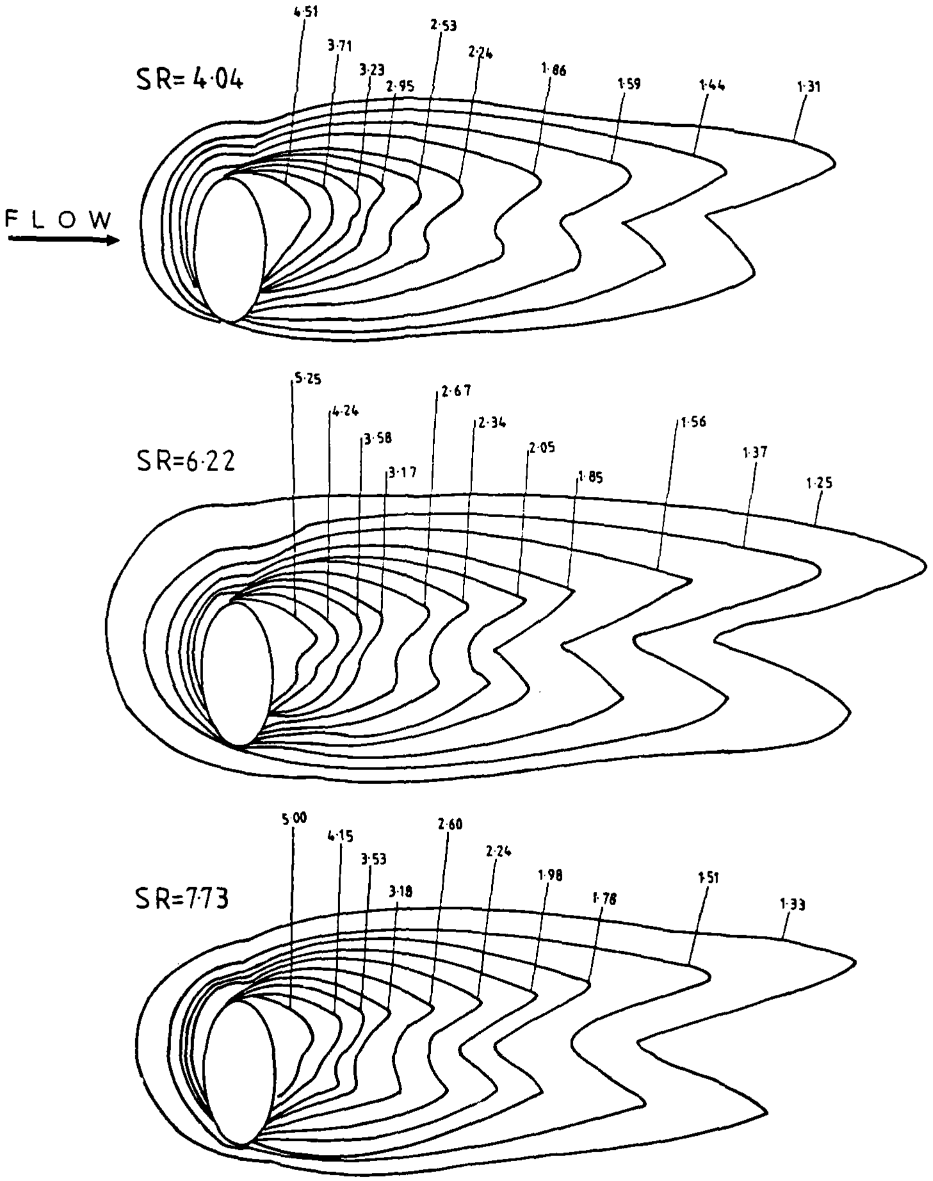

Figure 5.12: Enhancement factor contours for the *sideways hole* The hole is angled upwards.

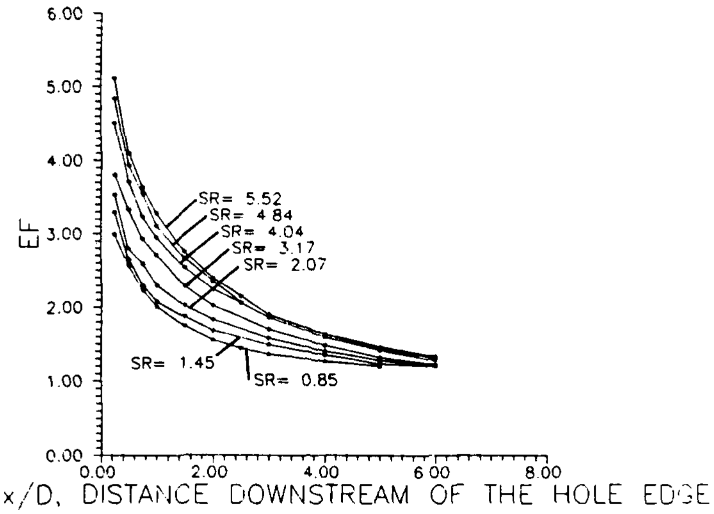

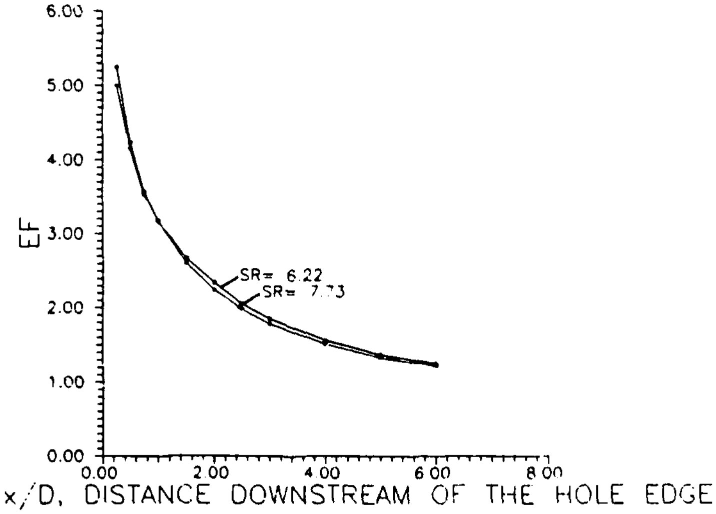

Figure 5.13: Centreline enhancement factor versus x/D for the *sideways hole*

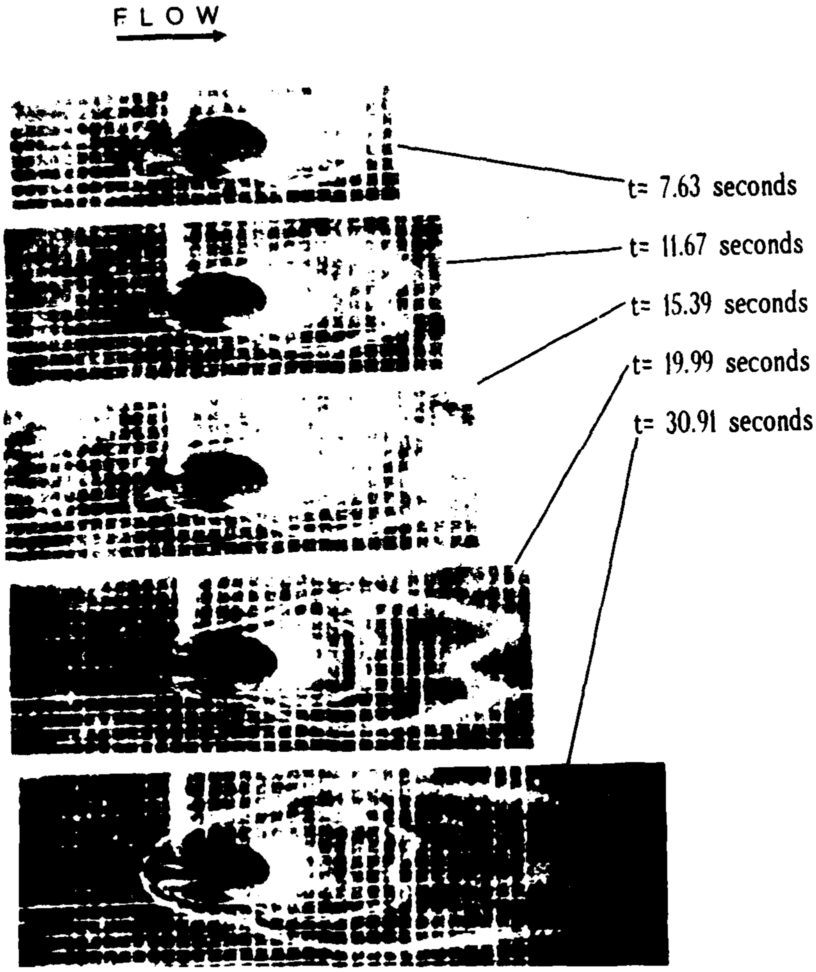
FLOW
t= 7.63 seconds
t= 11.67 seconds
t= 15.39 seconds
t= 19.99 seconds
t= 30.91 seconds

Figure 5.14: **Time-elapsed photographs of colour play for the 30° *hole* ($SR = 5.87$)**

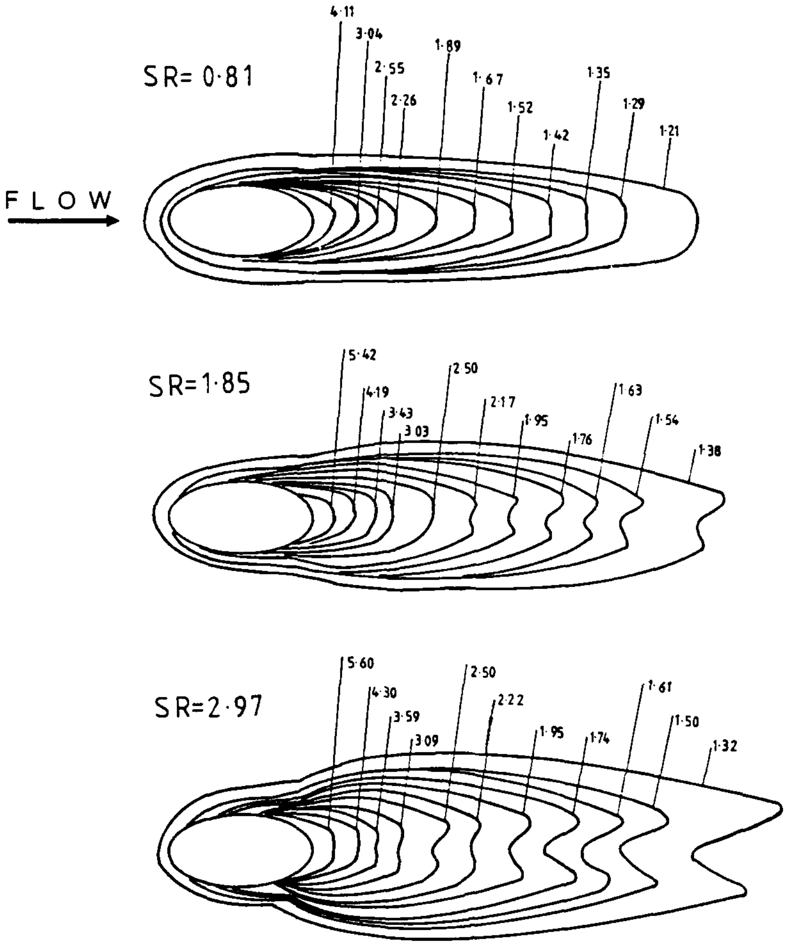

Figure 5.15: **Enhancement factor contours for the 30° *hole***

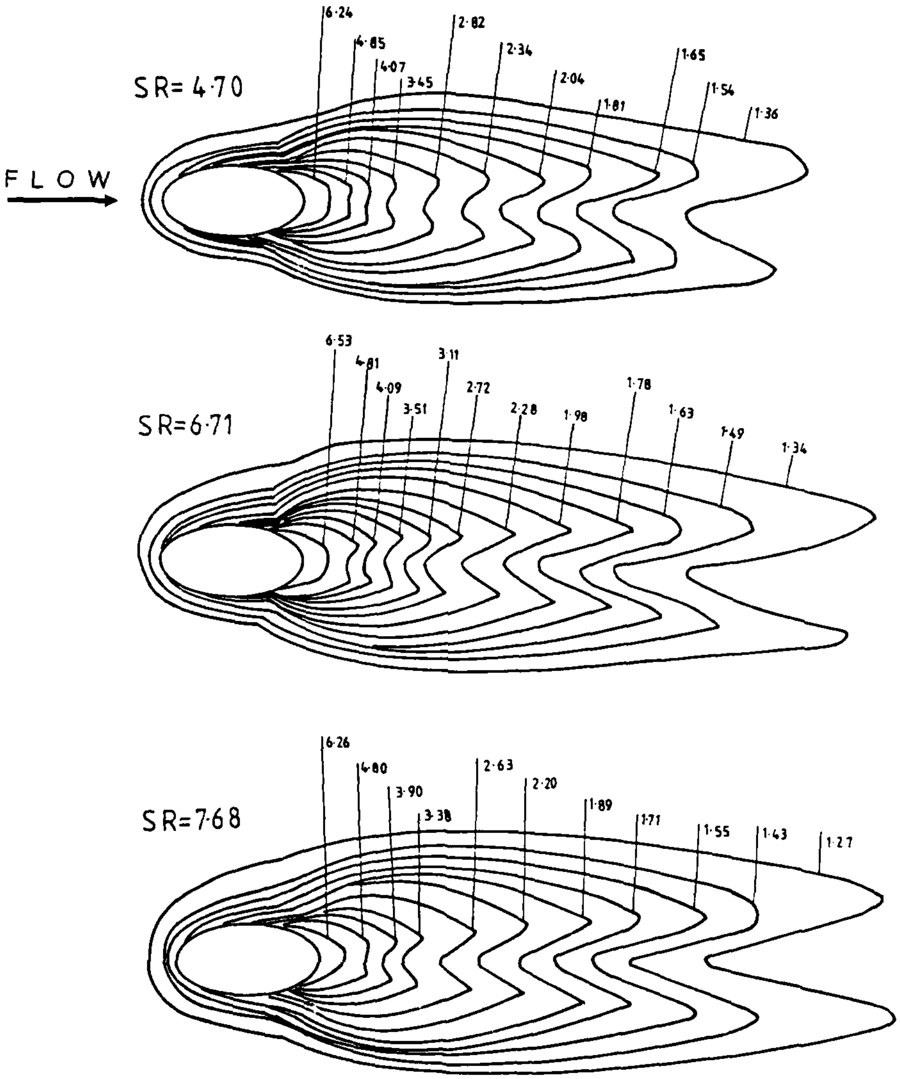

Figure 5.16: **Enhancement factor contours for the 30° *hole***

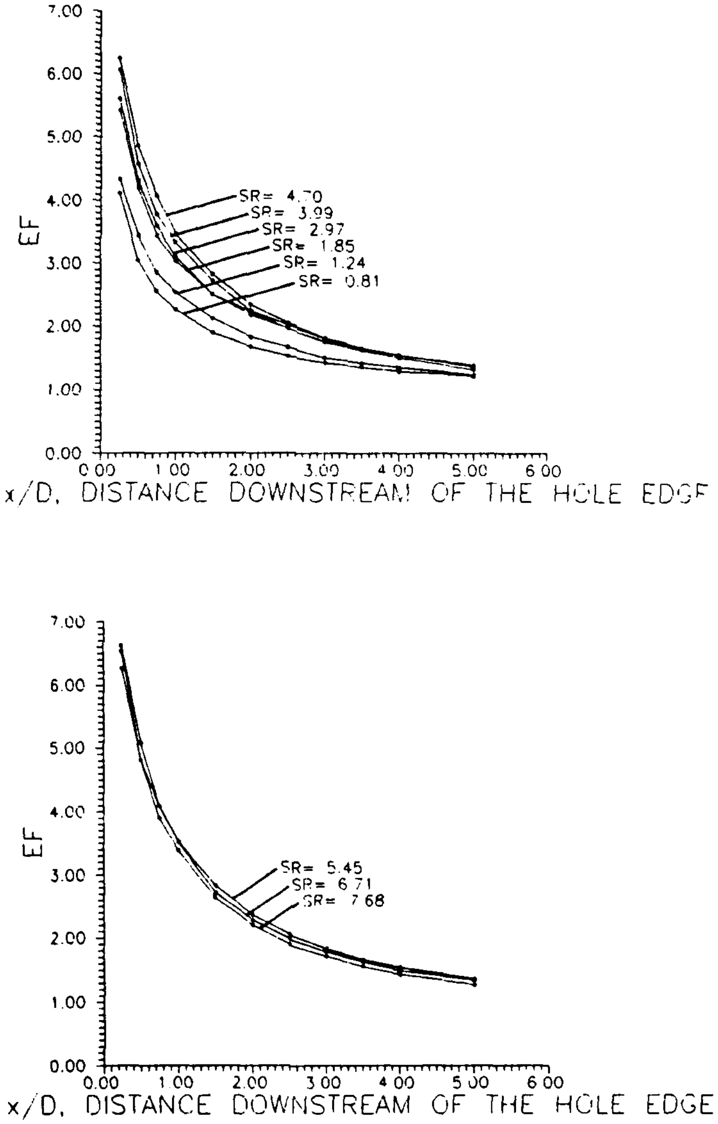

Figure 5.17: Centreline enhancement factor versus x/D for the 30° hole

5.4 Effects of Varying Experimental Parameters

As shown in the previous section, the liquid crystal method provides very detailed maps of the heat transfer distribution. However, a form of presentation which is also useful to the internal cooling passage designer is an area-averaged value. Area-averaged results also provide a basis of comparison between tests run with different hole inclination angles and flow conditions. The region selected for averaging was an area two hole diameters wide and up to six hole diameters long, and adjacent to the downstream hole edge. This particular region was selected because it seemed to be representative of the enhanced area for most of the test cases. Simple diagrams showing the division into these areas are included along with the results in *Figures 5.18-5.24. To obtain the area-averaged results,* a *digitizer was used to de*termine the area enclosed by each EF contour. The area-averaged EF's ($\overline{EF}$) were then evaluated according to

$$\overline{EF} = \frac{\int EF\, dA}{\int dA}$$

5.4.1 Effect of Varying the Hole Inclination Angle

Figure 5.18 shows the effect of varying the hole inclination angle in a plot of area-averaged $\overline{EF}$ versus the suction ratio (SR). At SR's less than two, the $\overline{EF}$ values for all the hole inclination angles are very close to each other. At higher SR's, the effect of hole inclination appears to be reasonably small unless the hole is angled backwards, forcing the flow to pass through an obtuse angle in order to enter the hole. The $\overline{EF}$'s for the 30°, 90°, and the *sideways hole* level off at approximately 2.1

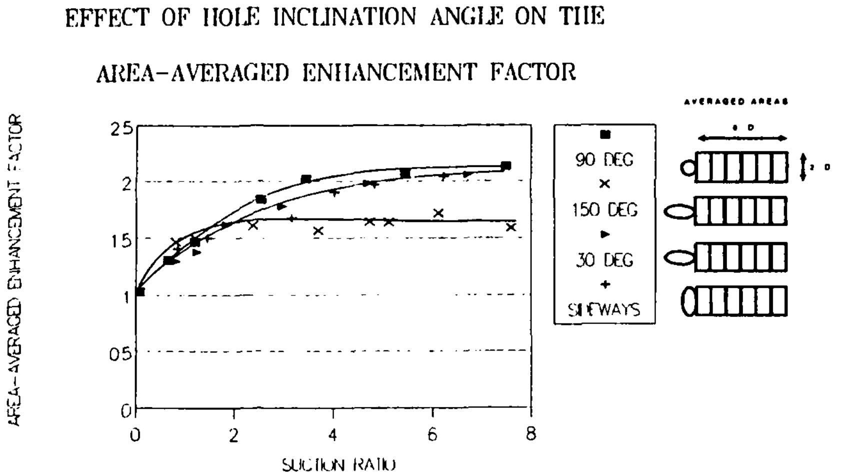

Figure 5.18: **Effect of hole inclination angle on $\overline{EF}$. Averaged areas are 2D x 6D regions adjacent to the downstream hole edge.**

for *SR's* greater than four, while the corresponding value for the 150° *hole* is lower at approximately 1.6. Finally when using these results in actual internal cooling design, it should be remembered that even though the $\overline{EF}$*'s* for the given area may level off at *SR's* around 4, the extent of the enhanced region continues to increase with *SR* all the way up to 8, the maximum *SR* tested. Of course, the heat transfer contour maps are the key to taking this into consideration.

Obviously, cooling designers may be interested in $\overline{EF}$*'s* for areas other than the region selected for Figure 5.18. Figures 5.19 and 5.20 show the effect of selecting regions that have different axial lengths. The results are plotted for lengths of one diameter to six diameters for both the 90° and 150° *holes*. Presenting the averages in this way effectively includes the streamwise variation of the enhancement factor.

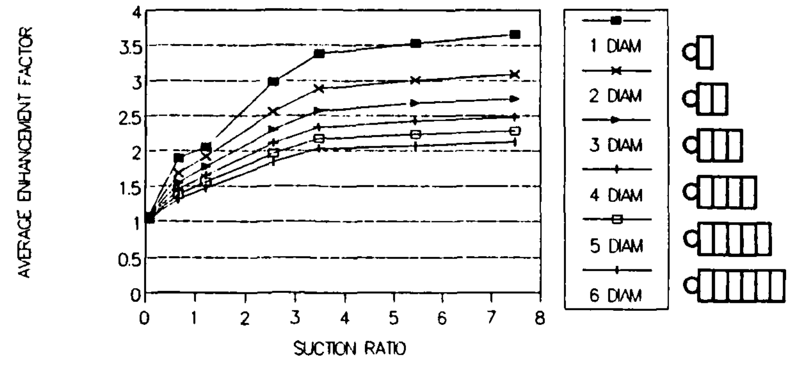
AREA-AVERAGED ENHANCEMENT FACTORS FOR

THE 90 DEG HOLE

Figure 5.19: $\overline{EF's}$ **for the 90° *hole*. Effect of enhancement area selection.**

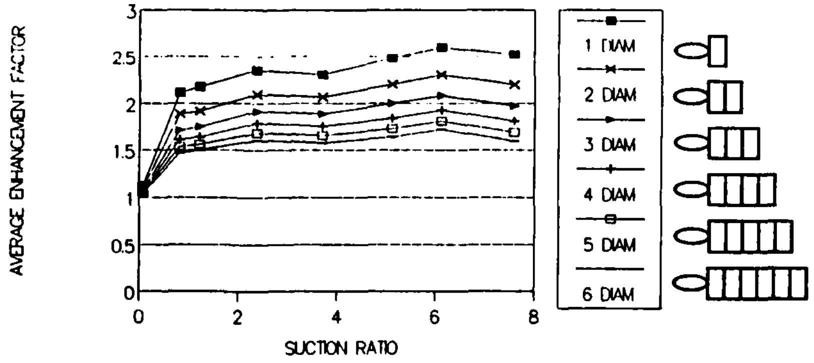
AREA-AVERAGED ENHANCEMENT FACTORS FOR

THE 150 DEGREE HOLE

Figure 5.20: $\overline{EF's}$ **for the 150° *hole*. Effect of enhancement area selection.**

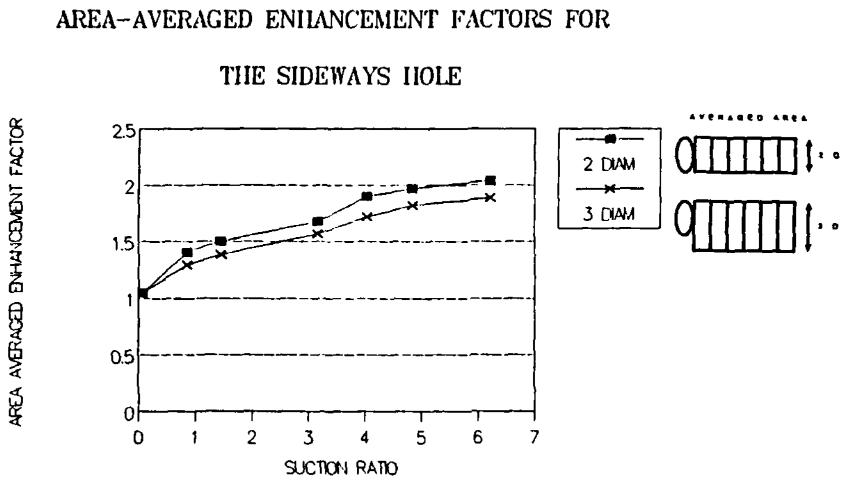

Figure 5.21: **$\overline{EF}$'s for the *sideways hole*. Effect of lateral enhancement area selection (2D versus 3D).**

Since the streamwise variation for the *sideways* and 30° *hole* is very similar to the variation for the 90° *hole*, Figure 5.19 can also be used for those hole angles as well, at least to first order accuracy.

Earlier the heat transfer contours for the *sideways hole* were presented which showed that the enhanced area on the main duct wall was skewed in the direction of flow extraction. This effectively created an enhanced area that was typically closer to three diameters in width rather than the two diameter width of enhanced area considered thus far. Figure 5.21 is a comparison of the $\overline{EF}$'s calculated for both of these regions. The key result is that increasing the area of the averaged region by 50% only involves a drop in $\overline{EF}$ of 10%. This fact may be important to internal cooling designers since the *sideways hole* is probably the most common of the four

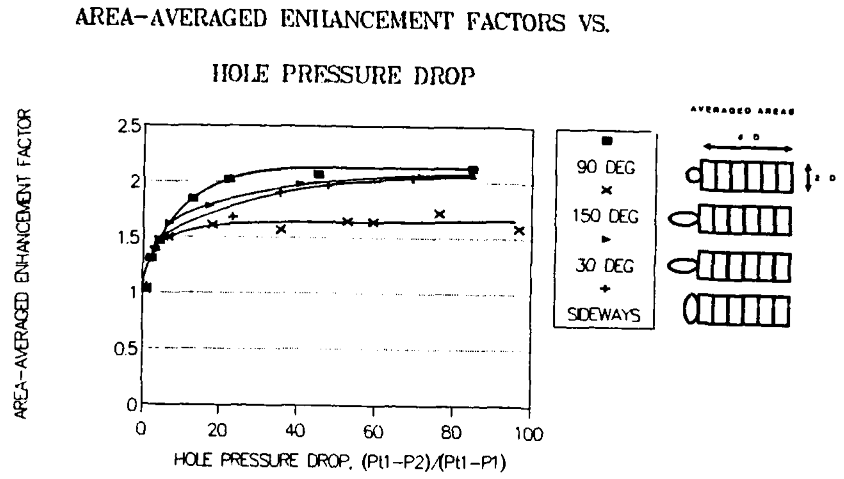

Figure 5.22: $\overline{EF}$ **versus hole pressure drop.**

hole inclination angles in actual film cooled turbine blades.

All of the results presented so far have been relative to changes in the suction ratio, a mass flow parameter, because the coolant mass flow rate is an important limiting factor which must be considered in cooling design. There is, however, at least one other important limiting factor; the pressure drop through the cooling channel must not be too severe or the coolant flow may be restricted to undesirably low levels, perhaps even leading to "hot spots". Figure 5.22 shows $\overline{EF}$*s* plotted versus the pressure drop across the hole. This figure looks much like Figure 5.18 where the heat transfer values were plotted against SR except that the 90° *hole* values appear to be slightly higher relative to the *sideways hole* and the 30° *hole* values. This is because the hole discharge coefficients (C_d'*s*) for the 90° *hole* are higher than the discharge coefficients for the other three inclination angles at all pressure drop ratios (or velocity head ratios) greater than 12 (to be substantiated in Chapter 10). Therefore, for a given pressure drop, more mass flow is extracted through the 90° *hole* than through the others which in turn leads to higher levels of heat transfer.

5.4.2 Effect of varying the main duct Re_L

For all of the tests mentioned so far, the duct Re_L was held constant at a nominal value of 25,000. At the beginning of the test program, it was assumed the $EF's$ would be insensitive to the value of the duct Re_L. A series of tests at both high and low Re_L values were performed to validate this assumption on the 30° *hole* configuration. To obtain the high Re_L value of 31,000, the duct velocity was increased to its maximum level by fully opening the appropriate gate valve. Conversely, to obtain a low Re_L value of 13,000, the gate valve was closed so as to reduce the flow velocity to a value just measurable on the micro-manometer. Figure 5.23 indicates that for $SR's$ less than three, the duct Re_L makes little difference. At higher $SR's$, however, the $\overline{EF}$ appears to be suppressed slightly as the duct Re_L increases. It is shown in Chapter 6 and 7 that the boundary layer which begins to form at the downstream hole edge is laminar while the region away from the hole in the main duct is fully turbulent. If the three-dimensional flow field effects (which are undoubtedly present) are neglected then $h_{laminar}$ is proportional to $Re_L^{0.5}$ and $h_{turbulent}$ is proportional to $Re_L^{0.8}$. Therefore to first order the EF should vary according to

$$EF = \frac{h_{enhanced}}{h_{baseline}} \propto \frac{h_{laminar}}{h_{turbulent}} \propto \frac{Re_L^{0.5}}{Re_L^{0.8}} \propto Re_L^{-0.3}.$$

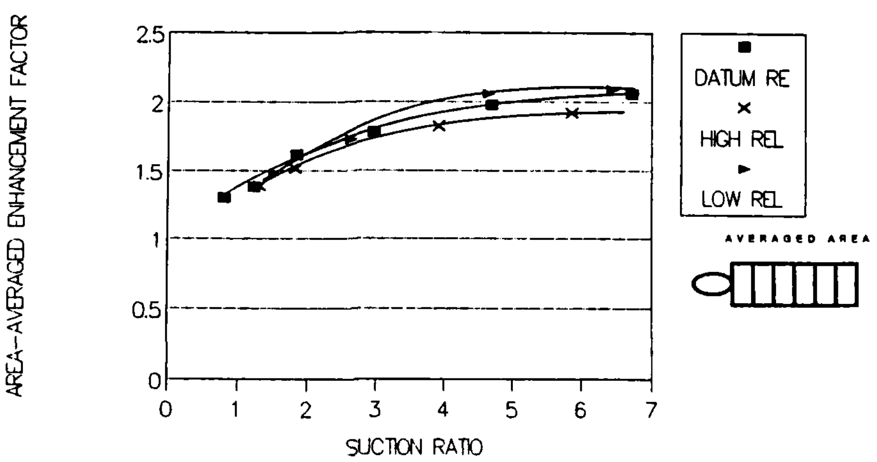

Figure 5.23: **Effect of varying the duct Reynolds number (Re_L) on $\overline{EF}$ for the 30° *hole*. Datum $Re_L = 25,000$; high $Re_L = 31,000$; low $Re_L = 13,000$.**

Figure 5.23 shows that the experimental results follow this general trend; the $\overline{EF}$ decreases as the Re_L increases.

5.4.3 Effect of Varying the Upstream Velocity and Temperature Profile

Figure 5.24 presents the results of a sensitivity study performed to determine the effect of altering the velocity and temperature profiles upstream of the film cooling hole. This was done simply by rotating a section of the tunnel wall through 180° so that the hole was nearer to the tunnel entrance. Of course, the measured temperature and velocity profiles at this new position were not as fully developed as they were in the original position approximately one metre ($\simeq 20L$) further downstream as shown in the profile comparisons given in Figure 5.25. Even though the reference

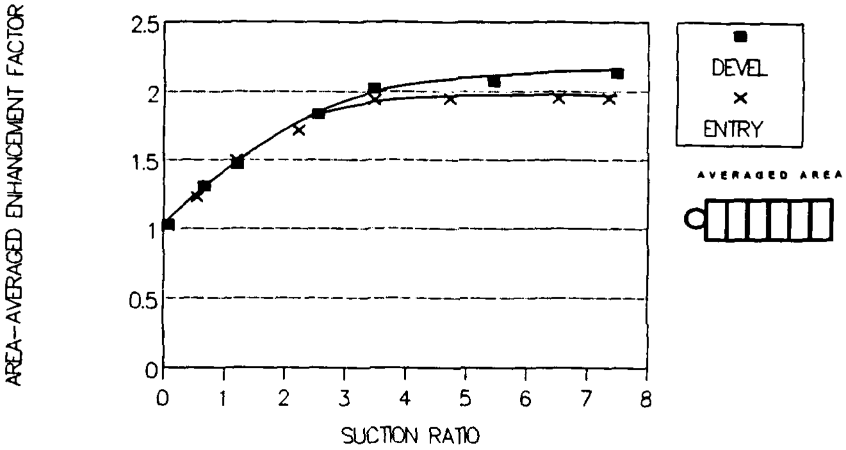

Figure 5.24: **Effect of changing the upstream temperature and velocity profiles on $\overline{EF}$.**

temperature and velocity were still measured in the same position relative to the hole, the baseline values of the heat transfer coefficient (h_o) were higher, which was to be expected since the hole was within the duct entry region. Figure 5.24 shows that for *SR's* less than three, altering the upstream profiles had almost no effect. For *SR's* greater than three, however, the *EF's* were 10% lower for the hole in the entrance region.

In summary, it seems that the area-averaged *EF* values were remarkably robust, especially at *SR's* less than three when variations in the hole inclination angles, main duct Re_L, and upstream velocity and temperature profiles made essentially no difference. It is shown in subsequent chapters that the dominant enhancement mechanism at low *SR's* is the removal of the upstream boundary layer and the formation

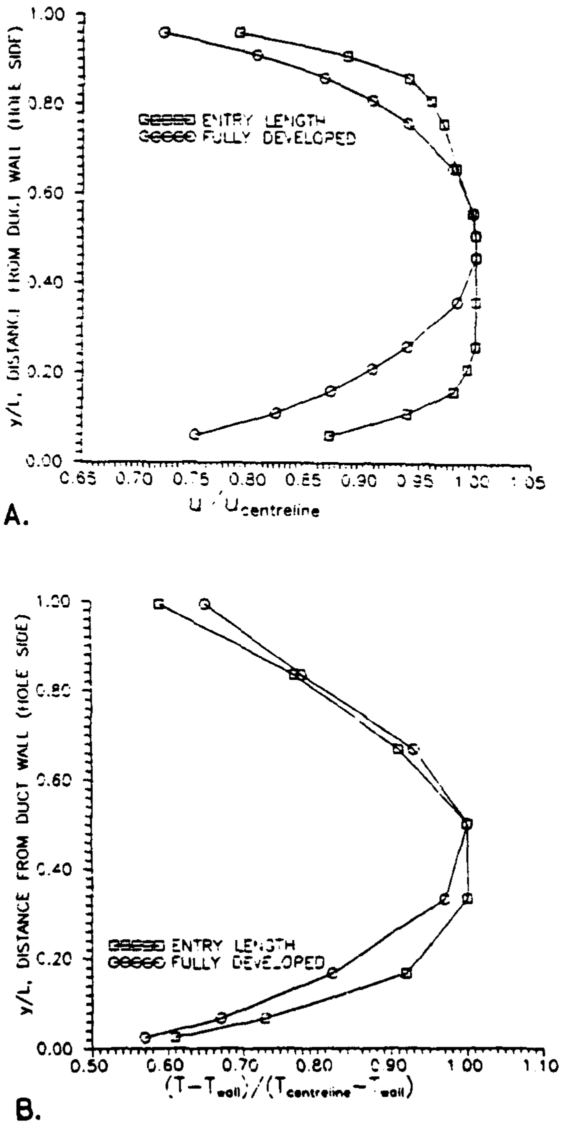

Figure 5.25: Comparison of the test section inlet conditions, downstream (fully developed) placement versus entry length placement. A.) velocity profile B.) temperature profile

of a new laminar boundary layer at the downstream hole edge. This takes place regardless of the inclination angle. At higher *SR's*, however, strong three-dimensional aerodynamic effects which are likely to be influenced by the hole inclination angle become important. These effects are discussed in subsequent chapters.

5.5 Uncertainty Analysis Issues

This section describes the steps taken to reach an estimate of the uncertainty in the measured heat transfer coefficient. The section also includes a discussion of how T_{gas} and $T_{crystal}$ can be chosen to reduce the experimental uncertainty.

5.5.1 Estimate of the uncertainty in h

Uncertainty analysis is the prediction of the uncertainty interval which should be associated with the final experimental result. Unfortunately, "there is a lot of uncertainty on uncertainty analysis ...", according to Professor R.B. Dowdell in his review of the paper, **"Contributions to the Theory of Single-Sample Uncertainty Analysis"** by **R.J. Moffat(1982)**. One major source of disagreement within the experimental community centres around the treatment of fixed or bias errors, and how to combine them with random errors, as it is not always possible or practical to separate the two. This issue becomes even more complicated when a transient experimental method is used, as opposed to a steady-state method which seems to be the focus of Moffat's paper. **Saabas et al(1987)** present an alternative method which they claim is more appropriate for the transient technique. Their main argument is that the uncertainty in measured quantities during a transient test does not always vary about some mean, true value, but instead exhibits a bias either above or below the true value. While the potentially biased portion of the uncertainty in our measured quantities is small relative to the random components, a "worst case" examination of the possible effects of bias was made. In view of the differing thoughts on uncertainty, and for completeness, the uncertainty in h was calculated using the different approaches put forward in the two papers mentioned above. Details of the calculations, tables of intermediate results, and the accompanying discussion are given in Appendix B. Additionally, the results of an independent check for errors using the time associated with the colour play of a second liquid crystal are presented and discussed in Appendix B. Briefly, these investigations support the conclusion that the relative uncertainty in h is within the $\pm$ 7% value reported by **Baughn, Ireland, and Jones (1988)** in which a direct comparison was made between heat transfer results obtained from the present method and those obtained from the steady-state, heated coating method.

5.5.2 Using uncertainty analysis to choose T_{gas} and $T_{crystal}$

During the initial stages in the design of a liquid crystal method experiment, the researcher should choose the gas temperature and the liquid crystal colour change temperature with the aim of reducing the overall uncertainty in the final result. Some guidance for determining the appropriate values can be gained from examining the following analytical expression for the relative uncertainty based on the method of

Saabas et al and derived in Appendix B.

$$\frac{\Delta h}{h} = \frac{\Delta T_{cry} + (\theta - 1)\Delta T_{init} - \theta \Delta T_{gas}}{\left[2\beta^2(\theta - 1) + \frac{2\beta}{\sqrt{\pi}}\right](T_{gas} - T_{init})}$$
$$-\frac{1}{2}\left(\frac{\Delta t}{t}\right) + \left(\frac{\Delta\sqrt{\rho c k}}{\sqrt{\rho c k}}\right)$$

It is obvious from this equation that to reduce the uncertainty contributions from the three temperatures, the term $(T_{gas} - T_{initial})$ should be as large as possible. This conclusion can also be drawn from the results of Moffat's **Jitter Program** (discussed in Appendix B) which are shown in Figure 5.26 for colour play times of 3 and 90 seconds. Since the $T_{initial}$ in the room in which the experiments took place could not be lowered at will (there was no laboratory air conditioning system), T_{gas} had to be increased. The upper limit on T_{gas} was approximately 100^oC, the temperature at which perpex begins to melt.

The second conclusion that can be drawn from the uncertainty analysis is that $T_{crystal}$ should be high enough to increase t, the time for the test surface to change colour. The maximum value of t used in the present work was approximately 90 seconds; all colour play had to be over by this time to make certain that the semi-infinite and one-dimensional assumptions remained valid. Of course, the last colour play takes place in the region away from the hole, representing the unenhanced, base- level of heat transfer. This value of h can often be predicted in advance using established correlations (such as that given in the base-level heat transfer results section). The predicted value of h along with the time of 90 seconds can be used to determine β which can in turn be used to calculate the required value of θ. Finally,

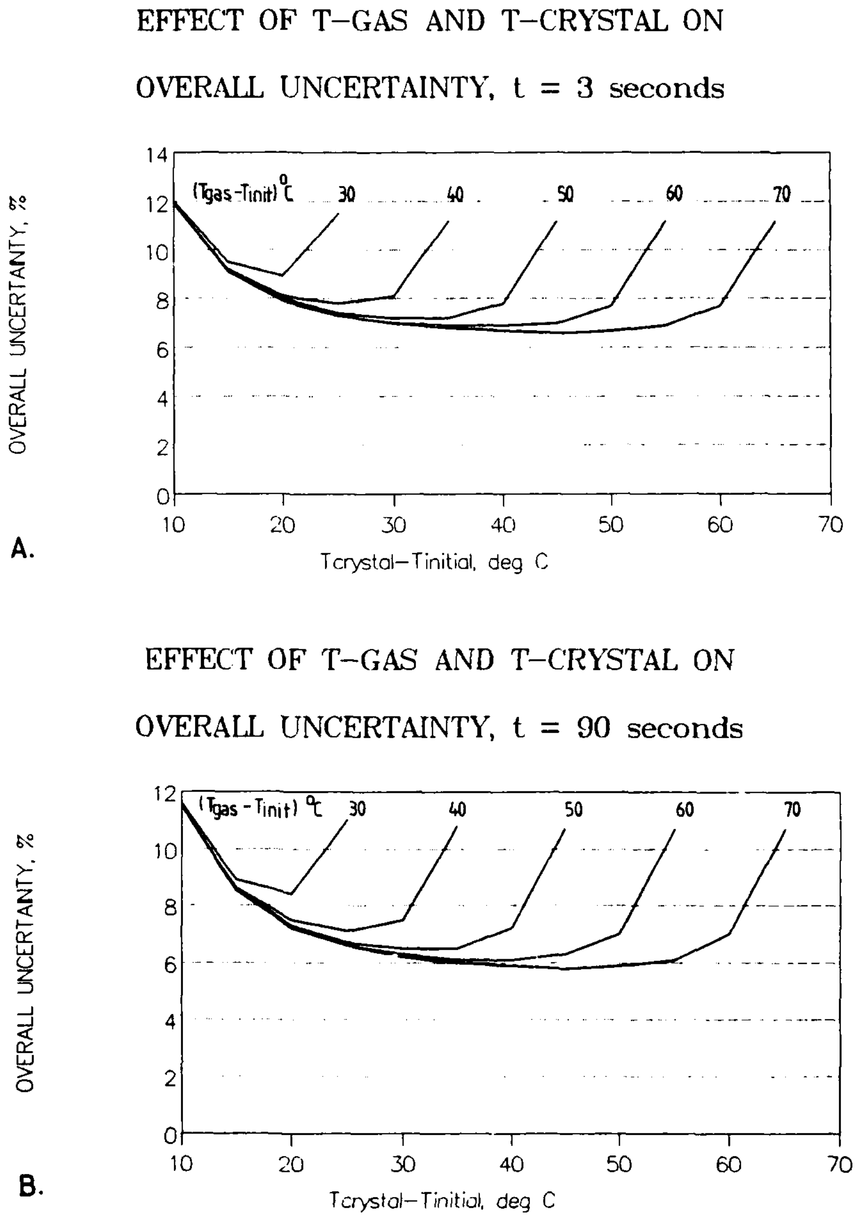
EFFECT OF T–GAS AND T–CRYSTAL ON OVERALL UNCERTAINTY, t = 3 seconds

EFFECT OF T–GAS AND T–CRYSTAL ON OVERALL UNCERTAINTY, t = 90 seconds

Figure 5.26: Effect of T_{gas} and $T_{crystal}$ on the overall relative uncertainty in h. A.) t= 3 seconds B.) t=90 seconds

$T_{crystal}$ can be determined from

$$T_{crystal} = \theta(T_{gas} - T_{initial}) + T_{initial}$$

There may be instances when the enhancement factors for a particular geometry are so large that the colour play occurs too quickly, increasing the effect of uncertainty in *time*, even though the base-level may still be changing colour at the latest acceptable *time* ($\approx$ 90 seconds). The solution to this problem is to apply a mixture of two liquid crystals with the second liquid crystal substance changing colour at a higher temperature. The base-level colour play for this second liquid crystal substance will take place after the 90 second limit, but it does not matter since the necessary information for the calculation of h_o will be captured by the first crystal. In other words, the second crystal colour play (with the higher colour play temperature) can be used for calculating the high levels of h, while the first liquid crystal colour play can be used to calculate the base-level value of h.

6 EXPERIMENTAL FLOW FIELD STUDIES

A series of experiments were performed to gain more insight into the physical reasons for the observed heat transfer distribution. The results from smoke visualization, surface flow visualization, wall static pressure measurements, velocity and temperature profile measurements, and boundary layer tripping experiments are presented and discussed. Several interesting features were discovered including: the general location of the dividing streamlines, the presence of a stagnation point downstream of the hole, the presence of a vortex pair, the removal of the near wall velocity and thermal boundary layers, and laminar flow downstream of the hole.

6.1 Smoke Visualization

Smoke visualization was performed on the 90° *hole* to determine the location of the dividing streamlines (the streamlines separating the flow going down the hole from the flow remaining in the duct), and to discover the reason why the double-lobed heat transfer enhancement contours appeared at the higher SR's. The tests were conducted using a paraffin- burning, wand-type smoke generator. The general technique involved moving the wand in and out of the catchment area, as shown in Figure 6.1, and videotaping the resultant location of the smoke. In order to make the smoke contrast with the background, the test room was darkened and the beam from a tungsten, automobile headlamp bulb was focused onto the area of interest. Figure 6.2 contains photographs of the $SR = 1.69$ case which illustrate the technique. Figure 6.2A shows the smoke bypassing the hole entrance as the wand was just

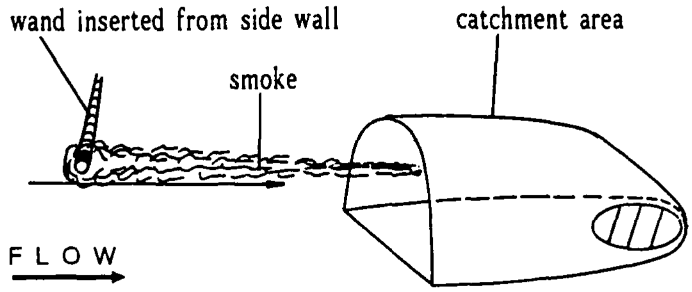

Figure 6.1: **Smoke wand and catchment area upstream of the hole.**

beneath the lower edge of the dividing streamline. In Figure 6.2B, an incremental movement of the wand upwards (in the lateral direction with respect to the hole) brought the wand into the catchment area and the smoke is shown going down the hole. Figure 6.2C reveals the location of the upper edge of the catchment area as the wand was lifted away from the near wall surface (in the vertical direction). The hole then fills with smoke. While this method had serious drawbacks (the wand's positioning was imprecise and it's presence altered the flow field), it was useful for obtaining a qualitative understanding of the flow field.

This method was also used at $SR's$ of 3.02 and 7.80. The general locations of the dividing streamlines are shown in Figure 6.3. As the SR was increased, the dividing streamlines moved outwards in the lateral direction and upwards in the vertical direction (away from the hole side of the wall) reflecting an increase in the extent of the catchment area. The smoke visualization also revealed the movement of the stagnation point downstream of the hole at $SR's$ greater than 3.

Although evidence is presented later in the thesis that points to the existence of a

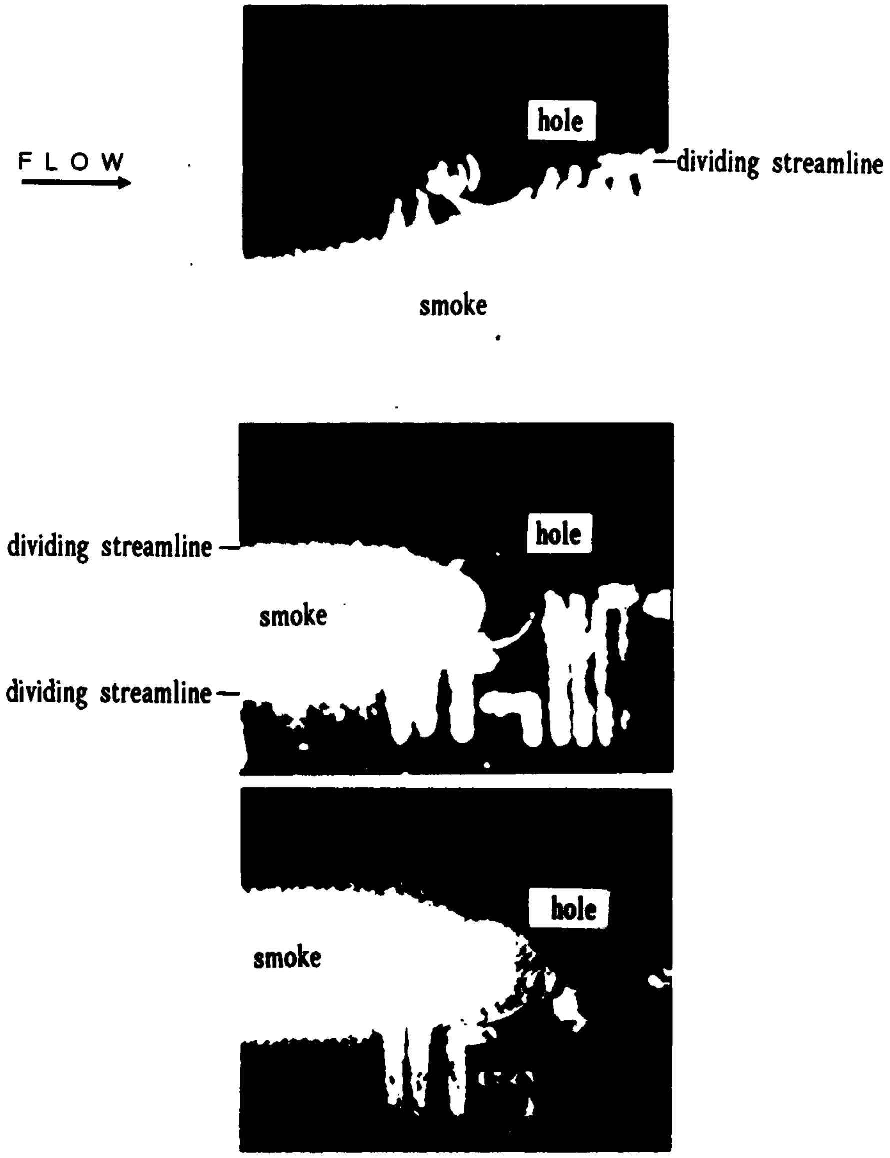
FLOW
hole
dividing streamline
smoke
dividing streamline
hole
smoke
dividing streamline
hole
smoke

Figure 6.2: Smoke visualisation results for $SR = 1.69$. Smoke wand positioned upstream of hole and A.) slightly below catchment area. B.) within the catchment area and close to the wall surface. C.) within the catchment area but slightly above the wall surface.

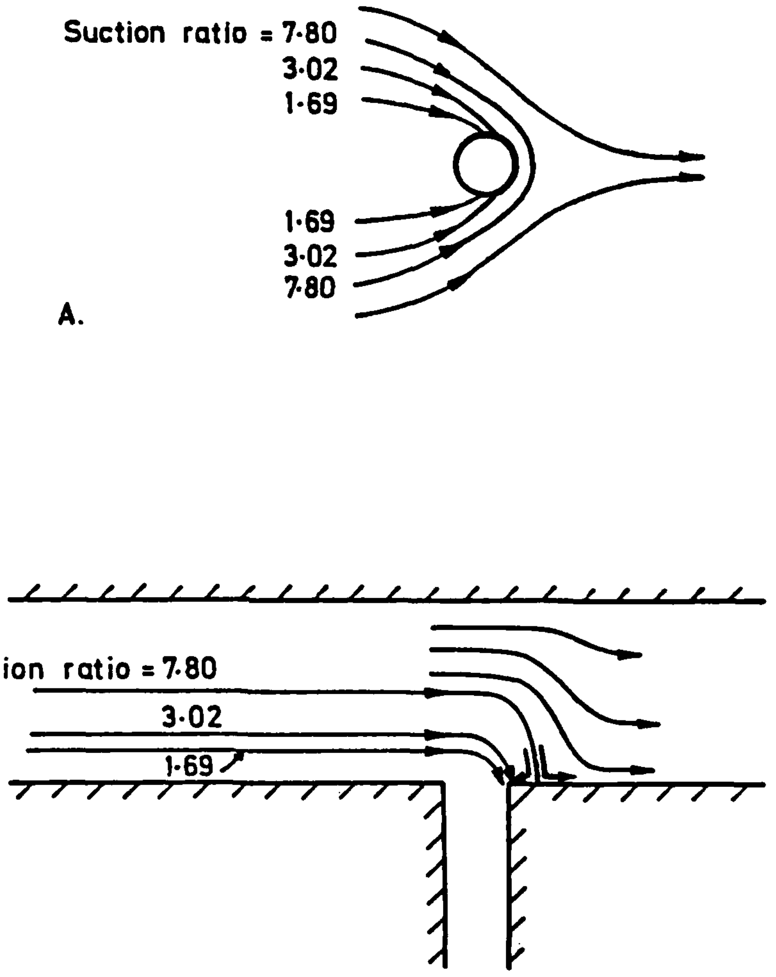
Suction ratio = 7·80
3·02
1·69
1·69
3·02
7·80
A.
Suction ratio = 7·80
3·02
1·69
B.

Figure 6.3: Location of dividing streamlines as a function of SR. A.) plan view. B.) side view.

vortex pair downstream of the hole, smoke visualization failed to do so. There are two possible reasons why smoke visualization did not make the vortex pair observable. First of all, the computational results presented in Chapter 8 indicate that the vortex pitch was very long because the rotational component of velocity was small relative to the axial velocity. Secondly, the fairly high duct turbulence level probably caused the smoke to diffuse rapidly into the flow thereby masking all but the bulk movement of the flow.

6.2 Surface Flow Visualization

The movement of the stagnation point downstream of the hole edge observed using smoke visualization was unexpected since the peak in heat transfer for the 90° *hole* was always located precisely at the downstream hole edge for all *SR's*. Therefore, surface flow visualization was performed to verify this movement and also hopefully to provide evidence of the vortex pair. The results from three methods of surface flow visualization are presented including water injection, the oil-of-wintergreen method, and the shear-sensitive liquid crystal method.

6.2.1 Water injection

Water was injected through a small hole $0.25D$ downstream of the hole edge with a hypodermic needle to determine the direction of the flow. The test wall had been fitted with a number of static pressure ports for wall static pressure measurements (which are discussed later in this chapter). Figure 6.4 contains photographs for the $SR = 1$ and $SR = 8$ cases. The water is shown dripping down the vertical wall in a

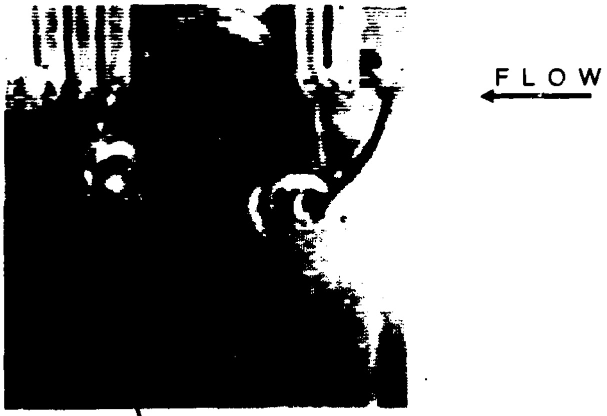

SR= 1, water dripping down the duct wall

SR=8, water being drawn into the hole by the reverse flow

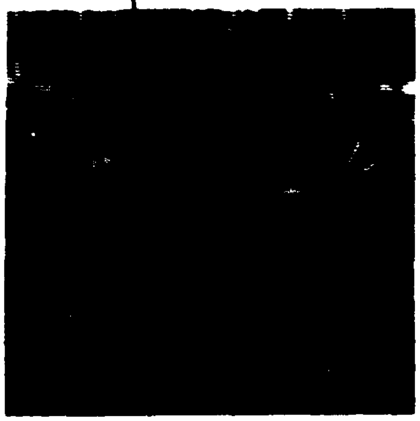

Figure 6.4: Water injection into the main duct at a point $0.25D$ downstream of the hole edge. A.) At $SR = 1$ the water dripped down the duct wall. B.) At $SR = 8$ the water was drawn back into the hole by the reverse flow.

downstream-diagonal direction when $SR = 1$ and the stagnation point was located at the downstream hole edge. When the SR was increased to 8, the water was drawn back into the hole by the reverse flow which existed downstream of the hole and upstream of the stagnation point. This somewhat crude experimental method successfully confirmed that the stagnation point did indeed move downstream of the hole edge to a distance greater than $x/D = 0.25D$.

6.2.2 Oil-of-wintergreen method

Since **Ireland (1987)** successfully employed the oil-of- wintergreen surface flow visualization method described by **Langston and Boyle (1982)** to obtain results for the horseshoe vortex, it was also attempted in the present work. This method, which is especially suitable for low-speed wind tunnels, provides a permanent record of ink traces that show surface-streamline direction and shape. Figure 6.5A is a photograph of a matrix of ink dots marked on drafting film mounted flush to the test surface near the entrance to the film cooling hole. The dots were made with a felt-tipped pen *(Staedtler Lumocolor 317)* containing water-insoluble blue ink. The drafting film was mounted to the test surface using *Scotch 3M SprayMount* adhesive. Immediately before flow initiation, an access door was opened and the test surface was sprayed with oil-of wintergreen (synthetic methyl salicylate) using an air brush so that the surface was covered with a thin, continuous liquid film. The access door was then closed and the tunnel triggered so that flow was introduced into the test section. The ink dots dissolved into the fluid and acted as tracers under the influence of the wall shear forces. The entire process was recorded on videotape.

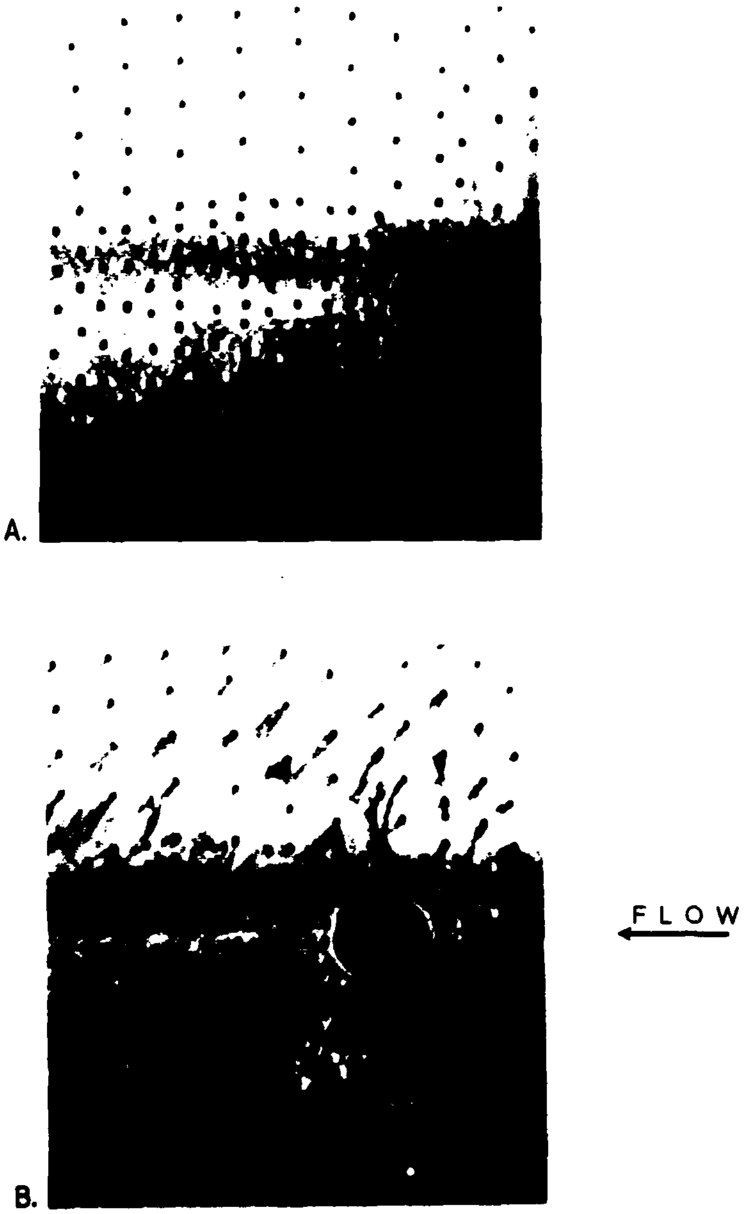

Figure 6.5: Oil-of-wintergreen method results for $SR = 1.7$. A.) Before flow initiation. B.) After flow initiation.

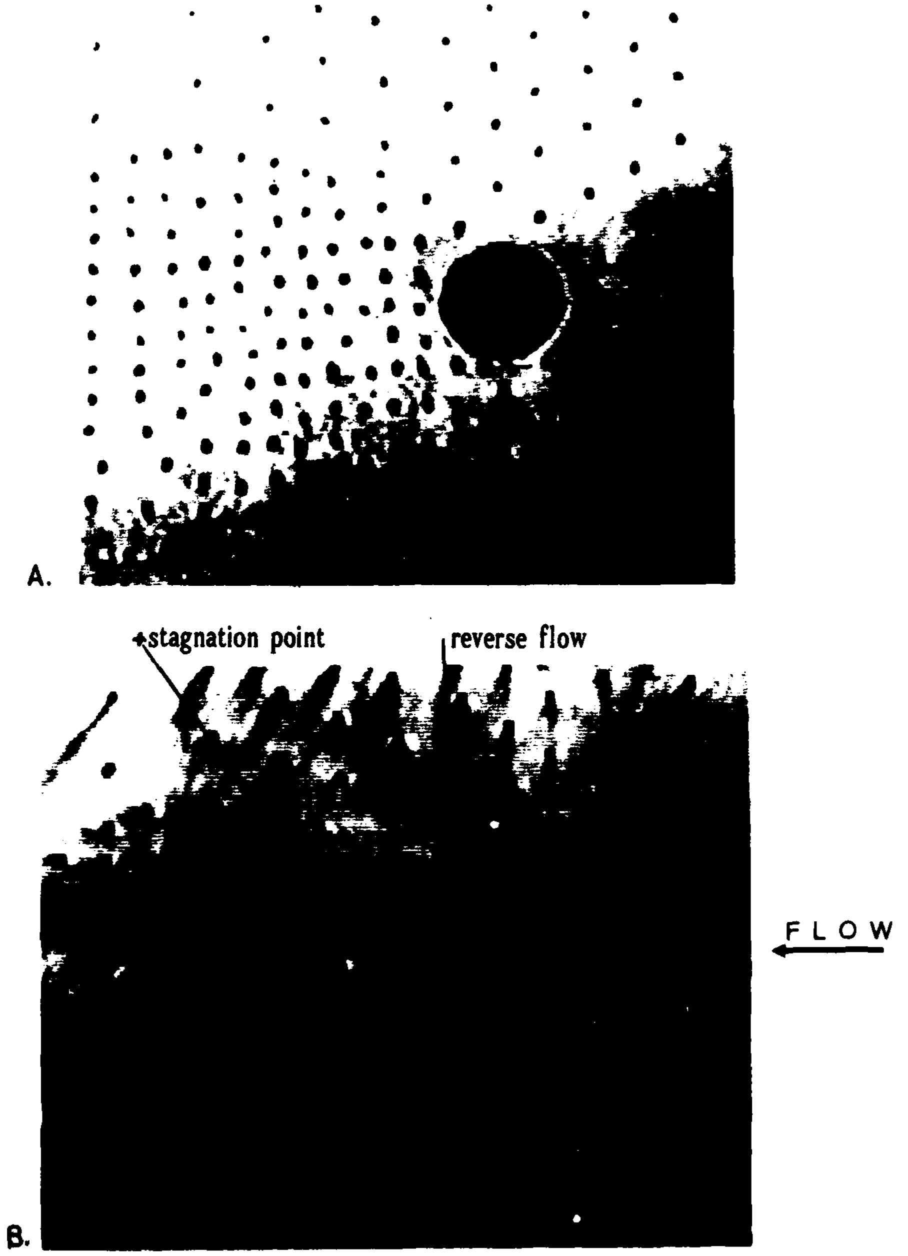
A.
stagnation point
reverse flow
FLOW
B.

Figure 6.6: Oil-of-wintergreen method results for $SR = 8.0$. A.) Before flow initiation. B.) After flow initiation.

The results for the $SR = 1.7$ case are shown in Figure 6.5. Unfortunately, it was not practical to make the duct wall horizontal so gravitational forces obscured the results, at least those away from the hole. Close to the hole, however, the wall shear forces were strong enough to dominate the gravitational forces so that the direction of the streaklines accurately reflected the direction of the surface streamlines. For the $SR = 1.70$ case, the stagnation point was located at the downstream hole edge so no reverse flow is apparent. However, for the $SR = 8$ case shown in Figure 6.6, the stagnation point was located downstream of the hole edge so the streaklines immediately downstream of the hole show that the flow had reversed direction in order to enter the hole.

6.2.3 Shear-stress sensitive liquid crystals

Much later in the test program after the 30° *hole* configuration was mounted in the test section, a new surface flow visualization technique was attempted. The technique was based on a new mixture of non-encapsulated, shear-sensitive, cholesteric liquid crystals described by **Bonnett (1989)**. Before the test, a thin, even coat of the liquid crystal substance was brush painted onto the test surface. A hot air gun was then used to heat the material into the clear isotropic phase. When the crystal substance cooled, it reentered the cholesteric phase, which was discussed in Chapter 3, but with a complex, disordered texture known as the *focal-conic* texture. In this form, the helical axis of the liquid crystal molecular planes are randomly aligned and hence constructive interference of reflected light does not occur. This results in the scattering of light which makes the *focal-conic* texture appear opaque with a milky-white colour. After flow initiation, however, surface shear forces that were above a certain threshold level induced a texture change from the disordered focal-conic texture to the ordered, *Grandjean* texture. This texture results in the selective reflection of wavelengths corresponding to colours within the visible spectrum. These textures are illustrated in Figure 6.7. There is one big advantage of this method over the oil-of-wintergreen method; the gravitational force on the liquid crystal coating was not great enough to produce the level of shear force required to exceed the texture change threshold. This permits the technique to be used on vertical or irregular wall surfaces. Another advantage of this method is that the surface finish always remains hydrodynamically smooth. Even after the molecular texture change occurs in response to the shearing effects of the flow, the liquid crystal material does not become rough.

A photograph of the results for the $SR = 8$ case is shown in Figure 6.8. The extremely high level of surface shear force near the hole entrance, which was caused by the local acceleration of the flow entering the hole, was sufficient to induce the desired texture change, hence the coloured ring. Unfortunately, however, the shear forces elsewhere were too weak, so no evidence of the vortex pair was provided. The presence of the coloured ring downstream of the hole corresponds to a region of reverse flow. The stagnation point location is downstream of the ring as shown in Figure 6.8.

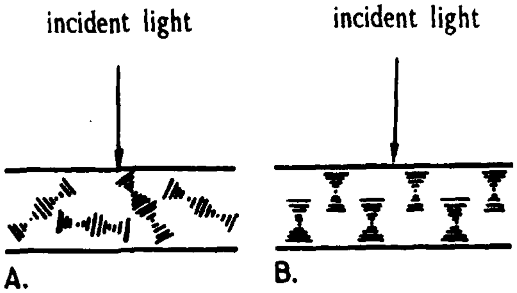
incident light
incident light
A.
B.

Figure 6.7: The texture change within the cholesteric phase induced by surface shear stress. A.) Focal-conic (disordered, opaque) texture present before flow initiation. B.) Grandjean (ordered, coloured) texture present after shear stress alignment.

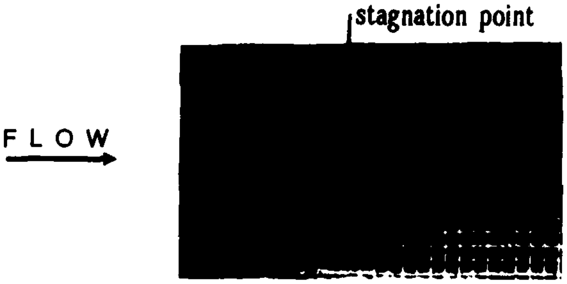
stagnation point
FLOW

Figure 6.8: Shear-stress sensitive liquid crystals applied to the entrance of the 30° *hole* for $SR = 8$.

6.3 Wall Static Pressure Measurements

While the smoke and surface flow visualization did confirm the movement of the stagnation point to a location downstream of the hole, the results generally lacked spatial precision. Also, a greater understanding of the near wall velocity field was needed. Therefore, wall static pressure measurements were made in the downstream direction along the axial hole centreline and also in the lateral direction. The measurement locations were chosen to correspond to areas of interest highlighted by the observed heat transfer EF patterns. The measured wall static pressures are given in terms of the coefficient of pressure

$$C_p(x) = \frac{(P(x) - P_1)}{(P_{t1} - P_1)}$$

where P_1 and P_{t1} are the static and total pressures at the reference location, 180mm upstream of the hole. This was far enough upstream of the hole to be uninfluenced by changes in the SR.

6.3.1 Pressure measurement procedure

The wall static pressures were measured using a single, calibrated, electronic differential-pressure transducer linked to 10 different pressure ports via a *Furness* switchbox as shown in Figure 6.9. Once the tunnel was running at the desired flow condition, the differential pressures $(P(x) - P_1)$ were measured sequentially. The switching process was controlled electronically using the output from a parallel I/O card mounted in the IBM-PC. The I/O card sent digital signals to a set of relays which in turn opened and closed the appropriate valves in the switchbox to select the desired pres-

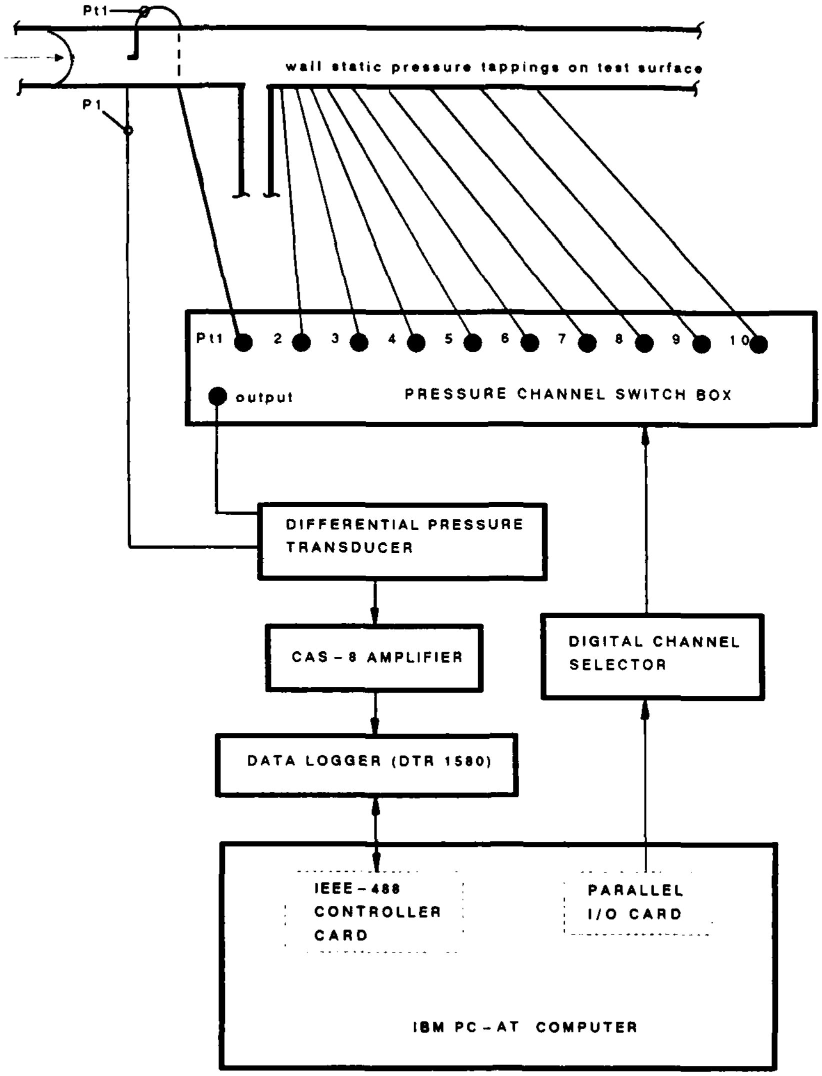
Pt1
wall static pressure tappings on test surface
P1
Pt1
2
3
4
5
6
7
8
9
10
output
PRESSURE CHANNEL SWITCH BOX
DIFFERENTIAL PRESSURE TRANSDUCER
CAS-8 AMPLIFIER
DIGITAL CHANNEL SELECTOR
DATA LOGGER (DTR 1580)
IEEE-488 CONTROLLER CARD
PARALLEL I/O CARD
IBM PC-AT COMPUTER

Figure 6.9: Schematic of wall static pressure measurement apparatus.

sure channel. The interface between the I/O card and the switchbox was designed and constructed in-house; further details are given in **Pitcher (1987)**. After the switch to each new pressure channel, the data acquisition program waited 20 seconds before the pressures were read to ensure that oscillations set up by the switching process had completely dissipated. The pressure transducer output was also monitored visually during the test on a digital voltmeter to make sure the readings were taken during a steady-state period.

6.3.2 Wall static pressure results

Figure 6.10 shows the results for the measurements taken along the plane of the *axial hole centreline downstream* of the hole for *SR's* 0 to 4.21. The location where $C_p(x)$ takes on a value of 1 corresponds to a stagnation point produced by flow from the centre portion of the duct. The figure shows that the stagnation point moved downstream of the hole edge as the SR was increased until it reached a location of $x/D = 0.25D$ at $SR = 4.21$. The first wall tapping was located at $x/D = 0.25$ so presumably the flow actually began to stagnate on the downstream duct wall at *SR's* less than 4.21. Another interesting feature is that for these relatively low *SR's*, the values of $C_p(x)$ in Figure 6.10 approach 0 at positions greater than $x/D = 3$. This implies that the local near-wall velocity approached that of the upstream centreline velocity, a result which is in agreement with velocity profile measurements presented in the next section. Also for $SR = 0$, an initial dip in the $C_p(x)$ curve corresponds to a region of heat transfer enhancement which suggests that increased turbulence may be present. Downstream of $x/D = 3$, the curve for $C_p(x)$ corresponds roughly

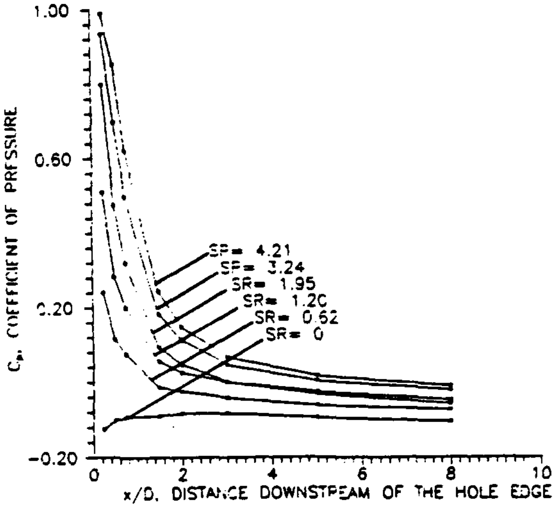

Figure 6.10: Effect of *SR* on wall static pressures downstream of the hole along the axial hole centreline (for *SR's* 0 to 4.21).

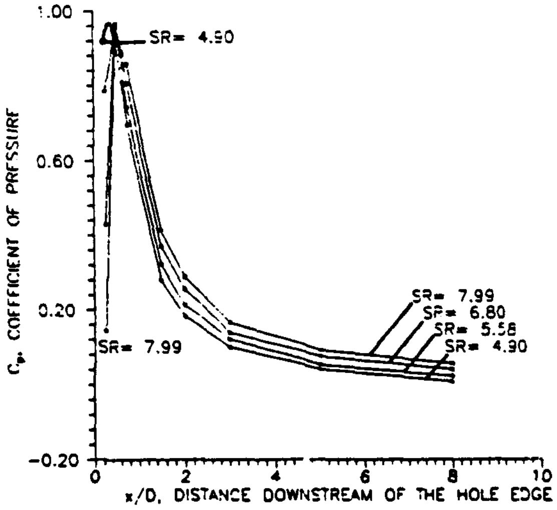

Figure 6.11: Effect of *SR* on wall static pressures downstream of the hole along the axial hole centreline (for *SR's* 4.90 to 7.99).

to a line with a negative slope which reflects the pressure drop within the main duct due to frictional losses. In fact, a line passing through the $SR = 0$ C_p curve at $x/D = 3, 5$, and 8 which is then extended backwards in the upstream direction, intercepts the *x-axis* near the reference location where P_1 was measured.

Figure 6.11 presents the results for $SR = 4.90$ to 7.99 which show that the stagnation point continued to move in the downstream direction until $x/D = 0.50$ at $SR = 5.58$. The stagnation point appears to have remained at this same location, as indicated by the nearly constant value of $C_p(x)$, even when the SR was increased still further to 7.99. Of course, the pressure tappings existed only at a few discrete locations so small shifts in location might not have been detected. Figure 6.11 also reveals the acceleration of the reverse flow at $x/D = 0.25$ which is indicated by a drop in C_p as the SR is increased.

Figure 6.12 shows the results of measurements taken in the lateral direction at a point $1.5D$ downstream of the hole. The interpretation of these results is made considerably easier by referring ahead to the numerically predicted, secondary flow velocity vectors presented in Chapter 8. These vectors confirm the presence of a vortex pair downstream of the hole. A simplified sketch of this vortex pair is shown in Figure 6.13. From this figure it is possible to see that the relatively large values of $C_p(x)$ that exist near the hole centreline ($z/D \approx 0$) correspond to the vortex pair downwash region while the dip in the $C_p(x)$ values around $z/D = 1$ corresponds to the location where the vortex is tangent to the wall surface. At the time these measurements were taken which was early in the test program and before

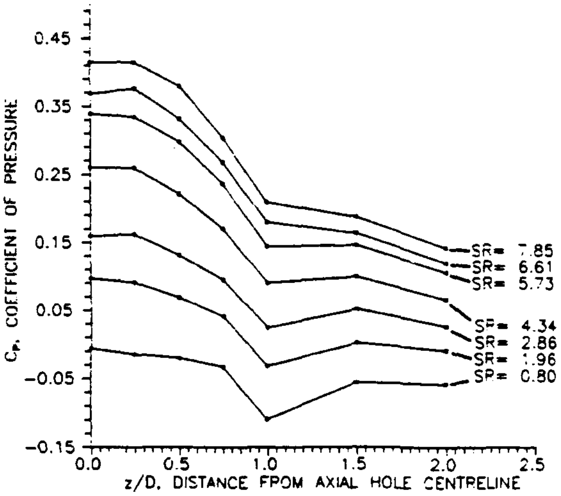

Figure 6.12: Effect of SR on the wall static pressure along a line in the lateral direction, $1.5D$ downstream of the hole.

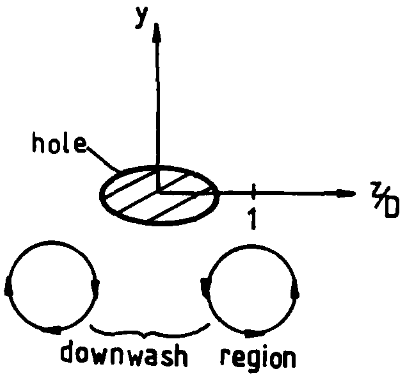

Figure 6.13: Simplified sketch of the vortex pair downstream of the hole. Viewpoint is looking upstream from a downstream position.

the computational predictions were made, this drop in $C_p(x)$ near $x/D = 1$ was completely unexpected. Therefore a number of checks were made to ensure that the unexpected results were due to a real effect rather than a measurement error. This included re-checking for flow blockage within the tube connecting the static pressure port to the switchbox and using a different transducer to sense the value of $P(x)-P_1$. Of course, the checks revealed that the measurements taken in the first place were accurate.

6.4 Velocity Profile Measurements

Velocity profile measurements were made 60mm ($\approx 3D$), 110mm ($5D$), and 180mm ($\approx 8D$) downstream of the hole using a "swan-neck" pitot-tube traverse. The pitot tube had an inside diameter of 0.9mm and an outside diameter of 1.24mm. The velocity values were calculated using the pitot-static pressure differential and Bernoulli's equation. For a total pressure traverse to accurately reflect the velocity profile, the static pressure measured at the orifice on the duct wall must be equal to the static pressure along the traversing plane. A check was therefore made by measuring the wall static pressures on either side of the duct wall, at locations which corresponded to the endpoints of the traversing plane. At the 60mm downstream location, the static pressure on the hole side of the duct wall was slightly higher (by an amount $\approx 5\%$ of $P_{t1} - P_1$) than the static pressure on the opposite side when $SR = 8$, the "worst case" situation. This was due to the flow's direction which was slightly downwards towards the hole side of the wall at the 60mm measurement location.

However, further downstream at the 110mm and the 180mm measurement locations the static pressure on both walls were equal to each other. Evidently, the error at the 60mm location was minimal, since the velocity profile trends at all three measurement locations are consistent. The velocity values were normalized with respect to the upstream reference centreline velocity (measured 180mm upstream of the hole).

Figures 6.14-6.16 are the velocity profiles for the 60mm, 110mm, and 180mm measurement locations, respectively. All three figures reveal that flow extraction effectively removed much of the slow moving, boundary layer flow near the hole side of the wall so that the velocity in the downstream region approached the upstream centreline value. As the SR was increased from 0 to 2, the local near wall velocity increased so the profile is shown to move forward from the *1/7th power law* profile. Since the slow moving flow near the wall was replaced by the fast moving flow from the centre of the duct, the profile remains stationary for SR's between 2 to 4. Finally, as the SR was increased above 4 the local velocity decreased causing the profile to move back towards the *1/7th power law* profile. This is probably due to the increased flow area for the air that does not pass into the hole, as illustrated in Figure 6.17, and hence velocity reduction according to continuity. Of course this argument only applies for $SR > 4$. For lower SR's, the removal of the near wall boundary layer appears to be the dominant effect.

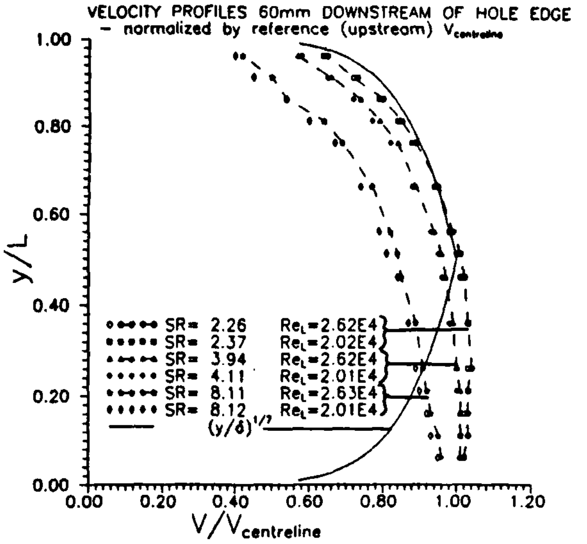

Figure 6.14: **Velocity profiles 60mm downstream of hole edge.**

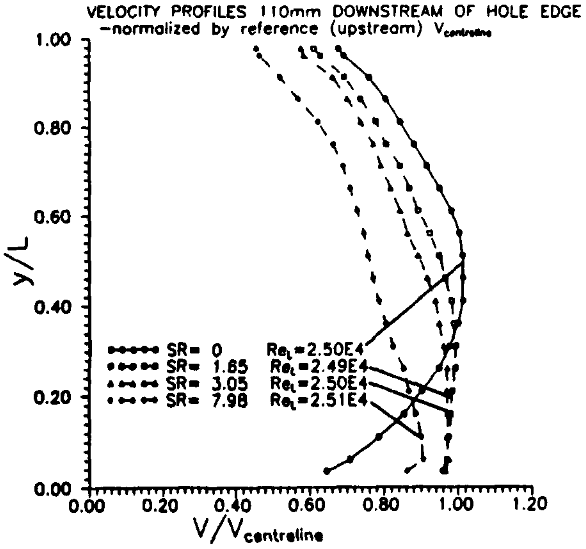

Figure 6.15: **Velocity profiles 110mm downstream of hole edge.**

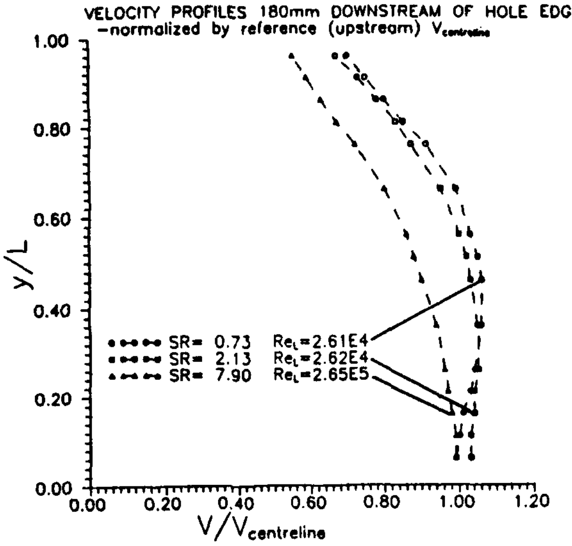

Figure 6.16: **Velocity profiles 180mm downstream of hole edge.**

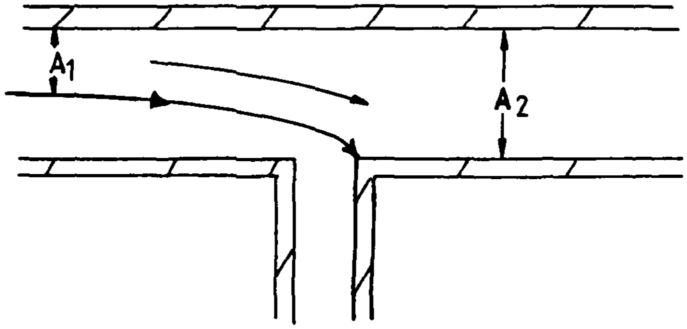

Figure 6.17: **The reason why the local velocity in the downstream region is less than the upstream centreline velocity for $SR's > 4$. The flow area A_2 is greater than the flow area A_1.**

6.5 Temperature Profile Measurements

A series of temperature profile measurements were made at a point 60mm downstream of the hole along the axial hole centreline using the thermocouple rake shown in Figure 6.18. The results are shown in Figure 6.19 in terms of

$$\frac{(T(y) - T_{wall})}{(T_{centreline} - T_{wall})}$$

where $T_{centreline}$ was the value measured at the upstream reference location. This enabled the temperature profiles at the downstream location to be related to the flow upstream of the hole in the same way the velocity profiles were. As the SR was increased from 0 to 2, the temperature near the wall increased to a value close to the upstream centreline value. This implies that much of the relatively cool near-wall boundary layer flow was removed. In its place, the hotter flow from the centre portion of the duct was brought down to the surface. As the SR was increased still further to values greater than 2, the temperature remained steady until $SR \approx 6$. For $SR's$ greater than 6, the near wall temperatures decreased. This was probably due to the cool flow from the far wall being brought down to the near wall surface. The important conclusion which can be drawn from the temperature profile study is that flow extraction through the film cooling hole effectively removed much of the upstream thermal boundary layer. This caused the local gas temperature to approach the upstream centreline value of gas temperature. This was certainly one of the reasons for the enhanced heat transfer downstream of the hole.

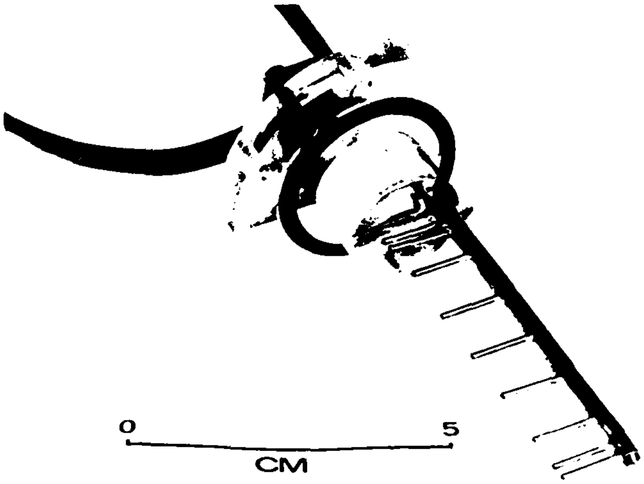

Figure 6.18: **Thermocouple rake used for measuring temperature profiles.**

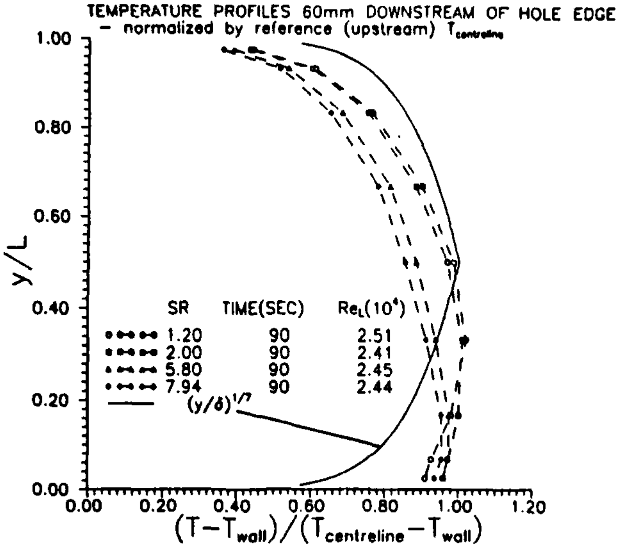

Figure 6.19: **Effect of SR on the temperature profiles at a point 60mm downstream of the hole along the axial hole centreline.**

6.6 Boundary Layer Tripping Study

Both the velocity and the temperature profile studies have shown that the near wall boundary layer is removed by the flow extraction process. Therefore it is quite likely that a new boundary layer begins to form at or near the downstream edge of the hole, with a local velocity and gas temperature that is very close to the upstream centreline values. Furthermore, this new boundary layer is probably laminar judging from the Reynolds number based on the duct centreline velocity at a position $2D$ downstream of the hole edge. The value of Re_x at this location is $1.9(10^4)$, which is a full order of magnitude below the critical Re_x normally associated with transition on a flat plate. To test this hypothesis, a series of experiments were performed to find out if the laminar boundary layer could be tripped into a turbulent boundary layer; the underlying idea being that a boundary layer already turbulent could not be tripped again. The test consisted of placing a 0.63mm (0.025in) diameter wire flush to the test wall surface and in a direction perpendicular to the flow at a position $2D$ downstream of the hole and then conducting an otherwise standard heat transfer experiment. The wire was long enough to span both the affected region immediately behind the hole (near the axial hole centreline) and the region which was known to be turbulent (further away from the hole centreline).

Time elapsed photographs of the colour play for the $SR = 0.63$ and 5.20 cases are shown in Figures 6.20 and 6.21 which indicate that the flow downstream of the hole was indeed tripped into a turbulent boundary layer. The photographs show that the heat transfer immediately downstream of the hole in the region thought to

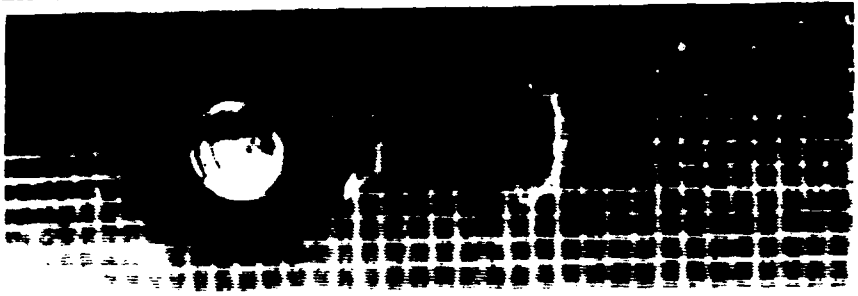

t= 15.32 seconds

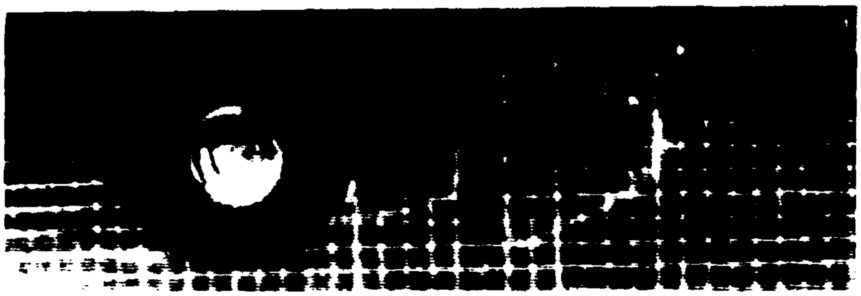

t= 31.12 seconds

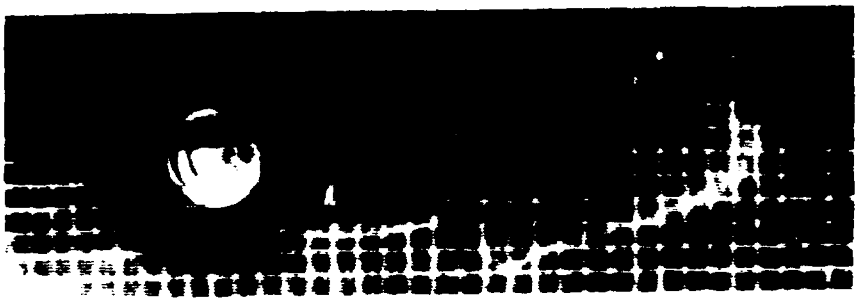

t= 45.24 seconds

Figure 6.20: **Time elapsed photographs showing the laminar boundary layer downstream of the hole being tripped to a turbulent boundary layer. ($SR = 0.63$)**

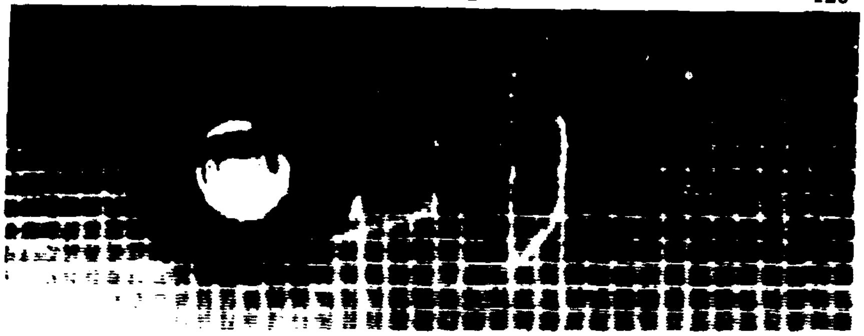

t= 9.62 seconds

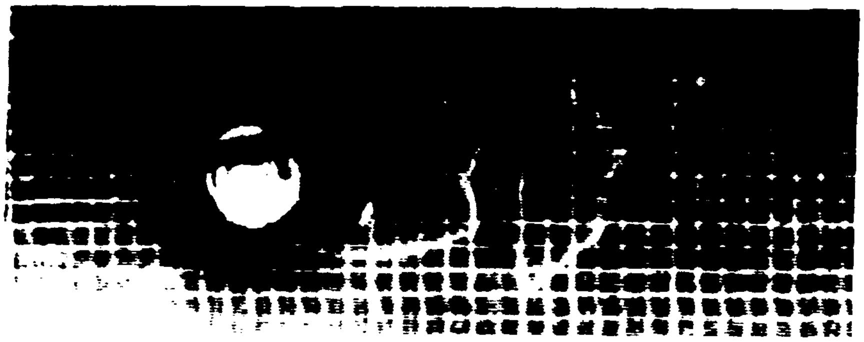

t= 14.18 seconds

t= 25.22 seconds

Figure 6.21: **Time elapsed photographs showing the laminar boundary layer downstream of the hole being tripped to a turbulent boundary layer. ($SR = 8.0$)**

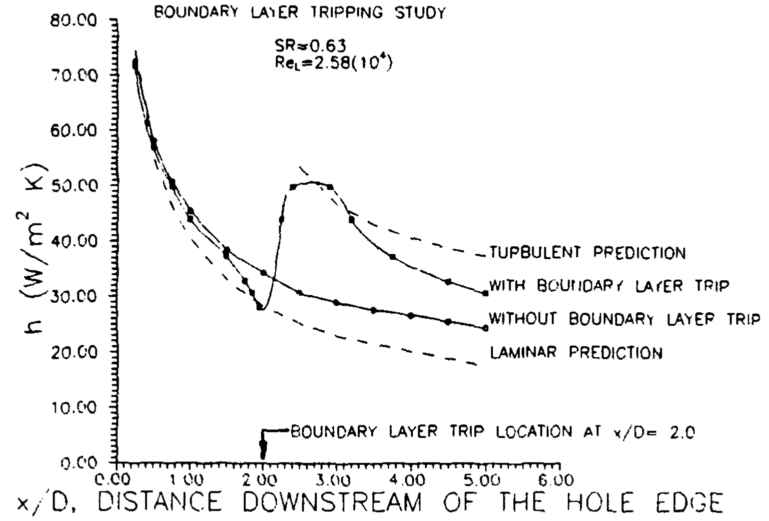

Figure 6.22: **Boundary layer tripping study- values of h along the axial hole centreline downstream of the hole.**

be laminar was enhanced while no enhancement was observed in the region known to be turbulent. Figure 6.22 is a plot of the centreline value of h versus x/D for the $SR = 0.63$ cases, both with and without the boundary layer trip. The h values are the same until shortly before the trip wire location but downstream of that position the h for the case with the trip greatly increases. Also shown are the laminar and turbulent predictions. The laminar prediction assumes the boundary layer begins at the downstream hole edge. The local freestream velocity is that from the wall static pressure measurements. Very good agreement exists until $x/D = 1$, but then the laminar prediction falls below the measured values, probably because of three-dimensional effects. The laminar prediction will be discussed in much greater detail in the Chapter 7. The turbulent prediction assumes the boundary layer begins at

$x/D = 2$, the location of the trip wire, and that the local freestream velocity is constant at the upstream centreline value. Although the velocity does vary slightly at this position according to the C_p measurements, **Kays and Crawford (1980)** points out that the shape of the turbulent velocity profile is much less sensitive to the variation of freestream velocity than is the case for the laminar boundary layer. Therefore, h was calculated using

$$h = (\rho uc)0.0287 Re_x^{-0.2} Pr^{-0.4}$$

the equation for turbulent flow on an isothermal flat plate with constant freestream velocity.

Discovering the laminar nature of the boundary layer downstream of the hole was very important since it provided the starting point for the analytical heat transfer predictions presented and discussed in the next chapter.

7 ANALYTICAL HEAT TRANSFER PREDICTIONS

This chapter describes an analytical investigation into the heat transfer enhancement downstream of the hole edge. In Chapter 6, the flow field studies suggested that the boundary layer downstream of the hole was laminar in nature. Therefore the analytical heat transfer predictions described in this chapter were based on the assumption that a new laminar boundary layer began to form at the downstream hole edge, as if it were the leading edge of a flat plate, as illustrated in Figure 7.1. (For the cases where the stagnation point was downstream of the hole edge, the boundary layer was assumed to have begun immediately downstream of the stagnation point.) An analytical prediction for the heat transfer coefficient (h) was therefore obtained by using the equation given in **Kays and Crawford (1980)** for a laminar, two-dimensional boundary layer forming on an isothermal flat plate with an arbitrarily varying freestream velocity

$$St_x = \frac{0.418\nu^{0.5}u(x)^{0.435}}{(\int_0^x u(x)^{1.87}dx)^{0.5}} \tag{7.1}$$

For both the two and three-dimensional cases, the value of $u(x)$ was deduced from the variation of the wall static pressure coefficients, $C_p(x)$. In the two-dimensional (or slot) case, an analytical prediction technique developed by **Morland (1989)** was used to obtain the required wall static pressure results. The Morland study of the inviscid flow field for two and three-dimensional suction was complementary to the present research and was suggested by the work reported here. For the three-

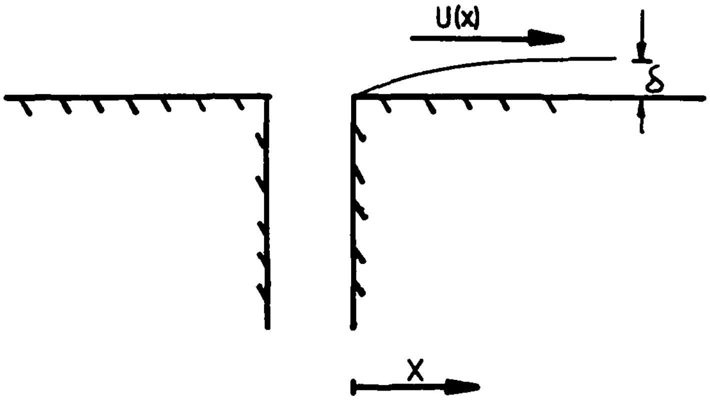

Figure 7.1: **Laminar boundary layer forming at the downstream hole (or slot) edge.**

dimensional case, measured values of wall static pressure along the hole centreline, which were presented in Chapter 6, were used. A simple check of the computer program written to calculate h from equation 7.1 was made by letting

$$u = u_\infty = constant$$

and verifying that the calculated value for h agreed with the value obtained from

$$Nu_x = 0.332 Re_x^{1/2} Pr^{1/3}$$

the exact solution for an isothermal flat plate in a uniform, constant velocity flow field.

7.1 Predicted Results for the Two-dimensional (Slot) Case and Comparisons with Experimental Results.

Morland's analytical prediction technique yielded values of $C_p(x)$ as a function of slot suction ratio where

$$C_p(x) = \frac{(P(x) - P_\infty)}{(P_{t\infty} - P_\infty)} = 1 - (\frac{u(x)}{u_\infty})^2 \tag{7.2}$$

The prediction was obtained using conformal mapping, a method for solving boundary value problems in two-dimensional potential flow theory. Therefore to use this method, Morland had to assume the flow was inviscid, incompressible, and irrotational which meant that the velocity profile upstream of the hole had to be uniform as shown in Figure 7.2. Morland found that his analytical results were in good agreement with measured values of wall static pressure obtained in a wind tunnel with a uniform velocity profile. In these tests, Morland used a boundary layer bleed, which was positioned upstream of the slot, to obtain the uniform velocity profile.

A series of heat transfer experiments for the two-dimensional (slot) case were performed to provide the experimental basis for a comparison with the theoretical heat transfer predictions derived from Morland's two-dimensional analytical predictions of the flow field. As shown in Figure 7.3, a photograph of typical colour play for slot heat transfer, it is clear that the slot's aspect ratio of 30:1 was large enough to reduce the influence of three-dimensional flow field effects to a negligible level, especially along the axial slot centreline.

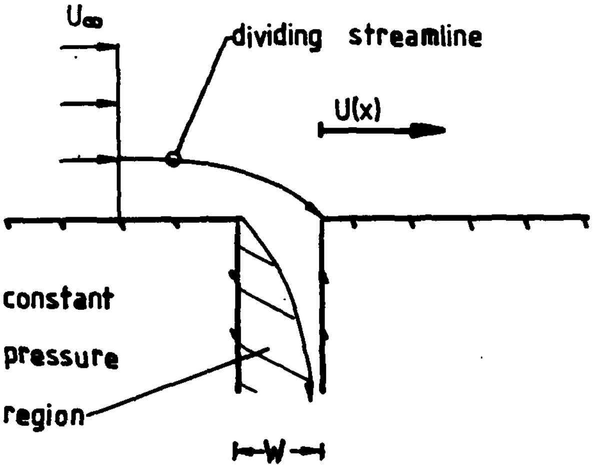
U_∞
dividing streamline
U(x)
constant
pressure
region
W

Figure 7.2: Model used in Morland's analytical solution for $C_p(x)$.

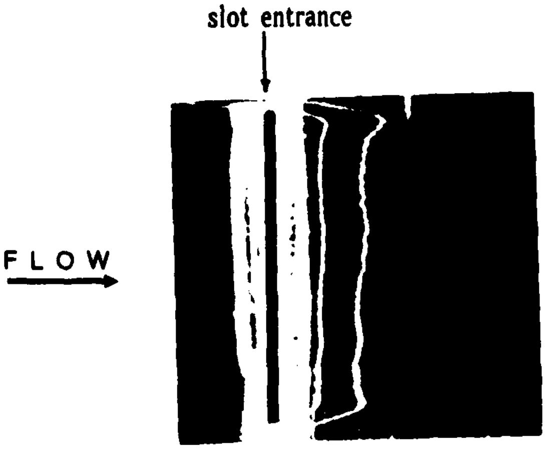
slot entrance
FLOW

Figure 7.3: Typical colour play for the slot heat transfer ($SR = 3.91$).

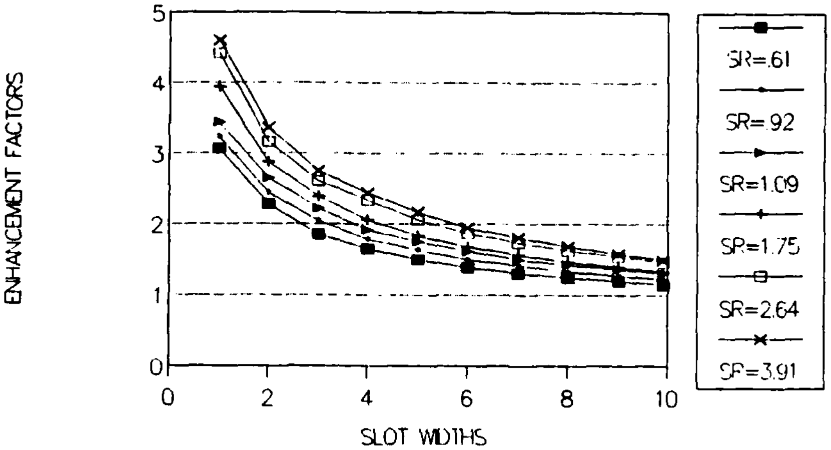

Figure 7.4: **Enhancement factors for the slot showing the effect of SR.**

The experimental slot heat transfer results are presented in Figure 7.4 as EF versus the distance in slot widths downstream of the slot edge (x/W). Both the streamwise variation of the EF and the effect of increasing the SR are very similar, in a qualitative sense, to those for the hole.

Figures 7.5 is Morland's predicted $C_p(x)$ distribution for the $SR = 0.61$ case. From the $C_p(x)$ distribution, the predicted velocity was obtained from equation 7.2 and used in equation 7.1 to calculate the predicted value of the heat transfer coefficient. Figure 7.6 is the corresponding comparison between the predicted and the experimental heat transfer distribution.

Notice that the experimental values are less than the predicted values until $x/W = 11$. This is probably due to the presence of boundary layer effects since at low SR's the upstream boundary layer may not be completely removed as illustrated in Figure 7.7. Unfortunately, the boundary layers in the experimental case

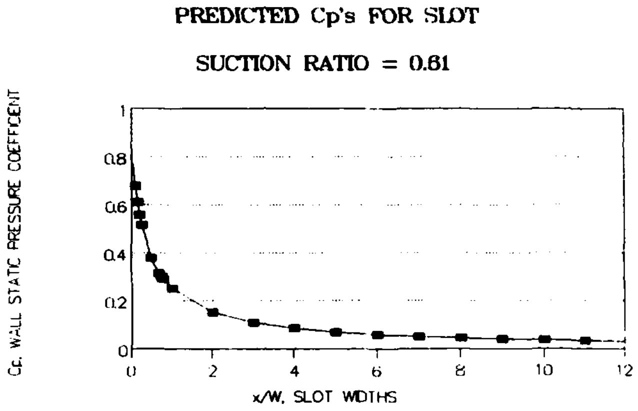

Figure 7.5: **Predicted $C_p's$ for slot- $SR = 0.61$.**

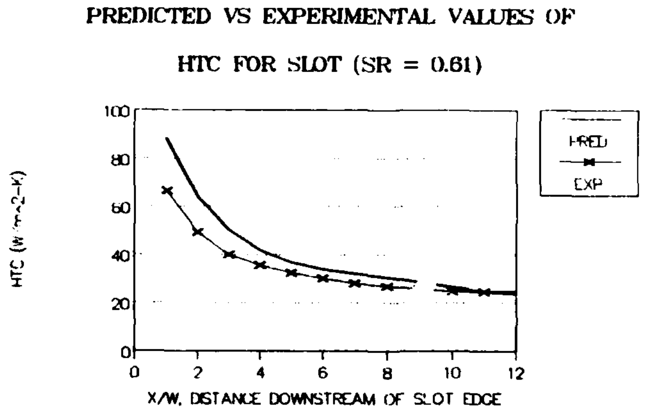

Figure 7.6: Predicted versus experimental values of h for the slot- $SR = 0.61$.

were present because there was no boundary layer bleed upstream of the test section in the tunnel used. Even though the slot was positioned within the entrance region of the main duct, rather than within the fully-developed region, the velocity and temperature profiles were non-uniform. (These profiles were presented in Figure 5.25). At higher $SR's$, however, the entire boundary layer would most likely be removed so that the uniform flow from the centre of the duct would be brought down to the near wall region and therefore more closely match the situation modelled by Morland. Figures 7.8-7.13 are the results for $SR's$ of 1.09, 1.75, and 3.63, cases for which there is much better agreement between experimental and predicted heat transfer results. Morland's wall static pressure predictions also revealed that the stagnation point, as indicated by a $C_p(x)$ value of one, moved downstream as the suction rate was increased. Therefore the boundary layers were assumed to begin immediately downstream of the stagnation point for the purpose of calculating h. Hence for the $SR = 1.75$ and 3.63 cases, the boundary layers were assumed to begin at x/W values of 0.2 and 0.8, respectively.

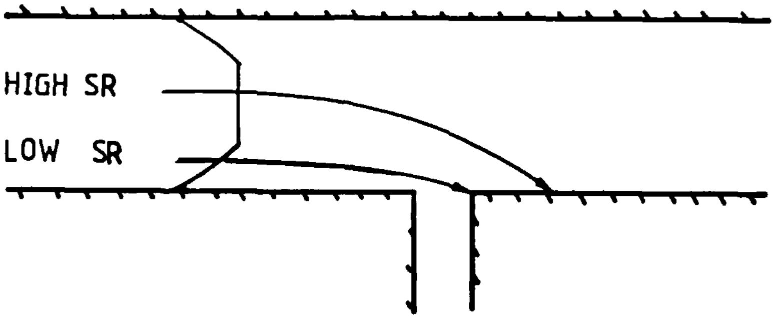

Figure 7.7: **Probable locations of dividing streamlines near the slot for high and low** $SR's$.

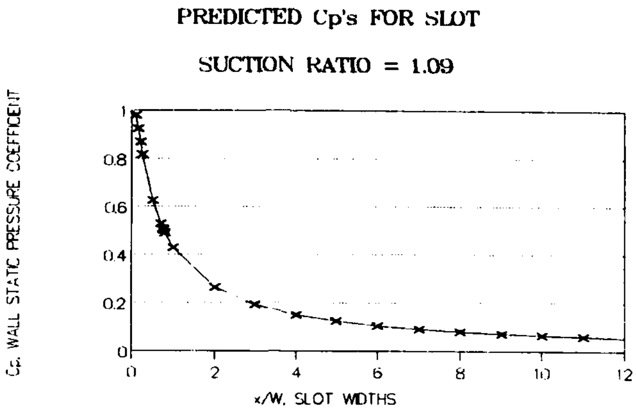

Figure 7.8: **Predicted $C_p's$ for slot-** $SR = 1.09$.

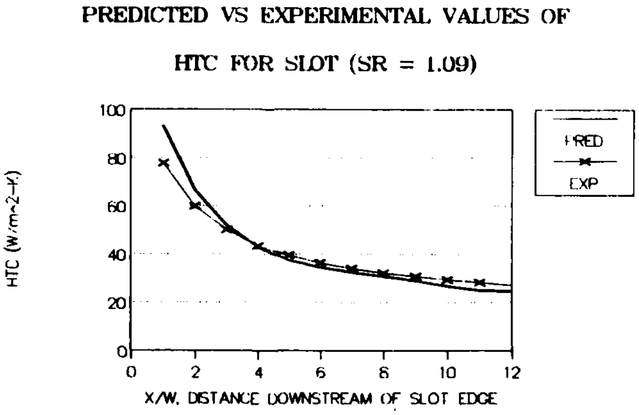

Figure 7.9: **Predicted versus experimental values of h for the slot-** $SR = 1.09$.

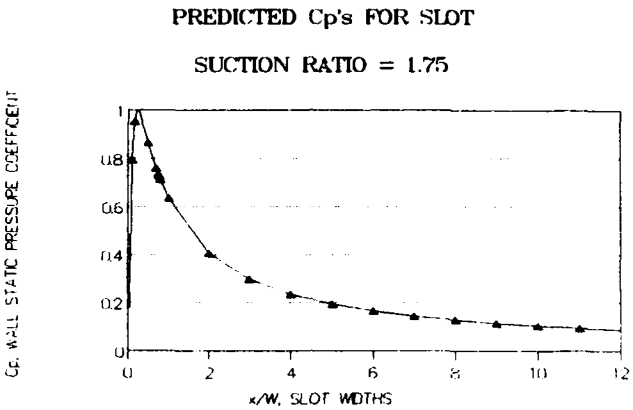

Figure 7.10: **Predicted $C_p's$ for slot- $SR = 1.75$.**

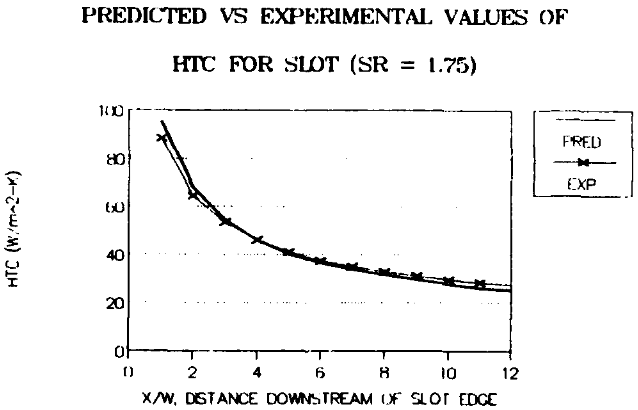

Figure 7.11: **Predicted versus experimental values of h for the slot- $SR = 1.75$.**

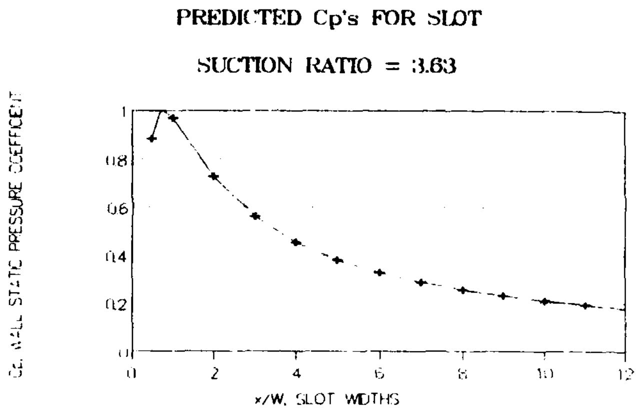

Figure 7.12: **Predicted $C_p's$ for slot- $SR = 3.63$.**

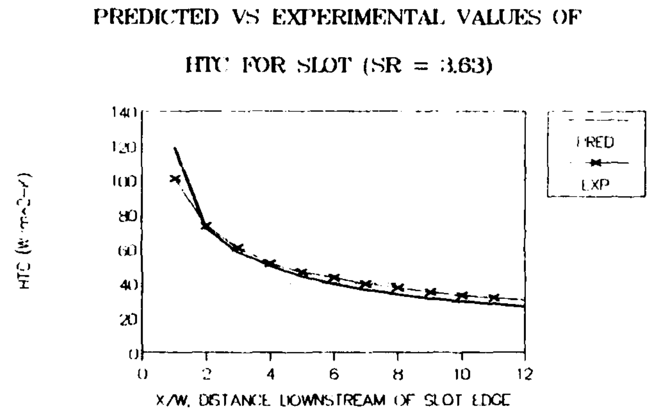

Figure 7.13: **Predicted versus experimental values of h for the slot- $SR = 3.63$.**

Figure 7.14 presents the predicted and experimental area-averaged heat transfer results for the slot. The region selected for averaging was an area adjacent to the downstream slot edge with dimensions 12 slot widths in length and one spanwise unit in width. There is excellent agreement except for the $SR = 0.61$ case which was discussed earlier. The results support the assumption that a laminar boundary layer was formed at the downstream slot edge.

Predicted versus experimental results for the slot C_d

Morland also developed discharge coefficient (C_d) predictions by assuming that the separated region within the slot along the upstream slot edge was a constant pressure region bounded by a free streamline as shown previously in the inserted Figure 7.2. As shown in Figure 7.15, there is good agreement in the trends shown by the experimental and predicted values. However, the experimental values are slightly greater than the predicted values which might be due to the three-dimensional effects present at the slot ends in the experimental case; the experimental slot was able to extract flow from the lateral direction, the direction theoretically inaccessible to Morland's two-dimensional slot. Therefore, the three-dimensional, experimental slot would show a greater mass flow for any given pressure drop.

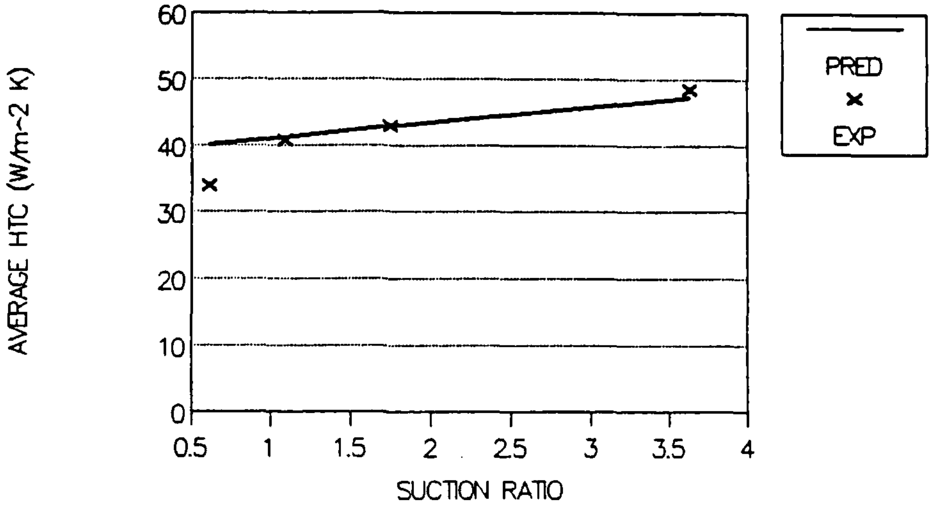

Figure 7.14: Predicted versus experimental area-averaged values of h for the slot. The rectangular area selected for averaging was adjacent to the downstream slot edge with dimensions 12 slot widths in length and one spanwise unit in width.

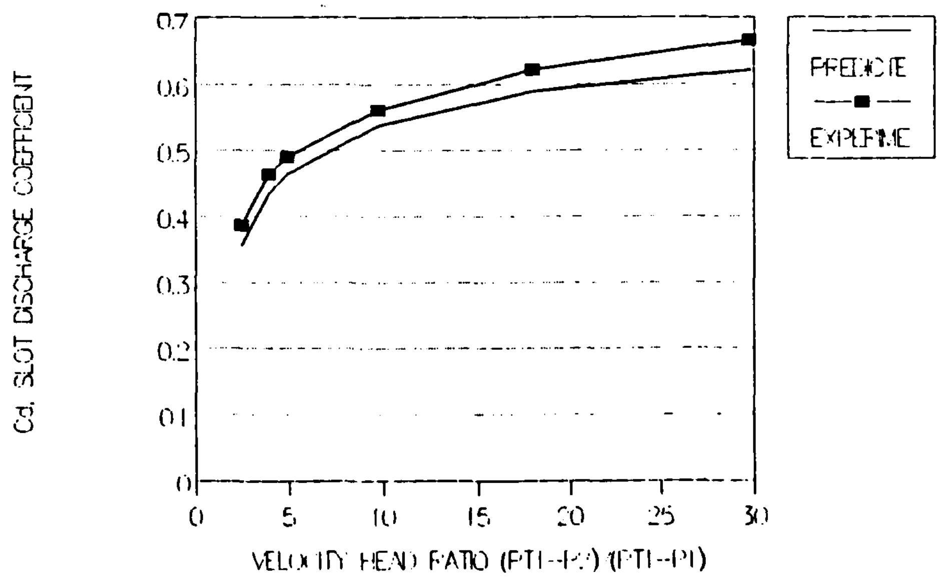

Figure 7.15: Predicted versus experimental values of C_d for the slot.

7.2 Predicted Results for the Three-dimensional Case and Comparisons with Experimental Results

The two-dimensional analytical method which successfully predicted the heat transfer downstream of the slot was extended to the case of the heat transfer downstream of the hole. Since the *x-y plane* passing through the hole centreline was a plane of symmetry, it was the plane least influenced by three- dimensional flow field effects that were present in the experimental case. Therefore the heat transfer along the hole centreline was considered suitable as the subject of a simple, first order, two-dimensional analysis. The experimental wall static pressure measurements were presented in Chapter 6 in terms of

$$C_p(x) = \frac{(P(x) - P_1)}{(P_{t1} - P_1)} \tag{7.3}$$

In these analytical predictions it was assumed that the total pressure close to the wall was equal to the centreline total pressure at the upstream reference location.

$$P_t(x) = P_{t1} \tag{7.4}$$

The velocity profiles presented in Chapter 6 show this to be a valid approximation. Therefore

$$C_p(x) = 1 - (\frac{u(x)}{u_{centreline}})^2 \tag{7.5}$$

where $u_{centreline}$ was the centreline velocity measured at the upstream reference location. The local value of $u(x)$ was therefore deduced from the measured values of $C_p(x)$ using equation 7.5 and substituted into equation 7.1 to obtain the predicted value of h. While the analytical predictions for the slot were in most cases very close to the experimental results, the predictions for the hole centreline were always lower than the experimental values as shown in Figures 7.16-7.19. It is also apparent that the predicted values fell even further below the experimental values as the hole SR was increased. One conclusion drawn from the hole heat transfer experiments and flow field studies was that three-dimensional effects become more pronounced at higher SR's. Therefore the increased influence of three-dimensional effects seems to be the likely explanation for the divergence between the two-dimensional hole centreline predictions and the experimental values. For this explanation to be consistent, however, the effect of the three-dimensional flow must be to thin the boundary layer, since the experimental values of h exceed the predicted values. Results from a CFD analysis which are presented in Chapter 8 show that the streamlines near the wall diverged, rather than converged, downstream of the hole. Of course, streamline divergence is consistent with a thinning of the boundary layer.

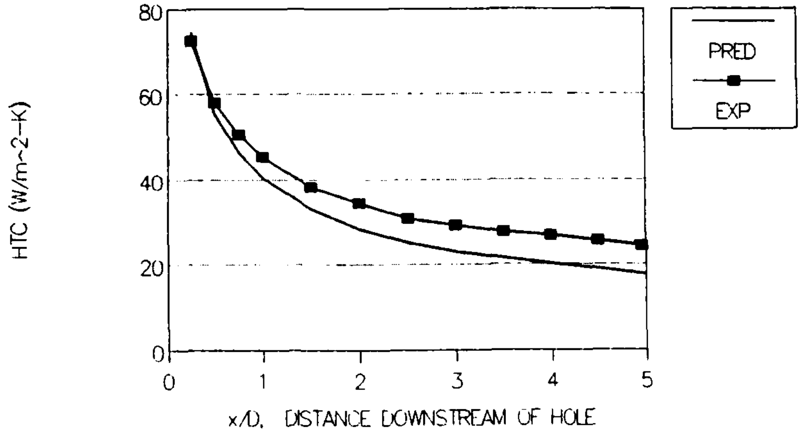

Figure 7.16: **Predicted versus experimental centreline values of** h **for the** 90° *hole-* $SR = 0.66$.

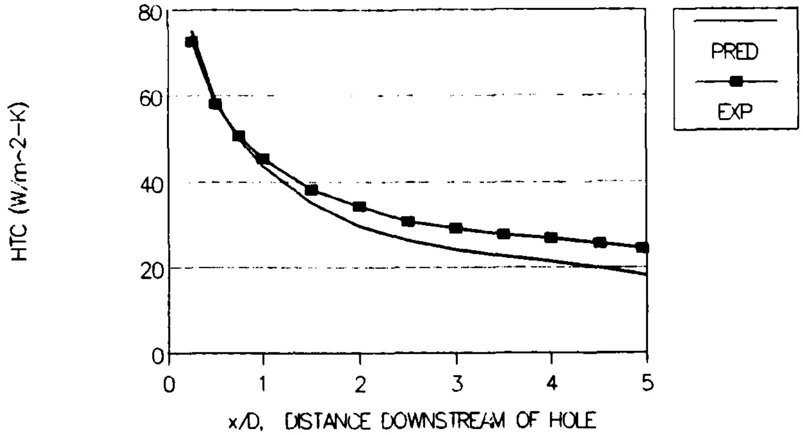

Figure 7.17: **Predicted versus experimental centreline values of** h **for the** 90° *hole-* $SR = 1.20$.

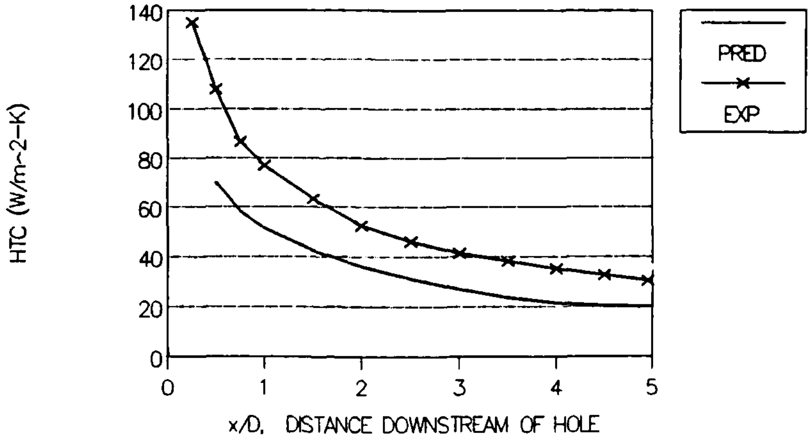

Figure 7.18: **Predicted versus experimental centreline values of** h **for the** 90° *hole-* $SR = 4.21$.

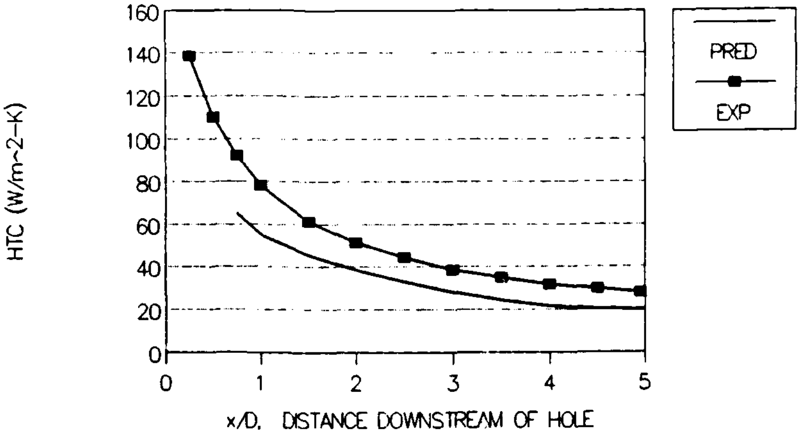

Figure 7.19: **Predicted versus experimental centreline values of** h **for the** 90° *hole-* $SR = 7.48$.

8 THREE-DIMENSIONAL COMPUTATIONAL STUDIES

This chapter describes a three-dimensional, numerical analysis of the heat transfer and fluid flow in the main duct near the entrance to the film cooling hole. The analysis was accomplished using **Fluent**[1], a commercial, general purpose CFD program presently installed on the Oxford University Digital Vax Cluster. **Fluent** uses the finite difference technique to discretize the equations for mass, momentum, and energy conservation. The program has the capacity to operate on a maximum of 10,000 cells in a grid arrangement which may be non-uniform for either laminar or turbulent flows. If the flow is considered to be turbulent, **Fluent** uses the logarithmic law of the wall to compute the shear stress at the wall and the $k-\epsilon$ turbulence model.

8.1 Computational Details

The computational model of the physical problem is shown in Figure 8.1A. The inlet conditions specified for the model were the experimentally measured velocity, temperature, and turbulence intensity profiles. The temperature and velocity profiles, measured at the upstream reference location (180mm upstream of the hole), and corresponding closely to the 1/7 power law profile, were presented in Chapter 3. The turbulence intensity profile was measured in the same tunnel at the same Re_L

---

[1] Fluent Version 2.93, Creare Incorporated, Hanover, New Hampshire, 03755, U.S.A.

by **Ireland (1987)**. The values of turbulence intensity ranged from 4% at the duct centreline to 15% near the duct wall. The hole inlet velocity was modelled as a uniform velocity field equal to the measured average hole velocity. Unfortunately, at low *SR's* a large region of separation was found to exist within the hole along the upstream hole edge. At high *SR's* when the stagnation point was downstream of the hole on the main duct wall, a region of separation existed which was distributed more or less evenly around the entire perimeter of the hole entrance. Therefore, the actual hole inlet velocity was more uniform, and therefore closer to the computational model, at the higher *SR's*.

The *x-y* plane of symmetry passing through the hole centreline is reflected in the choice of the computational domain shown in Figure 8.1B. The film cooling hole itself was represented by six rectangular cells, having a total area equal to the area of the hole. This was a technique used by **Patankar et al (1977)**, in a study of a turbulent jet entering a crossflow which is the reverse case of the present study. In the upstream *x-direction*, the *y-z* boundary plane was positioned at the upstream reference location because the inlet velocity, temperature, and turbulence intensity profiles had been measured there. This particular distance was also chosen because it was experimentally determined to be far enough upstream of the hole to be uninfluenced by changes in the *SR*. In the downstream *x-direction*, the *y-z* boundary plane was placed at a distance of five hole diameters, which provided enough room for the main area of interest according to the experimental results. The far *x-y* boundary plane was placed nine hole diameters away from the plane of the hole centreline to reduce the edge effects and thereby model the main duct as a two- dimensional duct. This plane was specified to be a plane of symmetry rather than a wall to prevent the creation of any gradients by this computationally necessary boundary. Finally, the extent of the domain in the *y-direction* was selected to match the experimental geometry of the test section. The top and bottom duct walls were treated as hydrodynamically smooth with all three components of velocity set to zero at the wall surfaces.

The nonuniform grid spacing used in this analysis is shown in Figure 8.2. The grid spacing was dense in the vicinity of the hole, especially in the downstream direction, as this was the region where high gradients were expected. The grid spacing was gradually increased in the direction away from the hole where the properties were expected to be more uniform. The spacing between adjacent gridlines was not changed by more than 30% from one gridline to the next, in accordance with a general CFD guideline which is intended to reduce the propagation of numerical errors. The number of grid planes normal to the x, y, and z directions were 32, 17, and 18 respectively, thus making a total of 9,792 grid points. Since **Fluent** is limited to a total of 10,000 grid points, it was not possible to increase the density of the grid to any significant degree, given the extent of the computational domain.

At each of the grid points the following values were computed: the local pressure; the u, v, and *w-velocities*; k, the kinetic energy of turbulence; ϵ, the rate of turbulent kinetic energy dissipation; and the local enthalpy. The flow field solution was considered to have converged when the sum of the normalised residuals was less than

$1(10^{-3})$ which normally occurred after approximately 600 iterations and 5 hours of CPU time on a VAX 8800 mainframe computer.

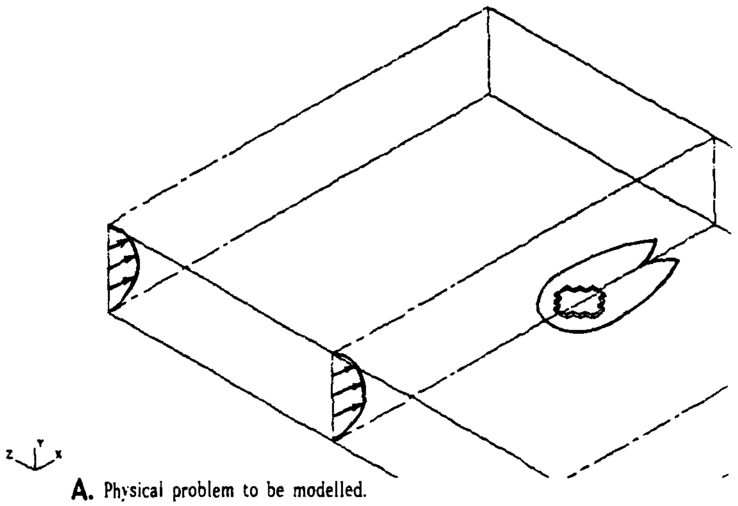

A. Physical problem to be modelled.

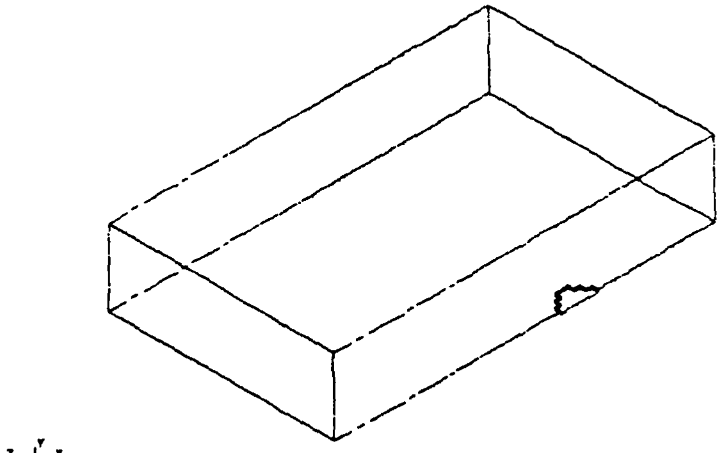

B. Outline of computational domain.

Figure 8.1: **A.) Physical problem to be modelled. B.) Outline of the computational domain.**

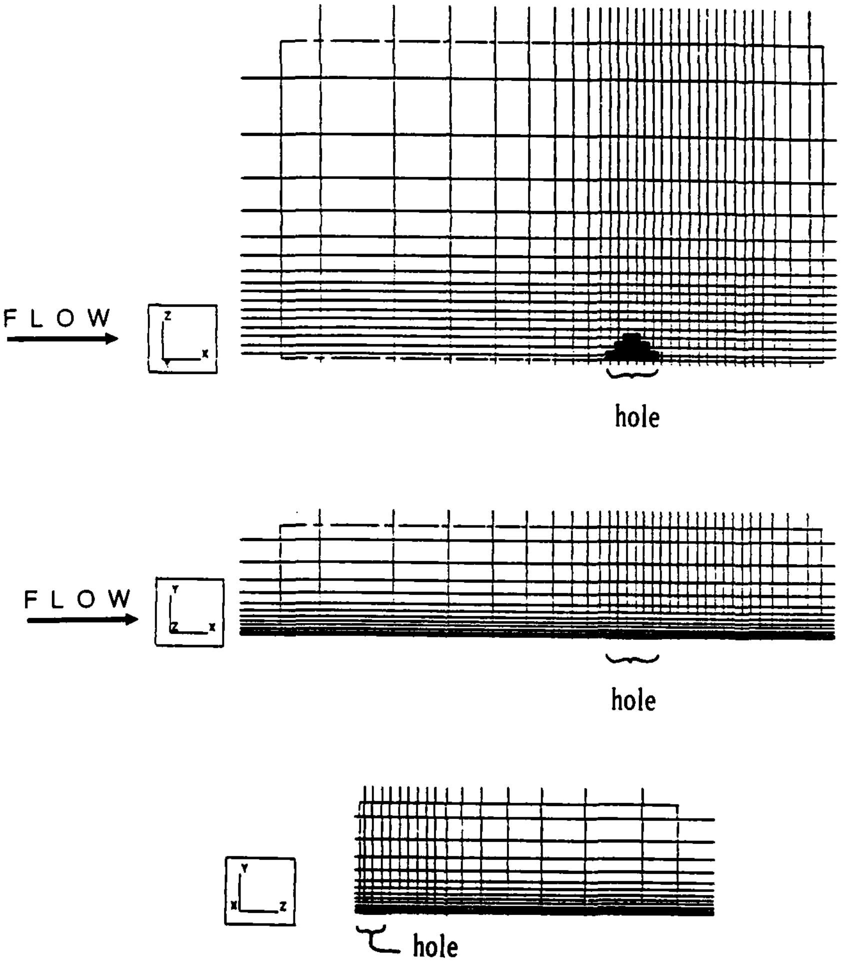
FLOW
Z
X
hole
FLOW
Y
Z
X
hole
Y
X
Z
hole
Computational grid for each of the three spatial dimensions.

Figure 8.2: **Computational grid for each of the three spatial dimensions.**

8.2 Numerical Heat Transfer Predictions

The feature enabling **Fluent** to calculate the heat transfer coefficient (h) was activated during the analysis. An isothermal wall boundary condition was specified since this was an approximate representation of the actual, experimental thermal boundary condition. The default reference temperature used by **Fluent** is the volumetric or bulk average temperature of all the "live", or fluid containing cells, so h_{Fluent} is defined as

$$h_{Fluent} \equiv \frac{q_o^{"}}{(T_{average} - T_{wall})}$$

where $q_o^{"}$ is the local heat flux at the wall. **Fluent** uses the overall bulk average temperature as the reference temperature for the same reason the upstream duct centreline temperature was chosen in the present work; the local bulk or mixing cup temperature, often used in simple internal flows, is not well defined in complex, three-dimensional flows where there is no preferential flow direction. Since the material properties for air were assumed to be constant, the continuity and momentum equations could be de-coupled from the energy equation. This was equivalent to assuming that the velocity and pressure fields were unaltered by the temperature gradients within the flow. This assumption allowed the value of h calculated by **Fluent** to be converted back to the value of h based on the upstream centreline temperature by applying a temperature difference ratio as shown below

$$h = h_{Fluent} \frac{(T_{average} - T_{wall})}{(T_{centreline} - T_{wall}})$$

The heat transfer results from the numerical prediction and comparisons with experimental results are shown in Figures 8.3- 8.5. The most important result is the correct prediction of the position and shape of the heat transfer contours, including the change from a single-lobe to a double-lobe shape as the SR is increased from one to eight. This implies that the key features of the velocity field were also reproduced so that the fundamental reasons for the heat transfer enhancement pattern can be examined.

It is interesting to note that the closest agreement between the predicted centreline $EF's$ and the experimental values occur when $SR = 8$, the highest SR value tested. The most likely reason for this is the specification of uniform velocity in the plane of the hole inlet. As mentioned previously, this inlet model was most closely realized experimentally at high $SR's$ when the separated region was more evenly distributed around the perimeter of the hole entrance.

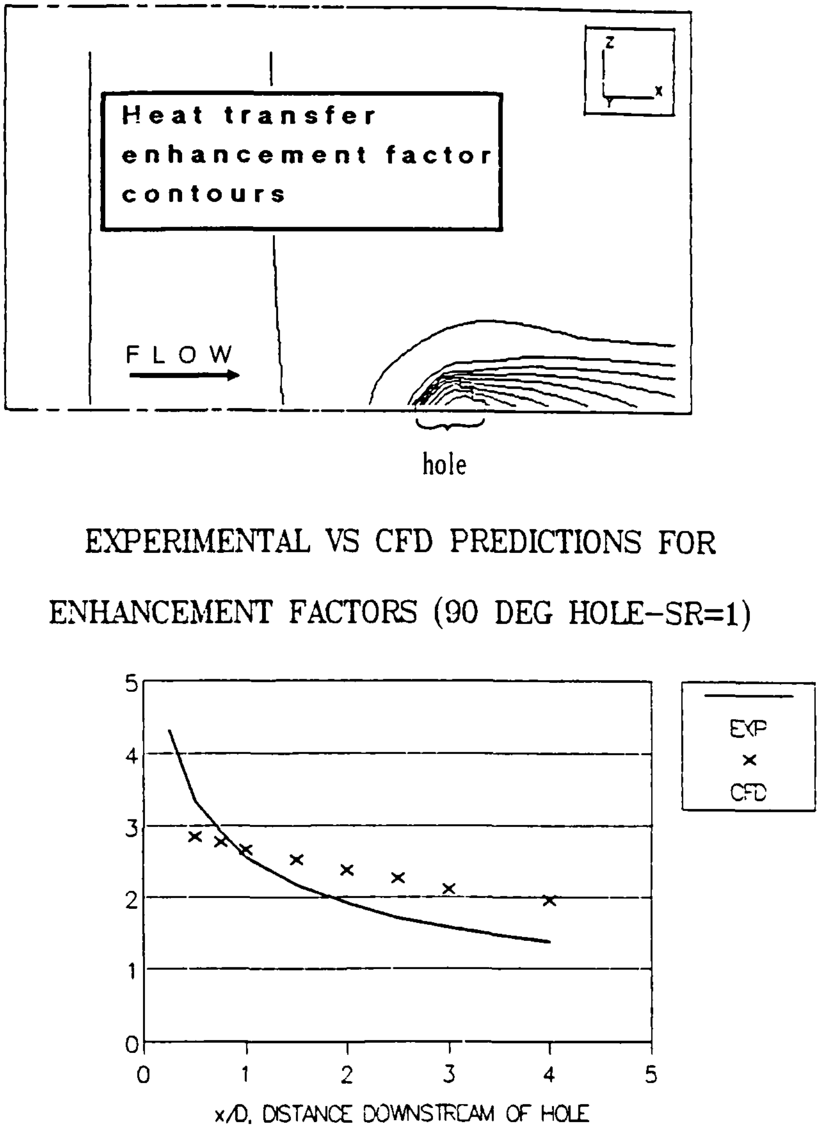

Figure 8.3: **Heat transfer results for $SR = 1$.**

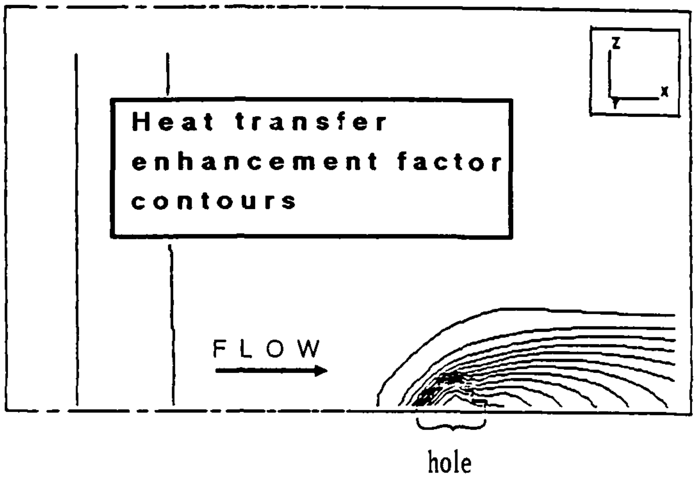

EXPERIMENTAL VS CFD PREDICTIONS FOR ENHANCEMENT FACTORS (90 DEG HOLE-SR=4)

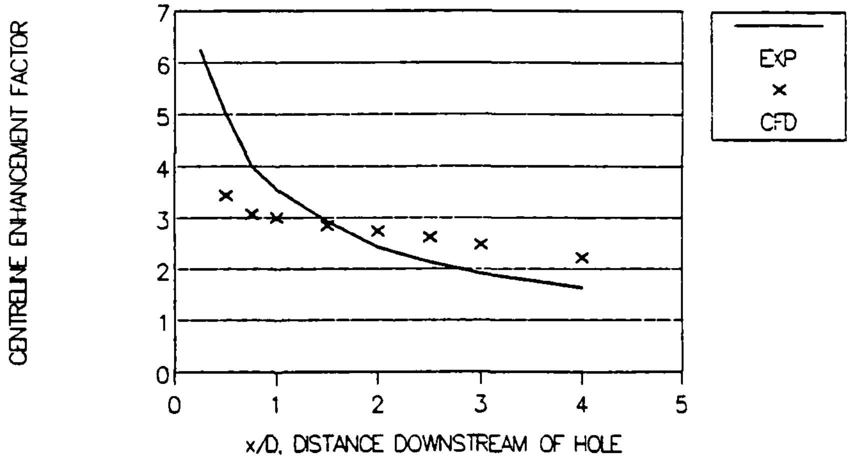

Figure 8.4: **Heat transfer results for $SR = 4$.**

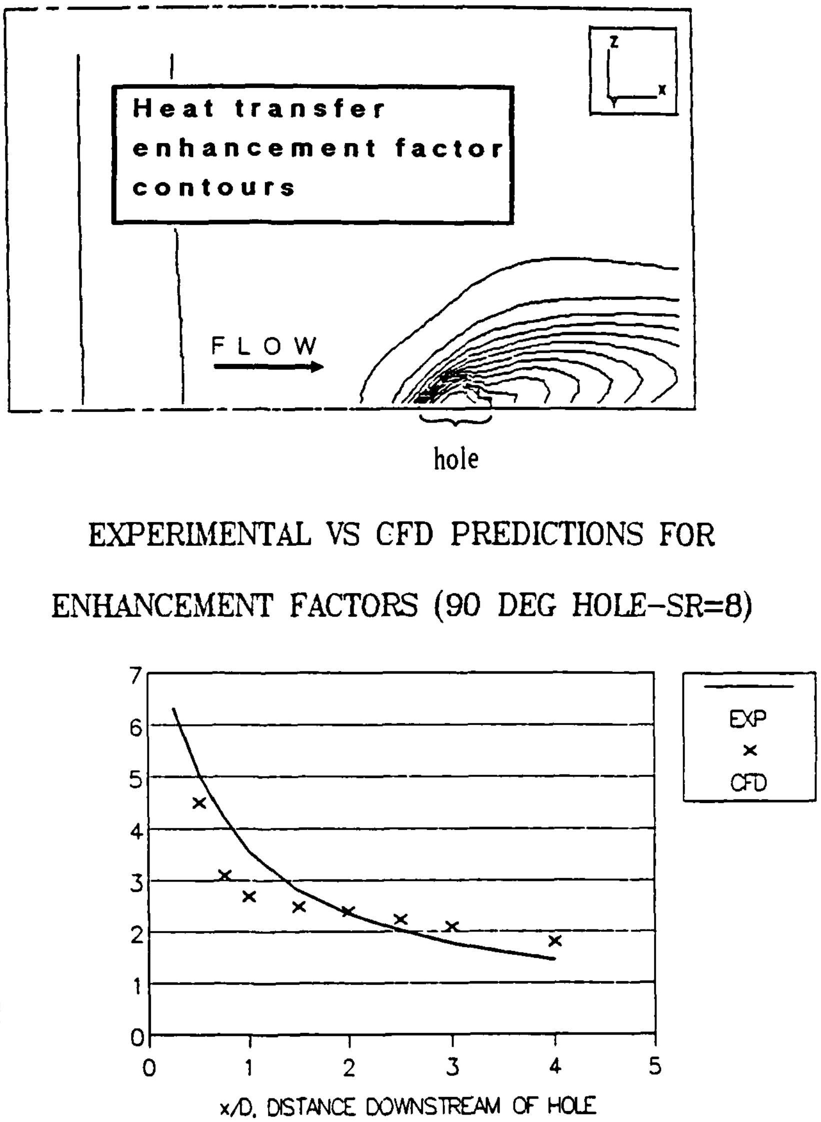

Figure 8.5: **Heat transfer results for $SR = 8$.**

8.3 Numerical Flow Field Predictions

The remaining figures illustrate features of the mean velocity field for the cases of $SR = 1$ and 8 which yield insight into the underlying reasons for the shape, magnitude, and location of the heat transfer distributions. The most important result is the confirmation of the existence of a vortex pair downstream of the hole. The vortex pair had been predicted on theoretical grounds but had evaded observation during the smoke and surface flow visualization tests. The only experimental clues to the vortex pair's existence were the EF contour "footprint" left by the vortex pair on the duct wall surface and the wall static pressure measurements presented in Figure 6.12. Figure 8.6 shows the predicted secondary flow velocity vectors downstream of the hole when $SR = 1$. The axial development of the vortex can be plainly seen as the vortex centre lifts away from the wall surface and the vortex shape becomes rounder. This feature was observed in an experimental study of vortices imbedded in turbulent boundary layers by **Eibeck and Eaton (1988)** which adds credence to the numerically predicted vortex behaviour.

Figure 8.7 shows profiles of *v-velocity* for the $SR = 1$ case. The maximum value of downwash occurs along the hole centreline which corresponds to the axis of maximum heat transfer. This correspondence between downwash in the velocity field and maximum wall heat transfer was also observed experimentally by both **Russell, Jones and Lee (1982)** and **Eibeck and Eaton (1988)**. While the strong downwash region existed over a fairly small area, a weak upwash region extended across a very wide area. This helps to explain why the vortices were not observed experimentally during the earlier smoke visualization tests. The pitch of the helix formed by the path of any given smoke particle was very long relative to the length of the test section. It is very that likely the smoke particle would have been completely out of visual range by the time it had travelled through one full 360° helical path.

Figure 8.8 shows the profiles of *w-velocity* downstream of the hole for $SR = 1$. A lateral component of velocity is shown to extend across a wide area but this apparently did not translate into any significant heat transfer enhancement outside of the downwash region, either numerically or experimentally.

Figure 8.9 illustrates the axial development of the vortex for the $SR = 8$ case. While the vortex centre lifts away from the wall surface as in the $SR = 1$ case, its location is much further away from the hole centreline in the lateral (or z) direction. Figure 8.10 shows that the location of maximum downwash is not along the hole centreline but closer to the lateral hole edge. The off-centreline location of the vortex downwash region is the reason for the double-lobed EF contour shape observed both experimentally and numerically since the location of maximum downwash again corresponds to the location of high heat transfer. Figure 8.11 presents the *w-velocity* profiles for $SR = 8$.

In addition to the vortex pair and the general heat transfer pattern being reproduced numerically, there are other flow features revealed by the CFD analysis which match those obtained in the experimental flow field studies such as the general location of the dividing streamlines, the presence and location of the downstream stagnation point, and the shape of the *u- velocity* profiles along the hole centreline downstream of the hole. Figures 8.12-8.14 present these numerical results for the cases of $SR = 1, 4$, and 8, respectively.

From the velocity vector plots in the x-z plane immediately above the wall surface and in the x-y plane of the hole centreline it is possible to determine the approximate locations of the dividing streamlines between the flow removed down the hole and the flow remaining in the main duct. These results match closely the results obtained from smoke visualization and surface flow visualization presented earlier.

Of course the stagnation point location is related to the dividing streamline location. It is clear for the $SR = 1$ case that the stagnation point is not present on the main duct wall. For $SR = 4$, however, the stagnation point is located approximately 0.25 hole diameters downstream of the hole edge, precisely the same location observed in smoke visualization and in the wall static pressure measurements. Finally, for $SR = 8$, the stagnation point is located approximately 0.50 diameters downstream, again matching the experimental results.

The *u-velocity* profiles in the plane of the hole centreline also reflect the trends observed in the experimental velocity profile measurements that were made three hole diameters downstream. For SR values of 1 and 4, the near wall portion of the boundary layer is removed so that the local velocity at a point three hole diameters downstream of the hole edge is very close in magnitude to the upstream centreline value. For the $SR = 8$ case, the *u-velocity* values at this same location are significantly less than the upstream centreline value. This mirrors the behaviour observed in the experimental results. Another interesting feature that is exhibited in the velocity profile predictions for $SR = 4$ is the location of the stagnation point where u becomes zero. Also at this same profile location for the $SR = 8$ case, significant reverse flow exists since this position is upstream of the stagnation point and the dividing streamline.

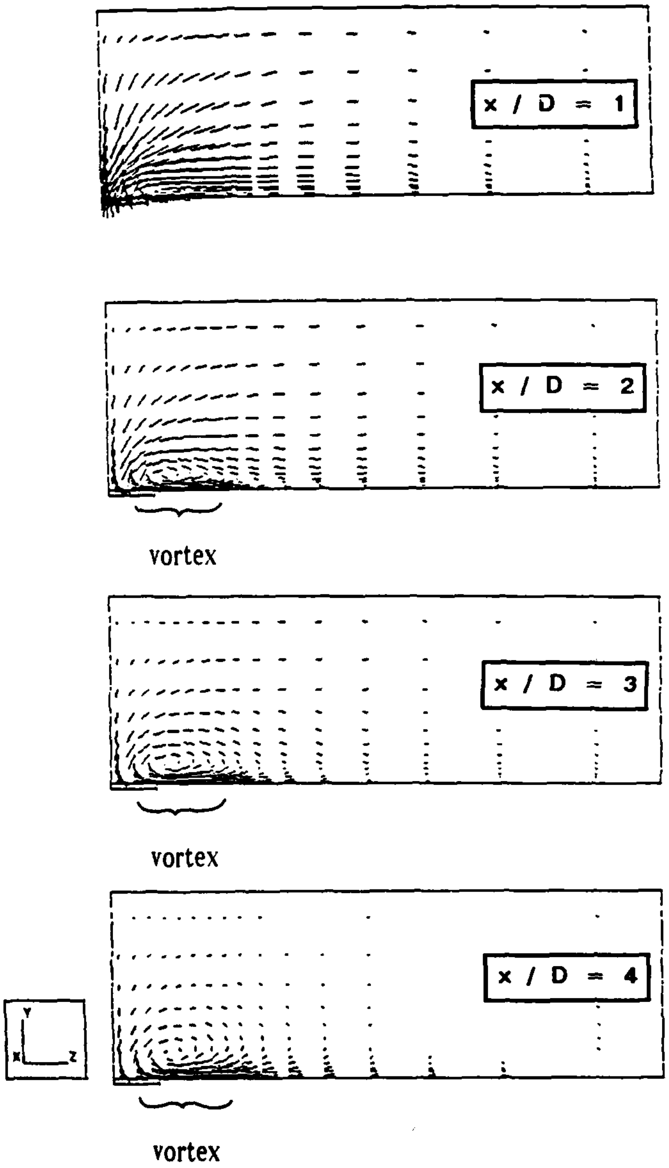

Figure 8.6: Secondary flow velocity vectors at four locations downstream of the hole- $SR = 1$.

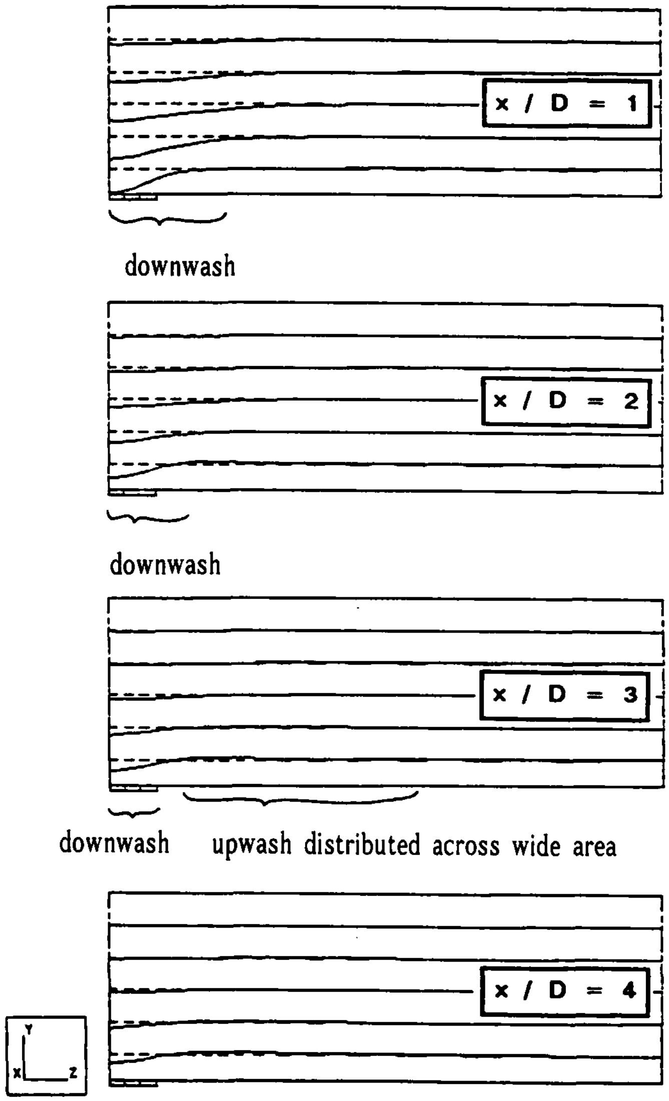

Figure 8.7: **Profiles of *v-velocity* at four locations downstream of the hole, $SR = 1$.**

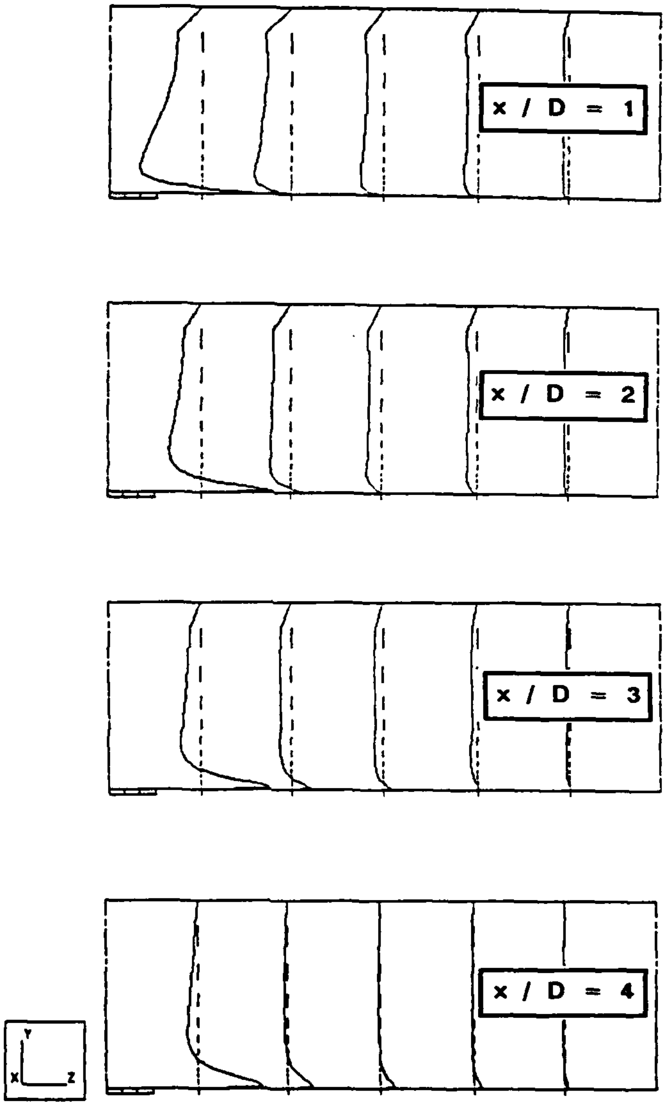

Figure 8.8: Profiles of *w-velocity* at four locations downstream of hole, $SR = 1$.

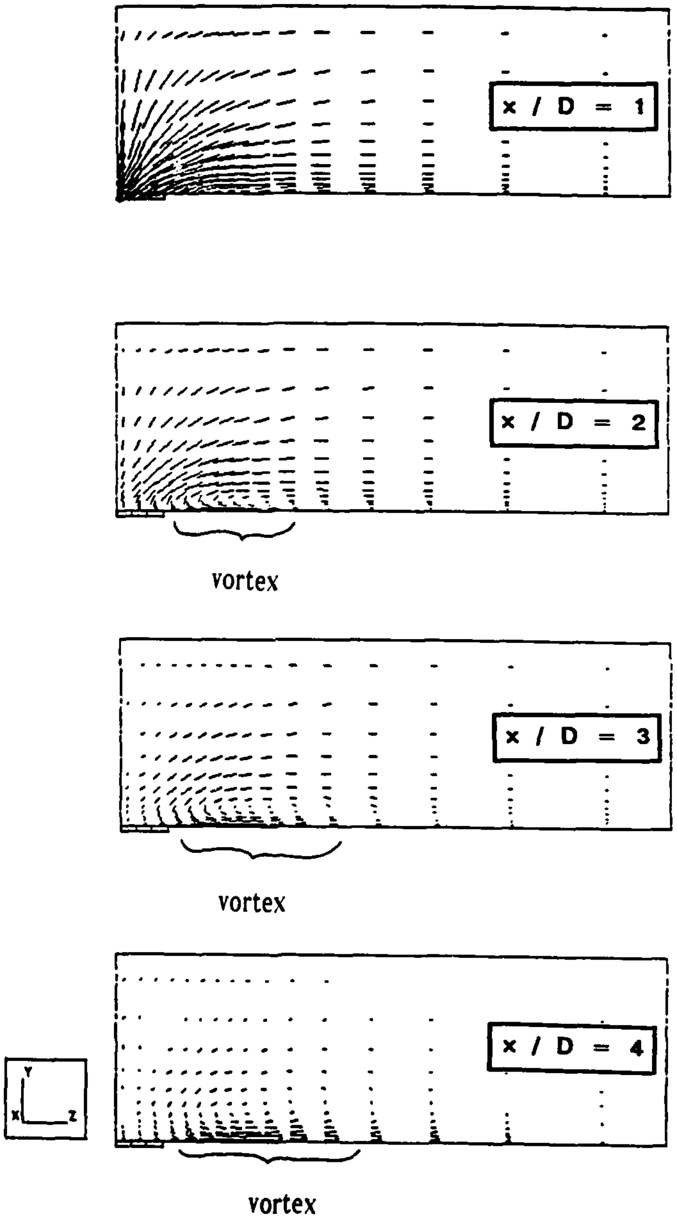

Figure 8.9: Secondary flow velocity vectors at four locations downstream of the hole, $SR = 8$.

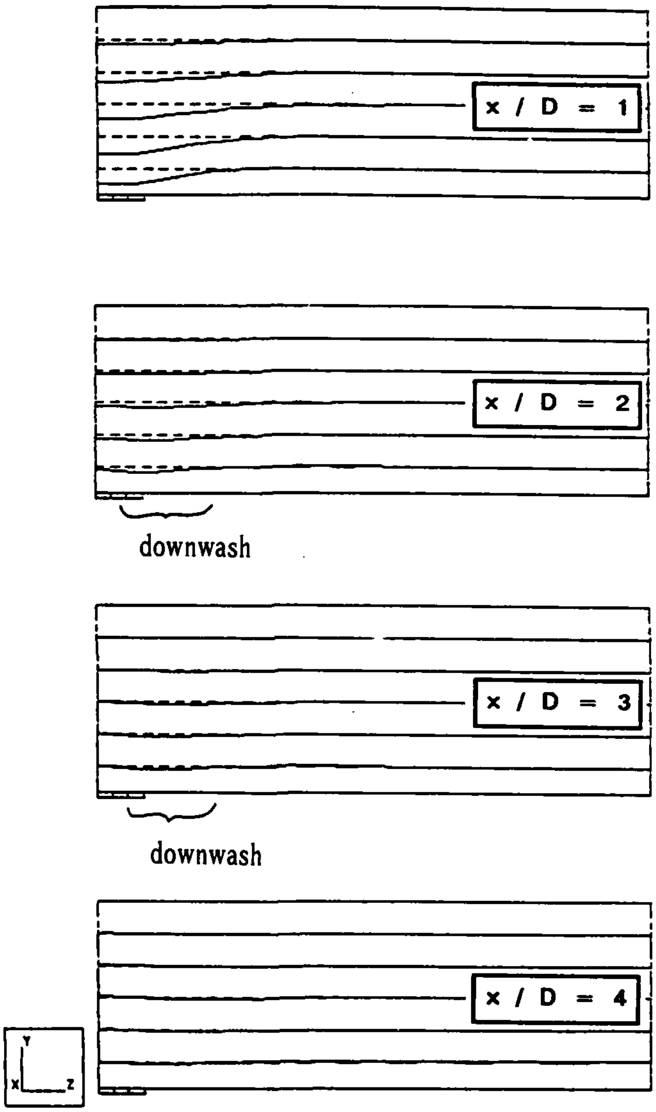

Figure 8.10: Profiles of *v-velocity* at four locations downstream of the hole, $SR = 8$.

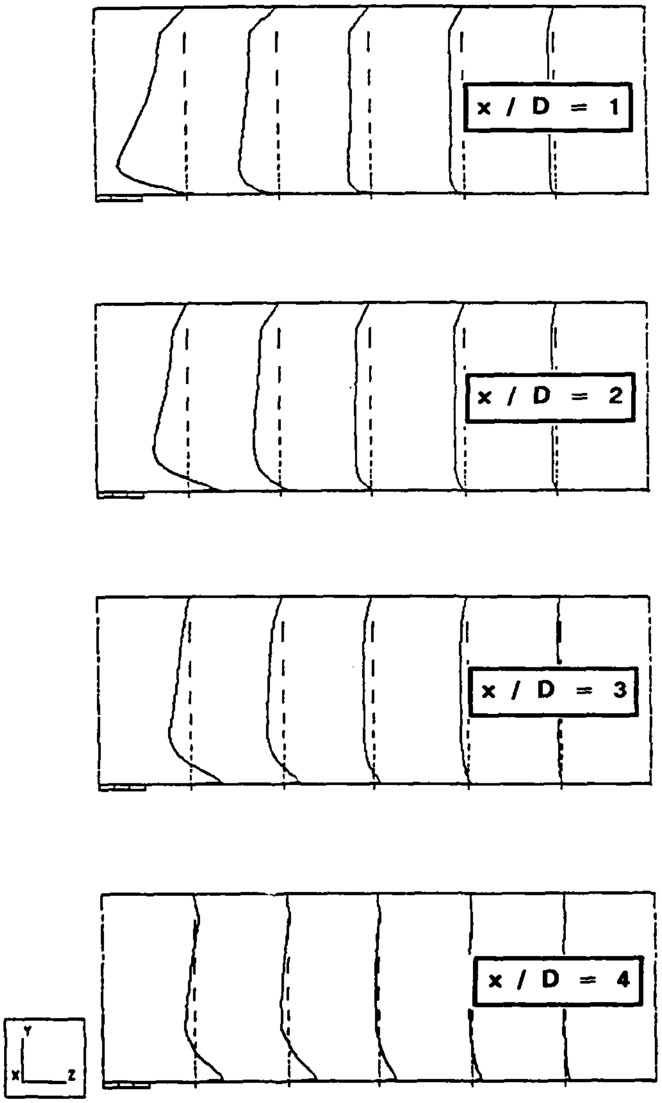

Figure 8.11: **Profiles of *w-velocity* at four locations downstream of hole,** $SR = 8$.

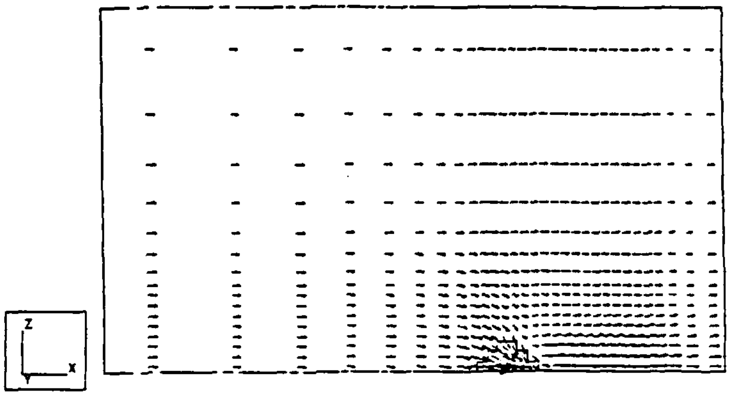

Velocity vectors in the plane immediately above and parallel to the wall surface. SR= 1.

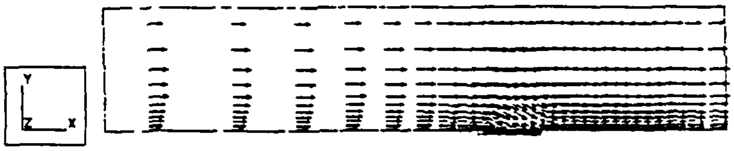

Velocity vectors in the plane of the hole centreline. SR = 1.

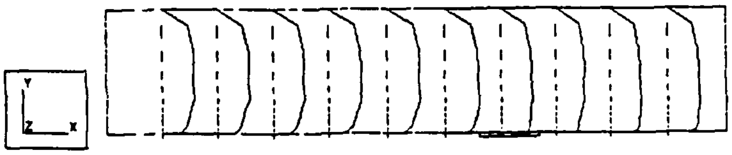

Profile of U-velocity in the plane of the hole centreline. SR = 1.

Figure 8.12: **Flow field results for $SR = 1$.**

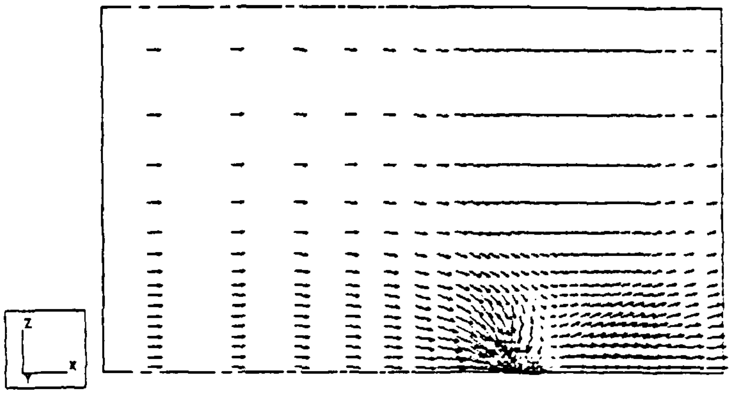

Velocity vectors in the plane immediately above and parallel to the wall surface. SR= 4.

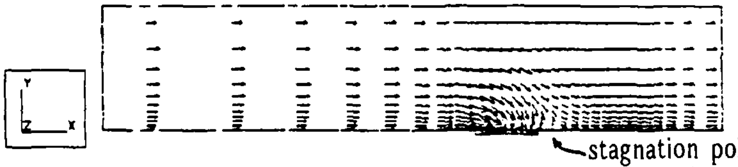

stagnation point

Velocity vectors in the plane of the hole centreline. SR = 4.

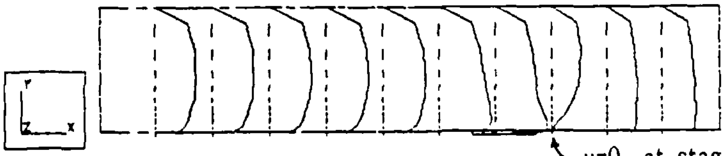

u=0 at stagnation poin

Profile of U-velocity in the plane of the hole centreline. SR = 4.

Figure 8.13: **Flow field results for $SR = 4$.**

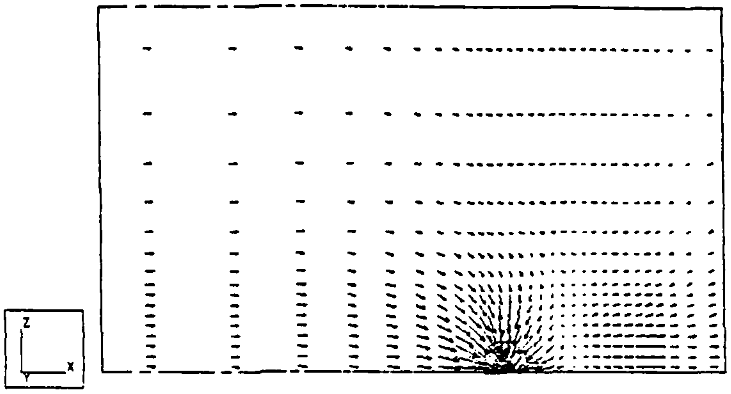

Velocity vectors in the plane immediately above and parallel to the wall surface. SR= 8.

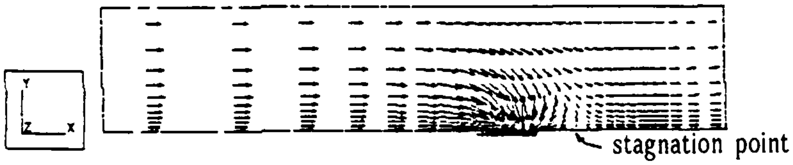

stagnation point

Velocity vectors in the plane of the hole centreline. SR = 8.

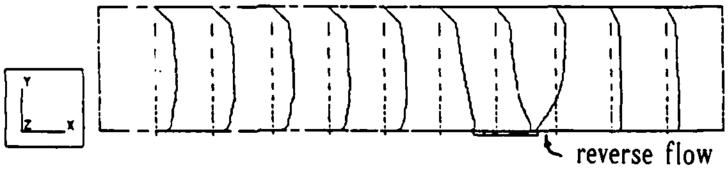

reverse flow

Profile of U-velocity in the plane of the hole centreline. SR = 8.

Figure 8.14: **Flow field results for $SR = 8$.**

8.4 Additional Insight Provided by the Computational Results

The computational results have addressed several other questions that were raised, but not answered, in the experimental and the analytical phases of the present work. A discussion of the additional insight provided into the following three subjects is now presented: 1.) the underprediction of the true value of h using the two-dimensional, analytical method 2.) a "vortex line" model which accounts for the shift from a single lobe contour shape to a double lobe contour shape, and 3.) the location of the peak value of h at the downstream hole edge.

8.4.1 Possible reason for the underprediction of h.

In Chapter 7, analytical predictions were presented which underestimated the value of h measured along the plane of the hole centreline in the downstream direction. Because the difference between predicted values and experimental values increased with increased SR, the underprediction was blamed on three-dimensional aerodynamic effects. Now that several important features have been correctly reproduced in the computational results, the predicted flow field can be examined in greater detail to see if three-dimensional effects might actually be the correct reason for the underprediction. Figures 8.12-14 show that the streamlines downstream of the hole in the x-z plane, immediately above the duct wall surface, do indeed diverge which would in turn lead to a thinning of the boundary layer, and the resultant increase in the heat transfer coefficient.

8.4.2 "Vortex Line" Model

Early in the experimental program, the presence of a vortex pair was predicted on the basis that vortex lines were being pulled down the hole at a point location, with the "tails" of the vortex lines wrapping around in the downstream direction as shown in Figure 8.15. This theory did not, however, fully account for the effect of increasing the SR and the accompanying transition from a single-lobe to a double-lobed heat transfer pattern. To make this model more complete, it needs to be extended only slightly. For low $SR's$, the vortex lines may still be considered drawn into the hole at a point location. As the SR increases, however, the point location expands to a line segment, eventually reaching a length on the order of one hole diameter, as shown in the Figure 8.16. This model helps to explain why the distance between the vortex pair increases with SR which in turn explains why the heat transfer patterns take on a double-lobed shape.

8.4.3 Location of Peak Value of h

The question concerning the location of maximum heat transfer on the duct wall still remains. For most flow situations, the location of maximum heat transfer normally corresponds to the stagnation point location, but this is obviously not the case in the present study. For the 90° *hole*, both the experimental results and the numerical predictions point to the downstream hole edge as the location of peak heat transfer even when the stagnation point is located as far away as $0.5D's$ downstream. This is due to the tremendous acceleration of the reverse flow that takes place between the

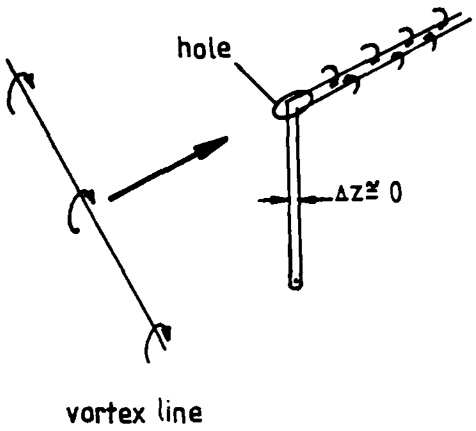
hole
ΔZ≅ 0
vortex line

Figure 8.15: Vortex lines at a low SR value. $\Delta Z \approx 0$.

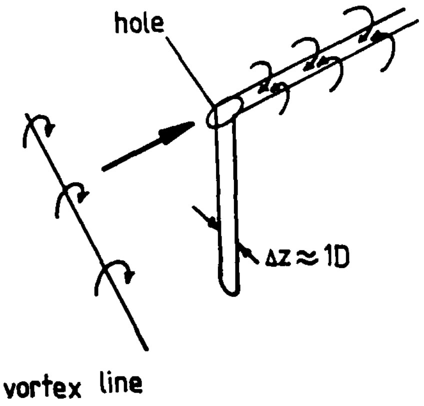
hole
ΔZ≈1D
vortex line

Figure 8.16: Vortex lines at a high SR value. $\Delta Z \approx 1D$.

stagnation point and the hole entrance which results in a thinning of the boundary layer in the direction of the local flow. Some idea of the magnitude of the acceleration in this area was given by the high values of wall shear stress revealed in the surface flow visualization experiments. Another way to evaluate the degree of acceleration, however, is to examine the velocity vectors in the x-y plane passing through the hole centreline as shown in Figure 8.14 and in Figure 8.17. Note the similarity between the actual path taken by the flow in this plane and the path taken in the corresponding *wedge-flow* as shown in the Figure 8.18. Potential flow theory reveals that the velocity along the wedge surface varies as

$$u(x) = Cx^m \tag{8.1}$$

where m is associated to the wedge angle, β, according to

$$m = \frac{\beta/\pi}{2 - \beta/\pi} \tag{8.2}$$

Similarity solutions for the laminar, incompressible boundary layer associated with this type of flow are given in **Kays and Crawford (1980)** for both the momentum and energy equations. Assuming that the thermal boundary condition is an isothermal wall, then

$$h(x) = \frac{(const)k}{\nu^{1/2}} x^{(m-1)/2} \tag{8.3}$$

It is clear from equation 8.3 that h increases with x only if $m > 1$. According to equation 8.2, this is true if the wedge half angle $(\beta/2)$ is greater than $\pi/2$, a condition satisfied in the present study as indicated in Figure 8.14 and 8.17. Evidently, the magnitude of the acceleration associated with the flow angling backwards to enter

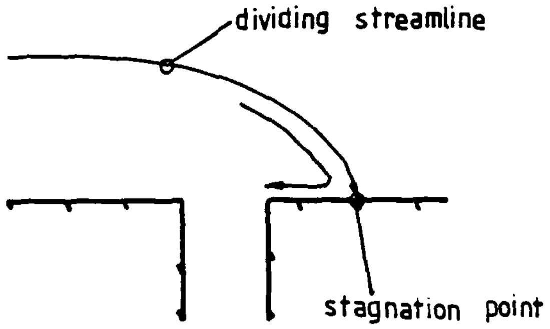
dividing streamline
stagnation point

Figure 8.17: The actual path taken by flow entering the hole.

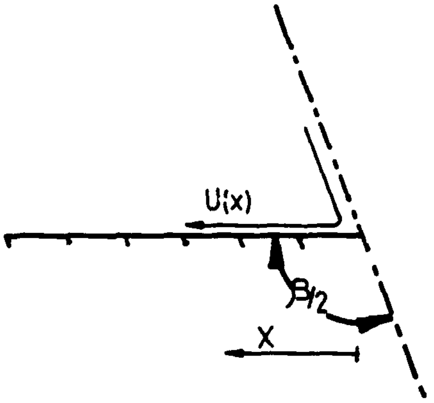

Figure 8.18: The corresponding wedge flow.

the hole is great enough to thin the thermal boundary layer in the direction of flow, thereby causing the downstream hole edge to be the location for the peak in heat transfer.

9 BLADE METAL TEMPERATURE PREDICTIONS

As discussed earlier, the main reason for undertaking the present study was to measure the heat transfer near the entrance to a film cooling hole because the resultant cooling contribution is believed to cause a significant reduction in the local blade metal temperature. To obtain an order of magnitude estimate of the cooling contribution in terms of a blade metal temperature reduction, a simple three-dimensional, convection-conduction model was developed and solved using **Fluent**. This computational model was a three-dimensional extension of a two- dimensional conduction-convection model presented by **Camci (1988)**. Surface isotherms on the internal (coolant) side of the blade wall are presented for $SR's$ of 1,4, and 8 and also those on the external (hot gas) side for $SR = 8$. For each of these surfaces, a comparison is made between the case with heat transfer enhancement in a 2D X 6D region downstream of the hole and the case without enhancement. Measured values of h from the present study were used as the internal convective boundary conditions while measured values from **Camci (1988)** were used for the external boundary conditions.

9.1 Previous work

Camci (1988) performed a two-dimensional experimental and numerical investigation of the heat fluxes and blade metal temperatures for a film cooled blade. In the experimental portion of his work, Camci measured the external heat transfer coefficient distribution in the presence of discrete hole film cooling on the suction side of a high pressure rotor blade. The film cooling holes were arranged in two staggered rows with a pitch of approximately 3 hole diameters. Camci used the measured data as external convective boundary conditions, along with the available internal heat transfer correlations for the internal convective boundary conditions, to generate two-dimensional computational blade metal temperature predictions. The resultant heat flux vectors, for the case in which the coolant-to-gas temperature ratio was 0.5 and the blowing rate was unity, is reproduced in Figure 9.1A. Also included in this figure is a close-up of the hole edge (actually a slot since the prediction was two-dimensional) which shows the heat flux vectors pointing into the flow. This reflects the very strong heat sink effect of the hole. In fact, most of the vectors on the suction surface of this part of the blade are pointing toward the hole. There is also a strong heat conduction tendency for the flow of heat from the downstream direction to the upstream direction.

The convective feature that Camci did not model however, was the enhancement near the entrance to the film cooling holes. As shown in Figure 9.1B, the blade metal near a film cooling hole is very similar to a section from the wall of a compact, cross- flow heat exchanger. The gradient of h on the external surface of Camci's blade occurred in the streamwise direction (with respect to the hot gas flow) while the main region of enhancement on the internal surface occurred in the direction downstream of the hole (streamwise with respect to the coolant flow). Therefore, to obtain a meaningful prediction of temperature in this region, a three-dimensional

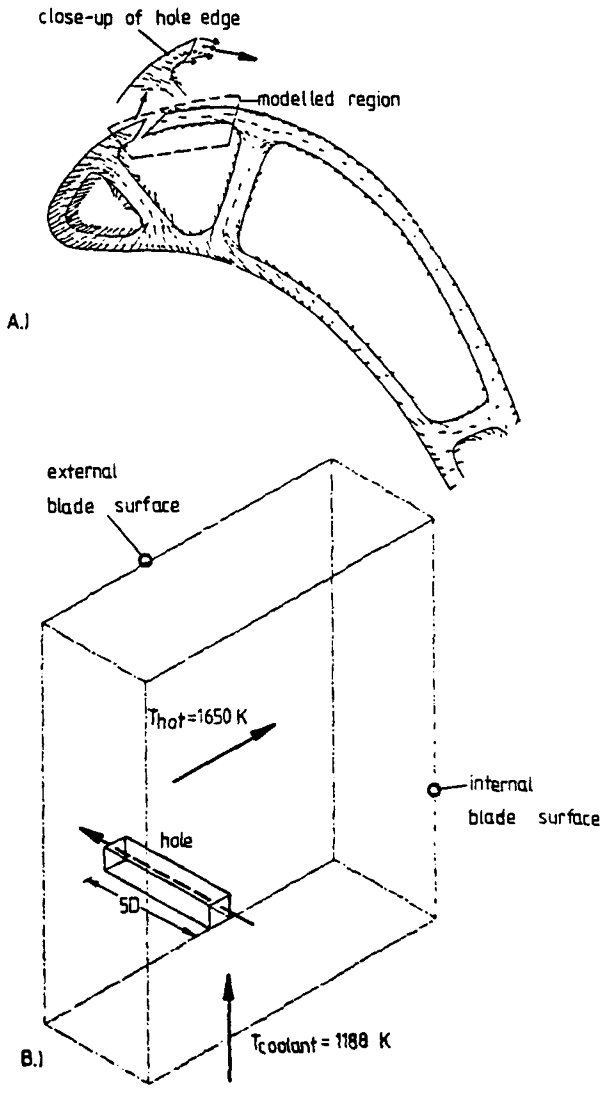
close-up of hole edge
modelled region
A.)
external blade surface
T_{hot}=1650 K
internal blade surface
hole
5D
B.)
$T_{coolant}$ = 1188 K

Figure 9.1: Convection-conduction models. Hole diameter = 0.8mm. A.) Two-dimensional prediction from CAMCI (1988). B.) Outline of the computational domain used in the three-dimensional prediction.

model was developed.

9.2 Computational Details

The outline of the computational domain used for the three- dimensional prediction is shown in Figure 9.1B. The extent of the domain was chosen to include all of the region most likely to be affected by the presence of the film cooling hole. Camci's results were used as a guide in determining this. Figure 9.1A indicates that heat flows towards the hole as far away as 10D in the downstream direction, and at least as far away as 3D in the upstream direction. Results from the present study indicate that the main region of enhancement on the coolant side of the blade was 6D downstream of the hole edge. In sizing the computational domain, another 5D was added to the 6D distance in the downstream direction (with respect to the coolant flow), as well as in the upstream direction to examine the extent of the hole heat transfer influence. The thickness of the wall was chosen to be 5D, the same thickness used by Camci. The end result was a domain with dimensions of 14D X 17D X 5D, as shown in Figure 9.1B. Finally, Camci's experimental, external values of h for the case of the coolant-to-gas temperature ratio of 0.72 were used along with his hot gas temperature of 1650K. The corresponding coolant temperature was therefore 1188 K.

Figure 9.2 shows the zones of constant h for both the internal and external surfaces. Wall zone 0 corresponded to the convective boundary condition inside the hole. As in Camci, the value of h in the hole was calculated using the Dittus-Boelter

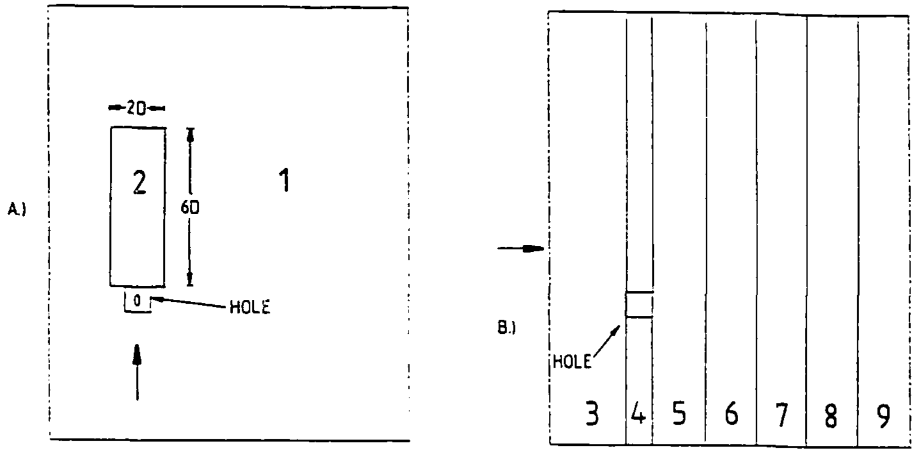

Figure 9.2: **Wall zones of constant h used in three-dimensional prediction. A.) Internal (coolant side) surface. B.) External (hot gas side) surface.**

equation for fully-developed turbulent flow

$$h = \frac{k}{D} 0.023 Re_D^{0.8} Pr^{0.4}$$

where the value of Re_D was related to the SR according to

$$Re_D = (SR)\,(Re_L)\,\left(\frac{D}{L}\right)$$

Of course, the L_{hole}/D of 5 was too small for the flow to be fully-developed so the value of h calculated from the correlation above was probably underestimated. The correlation was still useful, however, in obtaining an estimate of the internal wall cooling contribution.

Wall zone 1 corresponded to the unenhanced, base-level of heat transfer that was presented in Chapter 5. Since the heat transfer data was measured at $Re_L = 25,000$, this same value was assumed to represent the condition for wall zone 1 in the prediction, and the corresponding Nu_L was taken from Figure 5.1. (A Re_L value of 25,000 was also close to the duct Reynolds number used by Camci). Therefore, the h for wall zone 1 was calculated using

$$h_1 = \frac{k}{L} Nu_L$$

Then wall zone 2 which corresponded to the enhanced heat transfer region was calculated using

$$h_2 = \overline{EF}\ X\ h_1$$

where $\overline{EF}$ was the area-average enhancement factor presented as a function of SR in Chapter 5. For the unenhanced cases, wall zone 2 was considered to have the same convective boundary condition as zone 1 so $h_2 = h_1$.

The remaining wall zones are those on the external surface as shown in Figure 9.2B. Values of h were assigned to these zones using Camci's experimental data which is reproduced in Figure 9.3. Although the blade temperatures were predicted for three different SR values (1,4, and 8) which would correspond to three different blowing ratios, the external convective boundary conditions were fixed. Fixing the external convective conditions made the effects of the heat transfer enhancement on the internal surface more distinguishable. Furthermore, the value of h immediately downstream of the hole did not vary significantly over the range of blowing ratios that Camci tested, as shown in Figure 9.3. However, for blowing ratios large enough for the cooling jet to penetrate the hot freestream flow, there is evidence that suggests that the film cooling effectiveness is severely reduced. When this happens, the cooling effect on the internal wall becomes even more pronounced (and important)

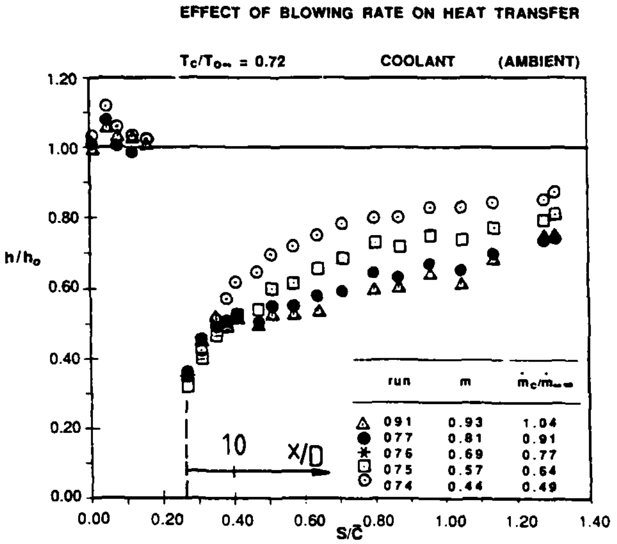

Figure 9.3: **Measured heat transfer coefficients on the suction surface of a HP rotor blade from CAMCI (1988).** ($h_o = 1000\ W/m^2K$, $\overline{C} = 80mm$)

as the external heat load increases dramatically. Finally, it should be emphasized that the external heat transfer zones in Figure 9.2B, whose h values are plotted in Figure 9.3, were measured on a two-dimensional blade with two staggered rows of holes spaced approximately 3D apart, while only a single hole was included in the present model. This is a major simplification of the physical situation, but one that was introduced to make the cooling contribution near a single hole more clearly distinguishable. Obviously, in the design of an actual blade, the conduction model should include multiple hole effects. The four remaining wall surfaces, those not shown in Figure 9.2, were considered planes of symmetry.

The computational grid, consisting of 3,990 grid points, is shown in Figure 9.4.

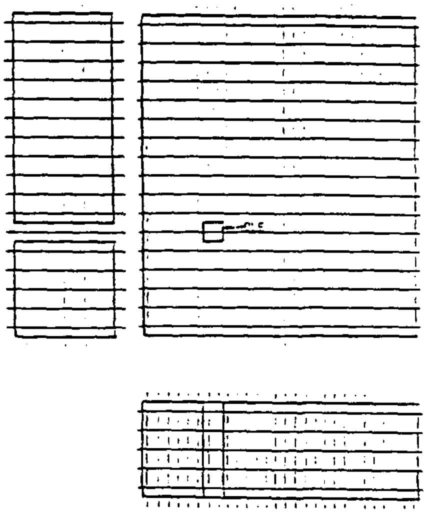

Figure 9.4: **The computational grid.**

The material properties of nickel-chrome steel at 1273 K were used including a thermal conductivity of 31 $W/m\ K$.

9.3 Computational Results

The temperature predictions for the internal (coolant) sides for $SR's = 1, 4$, and 8 are given in Figures 9.5-9.10. Surface isotherms are presented for both the enhanced and unenhanced cases which illustrate the heat sink effect of the hole and the effect of the internal cooling contribution. Also included are plots of surface temperature vs distance downstream of the hole edge along a line congruent with one streamwise axis of zone 2, the 2D X 6D region of enhancement. These plots highlight the temperature difference between the enhanced and unenhanced cases. Representative results for one external surface with $SR = 8$ are given in Figures 9.11 and 9.12. As expected, the blade metal temperature reductions and the associated isotherm distortions are much more prevalent on the internal surface than on the external surface. Table 9.1 is a summary of the effect of the enhancement in wall zone 2 on the blade temperature in this area. The average temperature reductions range from 2.0 to 4.2 K on the internal surface with the greater reductions associated with the larger *SR's*. As mentioned earlier in this chapter, the external film cooling effectiveness does not always increase with blowing rate (or *SR* from an internal perspective) because the cooling jet, at some point, begins to penetrate the freestream. It is important to note, therefore, that the cooling contribution on the internal side of the blade wall does continue to increase with *SR*.

While the 17D spanwise blade width chosen for the computational domain allows the extent of the single hole heat transfer influence to be examined, it should be noted that assigning such a large blade width to a single hole causes the predicted values of the blade metal temperature reductions to be on the conservative side. The enhanced area (2D X 6D) as a percentage of the total blade surface area (14D X 17D) in the model is smaller than that found in an actual blade where typical spacing between holes is approximately 3D. (A blade width of 17D would actually have about 4 holes.) Furthermore, if single hole enhancement data is found to be valid for multiple hole configurations, as preliminary tests indicate, then the appropriate *EF* values for holes spaced 3D apart should be based on the 2D X 3D area rather than on the 2D X 6D area. This is important since the *EF* for the 2D X 3D area is up to 25% higher than the $\overline{EF}$ for the 2D X 6D area, as shown in Figure 5.19. Therefore in a multiple hole model, the increase in both the percentage enhanced area and the $\overline{EF}$ would lead to larger blade metal temperature reductions.

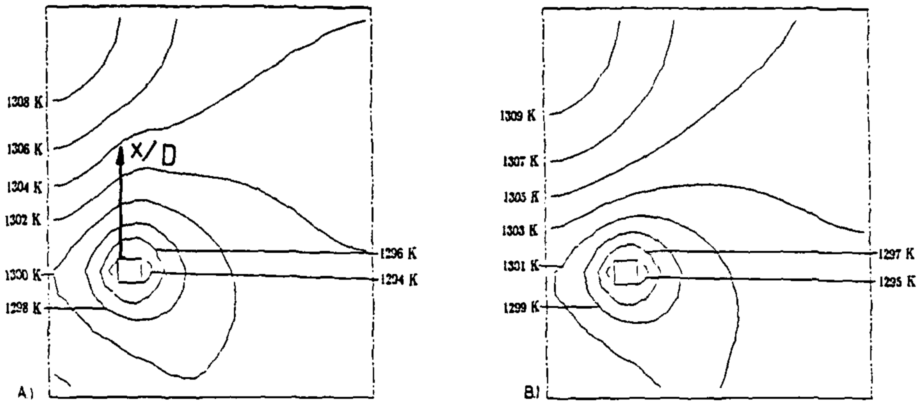

Figure 9.5: $SR = 1$, Internal surface. A.) Enhanced case. B.) Unenhanced case.

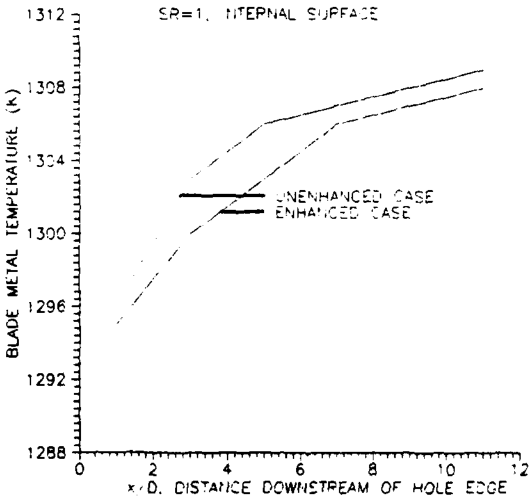

Figure 9.6: $SR = 1$, Internal surface. Effect of internal cooling contribution on blade metal temperature.

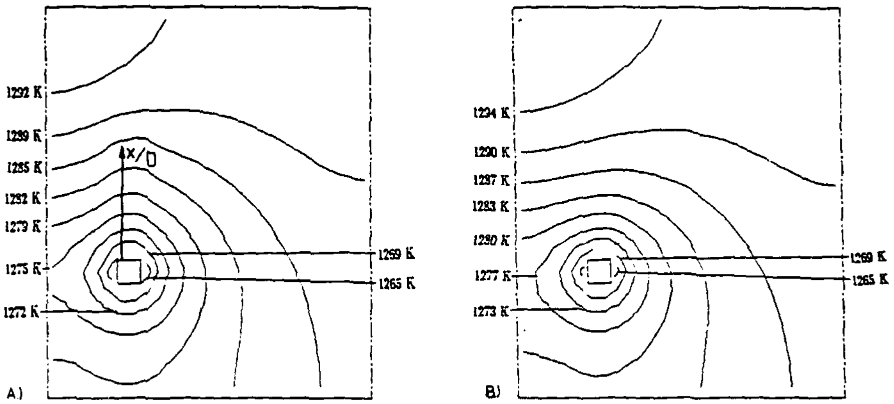

Figure 9.7: $SR = 4$, **Internal surface. A.) Enhanced case. B.) Unenhanced case.**

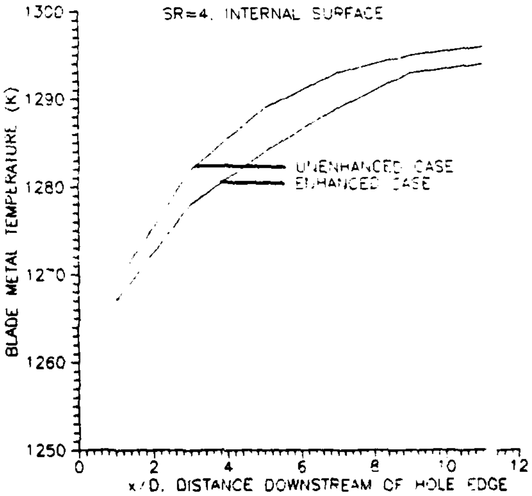

Figure 9.8: $SR = 4$, **Internal surface. Effect of internal cooling contribution on blade metal temperature.**

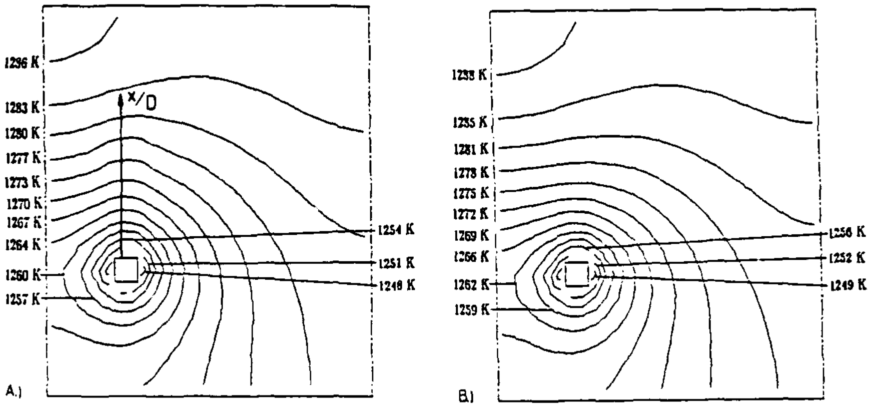

Figure 9.9: $SR = 8$, **Internal surface. A.) Enhanced case. B.) Unenhanced case.**

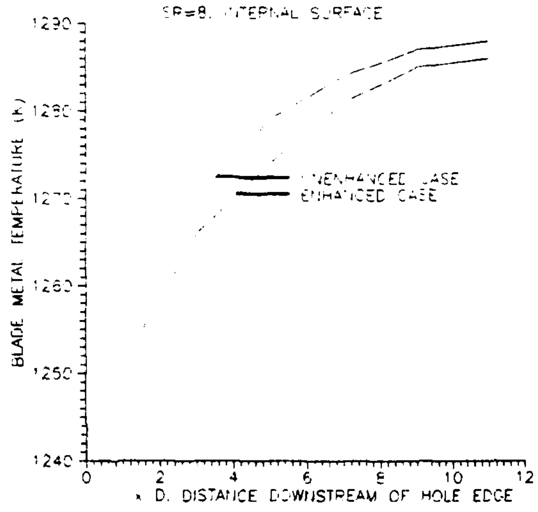

Figure 9.10: $SR = 8$, **Internal surface. Effect of internal cooling contribution on blade metal temperature.**

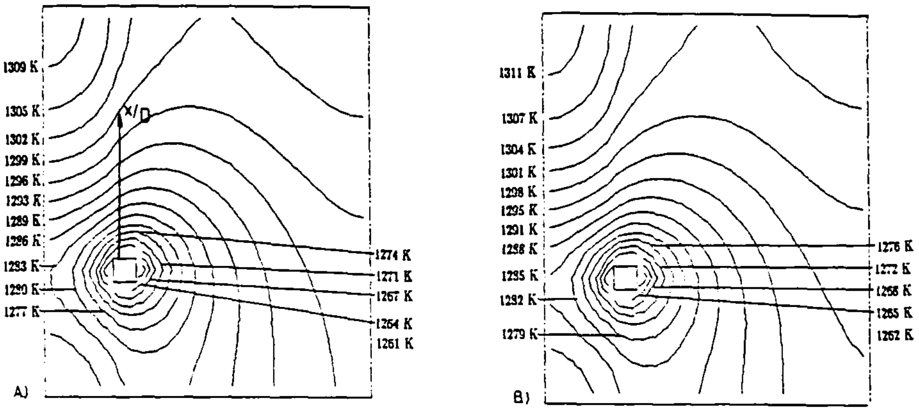

Figure 9.11: $SR = 8$, External surface. A.) Enhanced case. B.) Unenhanced case.

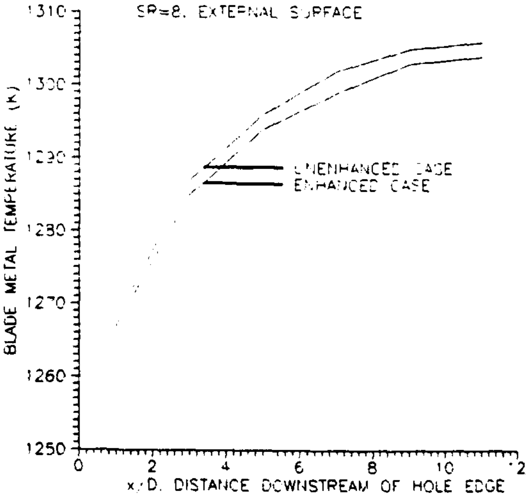

Figure 9.12: $SR = 8$, External surface. Effect of internal cooling contribution on blade metal temperature.

SR	INTERNAL SURFACE	EXTERNAL SURFACE
1	Range= 1 to 3K	1 to 2K
	Average= 2.0K	1.2K
4	Range= 2 to 5K	1 to 3K
	Average= 3.7K	2.0K
8	Range= 3 to 5K	1 to 2K
	Average= 4.2K	1.7K

Table 9.1: **Reductions of blade metal surface temperatures in wall zone 2 that are due to the internal cooling contribution. Both the range and the average temperature reductions are given.**

Another point to remember when evaluating these results is that the heat sink effect of the cooling hole, revealed by both Camci's two-dimensional predictions and the present three-dimensional predictions, has a dominant effect on the blade temperature distribution and therefore tends to obscure the cooling effect of the enhanced heat transfer on the internal blade passage.

In summary, it is clear that accounting for the cooling contribution near the entrance to a film cooling hole is important for accurate predictions of blade metal temperatures. The isothermal contours show that the cooling contribution of a single hole extends across a wide area of the blade. Finally, the values of the blade metal temperature reductions for a multiple hole system will be far greater than those presented in this chapter.

10 EXPERIMENTAL C_d MEASUREMENTS

In addition to the heat transfer measurements made during the experimental program, the hole discharge coefficients were also measured. The discharge coefficient parameter is important in the proper sizing and placement of film cooling holes so that the correct amount of coolant flow is provided to obtain the desired "blowing rate" (or suction rate from the internal cooling perspective). As demonstrated in Chapter 9, the "blowing rate" (or SR) strongly influences the blade metal temperature; providing a "blowing rate" too low might result in local "hot spots" while providing one too high might lead to coolant jet penetration into the hot freestream. Both of these would lead to a shortened blade life.

The discharge coefficient parameter relates the actual flow passing through a hole to the flow that would pass through a hole in the ideal case. It is defined as

$$C_d \equiv \frac{\dot{m}_{actual}}{\dot{m}_{ideal}}$$

To evaluate this expression, the actual mass flow rate through the hole was measured using the orifice plate described in Chapter 4, while the ideal mass flow rate was calculated using measured pressures. For the ideal case, the total pressure between stations 1 (in the main duct) and 2 (at the hole exit), as shown in Figure 3.2, would be constant. The ideal velocity at station 2 (the hole exit) was therefore calculated using Bernoulli's equation

$$u_{2-ideal} = \sqrt{\frac{2\left(P_{t2-ideal} - P_2\right)}{\rho}}$$

where

$$P_{t2-ideal} = P_{t1}$$

Of course in the actual case, the total pressure does not remain constant between the main duct and the hole exit because of flow separation at the sharp-edged hole entrance and the "pipe" friction along the length of the hole.

10.1 Previous Work

Substantial work in the area of discharge coefficients has already been accomplished. **Rohde, Richards, and Metger (1969)**, conducted an extensive series of tests to determine the effects of various flow and geometric conditions on thick plate orifices with the approach flow perpendicular to the orifice axis. **Hay, Lampard, and Benmansour (1983)** were the first to examine the combined effects of mainstream and coolant crossflows on film cooling holes. **Tillman and Jen (1982)** studied the discharge of air from holes in a cylindrical model representing the leading edge region of a turbine blade. **Tillman, Hartel, and Jen (1984)** extended the study to include blades with internal inserts running the spanwise length of the blade. **Chu, Brown, and Garrett (1985)** combined impingement and film cooling hole geometries. The early results from **Rohde et al** were later validated by several of the other workers.

10.2 Experimental Results

The experimental values of C_d are plotted versus the *velocity head ratio* in Figure 10.1 along with the results from **Rohde et al (1969)**. The *velocity head ratio*, defined as

$$\textit{velocity head ratio} \equiv \frac{(P_{t1} - P_2)}{(P_{t1} - P_1)}$$

was placed on the *x-axis* to be consistent with Rohde who used it to correlate data for a wide range of gas temperatures. The *velocity head ratio* is simply one way of describing the pressure drop across the hole; it can be thought of as the ratio of the ideal velocity (or dynamic) head for the hole flow to the velocity head for the main duct flow. A comparison of the results from the present work with Rohde's results shows good agreement even though Rohde's hole had an L_{hole}/D of 4 while the holes in the present study had L_{hole}/D*'s* of 10. This was expected since both **Hay et al (1983)** and **Tillman et al (1982)** found that increasing the L_{hole}/D above 4 did not effect C_d. This is because the losses associated with non-isentropic turbulent mixing downstream of the separated region are much greater than the frictional losses associated with flow through a pipe. Therefore, increasing the hole length to 10 hole diameters does not significantly affect C_d since the major losses occur within the first four diameters of the hole entrance.

Figure 10.1 also shows that the results from the present work diverge from Rohde's near a velocity head ratio of 50 which corresponds to relatively high values of *SR*. The difference in these results is probably due to the differences in the main duct geometries used in the two studies. Rohde's main duct was circular in shape

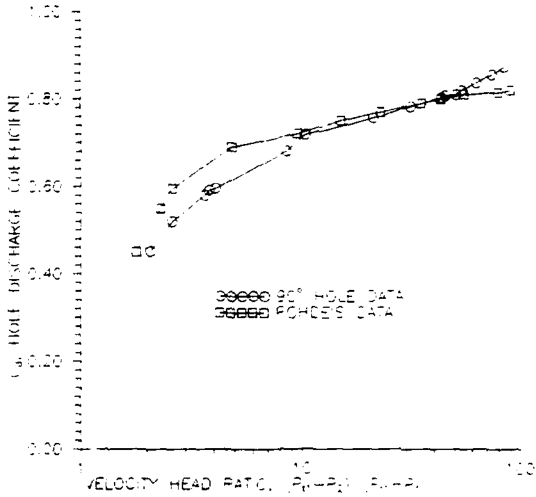

Figure 10.1: **Comparison of discharge coefficient results with other worker's results.**

with an inside diameter four times the diameter of the extraction hole. It is possible that during high levels of hole suction that a significant amount of flow was drawn into the hole from the lateral direction in the wide two-dimensional main duct which was clearly impossible in the narrower main duct of Rohde's study. Both the significant heat transfer enhancement observed in the lateral direction and the results from the flow field studies support this view.

Figure 10.2 shows the effect of hole inclination angle on C_d. Since the hole L_{hole}/D was 10 for all four inclination angles, the differences between the C_d values are due exclusively to the separation effects at the hole entrance. As expected, the C_d for the 150° *hole* was always the lowest since the flow turning angle was the largest. Also

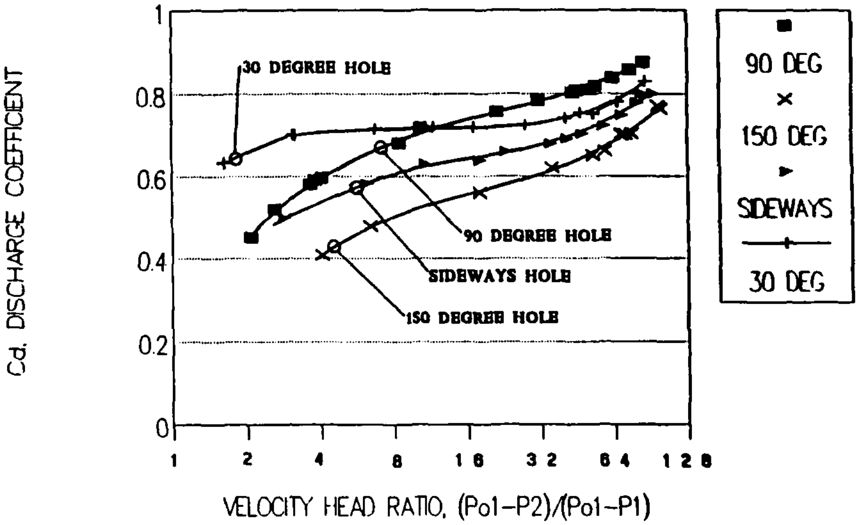

Figure 10.2: **Effect of hole inclination angle.**

expected were the high values of C_d for the 30° *hole* since the flow turning angle was the smallest.

An unexpected result, however, was the cross-over in C_d values that took place between the 30° *hole* and the 90° *hole*. At a *velocity head ratio* of around 12, the 90° *hole* C_d became larger than the 30° *hole* C_d. Referring back to the parametric study of hole C_d's by **Rohde et al (1969)**, a similar cross-over was observed in a comparison between a 90° *hole* and a 45° *hole* as shown in Figure 10.3, although no explanation for this phenomenon was given. Figure 10.4, however, does illustrate the probable explanation. For the 90° *hole* at low *SR's* a fairly large region of separation exists at the upstream hole edge. At high *SR's*, however, when the stagnation is positioned downstream of the hole, the separated region extends around the entire

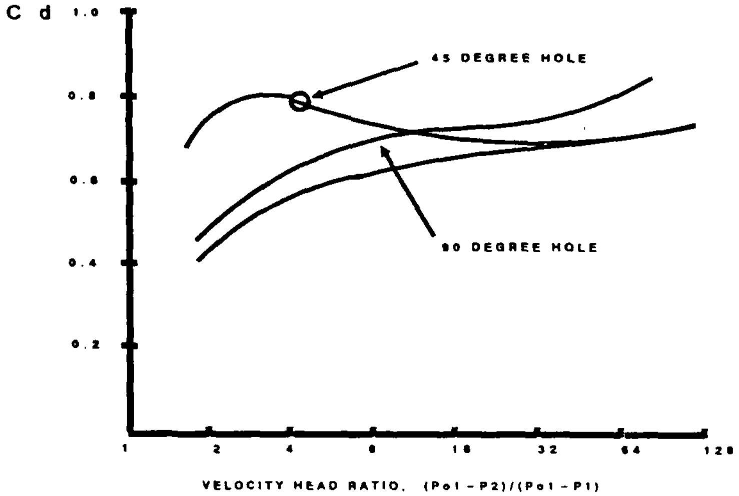

Figure 10.3: **Effect of hole inclination angle from ROHDE, RICHARDS, and METGER (1969)**

hole perimeter. The total extent of the separation at the higher SR is smaller than at the lower SR because of the more favourable pressure gradient for the flow passing into the hole. For the 30° *hole*, however, the situation is slightly different. At low SR's, the region of separation at the upstream hole edge is small because of the smaller flow turning angle. At higher SR's, though, when the stagnation point is positioned downstream of the hole, the reverse flow has to turn through a 150° *angle* to enter the hole. The resultant increase in the extent of the separated region is the most probable cause of the observed dip in the values of C_d.

The uncertainty in C_d was within 3.7% while the uncertainty in the *velocity head ratio* was within 3.5%.

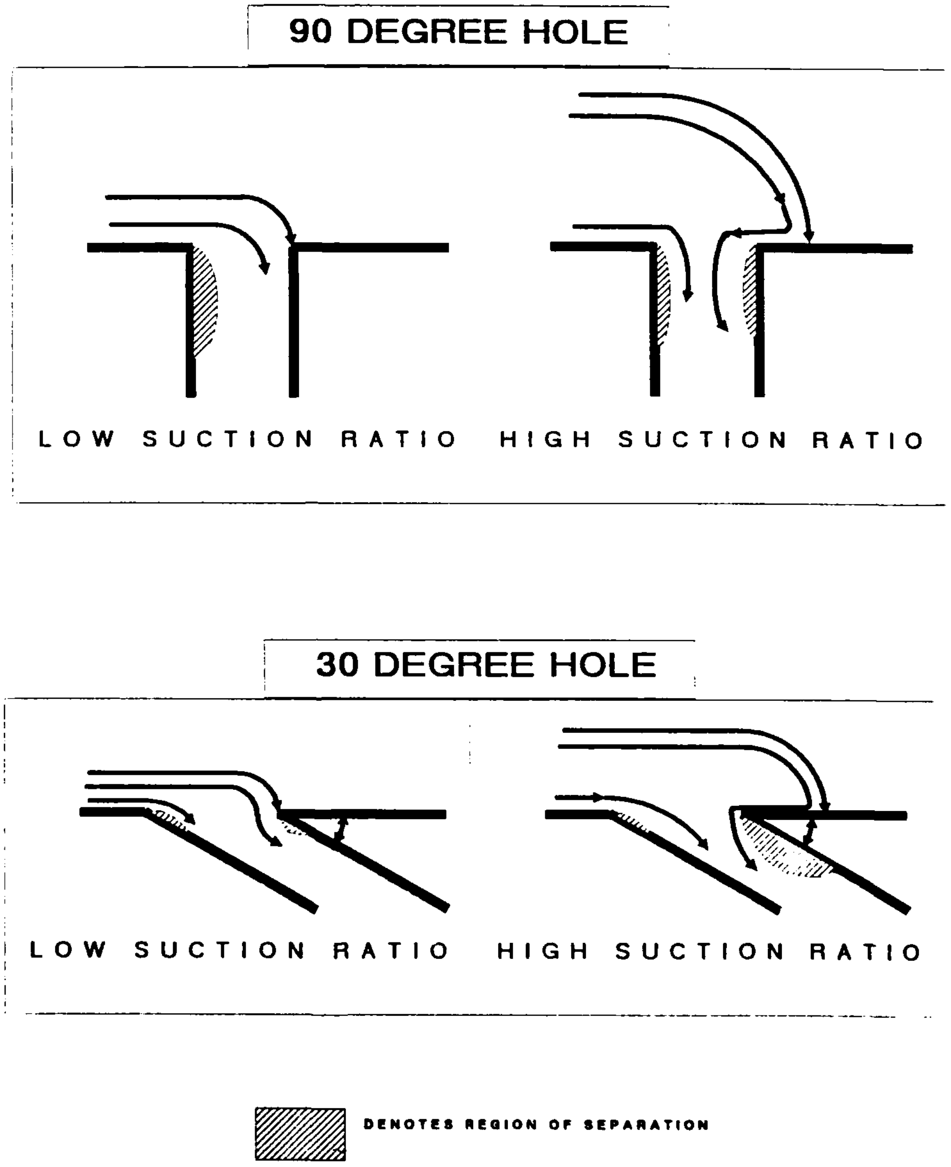
90 DEGREE HOLE
LOW SUCTION RATIO
HIGH SUCTION RATIO
30 DEGREE HOLE
LOW SUCTION RATIO
HIGH SUCTION RATIO
DENOTES REGION OF SEPARATION

Figure 10.4: **Explanation for the C_d cross-over.**

11 CONCLUSIONS

The important conclusions drawn from the experimental, analytical, and computational investigations of this hitherto unresearched subject are now *summarized*. The following three main subjects are addressed: the salient results, the mechanisms responsible for heat transfer enhancement, and possible extensions of this work which might form the basis of future research.

11.1 The Salient Results

The detailed heat transfer distributions near the entrance to a film cooling hole were measured and presented in this thesis for the very first time. Significant heat transfer enhancement was observed downstream of the hole covering an area with approximate dimensions of 2D X 6D. The local values of enhancement factor (EF) were as high as 6.5 while the area-averaged enhancement factors ($\overline{EF}$) went up to 2.15. The level of heat transfer enhancement was found to be strongly dependent upon the flow extraction rate, quantified in the present work by the suction ratio (SR). This parameter was more important than any of the others; in fact, for SR's less than two or three it was the only parameter that mattered since the area-averaged enhancement factor ($\overline{EF}$) for a given SR, was virtually the same regardless of the hole inclination angle, the duct Reynolds number (Re_L), and the upstream velocity and temperature profiles (over the range of conditions tested). The hole inclination angle was important at SR's greater than two, insofar as the $\overline{EF}$ for the 150° *hole* dropped below the others.

11.2 The Mechanisms Responsible for Enhancement

Obviously the enhanced heat transfer near the entrance to a film cooling hole is the result of a complex combination of boundary layer removal and three-dimensional flow features. Fortunately, the detailed pictures of heat transfer distribution provided by the transient liquid crystal measurement method along with the results from experimental and computational flow field studies have provided clues as to what the operative mechanisms are. These mechanisms are now summarized.

Figures 11.1 and 11.2 point out the mechanisms that are likely to be dominant locally in each of the enhancement regions for two different flow regimes: at relatively low $SR's$ when the stagnation point is located at the downstream hole edge ($SR < 4.2$ for the 90° *hole*) and at relatively high $SR's$ when the stagnation point is located downstream of the hole. Upstream of the hole for both flow regimes the enhancement is due to local acceleration of the flow drawn into the hole. Also for both flow regimes, enhancement downstream of the hole is due mainly to the removal of the upstream velocity and temperature boundary layers and the subsequent increase in the local gas temperature gradient at the wall.

The boundary layer downstream of the hole was found to be laminar in nature. The two-dimensional analytical predictions for the heat transfer downstream of a slot which were based on the assumption that a new laminar boundary layer began to form at the downstream slot edge were in good agreement with the measured experimental values. However, the effect of the three- dimensional flow field features became apparent when similar two-dimensional predictions were performed downstream of the hole. The predicted heat transfer values were slightly below the measured experimental values. However, the laminar prediction could be used to provide conservative, first-order estimates of the heat transfer downstream of the hole. Much better agreement between the predicted and the experimental values might be obtained by analytically accounting for the surface streamline divergence downstream of the hole.

For the low SR flow regime, as shown in Figure 11.1, the single lobe contour shape illustrates the effects of boundary layer thinning due to downwash from a vortex pair along the axial centreline and to surface streamline divergence on either side of the axial centreline. For the high SR regime, as illustrated in Figure 11.2, the lobed contour shape still corresponds to the location of vortex downwash; but since the distance between the vortex pair is greater the downwash occurs in two separate areas on either side of the axial centreline, rather than right along the centreline as before. The peak in heat transfer is still located at the downstream hole edge even though the stagnation point is located as far away as $0.5D$ downstream. The reason for this is the very high level of acceleration experienced by the reverse flow drawn back into the hole.

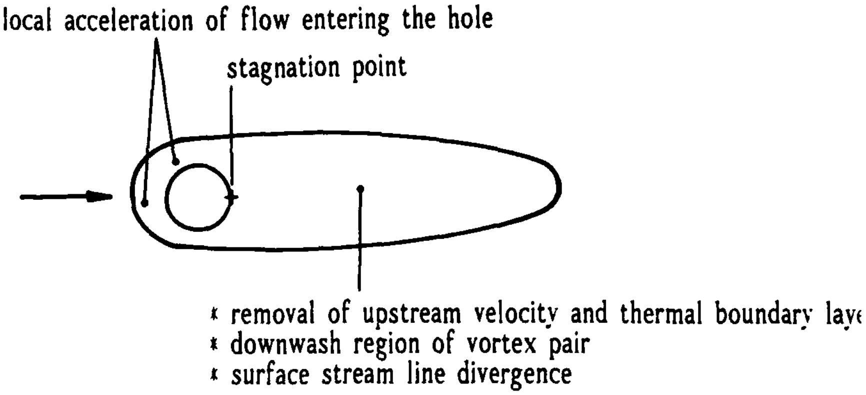
local acceleration of flow entering the hole
stagnation point
* removal of upstream velocity and thermal boundary laye
* downwash region of vortex pair
* surface stream line divergence

Figure 11.1: Mechanisms of enhancement for low *SR's*.

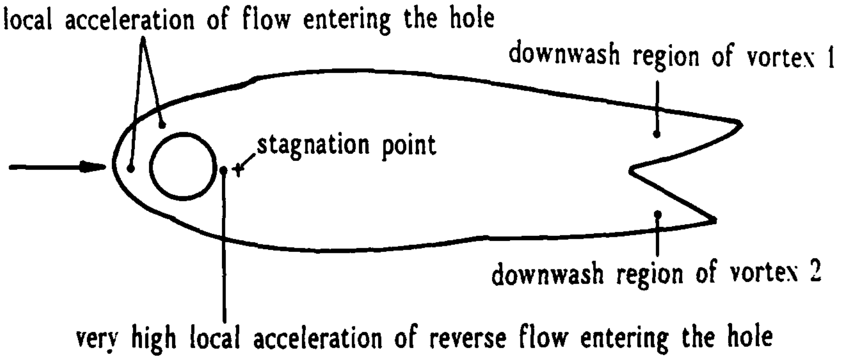
local acceleration of flow entering the hole
downwash region of vortex 1
stagnation point
downwash region of vortex 2
very high local acceleration of reverse flow entering the hole

Figure 11.2: Mechanisms of enhancement for high *SR's*.

11.3 Extensions of the Present Work

The present work provides a starting point for a great number of interesting and worthwhile extensions. Listed below are just a few that the author feels may be of particular importance:

- *Multiple hole effects*- film cooling holes are often spaced 2 or 3 hole diameters away from each other in single rows or staggered multiple rows. Further experimental (and computational) work needs to be performed to examine the effect of the interaction between the holes.

- *Heat transfer within the hole*- liquid crystals applied on the inside surface of the holes in the present work revealed a number of complex, but highly organized enhancement patterns which were strongly dependent upon SR and inclination angle. A sample of these patterns is given in Figure 11.3 in the form of time-elapsed photographs of the colour play within the entrance region of the 90° *hole* for $SR = 3.47$. The blade metal temperature predictions in Chapter 9 showed that the cooling contribution made by the hole was extremely important for determining both the maximum metal temperature and the temperature gradients. The *inside hole* results from the present work indicated that there were strong circumferential variations of the hole heat transfer which may have important implications for accurate blade temperature predictions. The double liquid crystal method could be used to calculate both the local value of h and the local driving gas temperature.

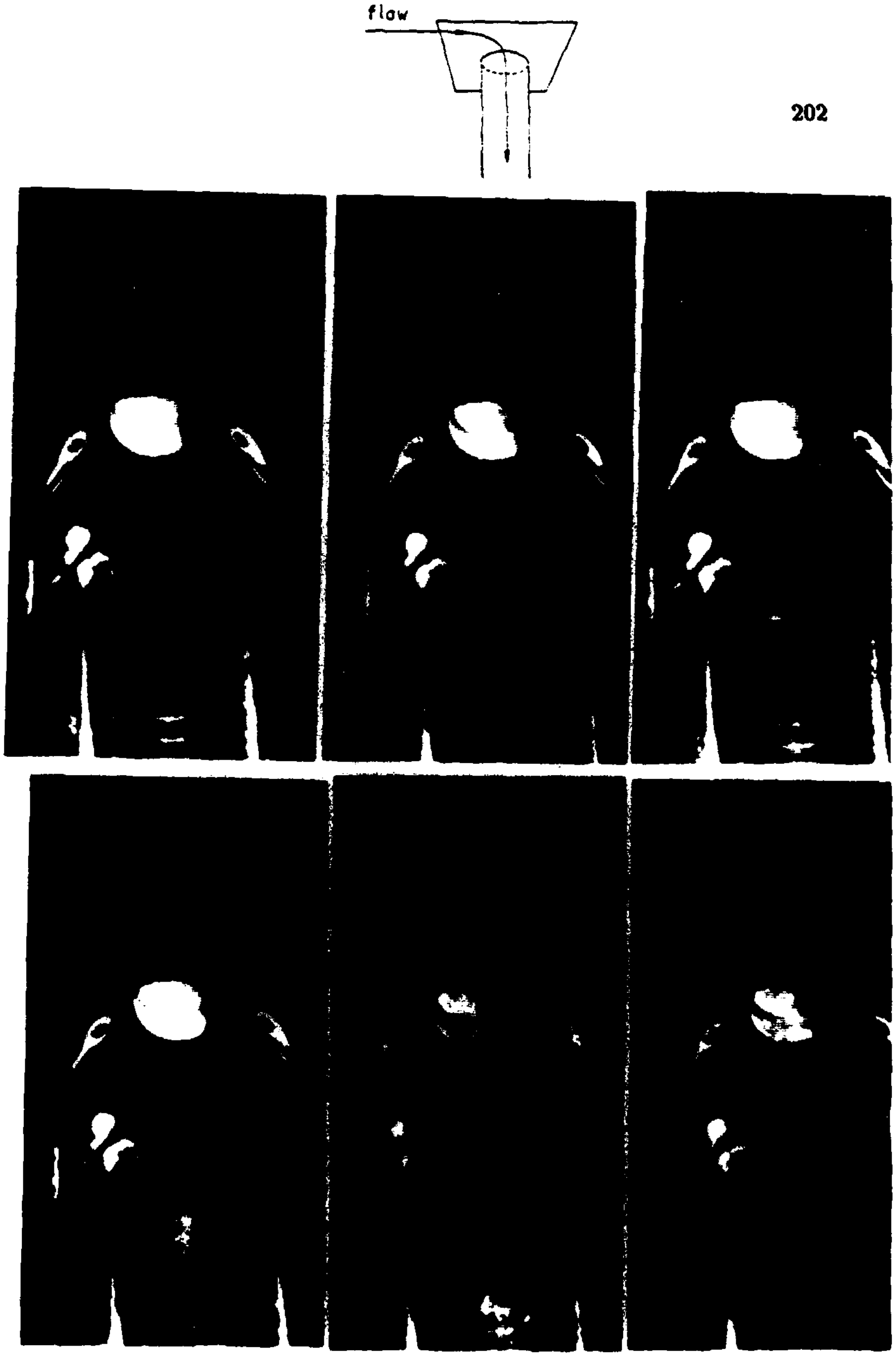

Figure 11.3: Time-elapsed photographs of the colour play within the entrance region of the 90° *hole* for $SR = 3.47$.

- ***Flow diagnostics for the* 150° *hole*- the heat transfer enhancement contours for the 150° *hole* revealed features unique to this particular inclination angle including peak heat transfer in oval shaped regions off of the axial centreline and a four-lobed contour shape. More flow field studies need to be made to establish the precise reasons for this phenomena.**

APPENDIX A- DETAILS OF THE THERMODYNAMIC MODELS

A.1 Flight condition

The flight condition was chosen to be Mach 0.7 at a standard altitude of 29,000 feet so

$$M_0 = 0.7$$

$$T_0 = 233.3\ K$$

A.2 Gas constants and recovery properties

The gas constants for the air upstream of the burner are

$$\gamma_c = 1.4$$

$$C_{pc} = 996.5\ \frac{J}{kg\ K}$$

while the properties of the flow leaving the burner (after fuel addition and combustion) are

$$\gamma_t = 1.35$$

$$C_{pt} = 1098.2 \frac{J}{kg\ K}$$

Other important equations involving gas properties are

$$R_c = \frac{\gamma_c - 1}{\gamma_c} C_{pc}$$

$$R_t = \frac{\gamma_t - 1}{\gamma_t} C_{pt}$$

$$a_0 = \sqrt{\gamma_c R_c T_0}$$

$$U_0 = M_0 a_0$$

The recovery properties are given by

$$\tau_r = \frac{T_{t0}}{T_0} = 1 + \frac{\gamma_c - 1}{2} M_0^2$$

$$\pi_r = \frac{P_{t0}}{P_0} = \tau_r^{\frac{\gamma_c - 1}{\gamma_c}}$$

A.3 Inlet (or Diffuser)

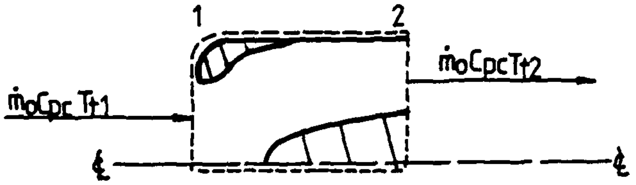

The diffuser is an adiabatic device with no shaft work interactions so an energy balance yields

$$\tau_d = \frac{T_{t2}}{T_{t1}} = 1$$

There is a small total pressure loss due to wall friction so

$$\pi_d = \frac{P_{t2}}{P_{t1}} = 0.96$$

A.4 Compressor

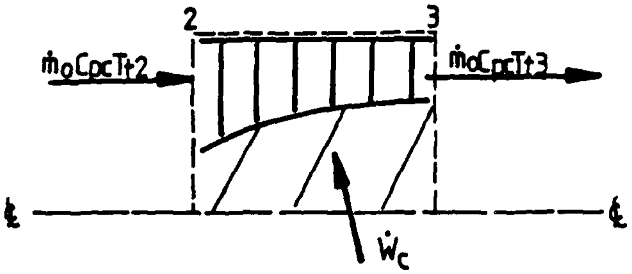

An energy balance on the compressor yields

$$\dot{W}_c = \dot{m}_o \, C_{pc}(T_{t3} - T_{t2})$$

The value of compressor pressure ratio

$$\pi_c = \frac{P_{t3}}{P_{t2}}$$

was varied from 10 to 40 to represent the possible design choices. The total temperature ratio is

$$\tau_c = \frac{T_{t3}}{T_{t2}} = \pi_c^{\frac{(\gamma_c - 1)}{\gamma_c e_c}}$$

where e_c is the polytropic efficiency of the compressor which was set to

$$e_c = 0.88$$

Polytropic efficiency, rather than isentropic efficiency, was used for the compressor and turbine so that the losses could vary with the respective pressure ratios. Obviously, the isentropic efficiency for a compressor operating at a high pressure ratio is less than that for a compressor operating at a lower pressure ratio. As **Oates (1984)** points out, the use of polytropic efficiency reflects the estimated behaviour of a family of compressors designed to different pressure ratios, through the use of different numbers of compressor stages. It does not reflect the expected behaviour for a given compressor operating at a different Mach number or altitude.

A.5 Burner

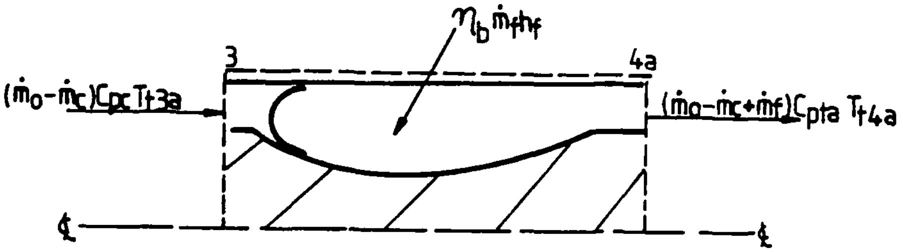

$\eta_b \dot m_f h_f$
3
4a
$(\dot m_o - \dot m_c)C_{pc}T_{t3a}$
$(\dot m_o - \dot m_c + \dot m_f)C_{pta}T_{t4a}$
℄
℄

An energy balance yields

$$(\dot m_o - \dot m_c)C_{pc}T_{t3a} + \eta_b \, \dot m_f \, h_f = (\dot m_o - \dot m_c + \dot m_f)C_{pta}T_{t4a}$$

where η_b is the burner efficiency and C_{pta} is the specific heat for the air/fuel/products-of-combustion mixture leaving the burner. The burner efficiency was assumed to be

$$\eta_b = 0.97$$

to account for incomplete combustion. The "heating value" of the fuel is

$$h_f = 4.5357(10^7) \; J/\; kg$$

The fuel-to-air ratio was defined as

$$f = \frac{\dot m_f}{\dot m_o}$$

and the percentage coolant flow as

$$\epsilon = \frac{\dot m_c}{\dot m_o}$$

Substitution into the energy balance equation yields

$$f = (1 - \epsilon) \left\{ \frac{\tau_\lambda - \tau_r \tau_c}{\frac{\eta_b h_f}{C_{pc} T_0} - \tau_\lambda} \right\}$$

where

$$\tau_\lambda = \frac{C_{pta} T_{t4}}{C_{pc} T_0}$$

The total pressure decreases across the combustor because of viscous effects within the combustion chamber and constant-area heat addition so

$$\pi_b = \frac{P_{t4a}}{P_{t3a}} = 0.98$$

A.6 NGV

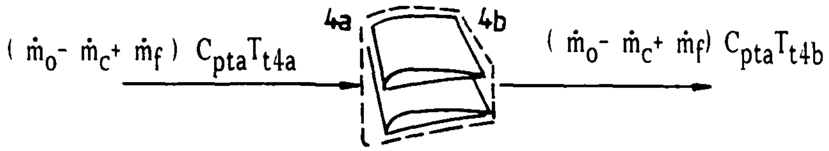
$(\dot{m}_0 - \dot{m}_c + \dot{m}_f)\ C_{pta} T_{t4a}$
4a
4b
$(\dot{m}_0 - \dot{m}_c + \dot{m}_f)\ C_{pta} T_{t4b}$

The flow through the NGV's was assumed to be adiabatic so

$$\tau_{NGV} = \frac{T_{t4b}}{T_{t4a}} = 1$$

but frictional losses are present so

$$\pi_{NGV} = 0.995$$

A.7 Coolant valve

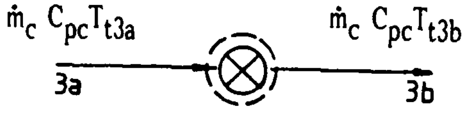
$\dot{m}_c\ C_{pc} T_{t3a}$
$\dot{m}_c\ C_{pc} T_{t3b}$
3a
3b

An energy balance yields

$$\tau_{valve} = \frac{T_{t3b}}{T_{t3a}} = 1$$

The total pressure drop across the coolant valve was assumed to be equal to the total pressure drop across the burner and NGV so

$$\pi_{valve} = 0.975$$

A.8 Adiabatic, constant pressure mixer- model 1

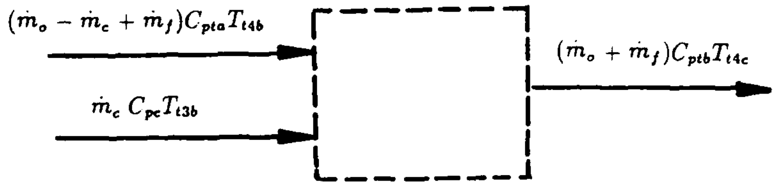
$(\dot{m}_o - \dot{m}_c + \dot{m}_f)C_{pta}T_{t4b}$
$\dot{m}_c\ C_{pc}T_{t3b}$
$(\dot{m}_o + \dot{m}_f)C_{ptb}T_{t4c}$

An energy balance yields

$$(\dot{m}_o - \dot{m}_c + \dot{m}_f)C_{pta}T_{t4b} + \dot{m}_c\ C_{pc}T_{t3b} = (\dot{m}_o + \dot{m}_f)C_{ptb}T_{t4c}$$

where C_{ptb} is a mass averaged value of specific heat to account for the mixed streams of coolant and combustor flow

$$C_{ptb} = \epsilon C_{pc} + (1 - \epsilon)C_{pta}$$

After substitution, the energy balance can be expressed as

$$\tau_{mixer} = \frac{T_{t4c}}{T_{t4b}} = \frac{1}{(1+f)}\left(\frac{C_{pta}}{C_{ptb}}\right)\left[1 + f - \epsilon + \left(\frac{\epsilon\tau_r\tau_c}{\tau_\lambda}\right)\right]$$

The mixing process was assumed to be a constant pressure process so

$$\pi_{mixer} = \frac{P_{t4c}}{P_{t4b}} = 1$$

A.9 Valve to account for aerodynamic penalties

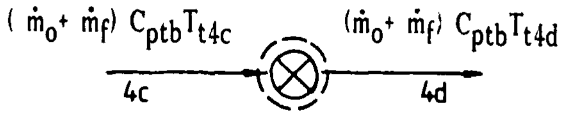
$(\dot{m}_0 + \dot{m}_f)\ C_{ptb}T_{t4c}$
$(\dot{m}_0 + \dot{m}_f)\ C_{ptb}T_{t4d}$
4c
4d

Unfortunately, film cooling causes certain aerodynamic losses which must be considered in any realistic thermodynamic model. These losses are associated with the emission of flow from the film cooling holes in the NGV blades which changes the effective blade profile. There are also losses stemming from the non- isentropic mixing of the coolant stream and the hot freestream. These losses can be modelled approximately as a total pressure drop which is dependent upon the percentage coolant flow (ϵ)

$$\pi_{penalty} = 1 - 0.2\epsilon$$

This relationship allowed for a 2% drop in total pressure when $\epsilon = 10\%$.

A.10 Turbine rotor- model 1

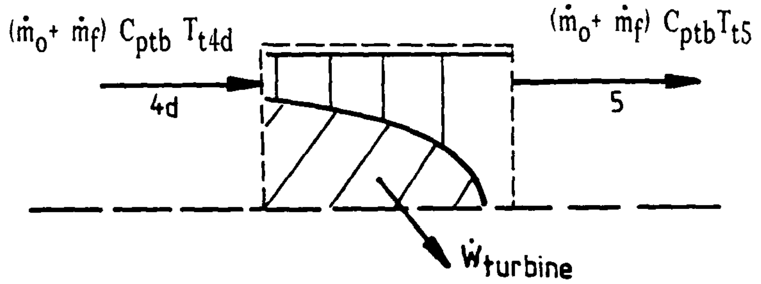
$(\dot{m}_o + \dot{m}_f)\, C_{ptb}\, T_{t4d}$
4d
$(\dot{m}_o + \dot{m}_f)\, C_{ptb} T_{t5}$
5
$\dot{W}_{turbine}$

An energy balance yields

$$\dot{W}_{turb} = (\dot{m}_o + \dot{m}_f)C_{ptb}(T_{t4d} - T_{t5})$$

The power balance between the turbine and compressor yields

$$\dot{W}_c = \eta_m\, \dot{W}_{turb}$$

where η_m is the mechanical efficiency to account for bearing losses

$$\eta_m = 0.99$$

Substitution yields

$$\dot{m}_o\, C_{pc}(T_{t3} - T_{t2}) = \eta_m(\dot{m}_o + \dot{m}_f)C_{ptb}(T_{t4d} - T_{t5})$$

and eventually

$$\tau_{rotor} = 1 - \left[\frac{\tau_r(\tau_c - 1)}{\eta_m(1+f)(\frac{C_{ptb}}{C_{pta}})\tau_{mixer}\ \tau_\lambda}\right]$$

The pressure drop across the rotor is therefore given by

$$\pi_{rotor} = \tau_{rotor}^{\frac{\gamma_{tb}}{(\gamma_{tb}-1)e_t}}$$

where γ_{tb} is a mass averaged value to account for the mixed streams

$$\gamma_{tb} = \epsilon\gamma_c + (1-\epsilon)\gamma_t$$

and e_t is the polytropic efficiency of the turbine

$$e_t = 0.91$$

A.11 Nozzle

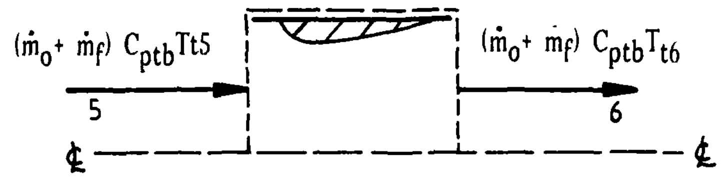
$(\dot{m}_0 + \dot{m}_f)\, C_{ptb} T_{t5}$
5
$(\dot{m}_0 + \dot{m}_f)\, C_{ptb} T_{t6}$
6
℄
℄

The nozzle was assumed to be adiabatic so

$$\tau_{nozzle} = \frac{T_{t6}}{T_{t5}} = 1$$

However, there are some frictional losses so

$$\pi_{nozzle} = 0.99$$

Finally, the flow was assumed to undergo a perfect expansion through the nozzle so

$$P_6 = P_0$$

A.12 Intermediate values

$$\frac{P_{t6}}{P_6} = \frac{P_0}{P_6} \pi_r \pi_d \pi_c \pi_d \pi_b \pi_{NGV} \pi_{penalty}\, \pi_{rotor}\, \pi_n$$

$$\frac{M_0 U_6}{U_0} = \left[\frac{2}{(\gamma_{tb} - 1)} \frac{\gamma_{tb}}{\gamma_c} \frac{R_{tb}}{R_c} \frac{C_{pc}}{C_{pta}} \tau_\lambda \tau_{mixer}\, \tau_{rotor} \left(1 - \frac{P_{t6}}{P_6}^{\frac{(1-\gamma_{tb})}{\gamma_{tb}}} \right) \right]^{1/2}$$

A.13 Specific thrust and thermodynamic efficiency

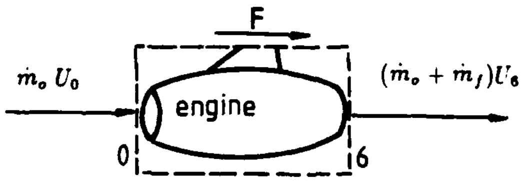

The momentum equation yields

$$F = (\dot{m}_o + \dot{m}_f) U_6 - \dot{m}_o\, U_0$$

where F is engine thrust. This equation can be put in terms of known quantities to obtain the expression for specific thrust

$$\frac{F}{\dot{m}_o} = a_0 \left[(1 + f) \frac{M_0 U_6}{U_0} - M_0 \right]$$

Finally, thermodynamic efficiency is

$$\eta_{th} = \frac{(\dot{m}_o + \dot{m}_f)U_6^2 - \dot{m}_o U_0^2}{2\,\dot{m}_f\,h_f}$$

which can be reduced further to

$$\eta_{th} = \frac{(1+f)U_6^2 - U_0^2}{2fh_f}$$

An analysis of Model 2 revealed that all of the equations presented so far for Model 1 remain applicable for Model 2 except for the equations involving the rotor and mixer. The appropriate equations for those components are listed below and were substituted into the final equations given above for the specific thrust and thermodynamic efficiency calculations for Model 2.

A.14 Turbine rotor- model 2

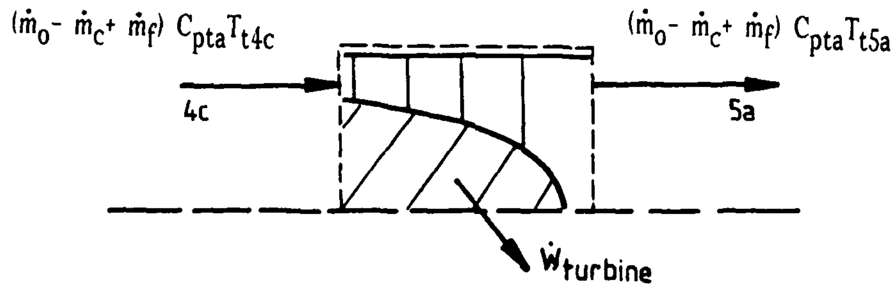
$(\dot{m}_0 - \dot{m}_c + \dot{m}_f)\ C_{pta}T_{t4c}$
$(\dot{m}_0 - \dot{m}_c + \dot{m}_f)\ C_{pta}T_{t5a}$
4c
5a
$\dot{W}_{turbine}$

An energy balance yields

$$\dot{W}_{turb} = (\dot{m}_o - \dot{m}_c + \dot{m}_f)C_{pta}(T_{t4c} - T_{t5a})$$

The power balance between the turbine and compressor yields

$$\dot{m}_o\,C_{pc}(T_{t3} - T_{t2}) = \eta_m(\dot{m}_o - \dot{m}_c + \dot{m}_f)C_{pta}(T_{t4c} - T_{t5a})$$

which can be simplified to

$$\tau_{rotor} = 1 - \left[\frac{\tau_r(\tau_c - 1)}{\eta_m(1 - \epsilon + f)\tau_\lambda}\right]$$

The pressure drop across the rotor is therefore given by

$$\pi_{rotor} = \tau_{rotor}^{\frac{\gamma_t}{(\gamma_t - 1)e_t}}$$

A.15 Adiabatic, constant pressure mixer- model 2

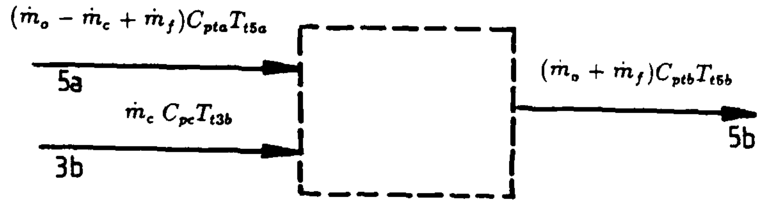
$(\dot{m}_o - \dot{m}_c + \dot{m}_f)C_{pta}T_{t5a}$
5a
$\dot{m}_c\ C_{pc}T_{t3b}$
3b
$(\dot{m}_o + \dot{m}_f)C_{ptb}T_{t5b}$
5b

An energy balance yields

$$(\dot{m}_o - \dot{m}_c + \dot{m}_f)C_{pta}T_{t5a} + \dot{m}_c\ C_{pc}T_{t3b} = (\dot{m}_o + \dot{m}_f)C_{ptb}T_{t5b}$$

which can be simplified to

$$\tau_{mixer} = \frac{T_{t5b}}{T_{t5a}} = \frac{1}{(1+f)}\left(\frac{C_{pta}}{C_{ptb}}\right)\left[1 + f - \epsilon + \left(\frac{\epsilon\tau_r\tau_c}{\tau_\lambda\tau_{rotor}}\right)\right]$$

APPENDIX B DETAILS OF THE UNCERTAINTY ANALYSIS

Appendix B presents the details, results and discussion of the uncertainty analysis for h.

B.1 Moffat-Kline method

Moffat (1982) discusses two ways of describing the relative uncertainty in a final experimental result (R) which is a function of N measured quantities

$$R = R(x_1, x_2, \dots x_N)$$

Worst case situation :

$$\frac{\Delta R}{R} = \left|\frac{1}{R}\frac{\partial R}{\partial x_1}\Delta x_1\right| + \left|\frac{1}{R}\frac{\partial R}{\partial x_2}\Delta x_2\right| + \dots \left|\frac{1}{R}\frac{\partial R}{\partial x_N}\Delta x_N\right| \tag{B.1}$$

Constant odds case :

$$\frac{\Delta R}{R} = \left\{\left(\frac{1}{R}\frac{\partial R}{\partial x_1}\Delta x_1\right)^2 + \left(\frac{1}{R}\frac{\partial R}{\partial x_2}\Delta x_2\right)^2 + \dots \left(\frac{1}{R}\frac{\partial R}{\partial x_N}\Delta x_N\right)^2\right\}^{1/2} \tag{B.2}$$

While the value calculated by the worst case method would be useful if the penalty for being wrong is catastrophic, most engineering purposes are served well by using the constant odds method. This method assumes that each of the x_i's is independent, comes from a Gaussian distribution, and possesses the same level of odds. If these conditions are met then the Root-Sum-Square equation reproduces the same level of odds in equation B.2, the final result for $\frac{\Delta R}{R}$.

The question then becomes one of finding the correct or appropriate values of $\Delta x_i'$s to use. Moffat describes three replication levels to be used as a guide in determining what should be included in Δx_i . The most appropriate level for use in this work is the *Nth Order* replication level which is useful for assessing the significance of differences between results from different experiments and between computation and experiment. This level of replication includes the uncertainty contributions from three separate sources:

1. interpolation (or instrument precision) uncertainty
2. unsteadiness effects (timewise variation or instability)
3. instrument calibration uncertainty

The uncertainties from these three sources are combined using the ***Root-sum-square*** equation

$$\Delta x_{i,N} = \left[(\Delta x_{i,1})^2 + (\Delta x_{i,2})^2 + (\Delta x_{i,3})^2\right]^{1/2}$$

To evaluate the derivatives in equations (B.1) and (B.2), which are effectively the x_i-*Sensitivity Coefficients*, the **"Jitter" Program** described by Moffat was

x_i	value	Δx_i	$\frac{\Delta h_i}{h} = \frac{1}{h} * \frac{\partial h}{\partial x_i} \Delta x_i$
time	3 seconds	0.2 seconds	3.3 %
T_{gas}	90.0 °C	0.3 °C	0.5 %
$T_{initial}$	20.0 °C	1.0 °C	5.9 %
$T_{crystal}$	36.2 °C	0.3 °C	2.3 %
$\sqrt{\rho c k}$	569 $\frac{W}{m^2K} sec^{1/2}$	29 $\frac{W}{m^2K} sec^{1/2}$	5.1 %
overall uncertainty (constant odds)			$^{+}_{-}$ 8.7 %
overall uncertainty (worst case)			$^{+}_{-}$ 17.1 %

Table B.1: Contributions of individual measurands for a typical high value of heat transfer coefficient.

x_i	value	Δx_i	$\frac{\Delta h_i}{h} = \frac{1}{h} * \frac{\partial h}{\partial x_i} \Delta x_i$
time	90 seconds	0.2 seconds	0.1 %
T_{gas}	90.0 °C	0.3 °C	0.5 %
$T_{initial}$	20.0 °C	1.0 °C	5.9 %
$T_{crystal}$	36.2 °C	0.3 °C	2.3 %
$\sqrt{\rho c k}$	569 $\frac{W}{m^2K} sec^{1/2}$	29 $\frac{W}{m^2K} sec^{1/2}$	5.1 %
overall uncertainty (constant odds)			$^{+}_{-}$ 8.1 %
overall uncertainty (worst case)			$^{+}_{-}$ 13.9 %

Table B.2: Contributions of individual measurands for a typical base-level value of heat transfer coefficient.

used. This program involved perturbing ("jittering"?) each measurand numerically to determine its effect on the final result as shown in the following equation:

$$\frac{\partial R}{\partial x_i} = \left(\frac{R_{x_i + \epsilon x_i} - R_{x_i - \epsilon x_i}}{2 \epsilon x_i} \right)$$

The results of this analysis are shown in the two tables above; Table B.1 contains the results for a typical high value of h with a colour play time of 3 seconds while Table B.2 contains the same information for a typical base-level value of h (h_o) with a colour play time of 90 seconds.

For both cases the major contributor to the overall uncertainty was the initial temperature of the perspex substrate. Unfortunately it was not possible to prevent the test section from heating slightly during the flow bypass stage of the experimental procedure. Even though the bypass duct was carefully insulated, enough energy managed to escape from the bypass duct to heat the ambient air, thereby causing the perspex wall temperature to rise 0.7 to 1.0°C over the 20 to 30 minute time period required for the air flow to reach steady-state. As mentioned previously, wall thermocouples were used to measure the temperatures on the inside and outside perspex wall surfaces both during the bypass phase and later during the test itself. Because of the "flow feedback" feature which allowed ambient air to travel backwards through the test section during the bypass phase, both surfaces increased in temperature at about the same rate (the typical temperature difference between the inside and outside surface was less than $0.2°C$). However it was still possible, although unlikely, for the middle of the wall to be at a lower temperatures. An independent check, which is to be discussed shortly, shows that the initial wall temperature was essentially uniform at this new, slightly elevated level. The value of the inside wall surface temperature immediately before flow triggering was the value used to calculate h.

The second largest contributor to the uncertainty in h was the thermal product ($\sqrt{\rho c k}$) of perspex. The value of this constant and it's associated uncertainty was measured and reported by **Ireland (1987)**. The remaining measurands were all minor contributors with values below 3.5%.

B.2 Saabas-Arora-Abdel Messeh method

Saabas et al (1987) argue that the Moffat-Kline approach towards uncertainty analysis is not appropriate because in transient tests not all measured quantities form a Gaussian distribution about the true value as they usually do during steady state tests. While the measured quantities still have random components of uncertainty, additional fixed or biased components also contribute in ways that make it impossible or impractical to separate the two types.

In the present work's experimental situation, some sort of bias might possibly have affected the following three measurands:

- $\Delta T_{initial}$ might possibly have had a positive bias since the deviation of the measured value from the true value was likely to be positive. As mentioned previously, the value of $T_{initial}$ used to calculate h was the value measured immediately before tunnel triggering. Although there is reason to believe that the wall temperature was essentially uniform, it was possible that the temperature within the middle of the wall might have been slightly lower than at the surface.

- $\Delta time$ might also have had a positive bias since the flow triggering and initialisation did not take place instantaneously. By assuming that it did, the measured value of time was slightly larger than the time that the flow was actually sensed by the test wall surface.

- ΔT_{gas} might have had a negative bias. Even though the thermocouple stem conduction losses and the radiation losses were shown to be negligible in magnitude, the measured values of the gas temperature were still slightly less than the true value.

Since this is a "worst case" examination of the effect of bias, the entire value of Δx_i for each of the above is considered biased and is given the appropriate sign. The remaining two measured quantities, the liquid crystal colour play temperature and the thermal constant for perspex, did not possess any detectable bias. Both positive and negative values of the uncertainty for each of these two measurands are therefore considered in the following analysis.

To evaluate the relative uncertainty in h, **Saabas** proposed the use of the total differential as shown in the following. The exact solution to the semi-infinite, one-dimensional conduction equation used in this work is

$$\theta = 1 - exp(\beta^2)\,[1 - erf(\beta)] \tag{B.3}$$

where

$$\theta = \frac{(T_{crystal} - T_{initial})}{(T_{gas} - T_{initial})} \tag{B.4}$$

and

$$\beta = \frac{h\sqrt{t}}{\sqrt{\rho ck}} \tag{B.5}$$

Since h can not be solved for directly, the total differentials of (B.3) and (B.4) are obtained

$$\Delta\theta = \frac{\partial\theta}{\partial T_{cry}}\Delta T_{cry} + \frac{\partial\theta}{\partial T_{init}}\Delta T_{init} + \frac{\partial\theta}{\partial T_{gas}}\Delta T_{gas} \tag{B.6}$$

and

$$\Delta\theta = \frac{\partial\theta}{\partial h}\Delta h + \frac{\partial\theta}{\partial t}\Delta t + \frac{\partial\theta}{\partial\sqrt{\rho ck}}\Delta\sqrt{\rho ck} \tag{B.7}$$

Equating (B.6) and (B.7), then solving for Δh yields

$$\Delta h = \frac{1}{\frac{\partial\theta}{\partial h}}\left(\frac{\partial\theta}{\partial T_{cry}}\Delta T_{cry} + \frac{\partial\theta}{\partial T_{init}}\Delta T_{init} + \frac{\partial\theta}{\partial T_{gas}}\Delta T_{gas}\right.$$

$$\left. - \frac{\partial\theta}{\partial t}\Delta t - \frac{\partial\theta}{\partial\sqrt{\rho ck}}\Delta\sqrt{\rho ck}\right) \tag{B.8}$$

Each of the derivatives in (B.8) is now evaluated.The derivatives of θ with respect to the three temperatures are

$$\frac{\partial\theta}{\partial T_{cry}} = \frac{1}{(T_{gas} - T_{init})} \tag{B.9}$$

$$\frac{\partial\theta}{\partial T_{init}} = -\frac{1}{(T_{gas} - T_{init})} + \frac{(T_{cry} - T_{init})}{(T_{gas} - T_{init})^2} = \frac{-1 + \theta}{(T_{gas} - T_{init})} \tag{B.10}$$

$$\frac{\partial\theta}{\partial T_{gas}} = -\frac{(T_{cry} - T_{init})}{(T_{gas} - T_{init})^2} = -\frac{\theta}{(T_{gas} - T_{init})} \tag{B.11}$$

To evaluate the derivatives of θ with respect to t, $\sqrt{\rho ck}$, and h, the chain rule is employed. Therefore,

$$\frac{\partial\theta}{\partial t} = \frac{\partial\theta}{\partial\beta}\frac{\partial\beta}{\partial t} \tag{B.12}$$

$$\frac{\partial\theta}{\partial\sqrt{\rho ck}} = \frac{\partial\theta}{\partial\beta}\frac{\partial\beta}{\partial\sqrt{\rho ck}} \tag{B.13}$$

$$\frac{\partial\theta}{\partial h} = \frac{\partial\theta}{\partial\beta}\frac{\partial\beta}{\partial h} \tag{B.14}$$

To evaluate $\frac{\partial\theta}{\partial\beta}$, the first term in equations (B.12),(B.13), and (B.14), reference is made to the **Handbook of Mathematical Functions, (p.298)** to determine that

$$\frac{d}{d\beta}erf(\beta) = \frac{2}{\sqrt{\pi}}exp(-\beta^2) \tag{B.15}$$

Therefore

$$\frac{\partial\theta}{\partial\beta} = -2\beta\ exp(\beta^2)\left[1 - erf(\beta)\right] + \frac{2}{\sqrt{\pi}} = -2\beta(1-\theta) + \frac{2}{\sqrt{\pi}} \tag{B.16}$$

The second terms in (B.12),(B.13), and (B.14) are

$$\frac{\partial\beta}{\partial t} = \frac{1}{2}\frac{h}{(\sqrt{\rho ck}\,\sqrt{t}\,)} \tag{B.17}$$

$$\frac{\partial\beta}{\partial\sqrt{\rho ck}} = -\frac{h\sqrt{t}}{(\sqrt{\rho ck})^2} \tag{B.18}$$

$$\frac{\partial\beta}{\partial h} = \frac{\sqrt{t}}{\sqrt{\rho ck}} \tag{B.19}$$

Substitution of the derivatives back into (B.8) yields the final analytical expression for Δh.

$$\Delta h = \frac{\Delta T_{cry} + (\theta-1)\Delta T_{init} - \theta\Delta T_{gas}}{\left[2\beta(\theta-1) + \frac{2}{\sqrt{\pi}}\right]\left(\frac{\sqrt{t}}{\sqrt{\rho ck}}\right)(T_{gas} - T_{init})}$$

$$-\frac{1}{2}h\left(\frac{\Delta t}{t}\right) + h\left(\frac{\Delta\sqrt{\rho ck}}{\sqrt{\rho ck}}\right) \tag{B.20}$$

Finally, dividing by h, the expression for the relative uncertainty is obtained

$$\frac{\Delta h}{h} = \frac{\Delta T_{cry} + (\theta-1)\Delta T_{init} - \theta\Delta T_{gas}}{\left[2\beta^2(\theta-1) + \frac{2\beta}{\sqrt{\pi}}\right](T_{gas} - T_{init})}$$

$$-\frac{1}{2}\left(\frac{\Delta t}{t}\right) + \left(\frac{\Delta\sqrt{\rho ck}}{\sqrt{\rho ck}}\right) \tag{B.21}$$

The uncertainty contributions for each of the measurands were calculated using this equation and are listed in Table B.3. One thing immediately becomes apparent;

x_i	value	*biased* Δx_i	$\frac{\Delta h_i}{h} = \frac{1}{h} * \frac{\partial h}{\partial x_i} \Delta x_i$
time	3 seconds	+0.2 seconds	-3.3 %
time	90 seconds	+0.2 seconds	-0.1 %
T_{gas}	90.0 °C	-0.3 °C	+0.5 %
$T_{initial}$	20.0 °C	+1.0 °C	-5.9 %
$T_{crystal}$	36.2 °C	+0.3 °C	+2.3 %
$T_{crystal}$	36.2 °C	-0.3 °C	-2.3 %
$\sqrt{\rho c k}$	569 $\frac{W}{m^2 K} sec^{1/2}$	+29 $\frac{W}{m^2 K} sec^{1/2}$	+5.1 %
$\sqrt{\rho c k}$	569 $\frac{W}{m^2 K} sec^{1/2}$	-29 $\frac{W}{m^2 K} sec^{1/2}$	-5.1 %

Table B.3: Contributions of individual measurands calculated using the method of Saabas et al.

the contributions for each measurand calculated using this method are precisely the same values as the contributions calculated using Moffat's **Jitter Program** except that the values in Table B.3 possess a positive or negative sign. Therefore, the only difference between the two methods is how the contributions are combined to yield the final uncertainty value. Furthermore, the signs of the contributions listed in Table B.3 seem reasonable:

- Overestimating the time to reach the colour play temperature resulted in underestimating h.
- Underestimating the gas temperature resulted in overestimating h.
- Overestimating the initial temperature resulted in underestimating h.

The final combined relative uncertainty values are given in Tables B.4 and B.5, for colour play times of 3 seconds and 90 seconds, respectively. Four values are given for each time to account for the four possible combinations of $\overset{+}{-} \sqrt{\rho c k}$ and $\overset{+}{-} \Delta T_{crystal}$ since those quantities to do not have any detectable component of biased uncertainty.

During the interpretation of these results, it should remembered that the sign of the bias was applied to the total value of Δx_i so the results given in Tables B.4 and B.5 represent the "worst case" situations for the possible effects of biased uncertainties. For the case of a positive $\Delta\sqrt{\rho c k}$ the estimated overall uncertainty using the method is very small because of cancelling errors; the uncertainty contribution from $\sqrt{\rho c k}$ cancels the contribution from $T_{initial}$. Unfortunately, for the case of a negative $\Delta\sqrt{\rho c k}$ the uncertainty contributions of $\sqrt{\rho c k}$ and $T_{initial}$ have the same sign which results in large values of overall uncertainty. Another interesting conclusion produced by this method is that the values of h presented in this work are likely to be less than the true values. This might be a source of reassurance since underestimating the cooling effect is probably more desirable from a cooling passage design standpoint than overestimating it.

$\frac{\Delta h}{h}$ (*time*= 3 seconds)	$+\Delta T_{crystal}$	$-\Delta T_{crystal}$
$+\Delta\sqrt{\rho ck}$	-1.3 %	-5.9 %
$-\Delta\sqrt{\rho ck}$	-11.5 %	-16.1 %

Table B.4: Results considering biased uncertainty contributions for a typical high heat transfer coefficient.

$\frac{\Delta h}{h}$ (*time*= 90 seconds)	$+\Delta T_{crystal}$	$-\Delta T_{crystal}$
$+\Delta\sqrt{\rho ck}$	+1.9 %	-2.7 %
$-\Delta\sqrt{\rho ck}$	-8.3 %	-12.9 %

Table B.5: Results considering biased uncertainty contributions for a typical baseline heat transfer coefficient.

B.3 An independent check provided by a second liquid crystal coating

As shown previously in Chapter 5, a mixture of two liquid crystal substances was applied to the test surfaces on three out of the four hole configurations as well as the slot configuration. The thermochromic properties of the second liquid crystal substance were such that it changed colour at a temperature approximately $5^{o}C$ higher than the first liquid crystal substance. Therefore, the double crystal method produced two complete sets of isothermal contours for every test. Of course, the first series of contours to appear during the test reflected the lower liquid crystal colour play temperature as the wall surface temperature rose above the room temperature. Later, as the wall surface temperature continued to increase, the second series of contours occupied precisely the same positions as the first contours. Therefore, for each contour position, two times were observed and recorded directly from the video. As shown in the following, the ratio of these two observed times should be constant for any given test. The calculation of this time ratio served as a useful test to examine the effects of parameters whose influence might change with time, including the effect of neglecting the *time* due to flow initialization at the beginning of the transient test, the uncertainty due to a nonuniform $T_{initial}$, the influence of the changing upstream thermal boundary condition, and the error caused by two-dimensional conduction.

The following argument shows that the ratio of the two colour play times for each isothermal contour position should be constant. The solution to the one-dimensional, semi-infinite conduction equation is given again below

$$\theta = 1 - exp\beta^2\left[1 - erf(\beta)\right]$$

The double crystal method provides two values of θ corresponding to the two colour change temperatures

$$\theta_1 = \frac{(T_{crystal\ 1} - T_{initial})}{(T_{gas} - T_{initial})} \qquad \theta_2 = \frac{(T_{crystal\ 2} - T_{initial})}{(T_{gas} - T_{initial})}$$

The solution then provides two unique values of β corresponding to the two values of θ

$$\beta_1 = \frac{h\sqrt{t_1}}{\sqrt{\rho ck}} \qquad \beta_2 = \frac{h\sqrt{t_2}}{\sqrt{\rho ck}}$$

The solution is based on the assumptions that the values of h, T_{gas}, and $\sqrt{\rho ck}$ remain constant with time and that the entire wall is initially uniform in temperature at $T_{initial}$. Therefore, equating h yields

$$t_2/t_1 = (\frac{\beta_2}{\beta_1})^2 = constant$$

This equation can be used to predict the value of t_2/t_1 by calculating β_1 and β_2 using the measured values of $T_{gas}, T_{initial}$, $T_{crystal\ 1}$, and $T_{crystal\ 2}$. This predicted value can then be compared to the observed value of t_2/t_1 taken directly from the video. The simplest check, however, and one that should be made immediately after the installation of any new test section, is to verify that t_2/t_1 is constant at all of the positions (and therefore for the duration of the test). This check does not even require any temperature instrumentation as only the times recorded from the video are used.

Figure B.1 shows typical results for the 150° *hole*, the 30° *hole*, and the *slot* configurations, respectively. As shown in Figures B.1A and B.1C, the observed values of t_2/t_1 are almost constant (standard deviation is less than 3%) and very close to the predicted values. The slight amount of scatter in the observed values can be attributed to the experimental uncertainty associated with picking the exact moment when the second contour matches the shape and position of the first contour due to the finite thicknesses of the contours. However, for each configuration, the average of the observed values of t_2/t_1 is very close to the predicted value.

These results answer several concerns involving experimental uncertainty including the effect of neglecting the flow initiation time at the start of the transient test. The flow initiation time which is on the order of 0.1 to 0.2 seconds was assumed to be negligible relative to colour play times on the order of 3 to 90 seconds. The time ratio results shown in Figures B.1 support this assumption. If accounting for the flow initiation time was important, the observed values of t_2/t_1 would have been above the predicted values in the region near the hole edge (the errors in time being more apparent at the shorter colour play times). No such variation was observed, as the actual ratio remained almost constant.

Another concern addressed by the time ratio check was the effect of a possible non-uniform initial temperature. If a significant depthwise variation in $T_{initial}$ existed, it would show up as a long term variation in t_2/t_1 as the thermal pulse passed through zones of different temperature. It appears that the uncertainty in $T_{initial}$ of 1°C resulting in an uncertainty contribution of 5.9% may have been overstated. This

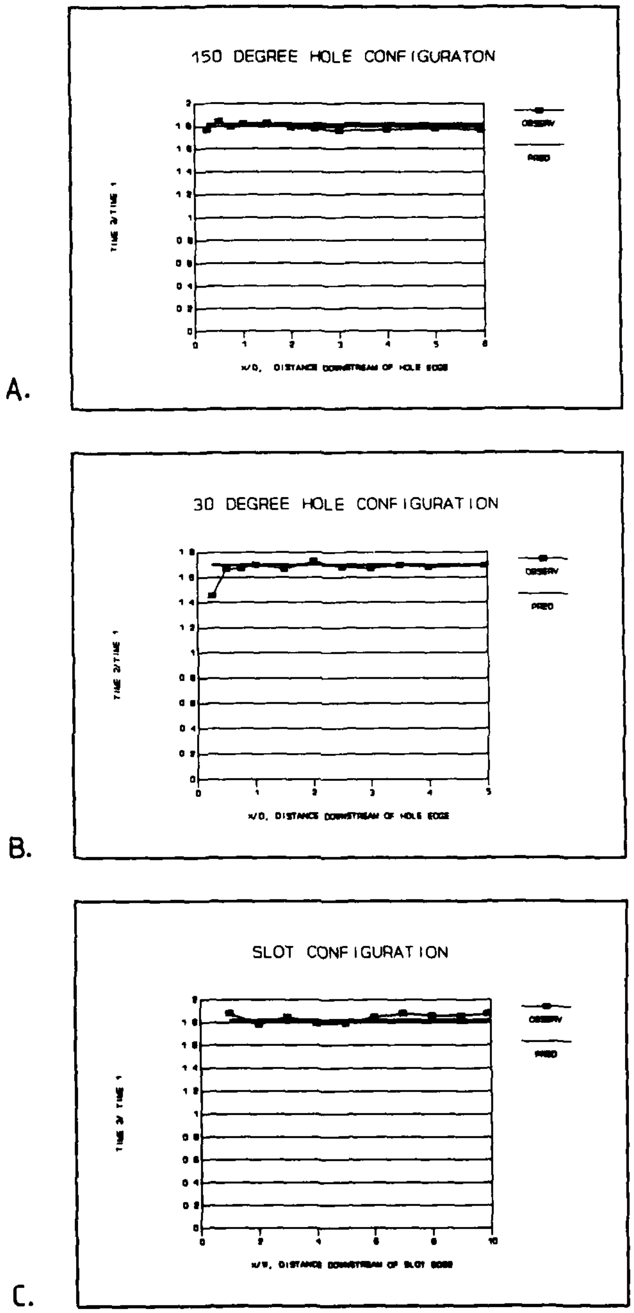

Figure B.1: **Observed versus predicted values of the time ratio for the A.) 150° *hole*. B.) 30° *hole*. C.) *slot* configuration.**

sort of variation certainly did not appear in the time ratio results. If the entire wall was indeed uniform, then a more appropriate value of $\Delta T_{crystal}$ would be $\pm\, 0.3^\circ\, C$ which would contribute only 1.8% to the total relative uncertainty resulting in $\frac{\Delta h}{h}$ values of $\pm\, 6.8\%$ for the 3 second colour play and $\pm\, 5.9\%$ for the 90 second colour play.

As mentioned previously, the definition of h is based on the assumption that the thermal boundary condition can be approximated as an isothermal wall. Obviously each test begins with an isothermal boundary condition as the entire wall is at $T_{initial}$, but wall temperature non-uniformities become present as the wall temperature begins to rise immediately after flow initiation. Although surface temperature variations do exist in the fairly limited region of the test section, these temperature differences are small relative to the driving potential $(T_{gas} - T_{wall})$. However, in the inlet region of the duct, approximately 1.5 metres upstream of the test section, large differences in surface temperatures exist due to the variation of h associated with a developing thermal boundary layer. **Ireland (1987)** showed both experimentally and analytically that this timewise variation in the upstream thermal boundary layer had a negligible effect on the value of h at a point in the tunnel test section. This is because the test section was sufficiently far away from the inlet region of the duct that the influences of the changing upstream thermal boundary condition and the associated wall temperature differences were not felt. All of this points to the fact that h should remain constant with time for the duration of the transient test. This assumption was an essential part in the argument above that the value of t_2/t_1 should be constant with time. The results shown in Figure B.1, indicating that t_2/t_1 does remain constant, support that assumption in accordance with the findings of **Ireland (1987)**.

Finally, the double crystal method provides a check for two- dimensional conduction. As shown in Figure B.1B, the values of t_2/t_1 for the 30 deg hole configuration at $x/D = 0.25$ is 9% lower than the predicted value while the value at $x/D = 0.50$ is 3% lower. The reason for this is two-dimensional conduction in a very small region downstream of the hole as shown in Figure B.2. The second crystal colour play time is lower than predicted because the thermal pulse from inside the hole has had enough time to reach and interact with the thermal pulse from the wall surface. Obviously, the first crystal colour play time was used in the calculation of h since there was less time for interaction between the two thermal pulses to affect the value of h.

B.4 Uncertainty analysis summary

Initially the Moffat-Kline method indicated that the uncertainty was $\pm\, 8.7\%$ based on an uncertainty in $\Delta T_{initial}$ of $\pm\, 1^\circ C$. An independent check using the double-crystal time ratios indicated that this level of uncertainty for the initial temperature was probably overstated. Therefore the updated value of $\frac{\Delta h}{h}$ based on a $\Delta T_{initial}$ of $\pm\, 0.3^\circ C$ was $\pm\, 6.8\%$. Finally as Moffat pointed out, one of the most reliable methods

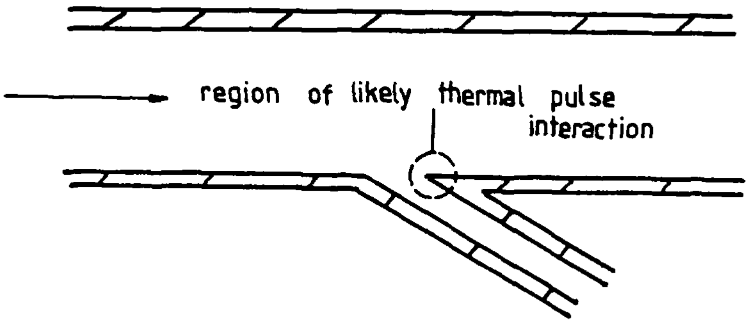

Figure B.2: **Possible thermal pulse interaction in the 30° *hole* configuration.**

for resolving the uncertainties that exist in uncertainty analysis is to compare a portion of one's own experimental results with an established correlation that has "stood the test of time". The base-level heat transfer results presented earlier suggest that the uncertainty is within $\pm$ 7%. Therefore 7% is the value of uncertainty that is assigned to the values of h presented in this thesis. This is also in agreement with the results of **Baughn, Ireland, and Jones (1988)**, in which a direct comparison was made between results obtained from the present method and those obtained from the steady-state, heated coating method.

REFERENCES

Ainsworth, R.W., and Jones, T.V., 1979, "Measurement of Heat Transfer in Circular, Rectangular and Triangular Ducts, Representing Typical Turbine Blade Internal Cooling Passages Using Transient Techniques", *ASME Paper No.79-GT-40.*

Andrews, G.E., Gupta, M.L., and Mkpadi, M.C., 1985, "Full Coverage Discrete Hole Film Cooling: Cooling Effectiveness", *International Journal of Turbo and Jet Engines*, Vol.2, pp.199-212.

Baughn, J.W., Ireland, P.T., Jones, T.V., and Saniei,N., 1988, "A Comparison of the Transient and Heated- Coating Methods for the Measurement of Local Heat Transfer Coefficients on a Pin Fin", *ASME Paper No.88-GT-180.*

Beacock, R.J., 1977, "Aerodynamics and Heat Transfer of Leading Edge Films", *Rolls-Royce Brochure No. 2D2-52D* (Restricted).

Bonnett, P., 1989, "Liquid Crystals in Heat Transfer", *D. Phil. Thesis*, University of Oxford.

B.D.H Chemicals Ltd , 1986, "Thermochromic Liquid Crystals", Broom Road, Poole, BH12 4NN, England.

Brown, A. and Saluja, C.L., 1978, "The Use of Cholesteric Liquid Crystals for Surface-Temperature Visualisation of Film-Cooling Processes", *J. Phys. E: Sci. Instrum.*, Vol.11, pp.1068- 1072.

Byerley, A.R., Ireland, P.T., Jones, T.V., and Ashton, S.A., 1988,"Detailed Heat Transfer Measurements Near and Within the Entrance of a Film Cooling Hole", *ASME Paper No.88-GT- 155.*

Byerley, A.R., Ireland, P.T., Jones, T.V. and Graham, C.G., 1988, "Detailed Measurements Near the Entrance to an Inclined Film Cooling Hole Inside a Gas Turbine Blade", *UK National Heat Transfer Conference (IMechE), Glasgow, UK, Paper No.C164/88.*

Byworth, S., 1986, "Design and Development of High-Temperature Turbines", *The Rolls-Royce Magazine*, No.29.

Camci, C., 1988, "An Experimental and Numerical Investigation of Near Cooling Hole Heat Fluxes on a Film Cooled Turbine Blade", *ASME Paper No.88-GT-9.*

Chu, T., Brown, A. and Garrett, S., 1985, "Discharge Coefficients of Impingement and Film Cooling Holes", *ASME Paper No.85-GT-81.*

Clifford, R.J., Jones, T.V., and Dunne, S.T., 1983, "Techniques for Obtaining Detailed Heat Transfer Coefficient Measurements within Gas Turbine Blade and Vane Cooling Passages", *ASME Paper No.83-GT-58.*

Cooper, T.E., Field, R.J., and Meyer, J.F., 1975, "Liquid Crystal Thermography and its Application to the Study of Convective Heat Transfer", *ASME Journal of Heat Transfer*, Vol.97, pp.442-450.

Crane, R.I., and Sabzvari, J., "Liquid Crystal Mapping of Laminar Convective Heat Transfer in the Presence of Görtler Vortices", *UK National Heat Transfer Conference (IMechE), Glasgow, UK, paper number C101/88.*, pp.687-700.

Dunne, S.T., 1982, "A Study of Flow and Heat Transfer in Gas Turbine Blade Cooling Passages", D.Phil Thesis, Department of Engineering Science, University of Oxford, England.

Eibeck, P.A., and Eaton, J.K., 1987, "Heat Transfer Effects of a Longitudinal Vortex Embedded in a Turbulent Boundary Layer", *Journal of Heat Transfer*, Vol.109, pp.16-24.

Ferguson, J.L., 1964, "Liquid Crystals", *Scientific American*, Vol.211, No.2.

Frisch, B., 1988, "Kryptonite they are not", *Aerospace America*, Vol.5, pp.16.

Goldstein, R.J. and Chen, H.P., 1985, "Film Cooling on a Gas Turbine Blade Near the End Wall", *Journal of Engineering for Gas Turbines and Power*, Vol.107, pp. 117.

Hay, N., Lampard, D. and Benmansour, S., 1983, "Effect of Crossflows on the Discharge Coefficient of Film Cooling Holes", *Journal of Engineering for Power*, Vol.105.

Hippensteele, S.A., Russell, L.M., and Stepka, F.S., 1981, "Evaluation of a Method for Heat Transfer Measurements and Thermal Visualization Using a Composite of a Heater Element and Liquid Crystals", *ASME Paper No.81-GT-93.*

Hippensteele, S.A., Russell, L.M., and Torres, F.J., 1985, "Local Heat-Transfer Measurements on a Large Scale-Model Turbine Blade Airfoil Using a Composite of a Heater Element and Liquid Crystals", *Journal of Engineering for Gas Turbines and Power*, Vol.107, pp.953-960.

Holland, M.J., and Thake, T.F., "Rotor Blade Cooling in High Pressure Turbines", *J. Aircraft*, Vol.17, No.6, Article No.80-4061, pp.412-418.

Ireland, P.T., 1987, "Internal Cooling of Turbine Blades", *D.Phil. Thesis*, University of Oxford.

Ireland, P.T. and Jones, T.V., 1985, "The Measurement of Local Heat Transfer Coefficients in Blade Cooling Geometries." *AGARD Conference on Heat Transfer and Cooling in Gas Turbines*, CP 390 Paper No.28, Bergen.

Ireland, P.T. and Jones, T.V., 1986, "Detailed Measurements of Heat Transfer On and Around a Pedestal in Fully Developed Passage Flow", *Proceedings of the 8th International Heat Transfer Conference*, San Francisco, (Hemisphere), Vol.3, pp 975-80.

Ireland, P.T. and Jones, T.V., 1987a, "The Response Time of a Surface Thermometer Employing Encapsulated Thermochromic Liquid Crystals", *Journal of Physics E: Sci. Instrum.*, Vol.20, I.O.P Publishing Ltd, England.

Ireland, P.T. and Jones, T.V., 1987b, " Note on the Double Crystal Method of Measuring Heat Transfer Coefficient", *Oxford University Department of Engineering Science Report No. 1710/87.*

Ireland, P.T., Wang, Z., Jones, T.V., and Byerley, A.R., 1988, "A Cold Heat Transfer Tunnel Employing Liquid Crystals for Measuring Full Surface Heat Transfer Coefficients over Turbine Blade Passages", *Proceedings of the 9th Symposium on Measurement Techniques for Transonic and Supersonic Flows in Cascades and Turbomachines*, St Catherine's College, Oxford.

Jeal, B., 1988, "Moving Towards the Non-Metallic Aero Engine", *The Rolls-Royce Magazine*, No. 36, pp.23.

Jones, T.V. and Hippensteele, S.A., 1987, "High Resolution Heat Transfer Coefficient Maps Applicable to Compound-Curve Surfaces Using Liquid Crystals in a Transient Wind Tunnel", *ASME HTD*, Vol.21, pp 17-25.

Kays, W.M., and Crawford, M.E., 1980, *Convective Heat and Mass Transfer*, McGraw-Hill Book Company, New York.

Langston, L.S. and Boyle, M.T., 1982, "A New Surface-Streamline Flow-Visualisation Technique", *J. Fluid Mech.*, Vol.125, pp.53-57.

Linsell, D.F., 1983, "Liquid Crystal Thermography for Visualization of Surface Effects of Fluid Jets in Crossflow", *RNEC-TR-83004*, Royal Naval Engineering College, Manadon, Plymouth.

Lloyd, S., and Brown, A., 1985, "Fluid Flow and Heat Transfer Characteristics in the Entrance Region of Circular Pipes," *ASME Paper No.85-GT-121.*

Lloyd, S., and Brown, A., 1986, "Velocity and Turbulence Fields in Pipe Entrance Regions in the Presence of Cross Flows," *ASME Paper No.86-GT-119.*

Mahle, R.E., 1988, private communication.

Makow, D.M., 1979, "Color Properties of Liquid Crystals and Their Application to Visual Arts", *COLOR research and application*, Vol.4, No.1., pp.25-32.

McDonnell, D.G. and Sage, I., 1982, "New Thermochromic Liquid Crystals", *Advances in Medical Thermology*, Plenum Press, p.305.

Metzger, D.E., and Cordaro, J.V., 1979, "Heat Transfer in Short Tubes Supplied From A Cross Flowing Stream", *ASME Paper No.79-WA/H-16.*

Metzger, D.E. and Mahle, R.E., 1983, "Gas Turbine Engines", *Mechanical Engineering*, pp. 44-52.

Metzger, D.E., and Larson, D.E., 1986, "Use of Melting Point Surface Coatings for Local Convection Heat Transfer Measurements in Rectangular Channel Flows With 90-deg Turns", *Journal of Heat Transfer*, Vol.108, pp.48-54.

Moffat, R.J., 1982, "Contributions to the Theory of Single- Sample Uncertainty Analysis", *Journal of Fluids Engineering*, Vol.104, pp.250.

Morland, L.C., 1989, "Mathematical Models for a Fluid Flow Arising in Turbine Blade Cooling Passages", *D.Phil. Thesis*, University of Oxford.

Oates, G.C., editor, 1978, "Aerothermodynamics of Aircraft Gas Turbine Engines", USAF Report AFAPL TR 78-52, Wright- Patterson AFB, Ohio 45433

Oates, G.C., 1984, *Aerothermodynamics of Gas Turbine and Rocket Propulsion*, AIAA Education Series.

Petty, J.S. and Henderson, R.E., 1986, "The Coming Revolution in Turbine Engine Technology", Turbine Engine Division, Air Force Wright Aeronautical Laboratories, Wright-Patterson Air Force Base, Ohio, U.S.A. 45433.

Patankar, S.V., Basu, D.K., and Alpay, S.A., 1977, "Prediction of the Three-Dimensional Velocity Field of a Deflected Turbulent Jet", *Journal of Fluids Engineering*, Vol.99, p.758.

Pitcher, I.C., 1987, "*IBM* Parallel Input/Output Card Interface and Junction Technical Manual", Osney Internal Cooling Group pamphlet.

Rhee, H.S., Koseff, J.R., and Street, R.L., 1984, "Flow Visualization of a Recirculating Flow by Rheoscopic Liquid and Liquid Crystal Techniques", *Experiments in Fluids*, Vol.2, pp.111-118.

Rohde, J. E., Richards, H.T.,and Metger, G.W., 1969,"Discharge Coefficients for Thick Plate Orifices with Approach Flow Perpendicular and Inclined to the Orifice Axis", *NASA TND-5467.*

Rogers, T. and Hersh, A.S., 1975, "The Effect of Grazing Flow on the Steady State Resistance of Square-Edged Orifices", *AIAA Paper No.75-493.*

Russell, C.M.B., Jones, T.V., and Lee, G.H., 1982, "Heat Transfer Using Vortex Generators", *Proceedings of the Seventh International Heat Transfer Conference*, Munich, Fed.Rep. of Germany, Vol.3 pp.283-288.

Saabas, H.J., Arora, S.C., and Abdel Messeh, W.A., 1987, "Application of the Transient Test Technique to Measure Local Heat Transfer Coefficients Associated with Augmented Airfoil Cooling Passages", *ASME Paper No.87-GT-212.*

Schultz, D.L. and Jones , T.V., 1973, "Heat Transfer Measurements in Short-Duration Hypersonic Facilities. " NATO Advisory Group for Aeronautical Research and Development (AGARD), *AG165.*

Schneider, P.J., 1957, *Conduction Heat Transfer*, Addison- Wesley Publishing Company, Inc., Reading,Massachusetts, p.263.

Simonich, J.C. and Moffat, R.J., 1982, "New Technique for Mapping Heat-Transfer Coefficient Contours", *Rev. Sci. Instrum.* , Vol.53, No.5, pp.678-683.

Sparrow, E.M., and Kemink, R.G., 1979, "Heat Transfer Downstream of a Fluid Withdrawal Branch in a Tube", *ASME Journal of Heat Transfer* Vol.101.

Sparrow, E.M., and Ortiz, M.C., 1982, "Heat Transfer Coefficients for the Upstream Face of a Perforated Plate Positioned Normal to an Oncoming Flow", *International Journal of Heat and Mass Transfer*, Vol.25, No.1, pp. 127-135.

Tillman, E.S., Jen, H. F., 1983, "Cooling Airflow Studies at the Leading Edge of a Film-Cooled Airfoil", *ASME Paper No.83-GT-82.*

Tillman, E.S., Hartel, E.O., and Jen, H.F., 1983, "The Prediction of Flow Through Leading Edge Holes in a Film Cooled Airfoil With and Without Inserts", *ASME Paper No.84-GT-4.*

Yeh, F.C. and Stepka, F.S., 1984, "Review and Status of Heat- Transfer Technology for Internal Passages of Air-Cooled Turbine Blades", *Nasa Technical Paper 2232.*

Zharkova, G.M., Kiselev, G.A., and Khachaturyan, V.M., 1986, "Liquid-Crystal Heat Flux Indicators", *Heat Transfer- Soviet Research*, Vol.18, No.3, pp.135-139.